Doctoral Dissertation

Tailored Electrode Structure Design for Enhanced Electrochemical Energy Devices: Topological Optimization of Macro- and Pore-Scale Models with Theoretical Insights from Non-Equilibrium Thermodynamics Based on Entropy Generation Analysis

ALIZADEHKOLAGAR SEYEDMEHRZAD

January 2025

Department of Mechanical Engineering
Graduate School of Engineering,
Osaka University

Abstract

Efforts are underway to improve the performance and efficiency of electrochemical devices like fuel cells and batteries, which share porous electrodes as a key component. The structure of these electrodes significantly affects their performance, cost, and durability, making it crucial to control their porosity. Inside, complex interactions between solid, liquid, and gas phases enable transport and reactions of molecules, electrons, ions, and heat. Computer-aided design, tied closely with mathematical modeling and optimization, plays a central role in optimizing these electrode structures for better performance.

A strong theoretical foundation is essential for understanding the physical principles behind these optimizations. Without it, the mechanisms driving performance improvements may remain unclear. Entropy generation analysis, based on non-equilibrium thermodynamics, helps quantify system inefficiencies, guiding design changes to reduce energy loss and improve efficiency. Integrating entropy generation into optimization offers insights into the trade-offs between performance metrics, supporting the creation of more efficient designs.

Chapter 2 begins by optimizing porosity in a two-dimensional reaction-diffusion system to improve reaction rates using topological optimization (TO). Chapter 3 extends this to electrochemical systems, optimizing material distribution to enhance electrode performance, using the Butler-Volmer equation for nonlinear kinetics and comparing two optimization strategies. An entropy generation model further highlights system inefficiencies.

Chapter 4 develops a two-phase flow model for a polymer electrolyte membrane fuel cell (PEMFC), optimizing its catalyst layer (CL) to boost output current density and improve oxygen delivery. Chapter 5 introduces a pore-level optimization framework that combines pore network modeling (PNM) with metaheuristic algorithms to optimize porous reactor designs, enhancing reaction rates and efficiency.

Ultimately, the objective of this thesis is to develop innovative design methodologies that enhance the structural configurations of electrodes and porous media in reactive-transport systems. By advancing the understanding of material distributions and transport phenomena, this thesis seeks to contribute to the development of more efficient, sustainable, and cost-effective electrochemical energy conversion technologies.

Contents

List of Figures

List of Tables

The way things are does not determine the way they ought to be.

- Michael Sandel

To my family

Chapter 1

Introduction

Abstract

Electrochemical energy devices hold great promise for addressing the intermittent nature of renewable energy sources, though their widespread adoption is hindered by suboptimal performance and high costs. Identifying the optimal electrode structure is crucial for improving device efficiency. Mathematical modeling and optimization provide powerful methods for discovering ideal structures that are not easily achievable through trial and error. In addition, physicochemical analysis of the optimization process can offer a theoretical framework for understanding effective design principles. This chapter outlines the necessity for improved electrode designs and reviews previous efforts in this area through a detailed literature survey, emphasizing topology optimization methods. Additionally, the discussion will highlight other significant techniques in the structural design of porous electrodes utilizing mathematical optimization. The chapter will also explain the insights gained from entropy generation analysis of an optimal design, aiming to clarify what constitutes a good design from a physics perspective. Finally, the scope of this doctoral dissertation will be outlined.

This chapter is partially published as:

M. Alizadeh, P. Charoen-amornkitt, T. Suzuki, and S. Tsushima. "Recent advances in electrode optimization of electrochemical energy devices using topology optimization", *Progress in Energy*, **7** (2025): 118739. https://doi.org/10.1088/2516-1083/ad8abd

M. Alizadeh, P. Charoen-amornkitt, T. Suzuki, and S. Tsushima. "Analysis of local-global entropy generation in an electrochemical system", In *International Heat Transfer Conference Digital Library*, (2023). https://doi.org/10.1615/IHTC17.440-20

1.1 Introduction

With energy production being a major contributor to greenhouse gas emissions, electrochemical energy storage and conversion systems are critical components in the global shift towards renewable energy adoption. One of the primary challenges in this transition stems from the intermittent nature of renewable energy sources, such as solar and wind power. While electricity can be generated efficiently from these sustainable resources, its production is subject to variations in weather conditions and daylight hours. Consequently, this intermittent availability poses limitations and uncertainties on a continuous and stable supply of energy. To address this challenge, electrochemical energy storage and conversion systems serve as vital solutions. These systems enable the efficient storage of excess energy generated during periods of high production, subsequently distributing it during times of low generation or high demand. The incorporation of electrochemical energy devices (EEDs), such as batteries and fuel cells, can enhance the reliability of renewable energy sources by mitigating the dependence on external factors like weather patterns. This improvement can take various forms, including but not limited to the storage of electricity through secondary batteries, the conversion of chemical energy stored in molecular bonds into electricity, as observed in fuel cells, or the utilization of surplus electricity to produce energy carrier substances and other valuable fuels or compounds, such as through water or carbon dioxide electrolyzers. In essence, these systems provide a means to bridge the gap between energy supply and demand, thereby facilitating the integration of renewable energy into the mainstream power grid. In addition to stationary applications, certain EEDs, exemplified by lithium-ion batteries, have found increasing utility in the transportation sector, particularly in electric vehicles. As a result, electrochemical energy storage and conversion technologies play a pivotal role in enabling a sustainable and resilient energy future.

EEDs comprise various components that depend on their specific type and application. However, they all share a critical component, the "electrode", which typically functions as a porous medium composed of one or several materials. Schematics of various EEDs with their components are shown in 1.1. The performance and lifespan challenges in EEDs are particularly associated with their electrodes, where essential electrochemical reactions occur alongside various transport phenomena. These phenomena include the transfer of mass, momentum, heat, and charge, all of which are critical for the device's overall performance. Electrodes serve as the interfaces

where electrochemical reactions take place, converting chemical energy into electrical energy (and vice versa) or breaking chemical bonds using electricity. However, achieving optimal electrode performance requires comprehensive understanding of complex interactions between the materials used, the design of the electrode structure as well as other components, and the dynamics of transport and rate processes within the device. To drive widespread adoption of EEDs in commercial applications, several key objectives must be addressed. First, there is a need to reduce the fabrication costs associated with electrode materials and manufacturing processes. This involves finding cost-effective materials and production methods without compromising performance or durability. Furthermore, there is a continuous push to enhance the overall performance of EEDs. This includes increasing energy efficiency and capacity, power output, and stability while minimizing losses and degradation over time. Improving electrode design and optimizing material properties are crucial aspects of achieving these performance enhancement requirements. Lastly, extending the operational lifespan of EEDs is paramount for their practical utility and economic viability. This involves developing electrode materials and configurations that can withstand prolonged operation under various operating conditions without significant degradation or loss of performance. Addressing the challenges associated with electrodes in EEDs requires a multidisciplinary approach that integrates materials science, engineering, and electrochemistry.

Given the pivotal role of electrodes in these devices, one of the key challenges in improving electrode performance lies in minimizing irreversible losses that are attributed to the transport phenomena and electrochemical reactions. Irreversible losses can result from various factors, including overpotentials, electrical resistance in the electrode materials, sluggish mass transport, and side reactions that consume energy without contributing to the desired output. To address these challenges and improve electrode performance, a direct approach involves redesigning the electrode structure to minimize these irreversible losses. This can include optimizing the material, composition, and morphology of the electrode to enhance their electrochemical activity and transport properties while mitigating undesirable side reactions and other phenomena. By focusing on minimizing irreversible losses in electrodes, researchers aim to maximize the efficiency and overall performance of EEDs.

In the quest to enhance the performance of EEDs, researchers have explored various

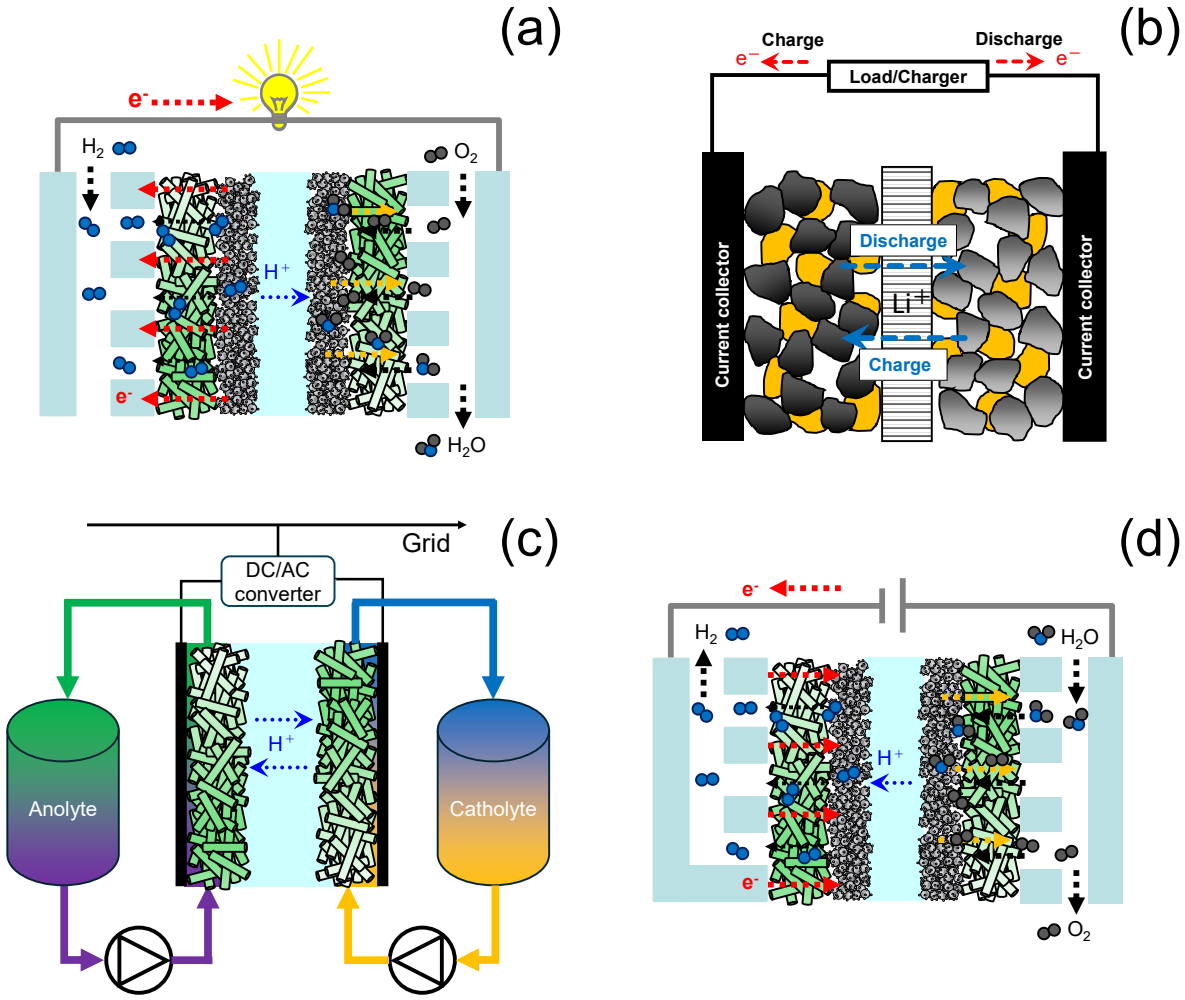

Figure 1.1: Schematic diagram showing the components of EEDs including (a) polymer electrolyte fuel cells, (b) lithium-ion batteries, (c) redox flow batteries, and (d) proton exchange membrane water electrolyzers.

avenues, including the synthesis of novel materials [1–3] and modification of electrodes [4–7]. However, despite these strides, many previous studies [8–10] have relied on a trial-and-error approach to optimize electrode performance. In this methodology, researchers systematically test different materials, configurations, or fabrication techniques to identify optimal conditions for device operation. While this approach has yielded valuable insights and incremental improvements, it can be time-consuming, resource-intensive, and limited in its ability to explore the full design space for a broad range of applications and operational conditions. Moreover, this approach primarily relies on the researcher's intuition and experience, potentially limiting the exploration of design solutions that may not be readily realizable. As a result, there is a growing recognition of the need for more systematic and efficient approaches to electrode design and optimization. By leveraging computational modeling and simulation, advanced characterization techniques, and optimization algorithms, researchers aim to accelerate the discovery and development of high-performance electrode materials and structures. These approaches allow for a more comprehensive exploration of the design space, enabling researchers to identify optimal design solutions more effectively while minimizing the need for extensive experimental testing. Furthermore, by integrating computational modeling with experimental validation, researchers can gain deeper insights into the underlying mechanisms governing multiphysics phenomena occurring in electrodes at nano to macro-scales. This synergistic approach enables researchers to develop a more fundamental understanding of electrochemical processes and design principles, leading to the development of next-generation EEDs with enhanced performance and functionality.

Topology optimization (TO) has emerged as a systematic bottom-up design approach in structural optimization, allowing for the spatial redistribution of materials to achieve enhanced structural performance within a specified design domain [11]. It is defined as a computational method for optimizing material distribution within a defined design space to achieve the best possible performance while meeting specific constraints. While TO has been successfully applied to address various physical challenges in engineering and design [12–18], its application in optimizing systems involving complex (electro-) chemical reactions, particularly in the realm of electrochemistry, has presented ongoing challenges. In the domain of EEDs, TO has previously been utilized for optimizing the design of components such as flow channels [19–21], cooling plates [22–25], and end plates [26–29]. However, recent years have witnessed a notable shift in focus towards the application of TO in the design of porous electrodes across various EEDs. The adoption of TO for porous electrode

design represents a departure from traditional approaches and opens up new possibilities for enhancing the performance of EEDs that was not possible through conventional methods. By systematically reshaping the microstructure of porous electrodes, TO offers the potential to optimize key transport and rate properties such as effective mass diffusivity, charge conductivity, and electrochemical reactive surface area. This shift in approach reflects a growing recognition of the importance of electrode design in determining overall device performance and efficiency. The adoption of TO in porous electrode design represents a promising avenue for advancing the field of electrochemical energy conversion and storage. By leveraging the principles of systematic design optimization, researchers aim to unlock new insights into the fundamental relationships between electrode microstructure, electrochemical performance, and device efficiency.

The mathematical aspect of TO is advancing and their application is expanding to many engineering problems. However, the studies in the literature do not explain how these topologically optimized layouts are beneficial from a fundamental standpoint. In other words, previous research works only focused on improving mathematical algorithms, providing no physical justification for their results. It is known that results of optimization algorithms are highly sensitive to their tuning parameters and mathematical schemes. For instance, choice of filter radius (as an example of tuning parameter) or type of filter (as an example of mathematical scheme) in a TO affects the produced results significantly [30]. This high sensitivity gives a rise to the necessity of a fundamental understanding of the TO process. This gap might be addressed by comparing the non-equilibrium characteristics of the system during the optimization.

Real systems, such as porous electrochemical reactors, are working under a non-equilibrium condition. Therefore, thermodynamic analysis cannot illuminate a thorough picture of the processes in these systems. Non-equilibrium thermodynamics (NET) is an extension of conventional equilibrium thermodynamics to the assess the systems which are not in global equilibrium [31]. Although the system may not be in equilibrium from a global viewpoint, NET assumes that the equilibrium condition holds at the local level. Therefore, fundamental thermodynamics relations, such as Gibbs equations, are valid at a local scale. Given this assumption, the irreversibilities of a system might be quantified in terms of entropy production. By tracing the changes in entropy generation rate during the optimization process, it could be understood how the optimization process leads to a better design from a physical standpoint. At a global level, a better performance (a system with lower

losses) corresponds to a lower total entropy production. This principle is known as Entropy Generation Minimization (EGM) [32] and particularly has been extensively studied in thermofluid systems (e.g., heat exchangers) [33]. Moreover, Equipartition of Entropy Production (EoEP) [34] is another principle that might be used in non-equilibrium thermodynamics analysis at a local level. This principle has been comprehensively studied in heat exchanger and membrane systems [35].

1.2 Topology optimization

TO is a computational technique employed for the automated creation of an optimal structural layout, achieved by identifying the most efficient spatial allocation of material across a predetermined design space [11, 12]. The primary objective of TO is to enhance the performance of a structure, adhering to prescribed design specifications and constraints. Though both fall under the umbrella of layout optimization, TO adopts a more radical approach compared to shape optimization. Unlike shape optimization, which refines an existing design by adjusting its boundaries while preserving the overall layout, TO transcends this limitation. It treats the design space as a vast, unexplored territory, employing computational algorithms to identify the optimal layout from scratch [36]. This allows TO to potentially discover entirely new configurations that may not have been conceived with traditional approaches. Essentially, TO entails iteratively modifying the material allocation within a designated design space to optimize structural performance. Through the elimination of material from non-essential zones and its redistribution to critical areas, the design is refined to fulfill performance goals, such as weight reduction, stiffness maximization, or stress concentration minimization. In the field of porous electrodes, these goals may extend to other factors beyond mechanical properties. These factors include but are not limited to high reactive surface area, electrical charge conductivity, and hydraulic permeability, which ultimately contribute to the overall performance of EEDs.

TO originates from structural engineering and computational mechanics. The concept of enhancing structural efficacy by optimizing material distribution emerged in the latter part of the 20th century [12]. An important contribution to contemporary TO methodologies is evident in the work of Bendsøe and Kikuchi, documented in their publication of 1988 [37]. In this paper, Bendsøe and Kikuchi pioneered the application of homogenization techniques to generate optimal structural topologies. This work represented a notable progression in structural optimization, showcasing

the viability of optimizing material configurations to attain enhanced structural integrity. Building on this foundational work, subsequent researchers advanced the theoretical framework, methodological approaches, and application domains of TO. The integration of mathematical optimization techniques, sophisticated algorithms, and computational advancements empowered engineers and designers to explore unconventional material distributions and generate high-performing structural designs. Consequently, the application of TO has proliferated across diverse problems, such as mechanical [12], chemical [38], thermal [13, 39], fluid [16], microfluidics [36], and acoustic [40] systems. The potential of TO to automate design processes and generate structurally efficient solutions has established it as an indispensable tool for engineers seeking to optimize performance through improved structural designs. As research efforts and computational methods continue to mature, the field of TO undergoes continuous evolution, unveiling novel avenues for structural optimization and fostering advancements in structural efficiency and design innovation.

The field of TO has witnessed significant advancements, with researchers introducing diverse strategies for optimizing structural configurations. Existing literature can be categorized based on various criteria, including parameterization methods, system modeling, optimization algorithms, and design update schemes, each offering advantages and drawbacks. Given the wide variety of TO approaches, we briefly introduce the main techniques used for electrode design. Interested readers may refer to previously published comprehensive reviews [11, 12, 41–44] for more details on mathematical and algorithmic foundations of TO. It is noteworthy that these reviews primarily focus on compliance optimization in mechanical design problems, such as the classical Messerschmitt–Bölkow–Blohm (MBB) beam and cantilever beam. In contrast, optimizing electrode structures involves multi-physics systems that integrate various physical and chemical phenomena, presenting challenges beyond the mathematical aspects of TO, which is the focus of the present thesis. Selecting the appropriate TO framework hinges on factors like problem formulation, geometric complexity, relevant physical phenomena, and chosen models for performance evaluation. Design parameterization refers to the method used to establish the connection between design variables and the resulting physical properties [45]. Two dominant approaches include density-based and level-set methods. Bendsøe and Kikuchi [37] introduced the concept of numerical homogenization, aiming to modify the internal topology for achieving anisotropic material properties instead of solely focusing on

boundary variations. This approach leverages homogenization theory, which estimates the effective material properties at a macroscopic level by treating the material as a uniform medium [12]. It is important to note, as pointed out in [12], that the terms "micro" and "macro" scales within this context are used comparatively and do not correspond to specific length scales (such as "microscale" or "microstructure" typically referring to sizes less than 1 mm). Following homogenization, a density-based method represented by Solid Isotropic Material with Penalization (SIMP) was introduced [46]. Density-based TO is a technique that modifies the density of elements within a fixed finite element mesh, using an interpolation function to adjust mechanical properties and determine the optimal distribution of solid and void material. SIMP, the most commonly used version of density-based TO, seeks to find the optimal material distribution based on an auxiliary density function assigned to each discrete element of the design domain, with values ranging from zero to one. Here, a density $\rho = 1$ and $\rho = 0$ represent solid and void phases, respectively. Intermediate density values ($0 < \rho < 1$) correspond to fictitious materials with properties (e.g., Young's modulus in mechanics or thermal conductivity in heat transfer) lying between those of solid and void phases. While these "gray elements" lack an explicit physical interpretation, the introduction of a continuous density function significantly simplifies the mathematical calculations by transforming the problem from an integer-based to a continuous formulation. It is crucial to remember that the material properties within each element are assumed to be homogeneous, even though the overall (global) material behavior exhibits heterogeneity throughout the entire design domain due to the varying density distribution. Although the properties of the solid and void phases are known, SIMP interpolation, i.e. a power-law relationship, is employed to estimate the properties of these intermediate-density elements. The penalized material density can then be defined as:

$$\rho_{\text{penalized}} = \rho_{\min} + (1 - \rho_{\min})\rho^p \tag{1.1}$$

where $\rho_{\text{penalized}}$ is the penalized density, $\rho_{\min}$ is minimum penalized density, and p is a penalty exponent. It is noteworthy that while the penalized density can theoretically reach zero, introducing a minimum penalized density is often necessary for numerical stability during optimization. The penalty exponent, p, plays a crucial role in steering the optimizer towards assigning either solid or void densities ($\rho = 0$ or 1). By increasing the cost associated with intermediate densities, the penalty term discourages the formation of "gray elements". In other words, assigning a partial density leads to higher material usage without a significant improvement in beneficial

properties like mechanical stiffness. Consequently, the optimizer prioritizes assigning densities close to either zero or one, ultimately leading to a clear distinction between solid and void regions within the design. The effective material properties in each element as a function of penalized density is given by [45]:

$$\lambda^{\text{eff}} = \lambda_{\min} + (\lambda_{\max} - \lambda_{\min})\rho_{\text{penalized}} \tag{1.2}$$

in which $\lambda_{\min}$ and $\lambda_{\max}$ are minimum and maximum values of physical properties, corresponding to the void and solid phases. Other interpolation schemes with similar principles exist, such as Rational Approximation of Material Properties (RAMP) and Darcy [47–49]. Porous electrodes in EEDs typically comprise multiple phases. For instance, carbon fiber electrodes contain a carbon phase and voids, while fuel cell catalyst layers involve a mix of catalyst material, support material, polymer binder, and voids. Extensive research has explored the connection between electrode microstructure and key properties like catalytic activity, mass diffusivity, reactive surface area, and permeability. These studies employ experimental, numerical, and theoretical approaches to establish correlations linking macroscopic material characteristics (e.g., volume fraction of each phase or porosity) to bulk material properties [50–59]. A prominent example is the Bruggeman equation, which relates tortuosity and porosity based on effective medium theory [53]. Despite their limitations, assuming these established relationships hold true at the microscopic (element) level, and considering that each element is isotropic and homogeneous, existing correlations could be leveraged for topological optimization of electrode microstructure instead of SIMP.

While density-based TO is popular due to its broad applicability and ability to avoid re-meshing during optimization, it struggles to capture intricate interface shapes between different phases. Level-set parameterization methods address this limitation by representing the structure's geometry with a level-set function. Unlike traditional explicit boundary representations, where the geometry is explicitly defined, the level-set method utilizes a higher-dimensional function, the level set function. This scalar function mathematically defines the interface between various materials or phases within the design space [60]. Each point in the design domain receives a value from the level-set function, with positive values indicating one material (e.g., solid), negative values indicating another (e.g., void), and zero representing the exact location of the interface, as expressed by:

$$\begin{cases} \Phi(\mathbf{X}) > 0; & \mathbf{X} \in \Omega \\ \Phi(\mathbf{X}) = 0; & \mathbf{X} \in \partial\Omega \\ \Phi(\mathbf{X}) < 0; & \mathbf{X} \in D \setminus \Omega \end{cases} \tag{1.3}$$

where Φ is the level-set function, $\mathbf{X}$ represent any point in the design domain, and D, ω, and $\partial\Omega$ are the design domain, material domain, and the interface between the two phases, respectively. By cleverly manipulating this level set function, the method can track the interface's motion implicitly. This method excels at capturing sharp boundaries and complex interfaces between materials, making it ideal for problems in which performance hinges on interfacial properties or behavior. This approach offers significant advantages by decoupling the representation of the geometry from its topology, allowing for seamless handling of complex topological changes such as merging, splitting, or evolving boundaries [61]. Moreover, the use of an implicit representation allows for easy incorporation of shape optimization techniques, offering designers and engineers a versatile toolset for achieving optimal geometric configurations tailored to specific design objectives [60]. However, the final design obtained from this method can be significantly influenced by the initial configuration provided [45]. The level set method's inherent numerical stability and avoidance of mesh-dependent spatial oscillations, such as staircasing, further enhance its applicability in diverse engineering domains [60]. Regardless of the chosen parameterization method, all TO procedures rely on optimization algorithms to update design solutions. Updating design solutions involve evolution of either density or level-set function through an algorithmic procedure. These algorithms can be gradient-based, such as Method of Steepest Descent [62], Sequential Linear Programming (SLP) [63], Method of Moving Asymptotes (MMA) [64], Globally Convergent MMA (GCMMA) [65]. Alternatively, derivative-free methods [66], such as evolutionary algorithms [67] can be employed. While evolutionary structural optimization methods are not the focus of this thesis, it is worth mentioning that these approaches are often computationally expensive and may get stuck in local optima.

Gradient-guided TO involves an iterative process, akin to other optimizations. The optimization process begins with defining the problem and formulating the objective function. The primary optimization loop then starts with an initialization step, where an initial design is created. Subsequently, the objective function value is assessed, typically as a function of one or multiple state variables, necessitating the solution of a set of governing equations constituting the mathematical model. Researchers employ various modeling and simulation techniques to describe system

behavior, such as the finite element method (FEM), finite volume method (FVM), and lattice Boltzmann method (LBM). Upon solving the state equations and obtaining the values of state variables, the objective function is determined. Next, a sensitivity analysis is performed to evaluate the gradient of the objective function with respect to the design variables (e.g. material densities), often employing variational calculus methods such as the adjoint state method [68]. Subsequent to sensitivity analysis, regularization techniques [30, 60] may be employed to address issues such as the checkerboard pattern problem [11, 69, 70], eliminate numerical artifacts, and to promote convergence and smooth solutions. The design variables are then updated utilizing the optimizer and the sensitivity information. This iterative process continues until a convergence criterion, such as a maximum number of iterations, is met. It is worth noting that, as with any optimization problem, the initial configuration (initialization step of optimization) and model boundary conditions play a critical role in shaping the optimization process. An unsuitable initialization may cause the method to converge slowly or get trapped in a local optima. Similarly, improper boundary conditions can lead to unrealistic or unphysical outcomes. To minimize these risks, sensitivity analysis can be conducted to assess how different initial configurations and boundary conditions influence the results. This involves running the optimization with various initial shapes (layouts) and boundary conditions to observe their impact on the final solution. Such analysis helps ensure that the results are robust and not overly dependent on arbitrary choices of conditions.

Although not within the scope of this thesis, other TO approaches are worth noting, including evolutionary structural optimization (ESO) [71], bi-directional ESO (BESO) [71], moving morphable component (MMC) [72], and moving morphable void (MMV) [73]. ESO optimizes structures by progressively removing elements with the least stress. BESO extends this by also adding new elements in high-stress areas, allowing for improvements from both directions. MMC and MMV, based on explicit Lagrangian descriptions, are dual methods. MMC uses adaptable components that can move, change shape, overlap, and merge, facilitating precise geometric designs and complex structures. In contrast, MMV employs voids to refine the topology. Both methods use geometric approaches to optimization, reviving classical shape optimization techniques.

1.3 Topology optimization for electrodes of electrochemical energy devices

In the preceding section, we discussed two primary methodologies employed in TO, namely level-set and density-based approaches. In the realm of porous electrode design, level-set methods have been prevalent in studies examining the influence of interfacial boundaries between different phases (e.g., electrode-electrolyte interface shape). In this case, interfaces between material phases are defined implicitly by iso-contours of a level-set function. This implicit function provides a clear description of the boundaries, enhancing the accuracy of the response captured near the boundaries and eliminating ambiguities associated with intermediate material phases encountered in density-based approaches. Consequently, the chosen mathematical model should be capable of capturing the specific phenomena under investigation, particularly how structural changes impact those phenomena. Density-based methodologies, on the other hand, find application in scenarios where optimization of macroscopic properties distribution—such as porosity or solid volume fraction—is the focal point. As previously mentioned, density-based methods describe the layout through a set of material distribution functions, comprising two or more phases, with one phase typically representing "no material" (i.e. the void phase). This material distribution is often discretized using element-wise constant or nodal shape functions. The following subsections review previous works that utilize these two approaches for structural design of porous electrodes in EEDs.

1.3.1 Level-set methods

The initial investigations in the area of electrode optimization focused on employing structural TO using level-set methods. This can be traced back to 2011 (see Fig. 1.2a-c) when Iwai et al. [74] conducted optimization based on level-set techniques to explore the optimized cathode-electrolyte interface of solid oxide fuel cells (SOFCs) at meso-scale. The authors used a 2D model of a SOFC to find the best design for maximizing current density at a fixed voltage level. Their simulation included the entire cell: the anode, electrolyte, and cathode. These components were 300 microns long (through-plane direction) and 50 microns wide (in-plane direction). However, they only optimized the design of a smaller rectangular area within the cathode and electrolyte, measuring 150 microns long by 50 microns wide. They discovered that

a non-flat wavy design of the cathode-electrolyte interface led to improved performance compared to the conventional flat interface as seen in Fig. 1.2a. This figure depicts the changes of interface shape throughout the optimization process. As shown in Fig. 1.2a the initial interface had a step-like rectangular shape; however, the optimizer favored a more curved form in the final step. The optimal interface shape, however, depends on the simulation conditions. Their findings suggest that a flatter interface is preferable when gas diffusion resistance within the cathode is higher. Although the fabricated interface did not precisely match the optimized design obtained from mathematical optimization (see Fig. 1.2b), preliminary experiments involving the modification of the interface, such as fabricating grooved electrodes (a structure similar to the optimized results to some extent), demonstrated enhanced performance compared to electrodes with a flat interface. As illustrated in Fig. 1.2b, two configurations with varying groove sizes—small and large—were fabricated, both with an overall thickness of 500 microns. Fig. 1.2c compares the experimental I-V curves of modified electrodes with small and large grooves, at various operating temperatures, to that of a conventional electrode. It reveals a noticeable increase in current density across a range of terminal voltages. This finding highlights the practical challenges and opportunities in translating optimized designs into real-world applications. The experiments underscore the potential for performance gains through interface modification, even when the fabrication does not perfectly align with the theoretical optimization.

In 2013, Zadin et al. [75] embarked on a study aimed at enhancing the design of 3D-microbatteries, as depicted in Fig. 1.2d-f. To achieve this, they employed a structural TO based on the level-set method. The investigation centered around optimizing the geometries, displayed in Fig. 1.2d, of the positive electrode ($LiCoO_2$) and negative electrode (LiC_6) separated by a $LiPF_6 \cdot PEO_{20}$ polyethylene oxide polymer electrolyte. With the idea of obtaining a more uniform electrochemical activity on the electrode surface, the researchers formulated the optimization problem as a function of current density. Moreover, to maintain the volume of electrode material in the cell, a Heaviside function was applied to the level-set variable, helping to control the electrode volume over the optimization course. Following the optimization process, the researchers found that coating the current collectors with active material distributed in a non-uniform manner yielded favorable results (see Fig. 1.2e) Further analysis compared the performance of the optimized battery designs with those that were not optimized. It was discovered that geometry optimization led to a remarkable increase in cell performance, with improvements of up to 2.25 times observed, as

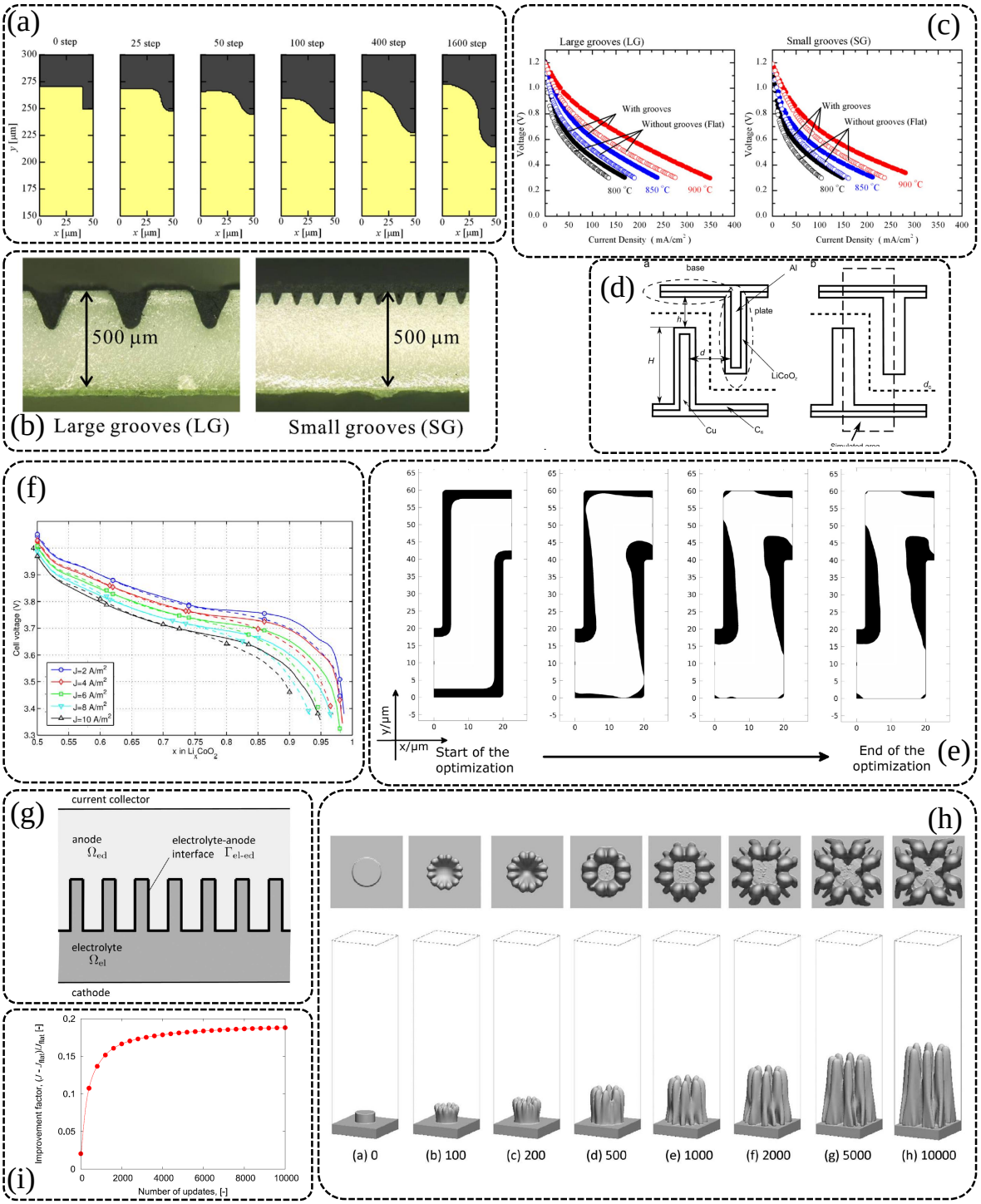

Figure 1.2: Examples of applying topology optimization based on level-set techniques to optimize the electrode/electrolyte interface in EEDs.

Figure 1.2 ***(continued from previous page)*:** Schematics and images show (a) the evolution of the cathode/electrolyte interface of a solid oxide fuel cell during the optimization process, (b) a cross-section view of the cathode/electrolyte interface with small and large grooves, (c) a comparison of IV performance curves of cells with grooved and flat electrolytes (Reprinted from Ref [74], Copyright (2011), with permission from Elsevier); (d) a schematic illustration of a 3D-microbattery considered in the study of applying the level-set method with topology optimization, (e) the evolution of the electrode/electrolyte interface of the 3D-microbattery during the optimization process, (f) discharge curves of cells with optimized and non-optimized electrode/electrolyte interfaces at various current densities, where dashed lines represent the non-optimized interface and solid lines represent the optimized interface (Reprinted from Ref [75], Copyright (2013), with permission from Elsevier); (g) a schematic illustration of the solid oxide fuel cell considered in the study of applying the level-set method with topology optimization representing the anode electrode-electrolyte interface, (h) the evolution of the anode/electrolyte interface of a solid oxide fuel cell during the optimization process, and (i) the convergence history of the optimization (Reproduced from Ref [76], Copyright (2019), with permission from IOP Publishing).

shown in Fig. 1.2f. This significant enhancement was attributed to the mitigation of internal energy losses, which were caused by nonuniformities in the ionic transport occurring within the battery.

Onishi and Shikazono's research group [76–80] stands out among notable research teams that have utilized the level-set TO technique to enhance the performance of SOFCs. Their considered geometries are shown in Fig. 1.2g. Their approach involves considering the spatial distribution of the level-set function as a design variable, resulting in a design space with significant degrees of freedom. To address the challenges associated with this approach, they adopted the adjoint method, wherein adjoint equations are solved to compute the sensitivity of the objective function concerning the design variable. In their initial study, Onishi et al. [76] discovered that the optimal meso-scale structure for the electrolyte-anode interfaces of SOFCs exhibited multiple branches at the top side and characteristic sub-structures like wrinkles at the bottom side (see Fig. 1.2h). These wrinkles were found to contribute to performance enhancement by homogenizing the electrochemical potential. Fig. 1.2i illustrates that the optimized electrolyte-anode interfaces show an improvement of around 18.8% after 10,000 optimization iterations. Building upon this research, He et al. [78, 79] employed a similar approach, incorporating local radius constraints, to optimize the cathode porous microstructure of SOFCs made of $La_{0.6}Sr_{0.4}Co_{0.2}Fe_{0.8}O_3$ (LSCF). Subsequently, they extended their efforts [80] to apply TO with multiple level-set methods to the nickel-yttria-stabilized zirconia Ni – YSZ anode. Given that a single level-set function can only distinguish between two different phases, the multiphase level-set method was employed to parametrize structures with more than two phases. Simulation results indicated that the optimal microstructure comprised Ni particles embedded into YSZ scaffolds, exhibiting a pillar-like structure along the thickness direction. In addition to the studies focusing on the electrode-electrolyte interface of EEDs, Ishizuka et al. [81] utilized TO with level-set methods to design anodes placed in an electroplating bath. This application aimed to achieve uniform deposition thickness, a critical factor in ensuring desirable surface qualities in various products. The uniformity of the current density on a cathode was employed as the objective function in this context.

TO employing level-set methods has found widespread applications across various fields, ranging from electroplating to SOFCs and lithium-ion batteries. Typically, level-set methods are employed in scenarios where the focus lies on material interfaces. This preference stems from the fact that the interface between different material phases can be precisely defined by iso-contours of a level-set function. This

implicit function provides a clear delineation of boundaries, facilitating accurate representation of interfaces. Depending on how the interface is represented in the physical model, using level-set methods can enhance the accuracy of mechanical response predictions near boundaries. Additionally, employing level-set methods helps to mitigate the uncertainties associated with intermediate material phases, a challenge often encountered when utilizing density-based approaches. This inherent capability of level-set methods contributes to their widespread adoption in TO tasks.

1.3.2 Density-based methods

Building on a previous work [74], two years later, Song et al. [82] initiated a different modeling and optimization perspective. Iwai et al. [74] treated the cathode-gas as a homogeneous porous medium and aimed to find the optimal shape for the electrode-electrolyte interface. On the other hand, the subsequent research by Song et al. [82] shifted focus to the cathode-gas interface itself. The authors limited the scope of their study to a specific electrode configuration consisting of a mixed ionic-electronic conducting material deposited by infiltration onto an ionically conducting scaffold. In such a case, their model predicted that a larger perimeter and a greater amount of scaffold material, regardless of the specific electrode structure, resulted in lower Ohmic resistance. Consequently, to isolate the effect of shape exclusively during the optimization process, the authors introduced isoperimetric constraints on both the perimeter and the amount of material used. The researchers utilized a formulation of TO based on the SIMP method. Their approach involved design-dependent boundary conditions, necessitating a dynamic treatment of material boundaries within the optimization process rather than predefined delineations. Consequently, specialized methodologies were employed to address the implications of design-dependent boundary conditions. The investigation revealed notable enhancements in performance ranging from 18% to 50% across varied geometrical dimensions and material properties compared to conventional column designs. This underscores the considerable potential for performance improvement through meticulous organization of the cathode microstructure, yielding intricate configurations that were not realizable without a robust mathematical scheme. In addition to the efforts initiated by other researchers, Mathieu-Potvin and Gosselin [83] employed density-based methods to optimize platinum distribution in polymer electrolyte fuel cells (PEFCs). Their primary aim was to maximize current density while maintaining a fixed total amount of platinum. The findings of their study unveiled that the most effective design showcased a gradient-based distribution, concentrating the majority of platinum near the

membrane layer. It is crucial to acknowledge that Mathieu-Potvin and Gosselin simplified the system by assuming high conductivity in the solid phase, enabling rapid electron transport and eliminating Ohmic losses related to electron transport. Furthermore, their design domain mesh consisted of only 50 nodes along the in-plane direction and 15 nodes along the through-plane direction, indicating a relatively coarse discretization. A key limitation acknowledged by the authors is their model's inability to account for liquid water transport. This omission leaves the significant negative impact of flooding, caused by concentrating catalyst material in a confined space near the membrane, unaddressed in the results. Despite these simplifications, their research shed light on the potential advantages of optimizing platinum distribution in PEFCs for enhanced performance. Meanwhile, Lamb et al. [84–88] tackled a similar topic by optimizing catalyst distribution in PEFCs with the computational domain depicted in Fig. 1.3a. In these studies, TO is performed by allowing the catalyst amount to vary independently at each location within the design domain. This freedom translates to a significant increase in the number of design variables compared to Mathieu-Potvin and Gosselin [83], exceeding 10^4 , since the catalyst amount at each node of the finite element mesh becomes an optimization variable. They also considered the impact of land and channel on optimized catalyst distribution. In their findings, Lamb et al. recommended placing more catalyst material (i.e. platinum) under the gas channel than under landings and toward the membrane interface, as seen in Fig. 1.3b, might improve the output power. Fig. 1.3b also compares the optimized catalyst distribution under two different overall loadings of 0.1 and 0.2 $\mathrm{mg\,cm^{-2}}$. While the exact distributions are different, both cases show a similar increasing incremental trend when moving from the gas diffusion interface toward the membrane side. However, it is important to note that they solely considered the amount of catalyst as a design variable, without considering the reorganization of porosity and ionomer distributions, which could potentially benefit cell performance. Evidently, since the total volume fractions of all materials in an electrode must add up to unity, optimizing the amount of one component requires flexibility in another. For instance, if the amount of ionomer is fixed and uniform throughout the electrode, then the porosity needs to be freely adjustable when optimizing the catalyst loading. Lamb and colleagues acknowledged the limitation of their study in simultaneous optimization of multiple materials and successfully addressed it in 2020. In their recent studies [87, 88], they tackled the challenge of optimizing the distribution of multiple components within the catalyst layer, including platinum particles (catalyst material), Nafion polymer (ionic conductive material), carbon (catalyst support and electric conductive material), and porosity. They achieved this by

treating the volume fraction of each constituent as a design variable at every location within the layer. However, managing such a complex optimization problem presented a significant computational hurdle. To address this, the authors employed an adjoint variable method. Particularly, [88] involved optimizing the distribution of all constituents (catalyst, Nafion, carbon) simultaneously. Similar to the individual optimization of various constituents that was presented in [87], porosity was not directly optimized. The results consistently demonstrated that a higher volume fraction of catalyst and electrolyte material near the membrane was favorable as the proxy to the ion exchange membrane improves the overall electrochemical reaction rate. Additionally, higher porosity at the opposite side of the catalyst layer (near the diffusion layer) and under the channel area enhances oxygen delivery, ultimately boosting overall performance. It is important to note that, similar to the work by Mathieu-Potvin and Gosselin [36], their model does not account for two-phase flow, neglecting the transport of liquid water within the catalyst layer. In addition, since the models used in these studies are 2D, the impact of longitudinal direction on the final optimum design has not been well studied.

In addition to the advancements made in PEFCs, Mitchell and Ortiz [89] ventured into applying density-based TO to design optimal multifunctional silicon anode structures for lithium-ion batteries, aiming to develop next-generation high-performance secondary batteries. While the silicon anode holds promise due to its inherent high capacity for storing lithium ions, its structures undergo a substantial 310% volume expansion upon lithiation, leading to severe damage such as active particle pulverization and disconnected charge transport paths. Furthermore, the low intrinsic electric conductivity of silicon results in poor rate performance due to sluggish electron transport through the material. To tackle these structural and charge conduction design challenges, Mitchell and Ortiz employed TO methods. Initially, they considered the objectives individually and later extended the methodology to a bi-objective formulation to simultaneously address both the structural and conduction design criteria. Through their research, they discovered that a rigid frame structure served as an excellent compromise between the structural and conduction design criteria, offering both the required structural rigidity and direct conduction pathways. In a recent work by Pejman and Raeisi Najafi [45], the authors introduced a novel approach for multi-objective TO aimed at crafting Structural Battery Electrolytes (SBE) within multifunctional structural battery composites. The study aimed to overcome the inherent conflict in achieving both high mechanical strength (stiffness) and high ionic conductivity, while also minimizing heat generation in the electrolyte, which are

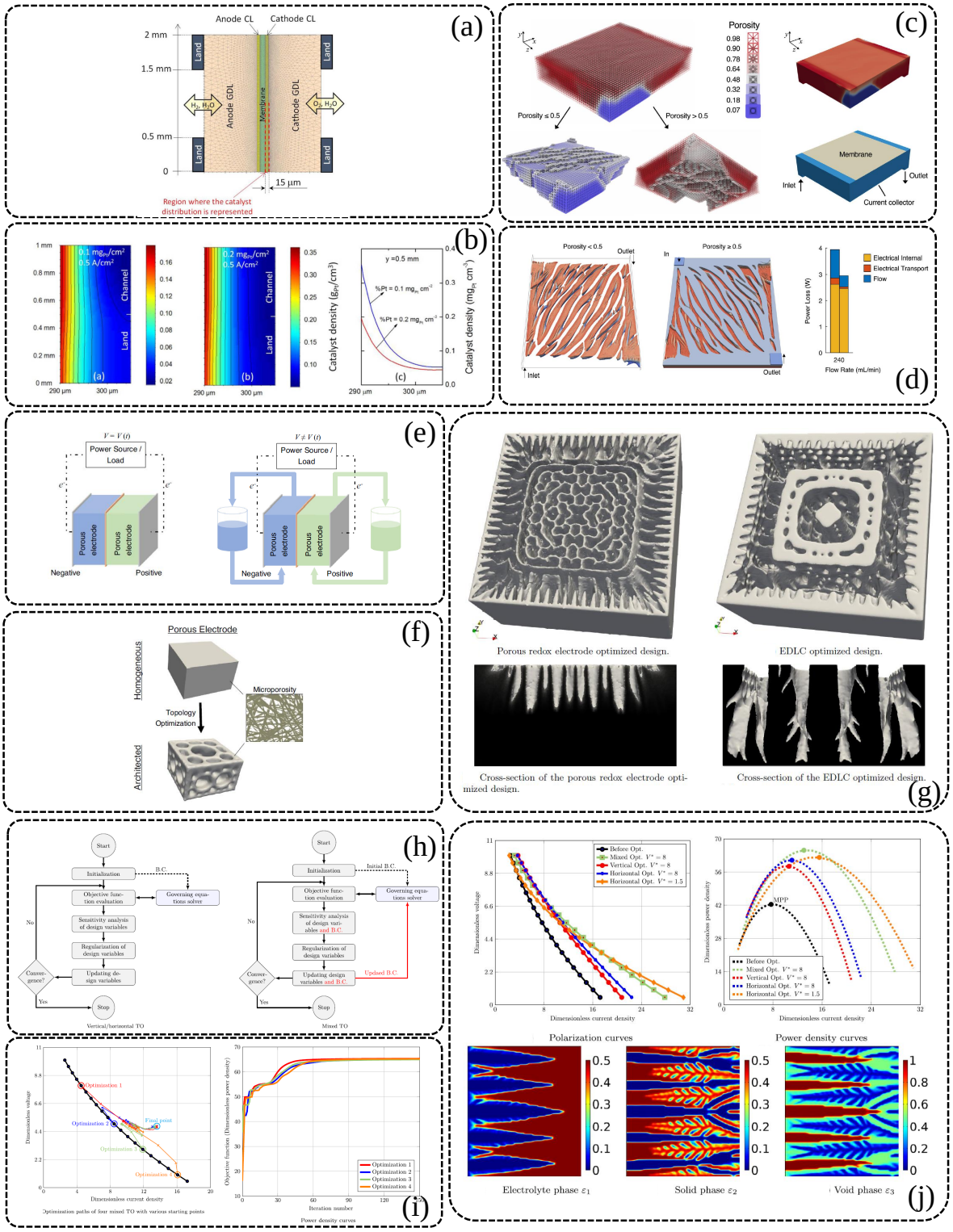

Figure 1.3: Examples of applying topology optimization based on density-based methods to optimize the electrode in EEDs.

Figure 1.3 ***(continued from previous page)*****:** Schematics and images show (a) the computational domain of a proton exchange membrane fuel cell considered in the study of applying the density-based method with topology optimization, (b) optimized catalyst distributions for two different Pt loadings and the 1D optimum platinum distribution at the middle of the computational domain [84]; (c) the computational domain of a negative half-cell compartment of a vanadium flow battery by which the electrode is split into portions with a unit cell, (d) optimized porosity distribution of the electrode (Reproduced from Ref [90], Copyright (2021), with permission from Elsevier); (e) two systems considered in the study of [91], which are a device operates through redox reaction and a device operates through charge storage using a double layer, (f) schematic diagram showing the porous electrode before and after optimization in which the material seen is, in fact, porous, (g) 3D optimized designs of two systems considered in the study (Reproduced from Ref [91], Copyright (2022), with permission from Springer Nature); (h) flowchart of the algorithm for conventional and mixed topology optimization, (i) convergence history of mixed topology optimization with various starting points showing its self-guidance feature, and (j) performance curves as well as the optimal volume fraction distribution of each material constituent (Reproduced from Ref [92], Copyright (2023), with permission from Elsevier).

crucial factors for maximizing battery performance. The researchers implemented a multiphysics, multi-objective gradient-based approach to simultaneously maximize both the ionic conductivity and stiffness of the SBE. To ensure prevention of overheating, the optimization process incorporated constraints on the maximum allowable temperature and void volume fraction. The proposed design framework integrates electrochemical, thermal, and structural physics, enabling the creation of an optimized SBE microstructure. The study investigated two optimization scenarios, including (1) bulk condition, and (2) carbon fiber included condition. The former focused on optimizing the microstructure of SBE assuming a bulk material, where carbon fibers were not explicitly included as part of the design solution. However, the latter scenario built upon the first by introducing carbon fibers as an explicit element within the design space. It is important to note that the carbon fibers were treated as fixed, non-optimizable elements during the optimization process. In both cases, two materials, including a solid phase and a compliant phase, were used. While the solid phase ensured high stiffness and thermal conductivity, the compliant phase enabled efficient electric charge transport. The study successfully generated a set of Pareto optimal microstructures with various trade-offs between effective ionic conductivity and compliance. Additionally, explicit incorporation of carbon fibers within the design space significantly altered the optimized SBE design compared to the bulk scenario.

Meanwhile, thermal mismatch significantly influences the stress state and lifetime of SOFCs. In response, Li et al. [93, 94] endeavored to mitigate this issue by designing LSM−YSZ cathodes and Ni−8 YSZ anodes using density-based TO. The microstructures of the cathode and anode took the form of periodic fiber bundles. The results demonstrated that the coefficients of thermal expansion of these microstructures closely matched those of the electrolyte layer at different temperatures, effectively eliminating thermal mismatch issues.

Inspired by the configuration of electrodes in redox flow batteries (RFBs), where the electrode typically comprises a disordered, homogeneous assembly of micron-scale electroactive particles like carbon fibers and felts, Beck and Worsley's research group [90, 91] stands out as a prominent contributor in applying TO to enhance porous electrode structures. The primary goal behind their design philosophy is to maximize surface reactions while minimizing overpotential and hydraulic losses. In their initial study, Beck et al. [90] focused on restructuring porosity distributions with the objective of minimizing power loss and creating electrodes with engineered

porosity distribution, as shown in Fig. 1.3c. A comparison between these architectured electrodes (demonstrated in Fig. 1.3d) and bulk, uniform porosity electrodes revealed enhanced power efficiency across various flow rates and currents. Continuing their investigation, Roy et al. [91] illustrated a framework of TO in designing porous electrodes for two applications: one involving a porous electrode driving a steady Faradaic reaction (as seen in RFBs), and the other operating transiently without a Faradaic reaction (like in electric double layer capacitors), as depicted in Fig. 1.3e. In their research, they utilized a porous model (illustrated in Fig. 1.3f), wherein the porous material is termed microporous to differentiate it from the larger pores formed through the optimization process. Across all scenarios, the optimized designs exhibited superior performance compared to undesigned, monolithic single porosity electrodes. In the case of RFBs, this translated to overpotentials reduced by up to 84%, while the electric double layer capacitor electrode showed energy losses reduced by up to 98%. Moreover, they demonstrated the versatility of these techniques by extending them to a three-dimensional electrode design (displayed in Fig. 1.3g), paving the way for manufacturing and testing high-performance architected electrodes. This exploration holds significant promise in advancing the efficiency and functionality of porous electrode systems across various electrochemical applications. However, the model developed by Roy et al. [91] has limitations regarding its consideration of concentration effects and hydraulic requirements. In systems with convective-reactive transport, like those in RFBs, the concentration of the solution flowing through the electrodes depends on the flow rate. This flow rate in turn affects the pressure drop needed to pump the solution (hydraulic requirements). Higher pressure drop requirements mean more power loss by the cell-pump system, which could affect the net generated power and should be considered in the optimization objective function. Another key factor is the difference between the concentration of the solution in the bulk and at the surface of the electrodes. Electrochemical reactions happen at the electrode surface, so for accurate simulations, it is necessary to distinct surface and bulk concentrations. This difference can be accounted for by including a mass transfer coefficient, which typically depends on the flow velocity. However, the authors oversimplified the modeling and optimization by ignoring the concentration effect and hydraulic requirements.

In a recent study, Charoen-amornkitt et al. [95] explored the application of TO in the design of anode catalyst layers for proton exchange membrane water electrolyzers (PEMWEs). They focused on a 2D electrochemical porous electrode model, which encompasses various processes such as water transport, species diffusion, electric

charge transport, ionic charge transport, and redox reactions. The porous electrode was conceptualized to consist of three phases: a void phase, an electrolyte phase, and a carbon-supported catalyst phase. Their optimization approach aimed to maximize cell performance by adjusting the volume fractions of the electrolyte and carbon-supported catalyst materials. The results revealed that introducing a heterogeneously-distributed structure led to more efficient cells. During the optimization process, changes in the volume fraction of constituent materials occurred, resulting in the formation of a zigzag interface in the reactor. This interface facilitated a sufficient supply of charges required for the electrochemical reaction. Compared to cases with uniform spatial distribution of constituent materials, the proposed heterogeneous structure demonstrated a notable enhancement in the electrochemical reaction, achieving approximately a 40% improvement. This highlights the effectiveness of TO in enhancing the performance of PEMWEs by optimizing the electrode design. Despite this, the authors simplified the system by disregarding the effects of oxygen bubble formation within the electrode, among other factors, resulting in a uniform distribution of porosity that eliminates the necessity for an oxygen bubble removal pathway. Additionally, their research indicates that distinguishing between electronically conductive materials and the catalyst, coupled with utilizing multi-objective optimization to minimize the catalyst volume fraction, has the potential to significantly reduce catalyst usage. While fuel cells have a longer history of modeling, water electrolyzers are catching up. Researchers are adapting their knowledge from fuel cells to improve existing electrolyzer models. However, water electrolyzers involve additional complexities, like bubble formation [49], which need to be factored in. The coverage of reaction sites by these bubbles is an additional limiting factor that requires detailed consideration of the bubble evolution process, such as nucleation and bubble growth. This means there is a need not only for better optimization methods, but also for more advanced modeling techniques to create robust and reliable electrode designs for electrolyzers. To overcome some of the limitations mentioned earlier, Passakornjaras et al. [96] optimized the anode catalyst layer of a PEMWE, accounting for limitations related to gas coverage and effects of temperature distribution. Although their modeling of physical phenomena differs, the optimization process is similar to that in [95]. The resulting optimized structures significantly outperformed a homogeneous electrode design, with electrode current densities 2.7 times higher at high operating voltage (2.03 V) and 1.2 times higher at low operating voltage (1.73 V). Future research on TO for PEMWEs should incorporate more advanced models of the various physical and chemical phenomena occurring in the electrode and consider the durability of optimized structures under

thermal and mechanical stress. Additionally, exploring multi-objective optimizations to balance reaction rates and material usage may be necessary.

While TO has been widely used to search for optimized electrode structures in EEDs, previous studies have not achieved maximum output power for power sources. This limitation arises because researchers are typically constrained to either minimizing overpotential at a fixed current density or maximizing current density at a specified overpotential. While both strategies can improve performance in terms of power density, they do not necessarily lead to maximum output power. Alizadeh et al. [92] proposed a novel mixed TO approach to enhance the performance of these systems by simultaneously modifying the electrode structure and the working conditions (see Fig. 1.3h). Unlike conventional approaches, this method focuses on enhancing the maximum power point. Their research demonstrates that the mixed TO approach outperforms conventional vertical and horizontal optimizations, where either terminal voltage or current density is optimized. Additionally, it has been tested under various starting points, as shown in Fig. 1.3i, consistently yielding the same output. This self-guidance feature of this method eliminates the need for a prior decision on the optimization starting point. Fig. 1.3j reveals that the optimal distribution of materials within the design domain resembles a complex tree-root-like structure. The formation of diffusion channels, facilitated by high concentrations of voids in certain parts of the system, enables the delivery of reactant material across the entire system. This structural pattern bears resemblance to the vascular layout observed in nature, such as in the leaves of plants. The network of veins in plant leaves, which transports water and nutrients, exhibits a similar structural pattern.

Charoen-amornkitt et al. [38] utilized TO to engineer porosity distributions within a system characterized by a 1D nature. In this system, the concentration remains constant at $x = 0$, and there are no fluxes at $x = L$. By exploring various dimensional models, they discovered that increasing the design dimensionality beyond one enhances system performance by minimizing entropy generation. However, they observed a relatively modest performance improvement when transitioning from 2D to 3D designs. This led to the hypothesis that due to the inherently 1D nature of the problem, a 2D model suffices to significantly enhance performance. Building on this insight, Long et al. [97] focused on systems with a 2D flow nature, specifically investigating the impact of rib structures and electrode thickness. They evaluated three different geometries, including one with fixed species concentration at the inlet and zero-flux boundary conditions, effectively confining the system to a 1D nature. To

increase the nature of the species diffusion to a 2D flow characteristics, they introduced a rib at the inlet. Beneath the rib, a region restricted reactant movement while allowing electron transfer. Additionally, they reduced the thickness to encourage more 2D flow characteristics. Their findings indicated that in rib-containing cases, reduced inlet area limited species availability, a challenge mitigated by decreasing reactor thickness. Examining the optimized porosity distribution, they observed the formation of diagonal channels in systems exhibiting 2D characteristics. Interestingly, augmenting the system model's dimensionality beyond its inherent nature did not significantly impact the reaction rate.

Until now, with a few exceptions, prior research primarily focused on maximizing the reaction rate within the designated design domain. However, as previously discussed, there exists an alternative approach: minimizing overpotential at a fixed current density. Alizadeh et al. [98] undertook a comparative analysis of two optimization strategies aimed at enhancing the performance of electrochemical reaction-diffusion systems, as displayed in Fig. 1.4a-c. These strategies involved minimizing overpotential at a fixed current density and maximizing current density at a specified overpotential. The researchers analyzed a 2D triple-material electrode, similar to the catalyst layer found in PEFCs. However, their model simplified the processes occurring in PEFCs by neglecting the two-phase flow of gas and liquid water, a common phenomenon in low-temperature fuel cells. The electrode consisted of solid, electrolyte, and void phases. While the solid phase was responsible for electron transport and provided necessary reactive surface area, the two other phases facilitated ion transport and mass diffusion. The optimization aimed to find the best distribution of constituents volume fractions through a density-based method. The resulting optimal layouts exhibited intricate root-like structures (see Fig. 1.4a), which facilitated transport processes and led to a remarkable improvement in the conversion rate of up to 116.7%. Further analysis revealed that the optimal layout varied significantly depending on the dominant processes at different voltages (or current densities). For instance, when the optimization focused on low voltages (high current density), where concentration overpotential limits performance, the algorithm favored designs with higher porosity and larger diffusion channels. Conversely, optimization at high voltages (lower current density) resulted in a design with a higher solid phase volume fraction distributed throughout the electrode. This increased the reactive surface area, thereby reducing activation overpotential.

density-based methods are more prevalent than level-set methods in optimizing the

structure of electrodes for EEDs, as evidenced by the abundance of studies employing this approach. A closer examination of these studies reveals a fundamental difference in the focal point of interest compared to those utilizing level-set methods. Density-based methods primarily concentrate on optimizing the distribution of materials within the electrode structure rather than delineating the interface between different materials. These density-based methods have found applications across a wide range of EEDs, spanning from power sources like PEFCs and SOFCs to power-consuming devices such as PEMWEs, as well as energy storage systems like lithium-ion batteries and RFBs. However, it is important to note that the treatment of material density may vary across different studies employing density-based methods. In density-based methods, material density typically ranges from 0 to 1, signifying regions containing a mixture of material and void. While this "gray area" typically holds no physical meaning in structural mechanics applications, it holds physical significance in the context of EEDs, particularly in porous models used at the macroscale level. Here, material density values between 0 and 1 are meaningful and directly inform the modeling process. To address the gray area and ensure meaningful material distribution for structural mechanics problems, projection methods are often employed. However, in EEDs, where porous models are prevalent, material density values between 0 and 1 are utilized and hold relevance in representing the actual physical structure of the electrode materials by assigning them as macroscopic properties, like volume fraction and porosity.

1.4 Entropy generation analysis and topology optimization

TO plays a pivotal role as a mathematical tool in the intricate design and optimization of complex structures. However, it is crucial to acknowledge the numerical nature of the solutions derived from TO, which are influenced by various factors including the choice of objective function, algorithmic approach, and tuning parameters. Consequently, it becomes imperative to establish a robust theoretical framework to underpin these optimized solutions. In addressing this need, Tsushima's research group [38, 92, 95, 97–100] advocates for the integration of principles derived from entropy generation minimization theory. Inspired by the widespread use of entropy generation analysis in evaluating thermal systems, their objective is to align with a system characterized by minimal entropy generation. This approach aims to lay the groundwork for a design methodology that is firmly grounded in physical

principles, thereby reducing reliance on arbitrary tuning parameters that are usually necessary for optimization algorithms (e.g. filter radius). Entropy generation analysis offers a rigorous framework for assessing the thermodynamic efficiency of systems, enabling the identification of optimal designs that minimize energy wastage and maximize performance. By incorporating these principles into the design process, it is anticipated that the resulting electrode structures will exhibit heightened reliability and effectiveness. This is because they are founded on fundamental physical principles rather than ad hoc parameter adjustments.

Charoen-amornkitt et al. [38], embarked on a comprehensive research endeavor, commencing with the utilization of TO to optimize the structure of porous electrodes (see Fig. 1.4d-f). To evaluate the entropy generation during this optimization process, they employed entropy generation analysis, recognizing the complexity of assessing entropy generation in the porous media of EEDs. The nonequilibrium nature of these systems, compounded by the presence of chemical reactions, posed significant challenges. In response, they adopted NET as a theoretical framework, enabling the assessment of local entropy generation rates in systems not in a state of global equilibrium. In their study, the researchers simplified the system by focusing solely on a porous reactor within reaction-diffusion systems involving a single species. As the optimization progressed with the objective of maximizing reaction within the design domain, entropy generation inevitably increased. To facilitate comparison, they introduced scaled entropy generation, mitigating the influence of the increasing objective function. An essential aspect of their investigation was to examine the effects of design dimensionality on optimization. They found that while 0D and 1D optimization results exhibited little difference in overall reaction, significant increases in reaction were observed when 2D or 3D optimization was permitted. This phenomenon stemmed from the emergence of a geometrically intricate diffusion field reminiscent of biological structures in 2D or 3D optimization. The 3D optimized porosity distribution obtained from their work is illustrated in Fig. 1.4d. As the optimization process advanced, not only did the global scaled entropy generation approach a minimum, but the distribution of scaled entropy generation in 1D also gradually transitioned towards greater uniformity (see Fig. 1.4e and f). These findings align with the equipartition principle, indicating that uniform entropy generation across space may result in less dissipation, leading to the minimum entropy generation rate and a thermodynamically optimal design.

In the subsequent phase of their research, Alizadeh et al. [99] expanded their investigation to encompass a reaction-diffusion system involving two species operating

in a steady-state mode, as depicted in Fig. 1.4g. They utilized a density-based TO algorithm, which resulted in a remarkable 57% improvement in system performance compared to a uniform layout with equivalent average porosity. Throughout the optimization process, the researchers closely monitored the porosity distribution, concentrations of reactant and product substances, and reaction rates. The study's outcomes underscore the importance of achieving a delicate balance between diffusion and reaction mechanisms to enhance performance. This equilibrium was achieved through the formation of primary and secondary channels within the reactor during the optimization process. The optimized porosity distribution, derived from the algorithm, exhibited a tree-root-like configuration, resembling patterns observed in previous research [38]. Similar to their earlier study, this research delved into dissecting the contributions to system entropy generation and quantifying them throughout the optimization procedure (see Fig. 1.4h and i). The findings revealed that the optimized design solution corresponded to the minimum scaled entropy generation resulting from chemical reactions. The researchers suggested that these findings could have significant implications for advancing the understanding of the theoretical upper limit of reaction-diffusion system performance, regardless of the inherent limitations of optimization methods.

Additionally, Alizadeh et al. [98] also introduced an entropy generation model to quantitatively evaluate irreversibilities in a system involving transport phenomena and electrochemical reactions. By analyzing entropy generation trends for both optimization approaches, the research provided insights into optimizing the distribution of constituents in porous electrochemical reactors and elucidated the relationship between TO and entropy generation rate. As depicted in Fig. 1.4b and c, the findings aligned with principles of entropy generation minimization [32] and equipartition of entropy production [34, 35]. It is noteworthy that when employing the strategy of maximizing current density at a specified overpotential, scaling of entropy generation is necessary to counteract the escalating entropy flux during optimization. However, the proper scaling becomes more complicated with additional physics introduced to the system. In contrast, minimizing overpotential at a fixed current density corresponds to reducing entropy generation without requiring scaling. This distinction arises intuitively as overpotential is commonly associated with irreversible losses within EEDs.

In various applications, researchers have observed intricately distributed pores that

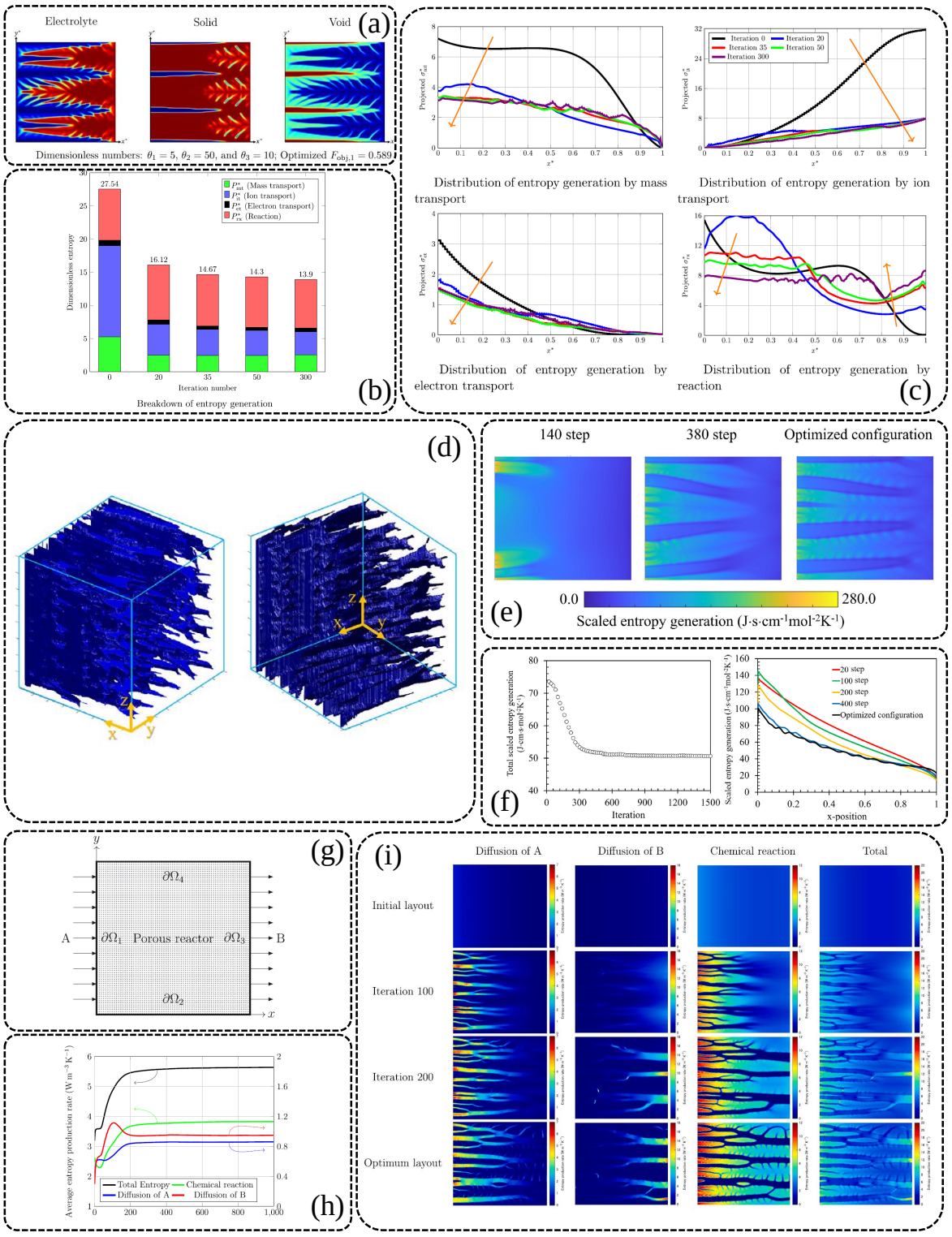

Figure 1.4: Examples of works attempting to draw connections between topology optimization and entropy generation minimization.

Figure 1.4 (*continued from previous page*): Schematics and images show (a) optimized volume fraction distribution of material constituents in electrochemical porous reactors, (b) global entropy generation of each phenomenon occurring in porous reactors, approaching minima post-optimization, (c) 1D projected entropy generation distribution of each phenomenon in porous reactors, displaying increased uniformity akin to the equipartition principle [98]; (d) 3D optimized porosity distribution from different angles, where surfaces represent areas with porosity higher than 0.95, (e) scaled entropy generation distribution during optimization, (f) history of global scaled entropy generation and 1D projected scaled entropy generation distribution, showcasing the approach towards minima and a more uniform distribution resembling the equipartition principle (Reproduced from Ref [38], Copyright (2023), with permission from Elsevier); (g) computational domain of two-species reaction–diffusion system, (h) history of global entropy generation during the optimization process, and (i) spatial distribution of entropy generation by various mechanisms at different iterations (Reproduced from Ref [99], Copyright (2023), with permission from Elsevier)

resemble tree-root-like structures, reminiscent of natural patterns such as root systems in trees and respiratory networks in lungs. These natural systems are characterized by efficient mass transport mechanisms, suggesting that exploring similar structures in engineered systems could enhance our understanding of natural design principles. The studies discussed above utilize TO techniques to design electrodes for electrochemical energy storage and conversion systems. By integrating these optimized structures with established theories like entropy generation minimization, researchers aim to uncover connections between engineered designs and natural phenomena. With a design reminiscent of nature, it may very well be the optimal design we are in search of, acknowledging that nature tends to design its systems in the most effective manner. By drawing parallels between topologically optimized structures and entropy generation minimization, researchers seek to unravel the underlying principles governing natural design. This area of research has the potential to bypass the optimization process by minimizing the need for repetitive evaluation of the objective function and governing equations. By doing so, it could significantly reduce the computational resources and the reliance on tuning parameters typically required in optimization tasks. This interdisciplinary field has the potential to revolutionize the design of various technologies by harnessing insights from nature's efficient solutions. Ultimately, by emulating nature's design strategies, humanity may unlock new avenues for innovation and enhance the performance of engineered systems.

One of the significant contributions in this field was made by Long et al. [101]. In their study, Long et al. [101] derived exact solutions for 0D optimization of reaction-diffusion systems, focusing on both maximization (maximizing the reaction) and minimization (minimizing the concentration at the boundary) problems. Their work provided critical insights into the relationship between optimized structure and entropy generation. Following this, they extended their research to 2D and 3D TO to explore the characteristics that an optimized system should possess. They projected the concentration distribution into a 1D representation, identifying that the key characteristic of an optimized system is a linear concentration distribution. Based on this observation, they developed a design theory suggesting that an optimized system should exhibit a linear concentration distribution. By assuming that the optimized structure consistently produces a linear concentration distribution, they were able to substitute this assumption into the governing equations to directly solve for the porosity distribution. This approach allowed them to obtain the porosity distribution without relying on an iterative optimization process. However, it is important

to note that this assumption was primarily applied to 1D optimization. Further research is necessary to extend these findings to 2D and 3D optimization, as the complexities introduced in higher dimensions may require additional considerations and refinements to the design theory.

1.5 Other notable numerical studies in electrode structural optimization

For innovative electrode design in EEDs, other approaches exist for optimizing electrode morphology. Over the years, researchers have utilized various mathematical techniques, such as parametric optimization and functionally graded methods, to improve the topographical design of electrode structures. Parametric optimization aims to find the optimal value(s) for one or more macroscopic properties (e.g., porosity) of a homogenous design to enhance overall cell performance. While TO adjusts material distribution locally, resulting in a heterogeneous design, parametric optimization operates at a global level, fine-tuning design variables. Examples include optimizing Nafion loading in PEFC catalyst layers for maximized power output or finding the ideal porosity or fiber diameter in RFB electrodes to balance reactive surface area with hydraulic permeability. While simpler to implement, these methods are limited in generating highly efficient designs. Functionally graded methods are more advanced approaches building upon parametric optimization. It can involve: (1) dividing the electrode design domain into multiple regions and performing independent parametric optimization on each [102], and (2) utilizing pre-defined distributions based on mathematical functions (e.g., sinusoidal or polynomial) [103]. Despite offering greater design freedom than standard parametric optimization, functionally graded methods are still limited by the number of pre-defined domains or functionalities. In contrast, TO provides a robust framework for automatically generating material distributions with high resolution. It is noteworthy that approaches like functionally graded design differ from the formal TO which automatically manipulates the material distribution itself. Nonetheless, the algorithmic approaches share similarities, as they both offer a heterogeneous material property distribution for improved performance. Here, some noteworthy works that have employed mathematical techniques for morphological modification and improved electrode performance are brefiely mentioned. These studies offer valuable insights for interested readers but are not in any way inclusive.

He et al. [104], for instance, investigated the effect of catalyst layer design on the performance of a PEFC. The researchers developed a macroscopic 3D multiphase non-isothermal model of PEFC to simulate the cell behavior under various conditions. The study aimed to understand how different design parameters, such as platinum (Pt) loading, platinum-to-carbon (Pt/C) ratio, ionomr-to-carbon (I/C) ratio, carbon particle radius, and electrochemical specific area (ECSA) of platinum particles, influence oxygen transport resistance, performance, water transport, and the oxygen transport process within the electrode. Through their numerical simulations and analysis, the researchers found significant correlations between the electrode design parameters and the performance of the cell. They observed that variations in Pt loading, Pt/C ratio, and I/C ratio directly impacted the oxygen transport resistance within the catalyst layer. Additionally, they highlighted the importance of considering the carbon particle radius and ECSA in optimizing the performance of PEFCs. While the study is primarily a parametric sweep analysis, rather than an algorithmic optimization, it provided valuable insights into the complex interplay between design parameters and performance metrics in PEFCs, offering a foundation for further research and development in the field of fuel cell technology. In a different application, Tsushima and Suzuki [105] used a bound optimization by quadratic approximation (BOBYQA) algorithm to simultaneously optimize fibrous electrode architecture of a vanadium RFB. The multi-parameter optimization included porosity, fiber diameter, and electrode thickness as well as two other channel-related geometrical parameters. Each of these parameters were allowed to vary in a given range. Their results showed that a combination of thinner fibers and thicker electrodes could enhance the overall cell performance thanks to a higher reactive surface area. However, this should be accompanied with a relatively high porosity (0.89) to facilitate electrolyte flow that can directly affect the active species transport resistance between bulk solution and solid/liquid interface. The authors suggested simultaneous optimization of various electrode parameters are crucial for a comprehensive design with boosted performance. Functionally graded electrode design has been used for various applications, such as fuel cells and batteries [102, 106]. Srinivasarao et al. [107] used a multi-layer design of catalyst layer to maximize the generated current density and minimize platinum loading. To achieve this, the researchers considered an innovative design with four catalyst layers as shown in Fig. 1.5a and optimized various design variables such as the platinum loading, ionomer loading, weight fraction of platinum on carbon, and thickness of layers under a range of cell voltages from 0.4 to 0.7 V. By optimizing these parameters for each layer, the study sought to achieve cost reduction and performance enhancement in comparison to the base case design

with uniform material distribution. The findings revealed that the PEFC with multiple catalyst layers exhibited superior performance compared to an optimized PEFC with a single catalyst layer across all operating voltages. Under all operating conditions, the optimization favored a higher porosity in the layers closer to the gas diffusion layer (see Fig. 1.5b). The optimal ionomer volume fraction, on the other hand, shows an opposite trend with more ionomers concentrated in the layer neighboring the membrane (see Fig. 1.5c). Additionally, the study demonstrated a significant reduction of 17% to 60% in platinum loading with an increase in the number of catalyst layers for low and high current density regions, respectively.

Although the formal implementation of TO typically involves coupling an optimization algorithm with a continuum macroscopic model to find the best distribution of continuous variables, applying topological optimization to electrode structures extends beyond this method. Various phenomena at micro- or nano-scales take place at electrodes of EEDs. Geometrically resolved models can describe these intertwined multiphysics phenomena at a higher resolution. However, the high computational cost of approaches like direct numerical simulation (DNS) of geometrically resolved structures has posed challenges in integrating these models with TO algorithms. As computer technology advances and more efficient modeling and mathematical schemes are developed, a new trend is emerging. Pore- and particle-scale models are now combined with optimization algorithms for morphological optimization of porous electrodes. An exemplary instance is the use of TO with the LBM. Previously applied in thermofluidic systems [108–111], TO using LBM has recently been extended to electrode design for RFBs [112]. Tanaka et al. [112] focused on fluid behavior in fibrous porous electrodes and optimized electrode structure using adjoint-state LBM. By updating solid and fluid distribution through a level-set function, the optimization algorithm aimed to minimize concentration flow rate at the outlet of a domain with a resolution of 1 micron per voxel. Fig. 1.5d compares the structure and vanadium ion concentration distribution of an ordered fibrous electrode with those of optimized one. According to Fig. 1.5e, compared to an ordered structure with fiber diameter of 4 microns, the optimized structure had a lower cost function value by about an order of magnitude in only 25 iterations. The optimization boosted reaction rate by minimizing the amount of active species leaving the electrode before reacting, leading to a more efficient process. Another research direction for designing electrodes with engineered microstructure, initiated by Forner-Cuenca's research group [113, 114], employs pore network modeling (PNM) together with metaheuristic optimization algorithms. This approach seeks optimal pore network topology

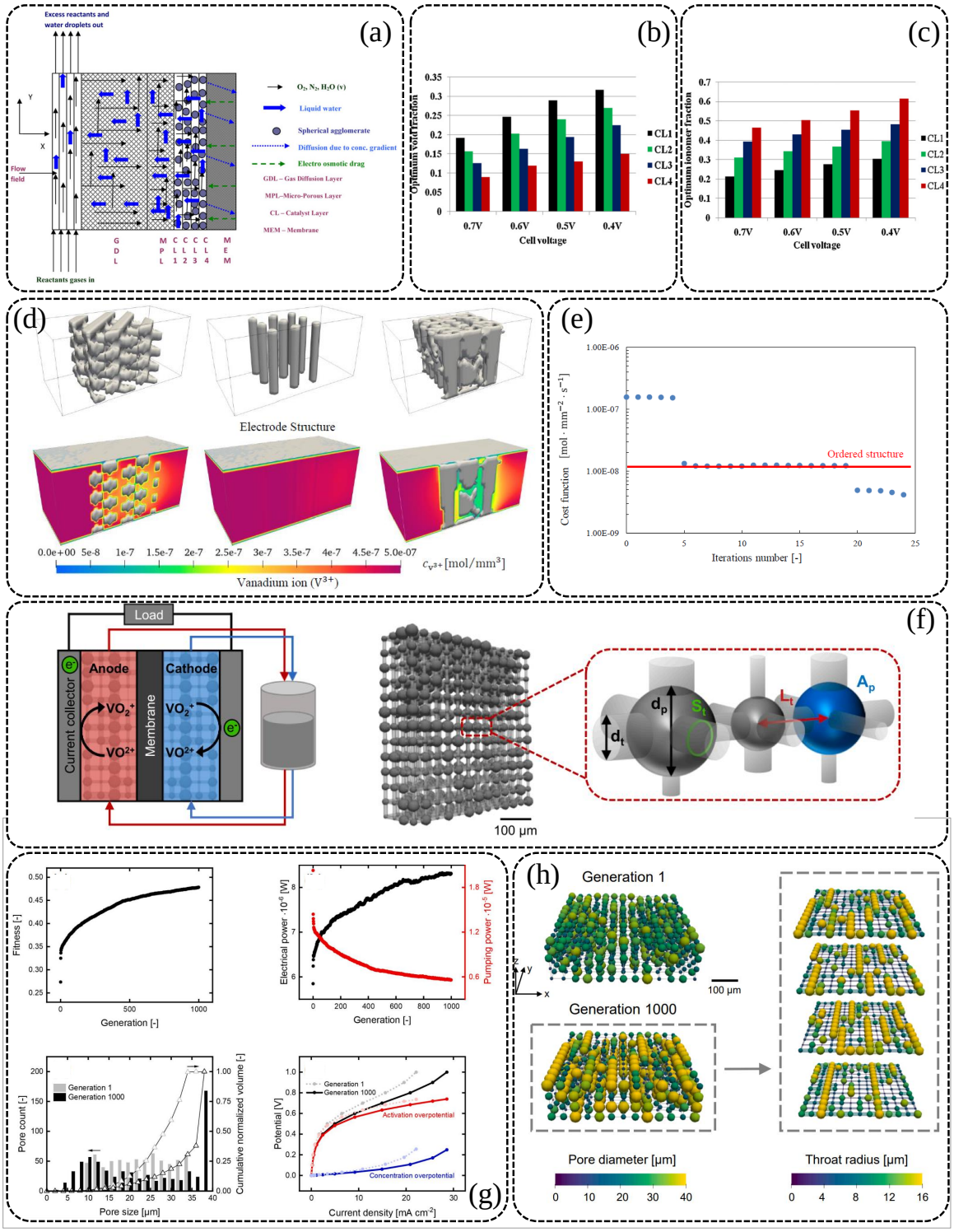

Figure 1.5: Examples of other notable efforts in electrode optimization (functionally graded design, LBM, and PNM).

Figure 1.5 ***(continued from previous page)*:** Schematics and images show (a) schematic of PEFC with multiple catalyst layer, (b) optimum void volume fraction (porosity), (c) optimum ionomer volume fraction in a multiple catalyst layer design under various terminal voltage conditions (Reproduced from Ref [107], Copyright (2012), with permission from Elsevier); (d) results of fiber-scale simulations of electrode structure and vanadium ion concentration distribution under charging condition (optimized structure is on the right; initial structure is in the center; left is the ordered structure with a fiber diameter of 4 microns), (e) evolution of concentration flow rate at the outlet of the domain (objective function) over the optimization course in comparison to that of ordered structure [103]; (f) schematic representation of pore network modeling of RFB electrode, (g) evolution history of cost function, electrical power, and pumping power during the optimization as well as comparison of pore size distribution and polarization curves before and after optimization, and (h) comparison of pore network morphologies, including pore diameter and throat radius, before and after optimization [113].

to enhance cell performance. Despite methodological differences with level-set or density-based TO, they also investigate how a heterogeneous design of porous electrodes could benefit overall cell performance. To achieve higher resolution not attainable through macroscale models and to mitigate the intensive computational cost of DNS methods, authors initially developed a PNM model of RFB (see Fig. 1.5f). With the goal of building a predictive design framework, the developed PNM model is coupled with a genetic algorithm (GA) to optimize network morphology based on a bottom-up design approach. In their first attempt [113], they employed a cubic lattice as shown in Fig. 1.5f and manipulated the pore and throat size distributions without changing the pores positions. The optimized structures exhibit improved fluid distribution through the formation of a bimodal pore size distribution (see pore size distribution in Fig. 1.5f), resulting in preferential longitudinal flow pathways (see Fig. 1.5g) and a 73% decrease in required pumping power as depicted in Fig. 1.5g. The optimization also led to a 47% increase in surface area and a 42% improvement in electrochemical performance. Despite the initial motivation for using PNM to capture various phenomena at a pore level, their model uses a uniform value for the mass transfer coefficient without considering the impact of local fluid velocity. Additionally, keeping porosity constant throughout the optimization iterations imposes an extra limitation on design freedom. The use of a cubic lattice also restricts pore movement within the design domain. This limitation was somewhat addressed in their subsequent study [114] by introducing a pore merging and splitting function. Their research highlights the importance of optimizing electrodes tailored to specific reactor designs and operating conditions. Results reveal that electrolyte kinetics and ionic conductivity can affect the final optimal design. Electrodes with a large number of tiny pores and a large surface area are more effective for kinetically slow electrolytes and high ionic conductivity. Conversely, low through-plane tortuosity and high hydraulic conductance are advantageous for kinetically active electrolytes with low ionic conductivity. A recent study [115] on multi-objective optimization of pore network morphologies in an advection-diffusion-reaction system addressed some limitations of earlier research [113, 114] by introducing a local velocity-dependent mass transfer coefficient and a morphable pore network that extends beyond a fixed cubic lattice. However, the model is limited to a first-order chemical reaction and does not account for electrochemistry-related phenomena, such as electric charge transport, species transport via electromigration, or electrochemical reactions.

1.6 Thesis objectives and outline

The increasing demand for efficient energy conversion technologies, such as fuel cells and electrochemical reactors, has underscored the critical need for enhanced structural designs of electrodes and porous media. A review of the literature revealed that traditional designs often face significant limitations in mass and charge transport, leading to suboptimal performance and heightened energy consumption. Numerous studies have emphasized the importance of optimizing material distributions within these systems to maximize reactant-to-product conversion rates while minimizing energy losses associated with irreversible thermodynamic processes. The primary objective of this thesis is to develop and apply advanced optimization methodologies to enhance the performance of reaction-diffusion systems, with a particular focus on electrochemical reactors. Specifically, this work aims to establish robust design frameworks for porous electrodes based on mathematical modeling and optimization across various length scales and resolutions. Additionally, a secondary objective is to elucidate the theoretical aspects of optimal design. To achieve this, the thesis incorporates a comprehensive analysis of entropy generation, quantifying the thermodynamic irreversibilities present in these systems. This analysis offers valuable insights into the factors contributing to energy losses and informs design modifications aimed at improving efficiency. Notably, the entropy generation analysis in this thesis was conducted as a post-processing step to identify the features that characterize a good design from a physicochemical perspective. However, further research is needed to understand how these characteristics could serve as guiding principles for designing optimal electrode structures. Through such studies, it is anticipated that future research may reveal a theoretical performance limit under non-equilibrium thermodynamic conditions. However, it is important to note that such an upper performance limit could be defined based on a theoretical foundation rather than optimization algorithms, as methods like TO are unable to guarantee a globally optimal solution.

This thesis is organized into five chapters. **Chapter 2** focuses on the topological optimization of a reaction-diffusion system, the simplest case involving mass transport via molecular diffusion and a first-order chemical reaction with reversible kinetics. The aim is to optimize the porosity distribution to maximize the reactant-to-product conversion rate. **Chapter 3** extends the scope to an electrochemical reactor, where mass and charge transport are coupled with an electrochemical reaction. The system is more complex due to multiple transport phenomena and nonlinear reaction

kinetics, resembling the catalyst layer of a PEFC. TO is applied to improve system performance from two distinct perspectives, while an entropy generation analysis provides critical insights into the characteristics of efficient designs. In **Chapter 4**, a macroscopic two-phase flow model of a PEMFC is developed and validated against experimental data. The catalyst layer structure is optimized using a density-based TO method. The performance improvement is analyzed in terms of key factors such as effective diffusivity, conductivity, and liquid water management, illustrating the advantages of heterogeneous designs. the systems and physical phenomena studied in **Chapters 2 to 4** differ, they share a common approach in using density-based topology optimization to design electrode structures through macroscopic mathematical modeling. Each chapter presents distinct modeling details, including the transport phenomena considered, reaction kinetics, and the composition of materials constituting the electrode. Specifically, **Chapters 2 and 3** provide a foundational study of reactive transport system optimization, with certain physical phenomena assumed, while **Chapter 4** applies this methodology to a real-world application of a PEMFC.

In all these chapters, a macro-scale mathematical model of reactive transport is coupled with density-based topology optimization to generate optimized designs for macroscopic properties of porous reactors, such as porosity. However, in the field of porous media modeling, macroscopic models rely on volume-averaging relationships that connect effective properties (e.g., effective diffusivity) with intrinsic properties (e.g., intrinsic diffusivity). These relationships typically use macroscopic structural properties (e.g., porosity) to form these connections, and numerous studies have examined them in depth. Despite extensive research producing various empirical, semi-empirical, and theoretical models, no universal relationship has emerged that accurately connects effective and intrinsic properties across all operational and structural conditions. This challenge is likely due to information loss regarding the porous media's microstructure during volume-averaging.

In the absence of a universal model describing porous media properties, shifting to geometry-resolved approaches—where the microstructure is fully or partially represented—could address some of the limitations inherent in low-resolution macroscale models. However, these geometry-resolved models come with increased computational demands. Therefore, **Chapter 5** adopts a different approach by optimizing the reactor structure at a pore-level resolution. This system, analogous to the electrode of a redox flow battery, involves both convective and diffusive mass transport. A pore network model is employed to simulate system behavior at the pore

scale, and a metaheuristic optimization algorithm is used to identify Pareto-optimal solutions in a multi-objective framework. Given the significance of convective flow, both conversion rate and pumping cost are considered to achieve an efficient design. In addition to establishing pore-level structural optimization with manageable computational costs, a key novelty of the proposed optimization framework is the introduction of the idea of background grid. This grid allows the optimizer to freely select any morphology that may yield higher performance. As aforementioned, although algorithmic optimization of pore networks has been previously attempted by another research group, their approach was limited to adjusting pore diameters within a fixed cubic lattice configuration, without enabling the optimizer to freely choose the optimal network morphology. Finally, **Chapter 6** presents the conclusions of the thesis and offers future research directions.

Abbreviations

BESO	Bi-directional evolutionary structural optimization
BOBYQA	Bound optimization by quadratic approximation
DNS	Direct numerical simulation
ECSA	Electrochemical specific area
EED	Electrochemical energy devices
EGM	Entropy generation minimization
EoEP	Equipartition of entropy production
ESO	Evolutionary structural optimization
FEM	Finite element method
FVM	Finite volume method
GA	Genetic algorithm
GCMMA	Globally convergent method of moving asymptotes
LBM	Lattice Boltzmann method
MBB	Messerschmitt–Bölkow–Blohm
MMA	Method of moving asymptotes
MMC	Moving morphable component
MMV	Moving morphable void
NET	Non-equilibrium thermodynamics
PEFC	Polymer electrolyte fuel cell
PEMWE	Proton exchange membrane water electrolyzer
PNM	Pore network modeling
RAMP	Rational approximation of material properties

RFB	Redox flow battery
SBE	Structural battery electrolytes
SIMP	Solid isotropic material with penalization
SLP	Sequential linear programming
SOFC	Solid oxide fuel cell
TO	Topology optimization

Nomenclature

D	Design domain
p	Penalty exponent
w	Material domain
$\mathbf{X}$	Point coordinates

Greek symbols

ρ	Density
λ	Physical properties
Φ	Level set function
$\partial\Omega$	Interface between two phases

Subscripts/superscripts

eff	Effective
max	Maximum
min	Minimum
penalized	Penalized

Bibliography

[1] S. Najib and E. Erdem, "Current progress achieved in novel materials for supercapacitor electrodes: mini review," *Nanoscale Advances*, vol. 1, no. 8, p. 2817–2827, 2019.

[2] A. Mishra, A. Mehta, S. Basu, S. J. Malode, N. P. Shetti, S. S. Shukla, M. N. Nadagouda, and T. M. Aminabhavi, "Electrode materials for lithium-ion batteries," *Materials Science for Energy Technologies*, vol. 1, p. 182–187, Dec. 2018.

[3] V. A. Sadykov, E. M. Sadovskaya, N. F. Eremeev, E. Yu. Pikalova, N. M. Bogdanovich, E. A. Filonova, T. A. Krieger, Y. E. Fedorova, A. V. Krasnov, P. I. Skriabin, A. I. Lukashevich, R. Steinberger-Wilckens, and I. C. Vinke, "Novel materials for solid oxide fuel cells cathodes and oxygen separation membranes: Fundamentals of oxygen transport and performance," *Carbon Resources Conversion*, vol. 3, p. 112–121, 2020.

[4] C. Lee, W. J. M. Kort-Kamp, H. Yu, D. A. Cullen, B. M. Patterson, T. A. Arman, S. Komini Babu, R. Mukundan, R. L. Borup, and J. S. Spendelow, "Grooved electrodes for high-power-density fuel cells," *Nature Energy*, vol. 8, p. 685–694, May 2023.

[5] W. Pfleging and P. Gotcu, "Femtosecond laser processing of thick film cathodes and its impact on lithium-ion diffusion kinetics," *Applied Sciences*, vol. 9, p. 3588, Sept. 2019.

[6] G. Okuhata, T. Tonoike, K. Nishida, S. Tsushima, and S. Hirai, "Effect of perforation structure of cathode gdl on liquid water removal in pefc," *ECS Transactions*, vol. 58, p. 1047–1057, Aug. 2013.

[7] I. Mayrhuber, C. Dennison, V. Kalra, and E. Kumbur, "Laser-perforated carbon paper electrodes for improved mass-transport in high power density vanadium redox flow batteries," *Journal of Power Sources*, vol. 260, p. 251–258, Aug. 2014.

[8] X. Wang, S. Chen, Z. Fan, W. Li, S. Wang, X. Li, Y. Zhao, T. Zhu, and X. Xie, "Laser-perforated gas diffusion layer for promoting liquid water transport in a proton exchange membrane fuel cell," *International Journal of Hydrogen Energy*, vol. 42, p. 29995–30003, Dec. 2017.

[9] J. K. Lee, T. Schuler, G. Bender, M. Sabharwal, X. Peng, A. Z. Weber, and N. Danilovic, "Interfacial engineering via laser ablation for high-performing pem water electrolysis," *Applied Energy*, vol. 336, p. 120853, Apr. 2023.

[10] W. Lv, Y. Luo, Y. Xu, K. Xu, and M. Zheng, "Laser perforated porous electrodes in conjunction with interdigitated flow field for mass transfer enhancement in redox flow battery," *International Journal of Heat and Mass Transfer*, vol. 224, p. 125313, June 2024.

[11] O. Sigmund and K. Maute, "Topology optimization approaches: A comparative review," *Structural and Multidisciplinary Optimization*, vol. 48, p. 1031–1055, Aug. 2013.

[12] J. Wu, O. Sigmund, and J. P. Groen, "Topology optimization of multi-scale structures: a review," *Structural and Multidisciplinary Optimization*, vol. 63, p. 1455–1480, Mar. 2021.

[13] J. S. Lee, S. Y. Yoon, B. Kim, H. Lee, M. Y. Ha, and J. K. Min, "A topology optimization based design of a liquid-cooled heat sink with cylindrical pin fins having varying pitch," *International Journal of Heat and Mass Transfer*, vol. 172, p. 121172, June 2021.

[14] J. Alexandersen, O. Sigmund, and N. Aage, "Large scale three-dimensional topology optimisation of heat sinks cooled by natural convection," *International Journal of Heat and Mass Transfer*, vol. 100, p. 876–891, Sept. 2016.

[15] K. Yaji, T. Yamada, S. Kubo, K. Izui, and S. Nishiwaki, "A topology optimization method for a coupled thermal–fluid problem using level set boundary expressions," *International Journal of Heat and Mass Transfer*, vol. 81, p. 878–888, Feb. 2015.

[16] J. Alexandersen and C. S. Andreasen, "A review of topology optimisation for fluid-based problems," *Fluids*, vol. 5, p. 29, Mar. 2020.

[17] X. Zhang, A. Takezawa, and Z. Kang, "Topology optimization of piezoelectric smart structures for minimum energy consumption under active control," *Structural and Multidisciplinary Optimization*, vol. 58, p. 185–199, Dec. 2017.

[18] Y. Wang, Z. Kang, and X. Zhang, "A velocity field level set method for topology optimization of piezoelectric layer on the plate with active vibration control," *Mechanics of Advanced Materials and Structures*, vol. 30, p. 1326–1339, Feb. 2022.

[19] K. Yaji, S. Yamasaki, S. Tsushima, and K. Fujita, "A framework of multi-fidelity topology design and its application to optimum design of flow fields in battery systems," in *Volume 2A: 45th Design Automation Conference*, IDETC-CIE2019, American Society of Mechanical Engineers, Aug. 2019.

[20] K. Yaji, S. Yamasaki, S. Tsushima, T. Suzuki, and K. Fujita, "Topology optimization for the design of flow fields in a redox flow battery," *Structural and Multidisciplinary Optimization*, vol. 57, p. 535–546, July 2017.

[21] C.-H. Chen, K. Yaji, S. Yamasaki, S. Tsushima, and K. Fujita, "Computational design of flow fields for vanadium redox flow batteries via topology optimization," *Journal of Energy Storage*, vol. 26, p. 100990, Dec. 2019.

[22] Z. Liu, X. Zeng, W. Zhao, Y. Gao, Y. Sun, and P. Yan, "A topology optimization design of three-dimensional cooling plate for the thermal homogeneity of lithium-ion batteries," *Energy Conversion and Management: X*, vol. 14, p. 100215, May 2022.

[23] X. Mo, H. Zhi, Y. Xiao, H. Hua, and L. He, "Topology optimization of cooling plates for battery thermal management," *International Journal of Heat and Mass Transfer*, vol. 178, p. 121612, Oct. 2021.

[24] V. Wanittansirichok, K. Mongkholphan, N. Chaowalitbumrung, Y. Sukjai, and P. Promoppatum, "Topology optimization for liquid-based battery thermal management system under varied charge rates," *Journal of Energy Storage*, vol. 55, p. 105703, Nov. 2022.

[25] Y. Sun, R. Bai, and J. Ma, "Design and thermal analysis of a new topological cooling plate for prismatic lithium battery thermal management," *Applied Thermal Engineering*, vol. 219, p. 119547, Jan. 2023.

[26] P. Lin, P. Zhou, and C. Wu, "Multi-objective topology optimization of end plates of proton exchange membrane fuel cell stacks," *Journal of Power Sources*, vol. 196, p. 1222–1228, Feb. 2011.

[27] B. Liu, M. Wei, G. Ma, W. Zhang, and C. Wu, "Stepwise optimization of endplate of fuel cell stack assembled by steel belts," *International Journal of Hydrogen Energy*, vol. 41, p. 2911–2918, Jan. 2016.

[28] D. Herzog, T. Röver, S. Abdolov, F. Becker, and C. Gentner, "Optimization and design for additive manufacturing of a fuel cell end plate," *Journal of Laser Applications*, vol. 34, Oct. 2022.

[29] D. Yang, Y. Hao, B. Li, P. Ming, and C. Zhang, "Topology optimization design for the lightweight endplate of proton exchange membrane fuel cell stack clamped with bolts," *International Journal of Hydrogen Energy*, vol. 47, p. 9680–9689, Feb. 2022.

[30] B. S. Lazarov and O. Sigmund, "Filters in topology optimization based on helmholtz-type differential equations," *International Journal for Numerical Methods in Engineering*, vol. 86, p. 765–781, Dec. 2010.

[31] Y. Demirel and V. Gerbaud, *Nonequilibrium Thermodynamics: Transport and Rate Processes in Physical, Chemical and Biological Systems*. Elsevier Science, 2018.

[32] A. Bejan, *Entropy Generation Minimization: The Method of Thermodynamic Optimization of Finite-Size Systems and Finite-Time Processes*. CRC Press, Oct. 2013.

[33] M. O. Petinrin, T. Bello-Ochende, A. A. Dare, and M. O. Oyewola, "Entropy generation minimisation of shell-and-tube heat exchanger in crude oil preheat train using firefly algorithm," *Applied Thermal Engineering*, vol. 145, pp. 264–276, 2018.

[34] D. Tondeur and E. Kvaalen, "Equipartition of entropy production. an optimality criterion for transfer and separation processes," *Industrial & Engineering Chemistry Research*, vol. 26, p. 50–56, Jan. 1987.

[35] E. Magnanelli, E. Johannessen, and S. Kjelstrup, "Entropy production minimization as design principle for membrane systems: Comparing equipartition results to numerical optima," *Industrial & Engineering Chemistry Research*, vol. 56, p. 4856–4866, Apr. 2017.

[36] X. Chen, "Topology optimization of microfluidics — a review," *Microchemical Journal*, vol. 127, p. 52–61, July 2016.

[37] M. P. Bendsøe and N. Kikuchi, "Generating optimal topologies in structural design using a homogenization method," *Computer Methods in Applied Mechanics and Engineering*, vol. 71, p. 197–224, Nov. 1988.

[38] P. Charoen-amornkitt, M. Alizadeh, T. Suzuki, and S. Tsushima, "Entropy generation analysis during adjoint variable-based topology optimization of porous reaction-diffusion systems under various design dimensionalities," *International Journal of Heat and Mass Transfer*, vol. 202, p. 123725, Mar. 2023.

[39] T. Dbouk, "A review about the engineering design of optimal heat transfer systems using topology optimization," *Applied Thermal Engineering*, vol. 112, p. 841–854, Feb. 2017.

[40] C. B. Dilgen, S. B. Dilgen, N. Aage, and J. S. Jensen, "Topology optimization of acoustic mechanical interaction problems: a comparative review," *Structural and Multidisciplinary Optimization*, vol. 60, p. 779–801, Mar. 2019.

[41] H. A. Eschenauer and N. Olhoff, "Topology optimization of continuum structures: A review*," *Applied Mechanics Reviews*, vol. 54, p. 331–390, July 2001.

[42] G. Rozvany, "Aims, scope, methods, history and unified terminology of computer-aided topology optimization in structural mechanics," *Structural and Multidisciplinary Optimization*, vol. 21, p. 90–108, Apr. 2001.

[43] G. I. N. Rozvany, "A critical review of established methods of structural topology optimization," *Structural and Multidisciplinary Optimization*, vol. 37, p. 217–237, Feb. 2008.

[44] J. D. Deaton and R. V. Grandhi, "A survey of structural and multidisciplinary continuum topology optimization: post 2000," *Structural and Multidisciplinary Optimization*, vol. 49, p. 1–38, July 2013.

[45] A. Fawaz, Y. Hua, S. Le Corre, Y. Fan, and L. Luo, "Topology optimization of heat exchangers: A review," *Energy*, vol. 252, p. 124053, Aug. 2022.

[46] M. P. Bendsøe, "Optimal shape design as a material distribution problem," *Structural Optimization*, vol. 1, p. 193–202, Dec. 1989.

[47] G. Dzierżanowski, "On the comparison of material interpolation schemes and optimal composite properties in plane shape optimization," *Structural and Multidisciplinary Optimization*, vol. 46, p. 693–710, Apr. 2012.

[48] F. Chen, J. Wang, and X. Yang, "Topology optimization design and numerical analysis on cold plates for lithium-ion battery thermal management," *International Journal of Heat and Mass Transfer*, vol. 183, p. 122087, Feb. 2022.

[49] J. Wang, X. Liu, and Y. Wang, "Topology optimization of micro-channel reactors using an improved multi-objective algorithm," *Chemical Engineering Journal*, vol. 458, p. 141420, Feb. 2023.

[50] J. Ott, B. Völker, Y. Gan, R. M. McMeeking, and M. Kamlah, "A micromechanical model for effective conductivity in granular electrode structures," *Acta Mechanica Sinica*, vol. 29, p. 682–698, Oct. 2013.

[51] D.-W. Chung, M. Ebner, D. R. Ely, V. Wood, and R. Edwin García, "Validity of the bruggeman relation for porous electrodes," *Modelling and Simulation in Materials Science and Engineering*, vol. 21, p. 074009, Oct. 2013.

[52] K. Zheng and M. Ni, "Reconstruction of solid oxide fuel cell electrode microstructure and analysis of its effective conductivity," *Science Bulletin*, vol. 61, p. 78–85, Jan. 2016.

[53] B. Tjaden, S. J. Cooper, D. J. Brett, D. Kramer, and P. R. Shearing, "On the origin and application of the bruggeman correlation for analysing transport phenomena in electrochemical systems," *Current Opinion in Chemical Engineering*, vol. 12, p. 44–51, May 2016.

[54] L. Froboese, J. F. v. d. Sichel, T. Loellhoeffel, L. Helmers, and A. Kwade, "Effect of microstructure on the ionic conductivity of an all solid-state battery electrode," *Journal of The Electrochemical Society*, vol. 166, no. 2, p. A318–A328, 2019.

[55] F. Tsutsui, T. Suzuki, and S. Tsushima, "Measurement and analysis of gas transport properties in catalyst layers of polymer electrolyte fuel cells with different ionomer to carbon ratio," *ECS Transactions*, vol. 98, p. 49–54, Sept. 2020.

[56] T. Suzuki, Y. Nakata, F. Tsutsui, and S. Tsushima, "Investigation of gas transport properties of pemfc catalyst layers using a microfluidic device," *Journal of The Electrochemical Society*, vol. 167, p. 124519, Jan. 2020.

[57] Z. Bao, Y. Li, X. Zhou, F. Gao, Q. Du, and K. Jiao, "Transport properties of gas diffusion layer of proton exchange membrane fuel cells: Effects of compression," *International Journal of Heat and Mass Transfer*, vol. 178, p. 121608, Oct. 2021.

[58] L. Maier, M. Scherle, M. Hopp-Hirschler, and U. Nieken, "Effective transport parameters of porous media from 2d microstructure images," *International Journal of Heat and Mass Transfer*, vol. 175, p. 121371, Aug. 2021.

[59] F. Wang, X. Li, J. Tan, X. Hao, and B. Xiong, "Pore-scale prediction of the oxygen effective diffusivity in porous battery electrodes using the random walk theory," *International Journal of Heat and Mass Transfer*, vol. 183, p. 122085, Feb. 2022.

[60] N. P. van Dijk, K. Maute, M. Langelaar, and F. van Keulen, "Level-set methods for structural topology optimization: a review," *Structural and Multidisciplinary Optimization*, vol. 48, p. 437–472, Mar. 2013.

[61] M. Y. Wang, X. Wang, and D. Guo, "A level set method for structural topology optimization," *Computer Methods in Applied Mechanics and Engineering*, vol. 192, p. 227–246, Jan. 2003.

[62] S. S. Petrova and A. D. Solov'ev, "The origin of the method of steepest descent," *Historia Mathematica*, vol. 24, p. 361–375, Nov. 1997.

[63] S. Rao, *Engineering Optimization: Theory and Practice*. New Age International, 2000.

[64] K. Svanberg, "The method of moving asymptotes—a new method for structural optimization," *International Journal for Numerical Methods in Engineering*, vol. 24, p. 359–373, Feb. 1987.

[65] C. Zillober, "A globally convergent version of the method of moving asymptotes," *Structural Optimization*, vol. 6, p. 166–174, Sept. 1993.

[66] D. Guirguis and M. F. Aly, "A derivative-free level-set method for topology optimization," *Finite Elements in Analysis and Design*, vol. 120, p. 41–56, Nov. 2016.

[67] D. J. Munk, G. A. Vio, and G. P. Steven, "Topology and shape optimization methods using evolutionary algorithms: a review," *Structural and Multidisciplinary Optimization*, vol. 52, p. 613–631, May 2015.

[68] D. Givoli, "A tutorial on the adjoint method for inverse problems," *Computer Methods in Applied Mechanics and Engineering*, vol. 380, p. 113810, July 2021.

[69] X. Huang and Y. Xie, "Convergent and mesh-independent solutions for the bi-directional evolutionary structural optimization method," *Finite Elements in Analysis and Design*, vol. 43, p. 1039–1049, Oct. 2007.

[70] A. Kawamoto, T. Matsumori, S. Yamasaki, T. Nomura, T. Kondoh, and S. Nishiwaki, "Heaviside projection based topology optimization by a pde-filtered scalar function," *Structural and Multidisciplinary Optimization*, vol. 44, p. 19–24, Aug. 2010.

[71] X. Huang and Y.-M. Xie, "A further review of eso type methods for topology optimization," *Structural and Multidisciplinary Optimization*, vol. 41, p. 671–683, Mar. 2010.

[72] Z. Li, H. Xu, and S. Zhang, "A comprehensive review of explicit topology optimization based on moving morphable components (mmc) method," *Archives of Computational Methods in Engineering*, vol. 31, p. 2507–2536, Jan. 2024.

[73] R. Xue, C. Liu, W. Zhang, Y. Zhu, S. Tang, Z. Du, and X. Guo, "Explicit structural topology optimization under finite deformation via moving morphable void (mmv) approach," *Computer Methods in Applied Mechanics and Engineering*, vol. 344, p. 798–818, Feb. 2019.

[74] H. Iwai, A. Kuroyanagi, M. Saito, A. Konno, H. Yoshida, T. Yamada, and S. Nishiwaki, "Power generation enhancement of solid oxide fuel cell by cathode–electrolyte interface modification in mesoscale assisted by level set-based

optimization calculation," *Journal of Power Sources*, vol. 196, p. 3485–3495, Apr. 2011.

[75] V. Zadin, D. Brandell, H. Kasemägi, J. Lellep, and A. Aabloo, "Designing the 3d-microbattery geometry using the level-set method," *Journal of Power Sources*, vol. 244, p. 417–428, Dec. 2013.

[76] J. Onishi, Y. Kametani, Y. Hasegawa, and N. Shikazono, "Topology optimization of electrolyte-electrode interfaces of solid oxide fuel cells based on the adjoint method," *Journal of The Electrochemical Society*, vol. 166, no. 13, p. F876–F888, 2019.

[77] J. Onishi and N. Shikazono, "Topology optimization of electrolyte-anode interfaces in solid oxide fuel cells," *ECS Transactions*, vol. 91, p. 2127–2135, July 2019.

[78] A. He, J. Onishi, and N. Shikazono, "Numerical optimization of the solid oxide fuel cell electrode-electrolyte interface structure with adjoint method," *ECS Transactions*, vol. 91, p. 2045–2054, July 2019.

[79] A. He, J. Onishi, J. Gong, and N. Shikazono, "Three-dimensional optimization of la0.6sr0.4co0.2fe0.8o3 cathode microstructure with particle radius constraint," *Electrochimica Acta*, vol. 398, p. 139287, Dec. 2021.

[80] A. He, J. Gong, J. Onishi, and N. Shikazono, "Three-dimensional topology optimization of ni-ysz anode for solid oxide fuel cells via multiphase level-set method," *Nano Energy*, vol. 103, p. 107817, Dec. 2022.

[81] N. Ishizuka, T. Yamada, K. Izui, and S. Nishiwaki, "Topology optimization for unifying deposit thickness in electroplating process," *Structural and Multidisciplinary Optimization*, vol. 62, p. 1767–1785, May 2020.

[82] X. Song, A. R. Diaz, A. Benard, and J. D. Nicholas, "A 2d model for shape optimization of solid oxide fuel cell cathodes," *Structural and Multidisciplinary Optimization*, vol. 47, p. 453–464, Sept. 2012.

[83] F. Mathieu-Potvin and L. Gosselin, "Optimal topology and distribution of catalyst in pemfc," *International Journal of Hydrogen Energy*, vol. 39, p. 7382–7401, May 2014.

[84] J. Lamb, G. Mixon, and P. Andrei, "Adjoint method for the optimization of the catalyst distribution in proton exchange membrane fuel cells," *Journal of The Electrochemical Society*, vol. 164, no. 11, p. E3232–E3242, 2017.

[85] J. Lamb, G. Mixon, and P. Andrei, "Mathematical optimization of the spatial distribution of platinum particles in the catalyst layer of pemfcs," *ECS Transactions*, vol. 77, p. 1179–1196, July 2017.

[86] J. Lamb and P. Andrei, "Analysis of sensitivity of pemfc parameters to non-uniform platinum deposition," *ECS Transactions*, vol. 80, p. 291–300, Aug. 2017.

[87] J. Lamb and P. Andrei, "Designing the ideal catalyst layer in pemfcs," *ECS Transactions*, vol. 97, p. 671–683, June 2020.

[88] J. Lamb and P. Andrei, "Optimizing the composition of the pemfc catalyst layer," *ECS Transactions*, vol. 98, p. 67–77, Sept. 2020.

[89] S. L. Mitchell and M. Ortiz, "Computational multiobjective topology optimization of silicon anode structures for lithium-ion batteries," *Journal of Power Sources*, vol. 326, p. 242–251, Sept. 2016.

[90] V. A. Beck, J. J. Wong, C. F. Jekel, D. A. Tortorelli, S. E. Baker, E. B. Duoss, and M. A. Worsley, "Computational design of microarchitected porous electrodes for redox flow batteries," *Journal of Power Sources*, vol. 512, p. 230453, Nov. 2021.

[91] T. Roy, M. A. Salazar de Troya, M. A. Worsley, and V. A. Beck, "Topology optimization for the design of porous electrodes," *Structural and Multidisciplinary Optimization*, vol. 65, May 2022.

[92] M. Alizadeh, P. Charoen-amornkitt, T. Suzuki, and S. Tsushima, "Mixed topology optimization: A self-guided boundary-independent approach for power sources," *Energy Conversion and Management*, vol. 294, p. 117567, Oct. 2023.

[93] Q. Li, G. Cao, X. Zhang, and G. Li, "Topology optimization of the microstructure of solid oxide fuel cell cathodes," *Acta Materialia*, vol. 201, p. 278–285, Dec. 2020.

[94] Q. Li, Y. Duan, D. Chai, X. Zhang, X. Min, and G. Li, "Topology optimization of microstructure of solid-oxide fuel cell anode to minimize thermal mismatch," *International Journal of Energy Research*, vol. 45, p. 3214–3230, Oct. 2020.

[95] P. Charoen-amornkitt, M. Alizadeh, T. Suzuki, and S. Tsushima, "Topologically optimized anode catalyst layers of proton exchange membrane water electrolyzers," *ECS Transactions*, vol. 111, p. 87–95, May 2023.

[96] P. Passakornjaras, P. Orncompa, M. Alizadeh, P. Charoen-amornkitt, T. Suzuki, and S. Tsushima, "Numerical modeling and topology optimization for designing the anode catalyst layer in proton exchange membrane water electrolyzers considering mass transport limitation," *Journal of The Electrochemical Society*, vol. 171, p. 074502, July 2024.

[97] M. Long, T. Suzuki, M. Alizadeh, S. Tsushima, and P. Charoen-amornkitt, "The influence of rib and porous reactor thickness on topologically optimized structure in reaction-diffusion systems," in *2023 IEEE Transportation Electrification Conference and Expo, Asia-Pacific (ITEC Asia-Pacific)*, IEEE, Nov. 2023.

[98] M. Alizadeh, P. Charoen-amornkitt, T. Suzuki, and S. Tsushima, "A numerical simulation of evolution processes and entropy generation for optimal architecture of an electrochemical reaction-diffusion system: Comparison of two optimization strategies," *Journal of The Electrochemical Society*, vol. 170, p. 114520, Nov. 2023.

[99] M. Alizadeh, P. Charoen-amornkitt, T. Suzuki, and S. Tsushima, "Investigation of transport-reaction dynamics and local/global entropy production in topology optimization of two-species reaction-diffusion systems," *Chemical Engineering Science*, vol. 275, p. 118739, July 2023.

[100] M. Alizadeh, P. Charoen-amornkitt, T. Suzuki, and S. Tsushima, "Analysis of local-global entropy generation in an electrochemical system," in *Proceeding of International Heat Transfer Conference 17*, Begellhouse, 2023.

[101] M. Long, M. Alizadeh, P. Charoen-amornkitt, T. Suzuki, and S. Tsushima, "A method for estimating optimized porosity distribution in reaction-diffusion systems without reliance on topology optimization," *Chemical Engineering Science*, vol. 298, p. 120420, Oct. 2024.

[102] L. Xing, W. Shi, H. Su, Q. Xu, P. K. Das, B. Mao, and K. Scott, "Membrane electrode assemblies for pem fuel cells: A review of functional graded design and optimization," *Energy*, vol. 177, p. 445–464, June 2019.

[103] P. Havaej, M. Kermani, M. Abdollahzadeh, H. Heidary, and A. Moradi, "A numerical modeling study on the influence of catalyst loading distribution on the performance of polymer electrolyte membrane fuel cell," *International Journal of Hydrogen Energy*, vol. 43, p. 10031–10047, May 2018.

[104] P. He, Y.-T. Mu, J. W. Park, and W.-Q. Tao, "Modeling of the effects of cathode catalyst layer design parameters on performance of polymer electrolyte membrane fuel cell," *Applied Energy*, vol. 277, p. 115555, Nov. 2020.

[105] S. Tsushima and T. Suzuki, "Modeling and simulation of vanadium redox flow battery with interdigitated flow field for optimizing electrode architecture," *Journal of The Electrochemical Society*, vol. 167, p. 020553, Jan. 2020.

[106] Y. Dai and V. Srinivasan, "On graded electrode porosity as a design tool for improving the energy density of batteries," *Journal of The Electrochemical Society*, vol. 163, p. A406–A416, Dec. 2015.

[107] M. Srinivasarao, D. Bhattacharyya, and R. Rengaswamy, "Optimization studies of a polymer electrolyte membrane fuel cell with multiple catalyst layers," *Journal of Power Sources*, vol. 206, p. 197–203, May 2012.

[108] S. Nørgaard, O. Sigmund, and B. Lazarov, "Topology optimization of unsteady flow problems using the lattice boltzmann method," *Journal of Computational Physics*, vol. 307, p. 291–307, Feb. 2016.

[109] F. Dugast, Y. Favennec, C. Josset, Y. Fan, and L. Luo, "Topology optimization of thermal fluid flows with an adjoint lattice boltzmann method," *Journal of Computational Physics*, vol. 365, p. 376–404, July 2018.

[110] K. Yaji, M. Ogino, C. Chen, and K. Fujita, "Large-scale topology optimization incorporating local-in-time adjoint-based method for unsteady thermal-fluid problem," *Structural and Multidisciplinary Optimization*, vol. 58, p. 817–822, Feb. 2018.

[111] Y. Tanabe, K. Yaji, and K. Ushijima, "Topology optimization using the lattice boltzmann method for unsteady natural convection problems," *Structural and Multidisciplinary Optimization*, vol. 66, Apr. 2023.

[112] D. Tanaka, T. Suzuki, and S. Tsushima, "Numerical study of fluid behaviors in fibrous porous electrodes and optimization of electrode structure using lattice boltzmann simulation," in *Proceedings of the 13th TSME International Conference on Mechanical Engineering*, 2023.

[113] R. van Gorp, M. van der Heijden, M. Amin Sadeghi, J. Gostick, and A. Forner-Cuenca, "Bottom-up design of porous electrodes by combining a genetic algorithm and a pore network model," *Chemical Engineering Journal*, vol. 455, p. 139947, Jan. 2023.

[114] M. van der Heijden, G. Szendrei, V. de Haas, and A. Forner-Cuenca, "A versatile optimization framework for porous electrode design," *Digital Discovery*, vol. 3, no. 7, p. 1292–1307, 2024.

[115] M. Alizadeh, J. Gostick, T. Suzuki, and S. Tsushima, "Topological optimization for tailored designs of advection–diffusion-reaction porous reactors based on pore scale modeling and simulation: A pnm-nsga framework," *Computers & Structures*, vol. 301, p. 107452, Sept. 2024.

Chapter 2

Investigation of transport-reaction dynamics and local/global entropy production in topology optimization of two-species reaction-diffusion systems

Abstract

There is a growing body of research on the enhancement of porous reactors through the modification of their structures. So far, however, there has been little elucidation on how altered spatial structure might be beneficial to reducing irreversible losses. To explain the optimization procedure from a theoretical basis, this study aims to investigate the dynamics of rate and transport processes in a reaction-diffusion system with two-species operating under a steady-state mode. A topology optimization method is employed to increase the overall reaction rate by modifying porosity distribution. Additionally, an entropy generation model is developed to examine the irreversibilities of the system. Based on this model, the local and global rates of entropy production in the system are evaluated, and contributions by various mechanisms are separately quantified. The results show that an optimal porosity distribution can boost the system performance by 57% through formation of proper primary and secondary diffusion channels.

This chapter is published as:

M. Alizadeh, P. Charoen-amornkitt, T. Suzuki, and S. Tsushima. "Investigation of transport-reaction dynamics and local/global entropy production in topology optimization of two-species reaction-diffusion systems", *Chemical Engineering Science*, **275** (2023): 118739. https://doi.org/10.1016/j.ces.2023.118739

2.1 Introduction

Heterogeneous catalysis is a catalytic process where more than one phase exists [1]. This type of catalysis, in contrast to homogeneous catalysis, includes most of industrial applications—chemicals production, chemical refining, photocatalysis, energy conversion, and environmental protection to name a few [1]. Porous catalytic reactors are extensively used in various chemical and electrochemical engineering applications, from synthesis of chemical products (e.g., hydrogen peroxide [2]) to fuel cells. Improving these porous reactors is therefore facilitating the transition to a more efficient and sustainable society which is an urgent task for researchers worldwide [3–5]. In a gas-solid reactor, the reactant species, that exists in a gas phase, is converted to product species through a chemical reaction. For instance, the catalyst layer of a fuel cell is a porous catalytic reactor in which the rate of a reduction/oxidation reaction is boosted by a noble catalyst metal [6]. Given the broad applications of heterogeneous catalytic reactors, improving their performance might have a significant impact on the cost-effectiveness of these systems. A typical porous catalytic reactor is a reaction-diffusion (RD) system in which the reactant gas is diffused through the pores of the reactor while getting converted to a desirable product in presence of a catalyst. In such a system, a transport phenomena (mass diffusion) is coupled with a rate process (chemical reaction). It is favorable to increase the production rate by enhancing the chemical reaction rate. This goal might be accomplished by using a better catalyst (with higher catalytic activity). However, catalyst materials are usually precious metals and therefore, using a more amount of them might increase the reactor fabrication cost substantially. Moreover, the rate of a chemical reaction typically depends not only on the catalytic activity of the catalyst but also on the concentration of reactant species. In a porous reactor, the reactant is delivered to the reaction site through the voids. Increasing the volume fraction of solid phase in a porous reactor and consequently decreasing the porosity might degrade the reactor performance due to insufficient reactant supply. Based on these explanations, the structural design of a porous reactor could have a decisive impact on its overall performance. In addition, the complexity of coupled transport and rate processes that are taking place in these systems makes the structural design of a porous reactor more complicated. As the system is complicated, our previous studies [7–9] aimed to characterize and quantify how porous media modification affected the active surface area, reaction rate constant, and mass transfer coefficient.

Historically, it was known that a non-uniform reactor in which the activity of the

pellet changes with position might be beneficial in some cases. Aris [10] discussed how the effectiveness factor of a pellet may be improved by a concentrated catalyst toward the outside. However, they do not provide any rigorous mathematical approach for obtaining such non-uniform distributions. Shape and sizing optimization have been widely employed to enhance system performance [11]. More recently, topology optimization techniques have drawn growing attention from researchers in a variety of engineering fields [12]. Topology optimization offers an innovative method to construct an optimal structure layout within a design domain automatically. While at first it was given a rise in structural mechanics [13], the application of topology optimization has now been extended to more complex systems with multiphysics, including heat and fluid [14]. Topology optimization has a high potential to generate pioneering structures that are able to prevail over the dissipation in the conventional porous reactors. Therefore, this technique might be used for structural design of porous reactors with the aim of increasing the overall conversion rate. Recently, some studies addressed utilization of topology optimization for design of porous reactors [15–17]. For instance, Bhattacharjee and Atta [15] investigated optimized porosity distribution in a bed microreactor for a non-Newtonian reactant. Their proposed method enhances the reaction rate without a need for changing the properties of the catalyst in a first-order exothermic reaction. While these studies introduce an inventive method for generating architectured reactors, they do not deal with the fundamental mechanism which leads to the system improvement. The need for a fundamental understanding of the system dynamics could be met by analyzing the irreversibilities caused by various processes taking place in the system. Based on the concept of non-equilibrium thermodynamics (NET) [18, 19], the irreversibility contribution by each mechanism could be quantified in terms of entropy generation rate. Despite the fact that the second law of thermodynamics was initially applied to systems at an equilibrium state, NET has been established to extend the application of this law to systems that are not in global equilibrium. From this angle, NET provides a powerful tool to examine a system only based on its local characteristics. This comprehension at the local scale provides further information about the interaction between various processes in a system and its behavior that is not achievable from a black box analysis. When combined with entropy generation minimization [20], NET analysis has been successfully used for the optimization of thermo-fluid systems (e.g., heat exchangers) [21–26]. For instance, Avellaneda et al. [22] investigated the multi-objective optimization of entropy generation and pressure drop for a gas flow in a channel with convective heat transfer using variational methods. Their findings show that improvement of heat transfer and increase of Nusselt number is

attributed to the reduction of entropy generation rate and increase of viscous dissipation. Moreover, Guo et al. [25] successfully addressed the optimization of shell-and-tube heat exchangers through entropy generation minimization and modified entropy generation number.

In recent years, researchers' attention has been drawn to the use of topology optimization methods for designing state-of-the-art reactors. Despite these breakthrough advancements in designing optimal porous reactors, to the best of the authors' knowledge, the working principles that explain how these optimized design solutions are better, have not been elucidated yet. To put it in another way, a closer look into the literature reveals that so far, researchers were only dealing with finding improved design solutions through mathematical optimization rather than being concerned about the physicochemical explanation behind the optimization process. It is well-known that the results obtained from optimization studies are always affected by the choice of mathematical scheme and tuning parameters. For instance, choice of filter radius in topology optimization or value of parameters in meta-heuristic algorithms (e.g., particle swarm optimization) [27], have a considerable effect on optimization performance. Therefore, the results of previous research work strongly depend on the mathematical scheme and tuning parameters used for the optimization process. Given the limitations of mathematical optimization techniques, the upper limit of performance of these systems is still unknown. This research gap in the previous studies comes from the lack of a well-established conceptual understanding of the transport processes and chemical reactions that are taking place in such systems. The dimensional effects on overall reaction rate and its relation with the averaged distribution of concentration is discussed in another publication by our research group [28]. The present study aims to address the aforementioned gap in knowledge through the concept of NET and provide a solid framework to elucidate the hidden mechanism behind obtaining an optimal design solution. To do so, a porous RD system with two species is considered. Specifically, this study aims to introduce a framework for NET analysis in designing more efficient RD systems. The developed mathematical model is implemented in FreeFEM++ [29], an open-source partial differential equation (PDE) solver, to solve the system of equations. The porosity of the system is then optimized using the adjoint field method and steepest descent algorithm. Moreover, the local entropy production rate in the RD system is evaluated according to the concept of NET. The improvement of system performance during the optimization process is comprehensively examined and explained in accordance

with the mechanisms taking place in the system. In addition, a comprehensive assessment is conducted to investigate the contribution of each dissipation source during the optimization process. A significant contribution of the present study lies in the establishment of an original framework to understand the working principles that leading to irreversibility in multiphysics systems like porous reactors. Such a physicochemical-based understanding might aid subsequent researchers to not only focus on mathematical aspects of developing better porous reactors but also reach a better grasp of their engineered designs. The contributions of this study open a new pathway to the potential determination of the upper bound for the performance of RD systems from a NET point of view which has been undiscovered so far. Moreover, it extends the concept of entropy generation minimization to two-species RD systems and analyze the topology optimization results from a NET point of view.

2.2 Mathematical modeling of the reaction-diffusion system

Reaction-diffusion processes could be found in a broad range of applications, from chemical engineering to non-chemical fields like biology, ecology, and physics [30–32]. In this study, only chemical reaction and mass transport are of our interest. A two-dimensional (2D) RD system is considered, as shown in Fig. 2.1. A previous study [28] showed that the difference between the topology optimization results of 2D and 3D cases are insignificant. Therefore, despite the fact that real systems are 3D, a 2D model is a proper choice since it reduces the computational cost substantially. Since this study aims to provide physicochemical insight of the topology optimization process rather than complex mathematical modeling, the system is kept simple. However, the established procedure in this study might be applied to more complex systems after some modifications. A first-order reversible chemical reaction is considered as follows.

$$\mathrm{A} \underset{k_\mathrm{b}}{\overset{k_\mathrm{f}}{\rightleftharpoons}} \mathrm{B} \tag{2.1}$$

In this reaction, chemical species A is converted to species B with a forward kinetic of k_f (s^{-1}). Also, the backward reaction, in which chemical species B is being converted to species A, is taking place with a kinetic of k_b (s^{-1}).

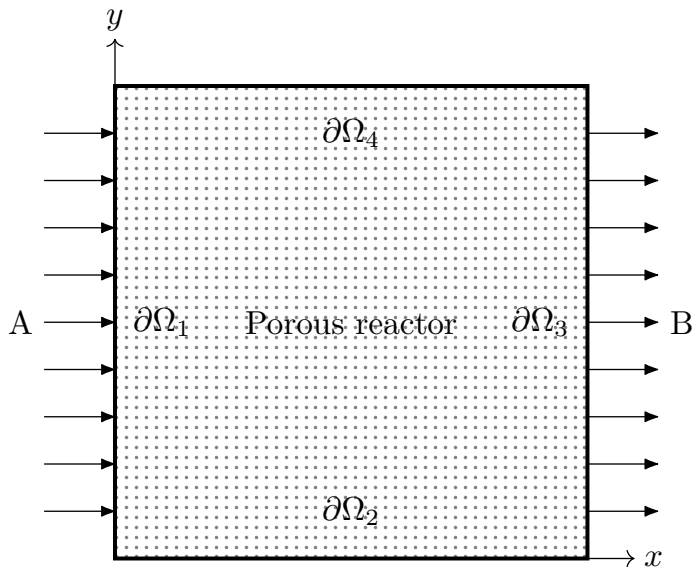

Figure 2.1: Schematic representation of 2D reaction-diffusion system

Moreover, the spatial diffusion of both species in the porous reactor (Fig. 2.1) is described using classical diffusion equation for binary systems, Fick's second law. By combining the diffusion equation with chemical reaction rate equation, the well known RD equation reads as:

$$\frac{\partial C_{\mathrm{i}}}{\partial t} = \nabla \cdot \left(D_{\mathrm{i}}^{\mathrm{eff}} \nabla C_{\mathrm{i}} \right) + R_{\mathrm{i}}^{\mathrm{eff}} \tag{2.2}$$

where C_{i} is the concentration ($\mathrm{mol\,m^{-3}}$), $D_{\mathrm{i}}^{\mathrm{eff}}$ is the effective diffusion coefficient ($\mathrm{m^2\,s^{-1}}$), and $R_{\mathrm{i}}^{\mathrm{eff}}$ is the effective reaction (production/consumption) rate ($\mathrm{mol\,m^{-3}\,s^{-1}}$) of spices i. Given that both forward and backward reactions are first order, the reaction rates are expressed as:

$$R_{\mathrm{f}} = k_{\mathrm{f}} C_{\mathrm{A}} \tag{2.3a}$$

$$R_{\mathrm{b}} = k_{\mathrm{b}} C_{\mathrm{B}} \tag{2.3b}$$

Since the reactor is considered a porous medium, it is necessary to adjust the diffusivity and reaction rate in accordance with the local porosity. Although effective diffusion coefficient in porous media has been the subject of numerous studies, such as [33–40], it is still in dispute among researchers, and there is no consensus on a unique method for its determination. A power-law relation, initially proposed by Bruggeman [41], is one of the alternatives that is extensively used and recognized

in the literature to correlate effective diffusivity with porosity. As a result, in this study, the effective diffusivity of chemical species is derived using a power law. The effective diffusivity coefficient is given as:

$$D_{\mathrm{i}}^{\mathrm{eff}} = D_{\mathrm{i}}^{0}\varepsilon^{\eta} \tag{2.4}$$

in which D_{i}^{0} is the bulk diffusivity ($\mathrm{m^2\,s^{-1}}$) of species i and η is the correction exponent. The value of η should be determined based on the exact porous microstructure; however, typically a value between 1.5 to 3.0 is reported in the literature for porous reactors [42, 43]. The rate of chemical reaction also needs to be corrected locally. The effective reaction rate, $R_{\mathrm{i}}^{\mathrm{eff}}$, is proportional to the volume fraction of catalyst material and is given by:

$$R_{\mathrm{A}}^{\mathrm{eff}} = -R_{\mathrm{f}}^{\mathrm{eff}} + R_{\mathrm{b}}^{\mathrm{eff}} = (-R_{\mathrm{f}} + R_{\mathrm{b}})(1-\varepsilon)^{\gamma} \tag{2.5a}$$

$$R_{\mathrm{B}}^{\mathrm{eff}} = R_{\mathrm{f}}^{\mathrm{eff}} - R_{\mathrm{b}}^{\mathrm{eff}} = (R_{\mathrm{f}} - R_{\mathrm{b}})(1-\varepsilon)^{\gamma} \tag{2.5b}$$

where $(1-\varepsilon)$ is considered to be the volume fraction of catalyst material required to initiate the chemical reaction. In this equation, a similar power-law relation used for diffusivity is employed with γ as the correcting exponent for reaction rate. It is noteworthy that the two reaction rates in Eqs. (2.5a) and (2.5b) are equal with different signs, which is induced by the nature of the chemical reaction Eq. (2.1). This could be interpreted as the amount of species A that is consumed is equal to the amount of species B that is produced and vice versa. By confining the scope of this study to the analysis of system performance under a steady-state, the system of PDEs describing this RD system can be identified as

$$\nabla \cdot \left(D_{\mathrm{A}}^{\mathrm{eff}} \nabla C_{\mathrm{A}}\right) - R_{\mathrm{f}}^{\mathrm{eff}} + R_{\mathrm{b}}^{\mathrm{eff}} = 0 \tag{2.6a}$$

$$\nabla \cdot \left(D_{\mathrm{B}}^{\mathrm{eff}} \nabla C_{\mathrm{B}}\right) + R_{\mathrm{f}}^{\mathrm{eff}} - R_{\mathrm{b}}^{\mathrm{eff}} = 0 \tag{2.6b}$$

By imposing sufficient boundary conditions (B.C.s), this system of equations could be numerically solved. In the present study, a Dirichlet B.C. is assumed for species A and B on boundaries $\partial\Omega_1$ and $\partial\Omega_3$ (Fig. 2.1), respectively. Since the governing equations are second-order PDEs, the given B.C.s are sufficient. The full mathematical representation of system B.C.s is as follows:

$$\text{B.C. of Eq. (2.6a)} \begin{cases} C_{\mathrm{A}} = C_{\mathrm{A}}^{\mathrm{in}} & \text{on } \partial\,\Omega_1 \\ -D_{\mathrm{A}}^{\mathrm{eff}} \nabla C_{\mathrm{A}} \cdot \hat{\mathbf{n}} = 0 & \text{on } \partial\Omega_2 \\ -D_{\mathrm{A}}^{\mathrm{eff}} \nabla C_{\mathrm{A}} \cdot \hat{\mathbf{n}} = 0 & \text{on } \partial\Omega_3 \\ -D_{\mathrm{A}}^{\mathrm{eff}} \nabla C_{\mathrm{A}} \cdot \hat{\mathbf{n}} = 0 & \text{on } \partial\Omega_4 \end{cases} \tag{2.7a}$$

$$\text{B.C. of Eq. (2.6b)} \begin{cases} -D_{\mathrm{B}}^{\mathrm{eff}} \nabla C_{\mathrm{B}} \cdot \hat{\mathbf{n}} = 0 & \text{on } \partial\Omega_1 \\ -D_{\mathrm{B}}^{\mathrm{eff}} \nabla C_{\mathrm{B}} \cdot \hat{\mathbf{n}} = 0 & \text{on } \partial\Omega_2 \\ C_{\mathrm{B}} = C_{\mathrm{B}}^{\mathrm{out}} & \text{on } \partial\Omega_3 \\ -D_{\mathrm{B}}^{\mathrm{eff}} \nabla C_{\mathrm{B}} \cdot \hat{\mathbf{n}} = 0 & \text{on } \partial\Omega_4 \end{cases} \tag{2.7b}$$

in which $C_{\mathrm{A}}^{\mathrm{in}}$ and $C_{\mathrm{B}}^{\mathrm{out}}$ are fixed concentrations of species A and B on boundaries, respectively. While the chosen B.C.s results in conversion of all amount of species A supplied from the boundary $\partial\Omega_1$ to species B, the problem is formulated in a way that various porosity distributions give different conversion capacities. Indeed, this study looks at the problem from a capacity perspective, not an efficiency standpoint (which usually deals with the ratio of system output and input). While capacity perspective is of interest in this study, the chosen perfectly absorbing B.C. is not an essential ingredient for the model to work. The developed model could be employed together with any other sufficient B.C.s to investigate the system characteristics. To generalize the applicability of the developed model, the non-dimensional formalism of RD equations (Eq. (2.6)) reads as:

$$\nabla^* \cdot (\varepsilon^{\eta} \nabla^* C_{\mathrm{A}}^*) - \psi_1 (1-\varepsilon)^{\gamma} C_{\mathrm{A}}^* + \psi_2 (1-\varepsilon)^{\gamma} C_{\mathrm{B}}^* = 0 \tag{2.8a}$$

$$\nabla^* \cdot (\varepsilon^{\eta} \nabla^* C_{\mathrm{B}}^*) + \psi_3 (1-\varepsilon)^{\gamma} C_{\mathrm{A}}^* - \psi_4 (1-\varepsilon)^{\gamma} C_{\mathrm{B}}^* = 0 \tag{2.8b}$$

where C_{A}^* and C_{B}^* are dimensionless dependent variables, ∇^* is differentiation with respect to dimensionless coordinates x^* and y^*. Also, ψ_1, ψ_2, ψ_3, ψ_4 are dimensionless parameters. The dimensionless groups are defined as:

$$\begin{gathered} \psi_1 = \frac{k_{\mathrm{f}} L^2}{D_{\mathrm{A}}^0}; \quad \psi_2 = \frac{k_{\mathrm{b}} L^2}{D_{\mathrm{A}}^0}; \quad \psi_3 = \frac{k_{\mathrm{f}} L^2}{D_{\mathrm{B}}^0}; \quad \psi_4 = \frac{k_{\mathrm{b}} L^2}{D_{\mathrm{B}}^0} \\ x^* = \frac{x}{L}; \quad y^* = \frac{y}{L}; \quad C_{\mathrm{A}}^* = \frac{C_{\mathrm{A}}}{C_0}; \quad C_{\mathrm{B}}^* = \frac{C_{\mathrm{B}}}{C_0} \end{gathered} \tag{2.9}$$

in which L and C_0 are the characteristic length and characteristic concentration of the system, respectively. A reasonable choice for the latter characteristic parameter might be made according to the boundary conditions of the RD system (Eq. (2.7)). Moreover, assuming that the characteristic time of the system is τ, the non-dimensional effective reaction rate is:

$$R^{\text{eff},*} = \psi_5(1-\varepsilon)^{\gamma} C_{\text{A}}^{*} - \psi_6(1-\varepsilon)^{\gamma} C_{\text{B}}^{*} \tag{2.10}$$

where ψ_5 and ψ_6 are dimensionless forward/backward kinetics and are defined as:

$$\psi_5 = k_{\text{f}}\tau; \quad \psi_6 = k_{\text{b}}\tau \tag{2.11}$$

Further discussion on non-dimensionalization is out of the scope of this study. Finally, the explained mathematical model is implemented in FreeFEM++ [29] to find the concentration distribution of both species within the reactor. The developed code is provided in the Supplementary Materials.

2.3 Entropy production

Irreversible thermodynamics first appeared in an endeavor to describe systems that are not in global thermodynamics equilibrium. Such a characterization might be provided by employing a local equilibrium assumption, which has been shown experimentally to be valid for extending the equilibrium thermodynamics to non-equilibrium systems [18]. In engineering systems, the entropy production rate is typically considered an index of performance degradation or dissipation. However, it is noteworthy that, in general, minimum entropy generation does not correspond to the maximum performance [44]. Otherwise, "doing nothing", which produces no entropy, would be definitely the best case. Therefore, when using entropy generation as a measure of how efficiently a system is working, a great deal of careful consideration should be taken into account to set sufficient constraints. The necessary conditions for equivalence of "minimum entropy production", and "maximum system performance" are comprehensively discussed by Salamon et al. [44].

2.3.1 Entropy production in RD system

Based on NET [18, 45], the local entropy generation rate could be estimated through the Gibbs differential equation as follows.

$$dU = TdS - pdV + \sum_{\mathrm{i}} \mu_{\mathrm{i}} dN_{\mathrm{i}} \tag{2.12}$$

where U, S, V, and N_{i} are internal energy (J), entropy ($\mathrm{J\,K^{-1}}$), volume ($\mathrm{m^3}$), and the number of moles (mol), respectively. Also, T, p, and μ are temperature (K), pressure (Pa), and chemical potential ($\mathrm{J\,mol^{-1}}$), respectively. It is assumed that all processes in the reactor are taking place at a constant temperature (isothermal condition), and the chemical species in the RD system are ideal gases. Therefore, it can be concluded that the local internal energy of the system is constant everywhere ($dU = 0$). It is noteworthy that this conclusion is only valid for the case of ideal gases (or other similar cases) where the potential energy of molecules is negligible, and as a result, the change of internal energy is only associated with the temperature. Considering that the volume of the system is constant, Eq. (2.12) could be expressed in the form of densities of entropy and mole numbers as:

$$ds = -\frac{1}{T} \sum_{\mathrm{i}} \mu_{\mathrm{i}} \frac{dN_{\mathrm{i}}}{V} = -\frac{1}{T} \sum_{\mathrm{i}} \mu_{\mathrm{i}} dC_{\mathrm{i}} \tag{2.13}$$

In Eq. (2.13), $s = S/V$ is entropy density ($\mathrm{J\,K^{-1}\,m^{-3}}$). Since the system does not have any convective flow, the time derivative of entropy density reads as:

$$\frac{\partial s}{\partial t} = -\frac{1}{T} \sum_{\mathrm{i}} \mu_{\mathrm{i}} \frac{\partial C_{\mathrm{i}}}{\partial t} \tag{2.14}$$

By substituting the right-hand side of Eq. (2.2) for $\frac{\partial C_{\mathrm{i}}}{\partial t}$ in Eq. (2.14) and doing some mathematical manipulation, the entropy accumulation is re-written as:

$$\frac{\partial s}{\partial t} = -\nabla \cdot \left[\frac{1}{T} (\mu_{\mathrm{A}} D_{\mathrm{A}}^{\mathrm{eff}} \nabla C_{\mathrm{A}} + \mu_{\mathrm{B}} D_{\mathrm{B}}^{\mathrm{eff}} \nabla C_{\mathrm{B}}) \right] + \frac{1}{T} \Big[\nabla \mu_{\mathrm{A}} \cdot (D_{\mathrm{A}}^{\mathrm{eff}} \nabla C_{\mathrm{A}}) + \nabla \mu_{\mathrm{B}} \cdot (D_{\mathrm{B}}^{\mathrm{eff}} \nabla C_{\mathrm{B}}) - R_{\mathrm{f}}^{\mathrm{eff}} (-\mu_{\mathrm{A}} + \mu_{\mathrm{B}}) - R_{\mathrm{b}}^{\mathrm{eff}} (\mu_{\mathrm{A}} - \mu_{\mathrm{B}}) \Big] \tag{2.15}$$

The entropy balance equation could be expressed as:

$$\frac{\partial s}{\partial t} = -\nabla \cdot \mathbf{J}_{\mathrm{s}} + \sigma \tag{2.16}$$

in which $\mathbf{J}_{\mathrm{s}}$ is entropy flux ($\mathrm{W\,K^{-1}\,m^{-2}}$) and σ is entropy source term ($\mathrm{W\,K^{-1}\,m^{-3}}$). The latter term indicate the local entropy production rate per unit volume. When Eqs. (2.15) and (2.16) are compared, entropy flux and local entropy production rate are separated as:

$$\mathbf{J}_{\mathrm{s}} = \frac{1}{T}(\mu_{\mathrm{A}} D_{\mathrm{A}}^{\mathrm{eff}} \nabla C_{\mathrm{A}} + \mu_{\mathrm{B}} D_{\mathrm{B}}^{\mathrm{eff}} \nabla C_{\mathrm{B}}) \tag{2.17}$$

and

$$\sigma = \frac{1}{T}\nabla\mu_{\mathrm{A}}\cdot(D_{\mathrm{A}}^{\mathrm{eff}}\nabla C_{\mathrm{A}}) + \frac{1}{T}\nabla\mu_{\mathrm{B}}\cdot(D_{\mathrm{B}}^{\mathrm{eff}}\nabla C_{\mathrm{B}}) - \frac{1}{T}R_{\mathrm{f}}^{\mathrm{eff}}(-\mu_{\mathrm{A}}+\mu_{\mathrm{B}}) - \frac{1}{T}R_{\mathrm{b}}^{\mathrm{eff}}(\mu_{\mathrm{A}}-\mu_{\mathrm{B}}) \tag{2.18}$$

The terms on the right-hand side of Eq. (2.18) are entropy generation contributions by transport of species A, transport of species B, forward chemical reaction, and backward chemical reaction, respectively. Furthermore, the total entropy production rate is computed by integrating the local production rate over the entire domain, Ω, as follows:

$$P = \int_{\Omega} \sigma d\Omega \tag{2.19}$$

From thermodynamics, it is known that the chemical potential of an ideal gas at a constant temperature is given by:

$$\mu = \mu^{\mathrm{ref}} + RT \ln \frac{C}{C^{\mathrm{ref}}} \tag{2.20}$$

where μ^{ref}, C^{ref}, and R are chemical potential at the reference point ($\mathrm{J\,mol^{-1}}$), reference concentration ($\mathrm{mol\,m^{-3}}$), and universal gas constant ($\mathrm{J\,K^{-1}\,mol^{-1}}$), respectively. For a chemical reaction given by Eq. (2.1), the difference between reference chemical potentials is expressed by:

$$\mu_{\mathrm{A}}^{\mathrm{ref}} - \mu_{\mathrm{B}}^{\mathrm{ref}} = RT \ln \frac{k_{\mathrm{f}}}{k_{\mathrm{b}}} \tag{2.21}$$

2.3.2 Entropy production under finite time/size condition

According to the second law of thermodynamics, the entropy production rate in a system in which one or several physical phenomena are taking place is larger than

or equal to zero. To put it in mathematical form

$$\sigma \geq 0 \tag{2.22}$$

In an ideal case, the entropy production of a system would be zero. In practice, however, systems are confined to finite-size devices and finite-time processes. Hence, within the context of finite time/size thermodynamics [46–48], some degree of entropy production is inevitable. Indeed, in practical situations, higher system duty (e.g., higher reaction rate or higher power output) is always associated with a higher rate of entropy generation. This is in accordance with the aforementioned discussion regarding the equivalence of "minimum entropy production" and "maximum system performance". In real-world problems, minimization of entropy production could result in more efficient systems only if the system duty is considered a constraint. This issue is further discussed in the subsequent section, where the results of entropy production evaluation are reported for the present RD system. Based on these explanations, the entropy production in any system could be divided into two parts, which we will call "inevitable contribution" ($P_{\text{inevitable}}$) and "controllable contribution" ($P_{\text{controllable}}$):

$$P = P_{\text{inevitable}} + P_{\text{controllable}} \tag{2.23}$$

The "inevitable contribution" is the entropy that is produced due to the limitations in time and size. In other words, according to finite time/size thermodynamics, systems are always doomed to some amount of entropy production, and this amount is increased with the increment of system duty. On the other hand, the "controllable contribution" could potentially be decreased by controlling the driving forces or transport properties within the system. In an ideal case (with no physical restrictions), full control of the driving forces could result in zero entropy production due to the "controllable contribution". However, in realistic cases, where driving forces cannot be controlled independently, reaching a zero entropy production by "controllable contribution" is impossible. The mathematical distinction between these two contributing terms depends on several factors, including but not limited to the flux-force relationship in the system. The entropy production rate is often expressed in terms of the product sum of conjugate flux and forces as given in Eq. (2.24). In this equation, J_{j} and X_{j} denote flux and forces j in the system. This expression of the second law is known as Onsager's formulation [45].

$$\sigma = \sum_{\mathrm{j}} J_{\mathrm{j}} X_{\mathrm{j}} \tag{2.24}$$

Without losing generality, the simplest case could be defined according to the following assumptions:

1. The system has only one driving force (X)
2. The force-flux relationship is linear as: $j = LX$, where L is phenomenological coefficient
3. The phenomenological coefficient, L, is constant over the entire system

Considering these simplifying assumptions, the total entropy production is expressed by:

$$P = \int_{\Omega} \sigma d\Omega = \int_{\Omega} LX^2 d\Omega = LA\bar{X}^2 + LA\,\mathrm{Var}(X) \tag{2.25}$$

in which P is total entropy production rate over domain Ω, $\bar{X}$ is average of driving force X over the entire system, $\mathrm{Var}(X)$ is the variance of the driving force X, and A is the total size of system domain. Knowing that the total flux, J, is given by

$$J = \int_{\Omega} j d\Omega = LA\bar{X} \tag{2.26}$$

the total entropy production rate could be re-written as:

$$P = \frac{J^2}{LA} + LA\,\mathrm{Var}(X) \tag{2.27}$$

According to Eqs. (2.25) and (2.27), for a fixed system duty (constant total flux), a proper control could result in lower entropy production rate (system dissipation) if the driving force is distributed uniformly ($\mathrm{Var}(X) = 0$). This fact gave the rise to the concepts of equipartition of entropy production (EoEP) by Tondeur and Kvaalen [49] and equipartition of force (EoF) by Sauar et al. [50]. The equipartition idea has been thoroughly discussed in the literature in the later studies and has been extended to other quantities like thermodynamic speed and thermodynamic length [51]. If the objective of an optimization problem is maximizing the overall flux in the system, the total entropy production given by Eq. (2.27) would inevitably increase. Hence, the scaled entropy is introduced by the following equation as an index to somehow suppress the impact of "inevitable entropy production".

$$P^{\text{scaled}} = \frac{P}{J^2} = \frac{1}{LA} + \frac{\text{Var}(X)}{LA(\bar{X})^2} \tag{2.28}$$

Although in more complicated cases, where the phenomenological coefficient is a direct function of the position, the expression of scaled entropy might be different, the same idea might be helpful for scaling the entropy generation.

2.4 Topology optimization algorithm

Mathematical optimization techniques provide powerful tools for determining the best size, shape, or topology for a given problem [52]. Topology optimization improves the structural layout of the system by controlling the material distribution within a given design domain. From this perspective, topology optimization gives additional degrees of freedom and design flexibility, making it more sophisticated than other approaches [53, 54]. While the roots of topology optimization can be traced in the research works by Maxwell [55] and Michell [56], the modern methods originate in Bendsøe and Kikuchi's study [57] in 1988, in which they introduced the homogenization method. Topology optimization could be interpreted as a material allocation problem in a given design domain, Ω, and mathematically be expressed as:

$$\rho_{\text{D}}(\mathbf{x}) = \begin{cases} 1 & \text{if } \mathbf{x} \in \Omega_{\text{M}} \\ 0 & \text{if } \mathbf{x} \in \Omega \backslash \Omega_{\text{M}} \end{cases} \tag{2.29}$$

in which $\mathbf{x}$ is any position in the design domain (Ω). Additionally, ρ_{D} is a discontinuous function representing material allocation condition in any position $\mathbf{x}$. In the material domain, Ω_{M} a value of $\rho_{\text{D}} = 1$ is assigned to this function, while a value of $\rho_{\text{D}} = 0$ indicates void. Since treating a discontinuous function causes mathematical complications, a relaxation method called "density method" [58] is typically used. In this approach, the discontinuous material distribution function is substituted with a continuous density function $0 \leq \rho_{\text{C}}(\mathbf{x}) \leq 1$.

2.4.1 Problem formulation

The performance of RD systems is degraded owing to several limiting mechanisms, including kinetic and concentration losses. While the former is due to sluggish reaction kinetics, the latter is associated with the lack of reactant at the reaction site. The

concentration loss becomes more serious when the reactor is working at a higher conversion rate which results in rapid consumption of the reactant. The topology optimization problem of the RD system described by Eq. (2.6) is defined as a maximization of the total reaction rate in the porous reactor. The optimization problem is mathematically presented as:

$$\begin{aligned} \max_{\varepsilon} \quad & F_{\text{obj}} = \int_{\Omega} \left(R_{\text{f}}^{\text{eff}} - R_{\text{b}}^{\text{eff}} \right) d\Omega \\ \text{s.t.} \quad & \text{Eq. (2.6)} \\ & 0 \leq \varepsilon(\mathbf{x}) \leq 1 \quad \forall \mathbf{x} \in \Omega \end{aligned} \tag{2.30}$$

where F_{obj} is the objective function. Since this optimization problem is constrained by Eq. (2.6), it is called a PDE-constrained optimization. In this problem, the local porosity distribution is considered a design variable. It is noteworthy that according to Eqs. (2.4) and (2.5), both mass diffusivity and reaction kinetics depend on local porosity. Hence, it can be understood that while higher porosity values improve the mass transport and consequently reduce the concentration loss, the activation dissipation will be increased due to the lower volume fraction of the catalyst material. Therefore, there is a trade-off between the activation and concentration losses, and an optimal distribution for the porosity might be identified. Hence, the ultimate goal of the aforementioned optimization problem is to increase the conversion capacity of the reactor with a proper distribution of porosity and catalyst material within the design domain.

2.4.2 Adjoint field and sensitivity analysis

A classic method for solving PDE-constrained optimization problems is using adjoint optimization [59] which is based on the evaluation of the sensitivity of objective function with respect to the design variables. In general, the total derivative of the objective function given in Eq. (2.30) with respect to the porosity is

$$\frac{dF_{\text{obj}}}{d\varepsilon} = \frac{\partial F_{\text{obj}}}{\partial \varepsilon} + \boldsymbol{\lambda}^{\intercal} \frac{\partial \mathbf{G}}{\partial \varepsilon} \tag{2.31}$$

where $\boldsymbol{\lambda}$ is the vector of adjoint variables and $\mathbf{G}$ is a system of PDE constraints. The adjoint variables could be computed by solving the following equation, known as the adjoint equation.

$$\left(\frac{\partial \mathbf{G}}{\partial \mathbf{C}}\right)^{\intercal} \boldsymbol{\lambda} = -\left(\frac{\partial F_{\mathrm{obj}}}{\partial \mathbf{C}}\right)^{\intercal} \tag{2.32}$$

in which $\mathbf{C}$ is the vector of state variables (concentration of species A and B in this case). Based on the objective given by Eq. (2.30) and the PDE constraints expressed in Eq. (2.6), the adjoint equations are given as follows after some mathematical manipulations:

$$-\nabla \cdot (D_{\mathrm{A}}^{0} \varepsilon^{\eta} \nabla \lambda_1) + k_{\mathrm{f}}(1-\varepsilon)^{\gamma}(\lambda_1 - \lambda_2) - k_{\mathrm{f}}(1-\varepsilon)^{\gamma} = 0 \tag{2.33a}$$

$$-\nabla \cdot (D_{\mathrm{B}}^{0} \varepsilon^{\eta} \nabla \lambda_2) + k_{\mathrm{b}}(1-\varepsilon)^{\gamma}(-\lambda_1 + \lambda_2) + k_{\mathrm{b}}(1-\varepsilon)^{\gamma} = 0 \tag{2.33b}$$

The adjoint variables are computed by solving this system of PDE equations according to the boundary conditions indicated by Eq. (2.34).

$$\text{B.C. of Eq. (2.33a)} \begin{cases} \lambda_1 = 0 & \text{on} \partial\, \Omega_1 \\ -D_{\mathrm{A}}^{\mathrm{eff}} \nabla \lambda_1 \cdot \hat{\mathbf{n}} = 0 & \text{on } \partial \Omega_2 \\ -D_{\mathrm{A}}^{\mathrm{eff}} \nabla \lambda_1 \cdot \hat{\mathbf{n}} = 0 & \text{on } \partial \Omega_3 \\ -D_{\mathrm{A}}^{\mathrm{eff}} \nabla \lambda_1 \cdot \hat{\mathbf{n}} = 0 & \text{on } \partial \Omega_4 \end{cases} \tag{2.34a}$$

$$\text{B.C. of Eq. (2.33b)} \begin{cases} -D_{\mathrm{B}}^{\mathrm{eff}} \nabla \lambda_2 \cdot \hat{\mathbf{n}} = 0 & \text{on} \partial\, \Omega_1 \\ -D_{\mathrm{B}}^{\mathrm{eff}} \nabla \lambda_2 \cdot \hat{\mathbf{n}} = 0 & \text{on } \partial \Omega_2 \\ \lambda_2 = 0 & \text{on } \partial \Omega_3 \\ -D_{\mathrm{B}}^{\mathrm{eff}} \nabla \lambda_2 \cdot \hat{\mathbf{n}} = 0 & \text{on } \partial \Omega_4 \end{cases} \tag{2.34b}$$

As a result, the sensitivity of the objective function is:

$$\begin{aligned} \frac{dF_{\mathrm{obj}}}{d\varepsilon} = \Big[& k_{\mathrm{f}}\gamma(1-\varepsilon)^{\gamma-1} C_{\mathrm{A}} - k_{\mathrm{b}}\gamma(1-\varepsilon)^{\gamma-1} C_{\mathrm{B}} + D_{\mathrm{A}}^{0}\eta\varepsilon^{\eta-1}\nabla C_{\mathrm{A}} \cdot \nabla \lambda_1 \\ & - \lambda_1 k_{\mathrm{f}}\gamma(1-\varepsilon)^{\gamma-1} C_{\mathrm{A}} + \lambda_1 k_{\mathrm{b}}\gamma(1-\varepsilon)^{\gamma-1} C_{\mathrm{B}} + D_{\mathrm{B}}^{0}\eta\varepsilon^{\eta-1}\nabla C_{\mathrm{B}} \cdot \nabla \lambda_2 \\ & + \lambda_2 k_{\mathrm{f}}\gamma(1-\varepsilon)^{\gamma-1} C_{\mathrm{A}} - \lambda_2 k_{\mathrm{b}}\gamma(1-\varepsilon)^{\gamma-1} C_{\mathrm{B}} \Big] \end{aligned} \tag{2.35}$$

2.4.3 Regularization

The checkerboard pattern, which are areas of alternating black and white elements, is a common challenge in any topology optimization process [58]. This issue has been addressed comprehensively in topology optimization literature [60–62] and some regularization methods, such as filtering and projection of solutions, are proposed to restrict the output produced by the optimization algorithms. In this study, a Helmholtz-type filter [60] is used along with a hyperbolic tangent projection [63] to obtain more robust results. This filter is the solution to a Helmholtz-type PDE with homogeneous Neumann boundary conditions as

$$\begin{aligned} -R^2\nabla^2\tilde{\rho_{\mathrm{C}}}(\mathbf{x}) + \tilde{\rho_{\mathrm{C}}}(\mathbf{x}) &= \rho_{\mathrm{C}}(\mathbf{x}) \\ \nabla\tilde{\rho_{\mathrm{C}}} \cdot \hat{\mathbf{n}} &= 0 \quad \text{on } \partial\Omega \end{aligned} \tag{2.36}$$

where $\tilde{\rho_{\mathrm{C}}}$ is filtered density function and R is the filter radius. The projection is conducted using a hyperbolic tangent function [63] as

$$\tilde{\tilde{\rho}}_{\mathrm{C}} = \frac{\tanh\left(\beta\left(\tilde{\rho_{\mathrm{C}}} - \rho_\beta\right)\right) + \tanh\left(\beta\rho_\beta\right)}{\tanh\left(\beta\left(1 - \rho_\beta\right)\right) + \tanh\left(\beta\rho_\beta\right)} \tag{2.37}$$

in which $\tilde{\tilde{\rho}}_{\mathrm{C}}$ is the projected density function, and β and ρ_β are projection steepness and projection point, respectively, which are used to control the amount of projection. The regularized density function is used to determine the spatial distribution of porosity in each iteration ($\varepsilon = \tilde{\tilde{\rho}}_{\mathrm{C}}$). While this function does not appear explicitly in the optimization problem (Eq. (2.30)), the relationship between the density function and porosity distribution defines its role in optimization process.

2.4.4 Updating scheme

For updating the solutions in each iteration, the well-known steepest descent method is used. The updating scheme is given by

$$\rho_{\mathrm{C}}^{\mathrm{new}}(\mathbf{x}) = \rho_{\mathrm{C}}^{\mathrm{old}}(\mathbf{x}) - \delta\frac{dF_{\mathrm{obj}}}{d\varepsilon} \tag{2.38}$$

where $\rho_{\mathrm{C}}^{\mathrm{new}}$ and $\rho_{\mathrm{C}}^{\mathrm{old}}$ are the density function of the current and previous iterations and δ is a given move limit. The complete steps of topology optimization algorithm is depicted in Fig. 2.2.

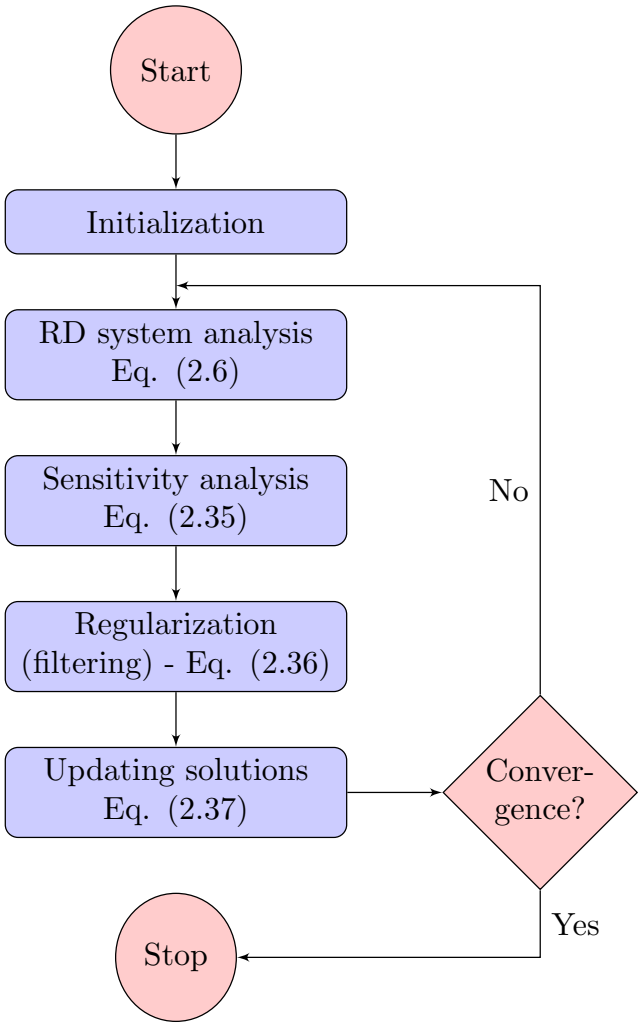

Figure 2.2: Flow chart of optimization algorithm

Table 2.1: The system specifications used for simulations

Parameter	Value	Unit
Reactor dimensions	1×1	$\mathrm{m} \times \mathrm{m}$
T	298.15	K
η	2	-
γ	2	-
$C_{\mathrm{A}}^{\mathrm{in}}$	1	$\mathrm{mol\,m^{-3}}$
$C_{\mathrm{B}}^{\mathrm{out}}$	1	$\mathrm{mol\,m^{-3}}$

2.5 Results and discussion

In order to increase the overall reaction rate in the porous reactor, the porosity distribution should be properly controlled so that the reaction becomes faster while ensuring an adequate reactant supply. Although according to Eq. (2.5), the local effective reaction rate can be improved by lower porosity (which is equivalent to a higher catalyst volume fraction), the mass transport can be facilitated only by larger diffusion fields. To address this engineering challenge, an optimization process is conducted with the purpose of finding the best porosity distribution. As a post-processing step, the entropy generation in the reactor is assessed according to the second law of thermodynamics concept. The system specifications used in the following simulations are reported in Table 2.1.

2.5.1 Parametric analysis

As a preliminary step, a parametric analysis is performed to evaluate the porosity dependence of system performance. At this stage, the total reaction rate is examined for a range of uniform porosity distributions. Since the porosity is assumed to be distributed uniformly in this analysis, only the value of porosity is used as a design variable. For the parametric study, the average reaction rate over the entire system is characterized by various porosity levels and compared under different working conditions. The impact of backward reaction kinetics and bulk diffusivity of species A is investigated while keeping the forward reaction kinetics and diffusivity of species B constant, respectively. The operating conditions of various cases examined in this step are presented in Table 2.2. To inspect the impact of the reaction rate on the optimized porosity, the backward reaction rate, k_{b}, is changed from an extremely low value of 0.01 to an extremely high value of 0.99. In the second investigation, the bulk diffusivity of the reactant, D_{A}^{0}, is varied between 0.1 and 10, which are respectively

lower and higher compared to that of the product species, D_{B}^{0}. It is notable that Cases 1-2 and 2-1 in Table 2.2 are identical.

As depicted in Fig. 2.3a, when the backward reaction kinetics is increased, the overall performance of the reactor gets decreased at any porosity. Moreover, at a fixed backward reaction rate of $k_{\mathrm{b}} = 0.01\,\mathrm{s}^{-1}$ (extremely low backward kinetics), the highest average reaction rate is achieved at a uniform porosity of $\varepsilon = 0.378$. However, with an increment of backward reaction rate (from Cases 1-1 to 1-5), the optimal porosity shifts toward higher values. This is due to the fact that at higher backward reaction rates, the supply of the reactant species A should be enhanced by facilitating mass transport to keep the average reaction rate as high as possible. The result of the porosity trade-off for a range of bulk diffusivity (Cases 2-1 to 2-5) is shown in Fig. 2.3b. This figure reveals that at higher bulk diffusivity levels, where reactant supply is guaranteed by enhanced mass transport, a lower porosity assists the reaction speed. Hence, the optimal porosity is diminished from a value of $\varepsilon = 0.5$ to $\varepsilon = 0.289$ when the diffusivity is increased by two orders of magnitude. The reaction rate curves presented in Figs. 2.3a and 2.3b are all comparable and have a single, optimal porosity point that strikes a compromise between the mass transport limitations and reaction rate. Moreover, it can be seen that the variance of optimum porosity is larger under different backward kinetics ($0.378 \leq \varepsilon \leq 0.462$) compared to the cases with different diffusivity ($0.289 \leq \varepsilon \leq 0.5$). Finally, the optimal porosity over a range of backward reaction kinetics and diffusivity levels is demonstrated in Fig. 2.3c. These different sets of parameters represent various diffusion-kinetic regimes that are described in classical resources [64]. As explained in [64], in a RD system, two limiting conditions may occur. When the reaction rate is relatively much faster than mass transport rate, it is called diffusion regime. Conversely, a high mass transport rate compared to chemical reaction leads into a kinetic regime. The minimum optimized porosity occurs at a low backward reaction rate and a high diffusivity. Under these conditions, high diffusivity assures sufficient mass transport, and low porosity boosts the reaction rate. Moreover, in the worst-case scenario in which the backward reaction kinetics is relatively high and bulk diffusivity is low, larger pores are required to achieve a higher average reaction rate. However, for median conditions, in which both backward reaction kinetics and bulk diffusivity values are relatively high or low simultaneously, the optimum porosity should be determined based on the absolute value of the working parameters. It is evident that for the given set of parameters, an extremely low bulk diffusivity (a diffusion-limited system) necessitates larger pores compared to an extremely fast backward reaction.

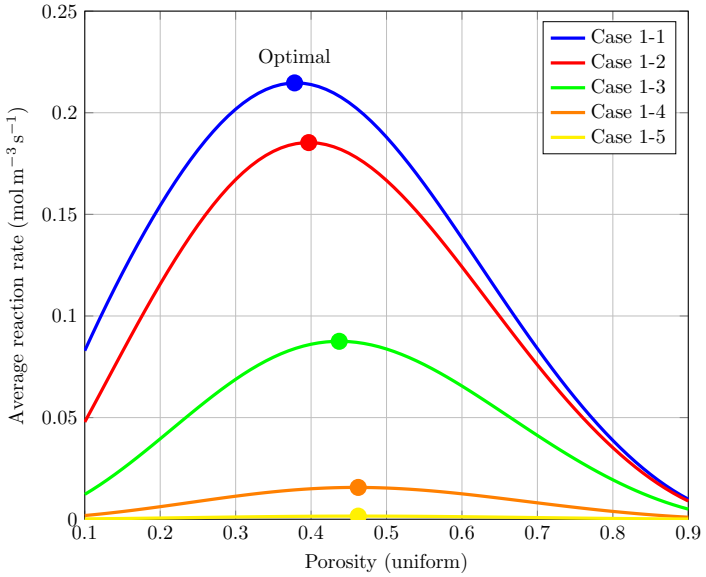

(a) Average reaction rate under different values of backward reaction kinetics at constant $k_{\mathrm{f}} = 1\,s^{-1}$, $D_{\mathrm{A}}^{0} = 1\,\mathrm{m}^2\,\mathrm{s}^{-1}$, and $D_{\mathrm{B}}^{0} = 1\,\mathrm{m}^2\,\mathrm{s}^{-1}$

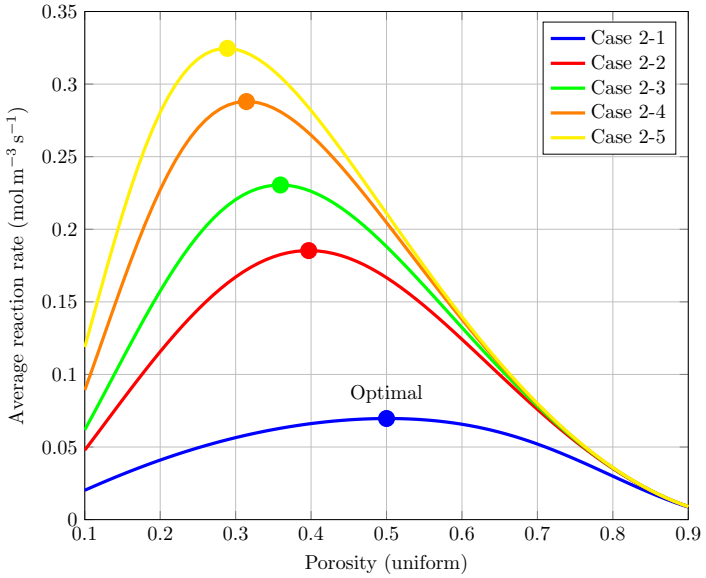

(b) Average reaction rate under different bulk diffusivity of reactant at constant $k_{\mathrm{f}} = 1\,s^{-1}$, $k_{\mathrm{b}} = 0.1\,s^{-1}$, and $D_{\mathrm{B}}^{0} = 1\,\mathrm{m}^2\,\mathrm{s}^{-1}$

Table 2.2: The system specifications used for simulations

Study	Case	$D_{\mathrm{A}}^{0}(\mathrm{m^2\,s^{-1}})$	$D_{\mathrm{B}}^{0}(\mathrm{m^2\,s^{-1}})$	$k_{\mathrm{f}}(\mathrm{s^{-1}})$	$k_{\mathrm{b}}(\mathrm{s^{-1}})$
Impact of reaction kinetics	1-1	1	1	1	0.01
	1-2				0.1
	1-3				0.5
	1-4				0.9
	1-5				0.99
Impact of diffusivity	2-1	0.1	1	1	0.1
	2-2	1			
	2-3	2			
	2-4	5			
	2-5	10			

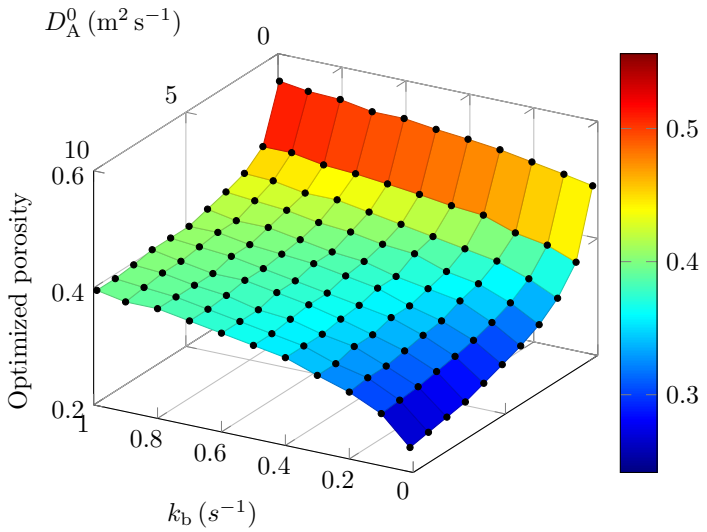

(c) Dependence of optimized porosity on the values of backward reaction rate, k_{b}, and bulk diffusivity of the reactant, D_{A}^{0}, at constant $k_{\mathrm{b}} = 0.1\,s^{-1}$ and $D_{\mathrm{B}}^{0} = 1\,\mathrm{m^2\,s^{-1}}$

Figure 2.3: Average reaction rate and optimized porosity under various reaction kinetics and diffusivity values

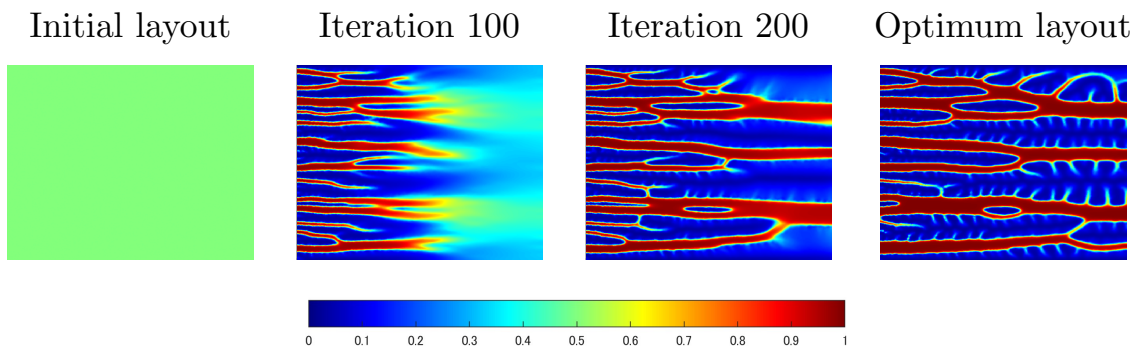

Figure 2.4: Changes of porosity layout during topology optimization process

2.5.2 Topologically optimized porosity layout

To investigate the topological optimization of porosity, the parameters are adjusted the same as those of Case 1-2 (or Case 2-1) in Table 2.2. Fig. 2.4 illustrates how the porosity distribution alters during the optimization iterations. Starting with a uniform porosity layout, the optimization process changes the local distribution of porosity in accordance with the previously mentioned methodology to achieve a higher overall reaction rate. The re-distribution procedure is accomplished such that the final design provides a compromise between the mass transport and reaction speed limitations. The findings of Fig. 2.4 show that while the porosity level was set to be $\varepsilon = 0.5$ at the beginning, the difference in local sensitivity of overall reaction rate with respect to porosity caused a porosity gradient in the system. This gradient in local porosity levels grows during the optimization process and finally leads to the formation of some large diffusion channels within the reactor. These channels first appeared in the area close to the inlet boundary and then expanded toward the outlet boundary. The diffusion channels are responsible for the reactant delivery to the regions far from the inlet boundary, where the reaction rate is restricted due to the deficient reactant. In addition, these channels provide an efficient path for the discharge of the reaction product, which is required to keep the overall reaction rate as high as possible. On the other hand, the regions with lower porosity have a higher potential for accelerated reactions due to a higher volume fraction of catalyst material and are primarily used as the chemical reaction sites. Finally, the optimization resulted in a complex tree-root-like structure with lots of secondary branches. These secondary channels further dispense the reactant from the main primary channels all over the reactor. With the advancement of fabrication methods and technologies [65, 66], it is anticipated that such complicated reactors to be realized experimentally in the near future.

The convergence trend of the optimization problem is shown in Fig. 2.5a. In this diagram, the average rate of overall reaction (i.e., objective function) is plotted together with those of forward and backward reactions. The data in this figure indicates that as the optimization proceeds, the average rate of both forward and backward reactions increases. However, the difference between the forward and backward rates is also increasing. The increment trend continues until the average overall reaction rate converges to a value of $0.291\,\mathrm{mol\,m^{-3}\,s^{-1}}$ at iteration number 1000. The average porosity over the entire reactor is computed at each iteration, and its variation is presented in Fig. 2.5b. While the average porosity changes severely in the first iterations, it tends to have a constant value at subsequent steps. According to Eq. (2.38), the local porosity is updated based on the sensitivity of the objective function. Since the sensitivity is higher in the early steps of optimization, this graph shows a sharp fall in average porosity at low iteration numbers. In this simulation, the average porosity converges to a value of $\varepsilon^{\mathrm{ave}} = 0.389$. This value is roughly close to optimal porosity obtained from a parametric study under a uniform porosity distribution for Case 1-2 (or Case 2-2), as shown in Fig. 2.3. It is interesting to note that a uniform porosity of 0.389 would result in an average overall reaction rate of $0.185\,\mathrm{mol\,m^{-3}\,s^{-1}}$. However, the same average porosity for a topologically optimized layout corresponds to an objective function of $0.291\,\mathrm{mol\,m^{-3}\,s^{-1}}$, which is 57% higher than the uniform distribution. This significant elevation of reaction rate is linked to the heterogeneous distribution of porosity which maintains a suitable balance between the supply and consumption of reactant. To further investigate the porosity evolution, the 2D distribution is projected on the x-direction by measuring the average of porosity along the other axis of the coordinate. Fig. 2.5c exhibits the average projected porosity for some selected iterations. As stated before, the optimization problem is initialized with uniform porosity. Hence, the projected porosity for the initial layout is a straight horizontal line. The distribution along the x-direction becomes increasingly asymmetric as the optimization process continues. Evidently, the optimum layout has the maximum difference between the projected porosity in areas close to the inlet ($x = 0$) and areas adjacent to the outlet ($x = 1$).

Fig. 2.6 compares the spatial distribution of porosity, concentration of reactant (species A), concentration of product (species B), and reaction rate through the optimization process. This figure reveals that, while the maximum local concentration of species A is fixed on the inlet boundary, the minimum concentration is getting reduced as the optimization proceeds. Thanks to the new distribution, the reactor has more

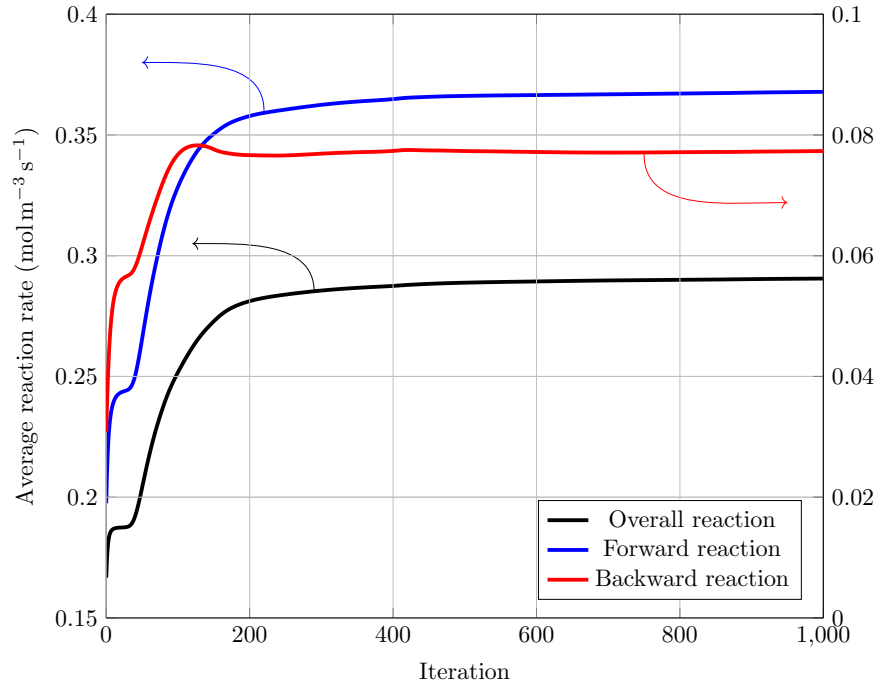

(a) Convergence of reaction rates during the optimization process

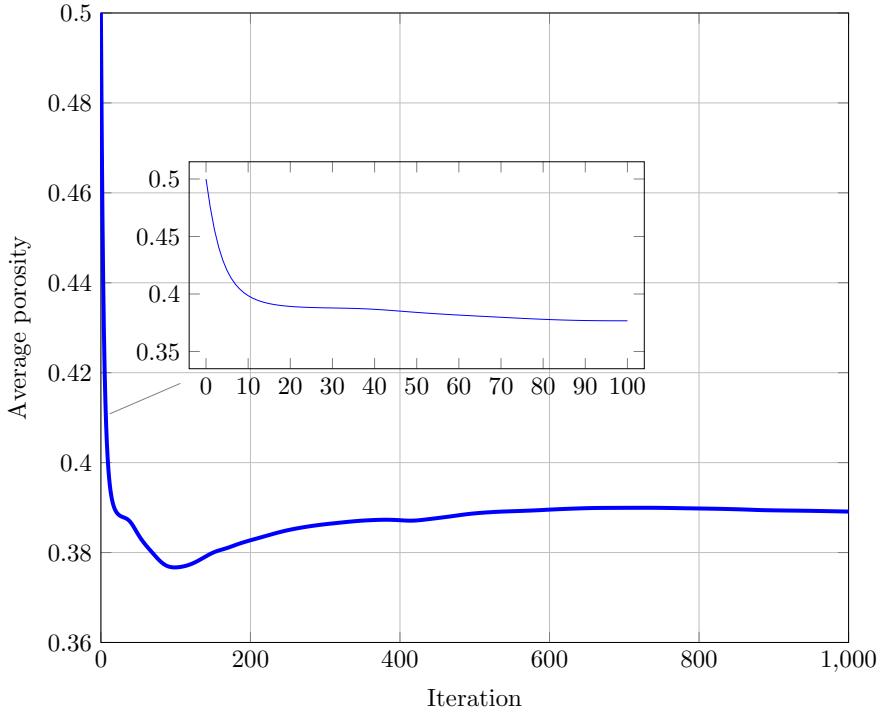

(b) Average porosity over the entire system during the optimization process

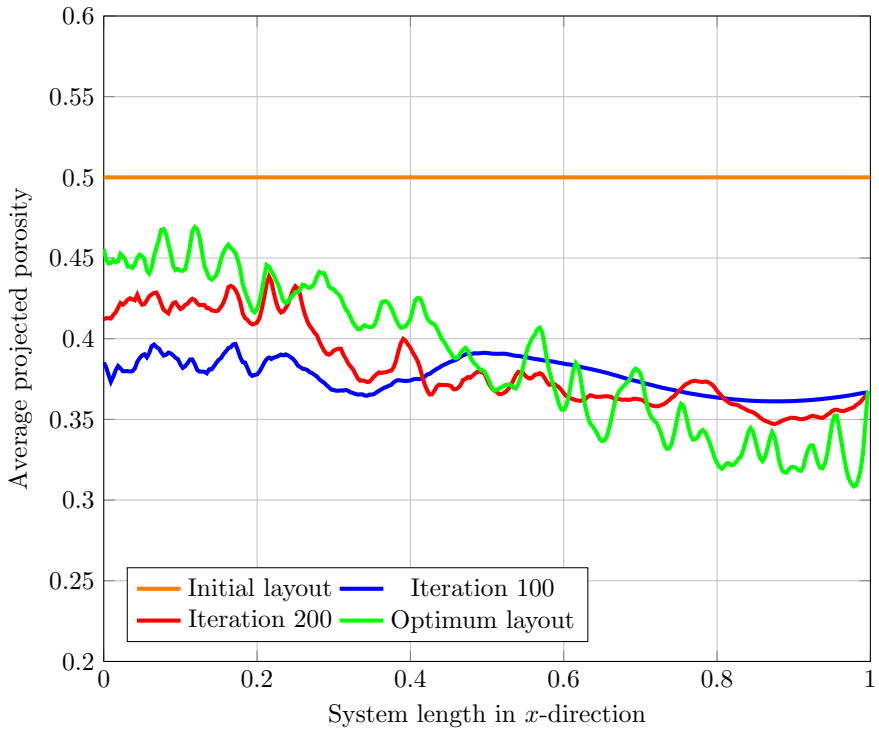

(c) Average projected porosity along the system length in x-direction

Figure 2.5: (a) Changes of average different reaction rates during the optimization process (b) Changes of average system porosity during the optimization process (c) Average projected porosity along the length of the system at various optimization iterations

potential for consuming the available reactant in the system. Indeed, this potential for higher consumption improves the rate of the forward reaction. For the case of species B, the minimum local concentration is fixed and dictated by the outlet boundary condition. However, as the optimization is progressing toward the optimal solution, the concentration of this species shows a fluctuating behavior. The maximum local concentration of species B first gets larger till iteration number 100 (from 1.35 at the initial step to a value around 2.1 at iteration number 100) and then declines till the optimized case (from 2.1 at iteration number 100 to a value of 1.85 for the optimal layout). The observed increase in the primary steps (up to iteration number 100) could be attributed to the enhanced forward reaction rate. On the other hand, as the optimization process goes on, the large diffusion channels are extended toward the outlet boundary. These channels assist discharge of the reaction product (species B), and consequently, the maximum local concentration of species B diminishes. This concentration reduction leads to a lower backward reaction rate after a peak at early iterations (see Fig. 2.5a). These findings prove the significant role of the diffusion phenomenon and how a well design may boost the performance of RD systems. Moreover, what stands out in this figure is that the difference between the minimum and maximum reaction rates becomes larger, which subsequently causes a higher degree of non-uniformity. A closer inspection of Fig. 2.6 shows how the large diffusion channels formed in the optimization process facilitate the reactant supply to the farthest regions (close to the outlet boundary) of the system. Although these regions had a very low overall reaction rate in the initial layout, an optimal porosity distribution led to a substantial escalation. From Fig. 2.6, it is apparent that in the case of optimized layout, the reaction rate in the channels, where porosity is $\varepsilon = 1$, the reaction rate is almost zero due to lack of catalyst material. In contrast, the reaction rate in other regions depends on both porosity and reactant concentration. As a result, areas near the reactor inlet (close to $x = 0$), in which the concentration of species A is higher, have the largest overall reaction rate.

Fig. 2.7, which illustrates the projected overall reaction rate, provides further insight on how the optimization procedure works. At the initial uniform layout, the reaction rate is more homogeneous over the domain; however, the average magnitude is low. As the system configuration gets more optimized, the reaction rate in the areas close to the inlet boundary almost doubled. This considerable rise caused a significant variance in the projected reaction rate of the porous reactor. This is associated with the fact that these areas have a higher potential for improvement because of the proximity to the inlet boundary. In the subsequent steps, the optimization algorithm

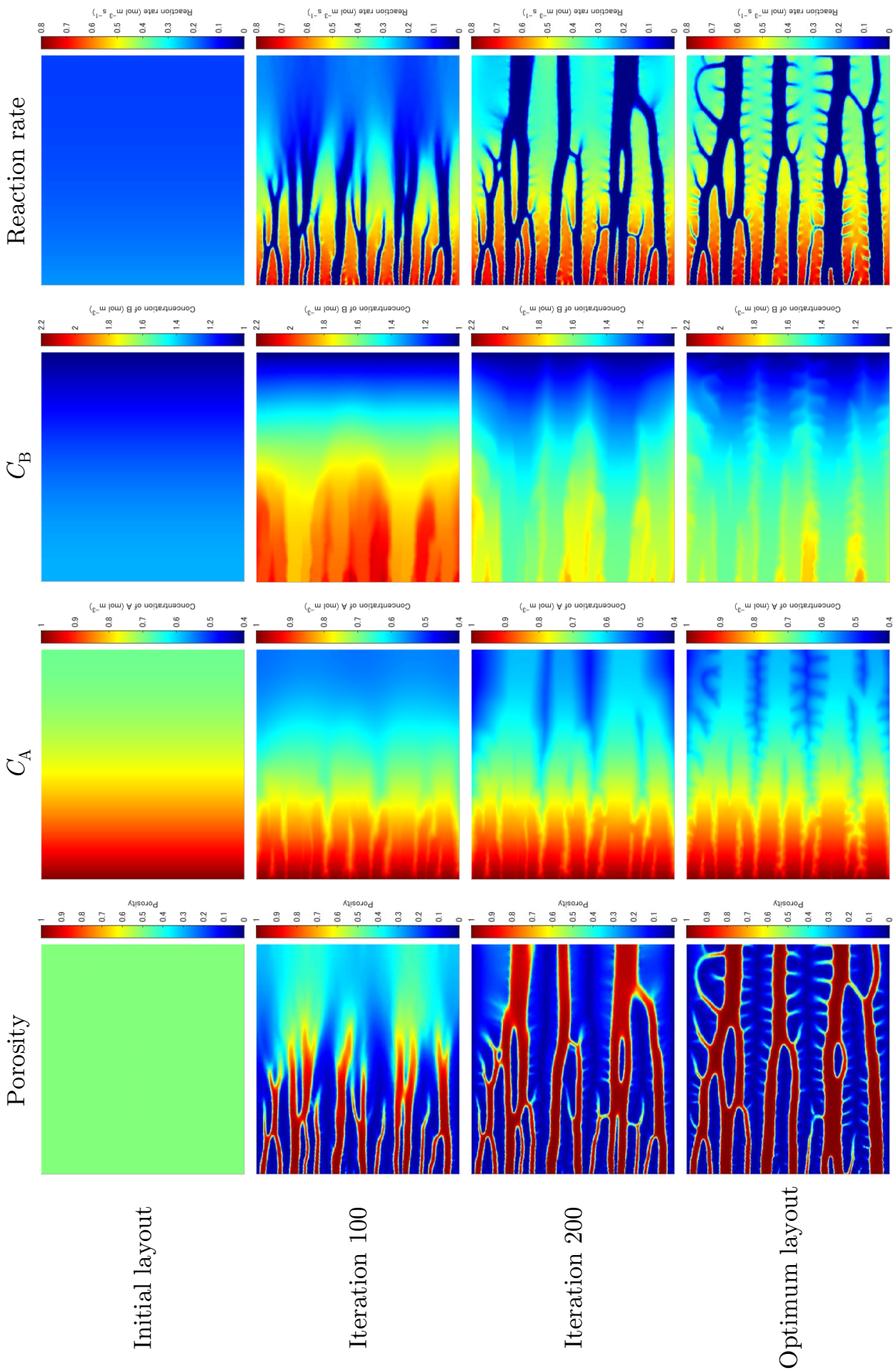

Figure 2.6: Spatial distribution of porosity, concentration of species A, concentration of species B, and reaction rate for selected iteration numbers

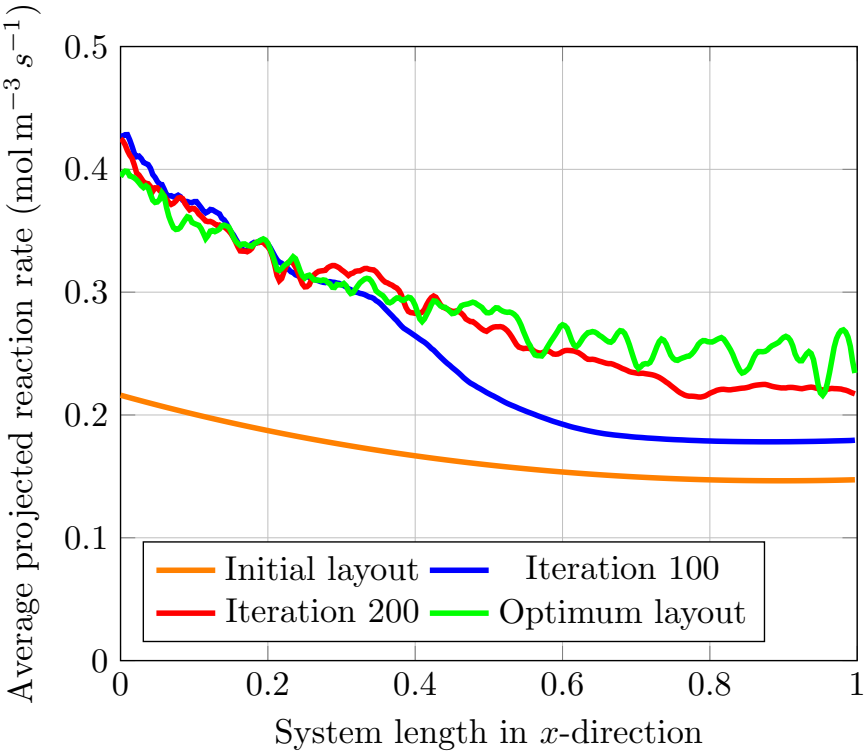

Figure 2.7: Average projected overall reaction rate along the system length in x-direction

attempts to reduce the raised non-uniformity by amplifying the overall reaction rate in the areas close to the outlet boundary.

2.5.3 Entropy production analysis

A comprehensive entropy generation analysis is conducted based on the entropy model developed in Section 2.3. As indicated before, an optimized layout with a higher reaction rate is expected to have larger entropy production. Hence, great care should be taken when interpreting the entropy production results. To put it in other words, when connected with a high overall reaction rate, a large total entropy generation is favorable. On the contrary, a large magnitude of total entropy generation due to a significant variance of local entropy production rate is negative. Based on the terms on the right-hand-side of Eq. (2.18), the entropy generation is divided into three sources, including contributions by diffusion of the reactant (species A), diffusion of the product (species B), and chemical reaction. Fig. 2.8 displays the history of total entropy production during the optimization process. As shown in this figure, for the given set of system parameters, the total entropy increases monotonically. The separate contributions of each phenomenon are also depicted in this figure. It

can be seen that the chemical reaction has a relatively greater share in total entropy compared to mass transports. It is noteworthy that the absolute magnitude of different contributions depends on the system parameters settings. What is interesting about the data in this figure is how each of the contributions is changing through the optimization. By expansion of the diffusion channels over the reactor, the reactant is transported more effectively, and in return, the entropy production by diffusion of species A rises. The situation for the diffusion of the reaction product is different. According to Fig. 2.8, the growth of entropy production by diffusion of species B is accompanied by a decline after early steps. This fluctuation finally becomes a constant value when the optimization problem converges. Similar to the reactant, the initial rise in entropy production of species B is attributed to the higher diffusion rate in the system. In fact, this rise in entropy production is favorable. On the other hand, as aforementioned, when the larger channels are formed in the areas close to the outlet boundary, the product is discharged from the reactor more easily. This causes a slight reduction in the average concentration of this species, which finally results in a more uniform concentration distribution throughout the reactor. Correspondingly, the entropy production by diffusion of species B experiences a depletion. Finally, the entropy production by chemical reaction also shows a small fluctuation. Because the overall reaction rate is increasing monotonically, the entropy generated by this source is also expected to grow. However, this entropy contributor shows a downward trend at the beginning. A possible explanation for this might be that although the reaction rate is improved in the initial steps, this improvement is due to the enhanced effective reaction kinetics. As discussed before, the average porosity also shows the same behavior. Lower porosity means a higher volume fraction of catalyst material and thus higher effective reaction kinetics. However, this reduction in porosity level causes a temporary drop in reactant supply. Therefore, further porosity reduction is not beneficial to the system performance due to the disruption of the balance between the supply and consumption of the reactant. The drop in reactant supply is compensated, and the chemical potential of reactant increases. Consequently, the entropy production by chemical reaction starts increasing.

Since the reaction rate changes with optimization of porosity distribution, a simple comparison of total entropy production is not possible. Another possible approach is to use the scaled entropy production introduced in Section 2.3. The scaled total entropy production, the scaled projected entropy production, and the entropy production ratio are demonstrated in Fig. 2.9. What can be clearly seen in Fig. 2.9a is

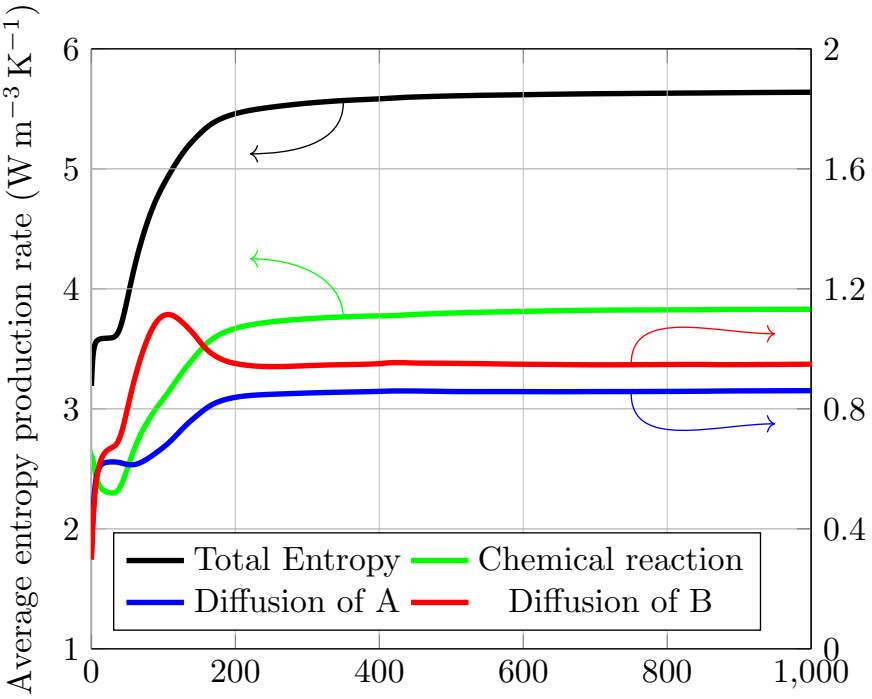

Figure 2.8: Change of average entropy production rates over the entire system during the optimization process

the continuous drop of scaled entropy. These results prove that the optimal configuration corresponds to the minimum scaled entropy production over the entire system. This relationship might be explained by looking at Fig. 2.9b that illustrates the scaled projected entropy generation for various iteration steps. As it can be seen, a more optimized layout not only is associated with lower scaled entropy on average but also corresponds to more equipartitioned entropy distribution. These outcomes are in agreement with those reported in the literature about the equipartition principle [49–51]. However, it is notable that the equipartition principle should be employed with a considerable amount of care. Magnanelli et al. [51] fully addressed the conditions under which the numerical optimum and equipartition principle concur. Based on their results, if the driving forces in the system cannot be controlled independently, the equipartition principle does not fully coincide with the numerical optimum. However, the equipartition of entropy production might provide an acceptable approximation. It is possible to hypothesize that even better configurations might be obtained under a more equipartitioned entropy production condition. As can be seen in Fig. 2.9b, there is a potential to improve the reaction rate in the areas close to the outlet boundary. However, this hypothetical configuration might not be necessarily favorable from a design viewpoint and needs further investigation, which is out of the scope of this study. Furthermore, the entropy production ratio

(f), which is defined according to the Eq. (2.39), is also shown in Fig. 2.9a. This parameter indicates the ratio of total entropy production contributed by the reaction process to the entropy contribution by the diffusion mechanism over the entire domain.

$$f = \frac{P^{\text{reaction}}}{P^{\text{diffusion}}} = \frac{\int_\Omega \sigma^{\text{reaction}} d\Omega}{\int_\Omega \sigma^{\text{diffusion}} d\Omega} \tag{2.39}$$

A well-designed reactor should provide a compromise between these two entropy generation contributors. As it can be seen from the plot of f in Fig. 2.9a, the entropy production ratio changes over the optimization course and finally reaches a value of 2.11. This ratio can specify which mechanism is degrading the reactor performance. At the initial configuration, this ratio is high, which shows that the overall system is diffusion-limited. By the formation of the diffusion channel in the reactor, the ratio f starts declining. Further decrease of this parameter takes the system to a reaction-limited condition. However, to increase the objective function, the optimization algorithm increases the ratio f from a minimum value of 1.72 to a final value of 2.11, which provides a compromise between the entropy generation by chemical reaction and mass transport. The exact optimized value of this ratio depends on the bulk parameters of the system, including forward/backward kinetics and species diffusivity coefficients. According to Fig. 2.9a, the system once passes the optimized entropy production ratio ($f = 2.11$) at early iterations (iteration number 7). While the value of f at that iteration is equal to the optimized configuration, the total entropy production, which is another essential factor impacting the system performance, is low (see Fig. 2.8). That is why both ratio f and the absolute value of total entropy production are important in obtaining an optimal design solution.

The contribution of different mechanisms to the entropy production in the RD system is depicted locally in Fig. 2.10. The largest values of entropy production by transport of the reactant are localized in the regions close to the inlet boundary. This is caused by a higher gradient of reactant concentration in these areas compared to those on the other side of the reactor. Moreover, by the emergence of the diffusion channels, the transport of reactant is enhanced and eventually leads to higher entropy production. This entropy rise is an inevitable kind of entropy production that has been discussed in Section 2.3 and, therefore, is positive. The entropy generation due to the diffusion of product is mainly located near the outlet boundary, where species B is discharged from. Unlike the reactant, the concentration of species B shows a large gradient in this region where there is a possibility for the reaction

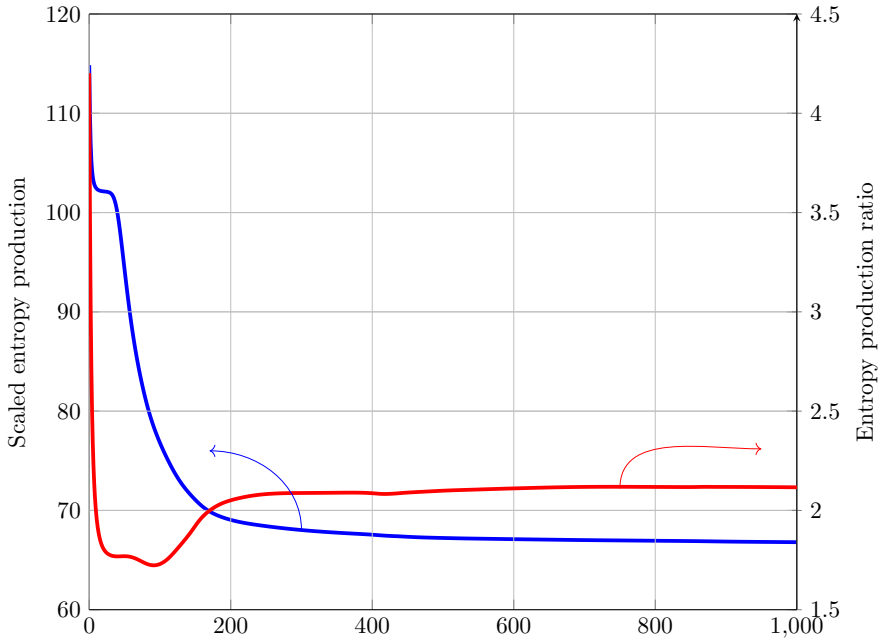

(a) Scaled global entropy production and entropy production ratio

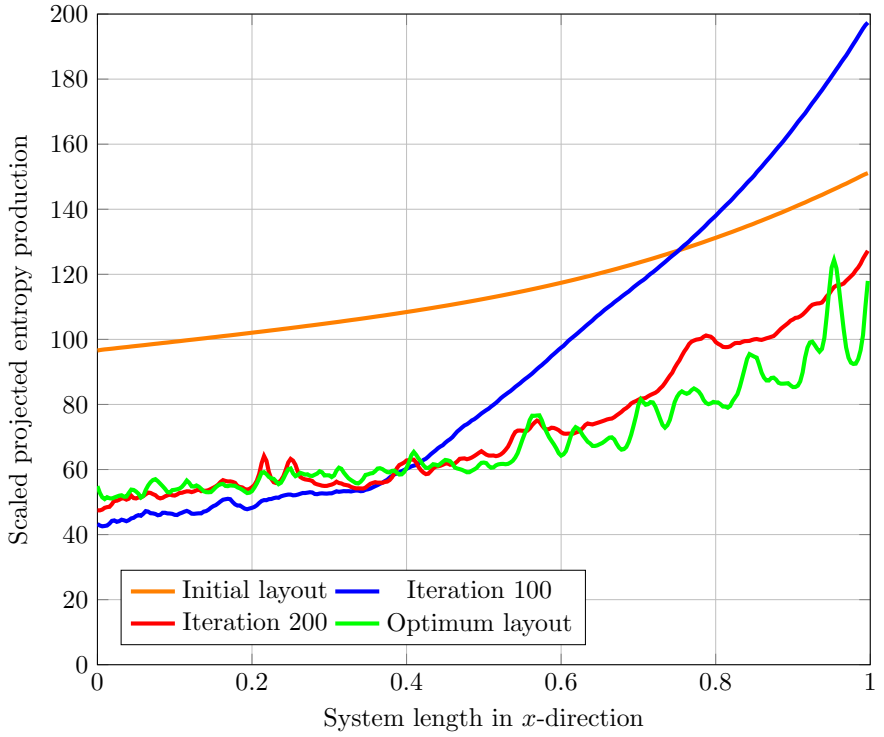

(b) Scaled projected entropy production along the system length in x-direction

Figure 2.9: (a) Changes of scaled global entropy production and entropy production ratio (f) during the optimization process (b) Scaled projected entropy production along the length of the system at various optimization iterations

product to go out of the system. From Fig. 2.10 it could be understood that as opposed to entropy production by diffusion phenomenon, the contribution by chemical reaction is larger in the areas outside of the diffusion channels. This is due to the higher rate of chemical reaction in areas with low porosity (see Fig. 2.6). As shown in Fig. 2.10, from a local distribution perspective, it seems that transport of species B produces the largest entropy. However, this big entropy contribution is limited to small areas in the calculation domain where there are narrow secondary channels. However, from a global point of view (see Fig. 2.8), the chemical reaction is the main contributor to entropy production.

2.6 Conclusions

This study deals with the modeling and optimization of a 2D reaction-diffusion system. RD systems in which a transport mechanism is taking place together with a chemical reaction are used in many industrial application. Hence, a deep understanding of transport and reaction dynamics provided by this research work could contribute to the development of these systems. A porous reactor with two species converted to each other through a simple first-order chemical reaction is mathematically modeled. This work also introduces an optimization technique for topological optimization of porosity distribution in RD systems with the aim of enhancing the overall reaction rate. The optimization algorithm employed in this research leads to a 57% enhancement of the system performance compared to a uniform layout with the same average porosity. The porosity distribution, concentration of reactant and product substances, and reaction rates are traced over the optimization steps. The results of this study show that a proper balance between the diffusion and reaction mechanisms is required to achieve higher performance. This balance is obtained by the formation of primary and secondary channels inside the reactor during the optimization. The optimal porosity distribution obtained from the optimization algorithm has a tree-root-like configuration. Moreover, it is revealed that an optimal layout has a higher porosity in the regions close to the inlet boundary and a lower porosity in the areas near the outlet boundary. In addition, an entropy analysis model is developed to investigate the irreversibilities of the system. This study has identified the various contributions to the system entropy generation and quantified them over the optimization process. To obtain a better understanding of the entropy production, the concept of scaled entropy is introduced, and the areas in the system which has a potential for further improvement are recognized. It is shown

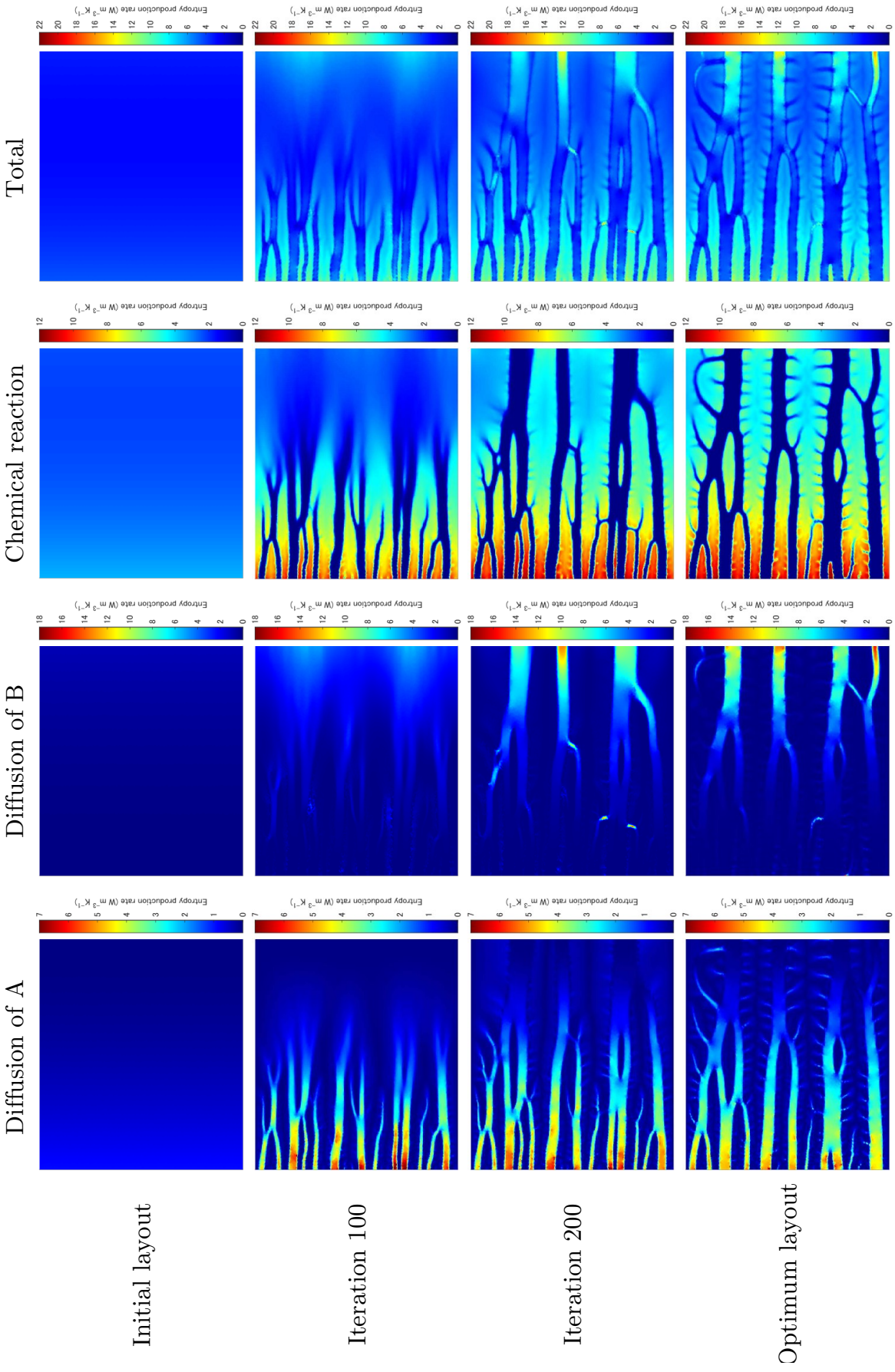

Figure 2.10: Spatial distribution of entropy production by various mechanisms

that an optimized design solution corresponds to the minimum scaled entropy generation by chemical reaction. The findings of this study have potentially significant implications for the understanding of the theoretical upper limit of RD systems performance irrespective of limitations of optimization methods. The present research establishes a quantitative framework for detecting the diffusion-reaction dynamics and irreversibilities caused by these mechanisms during a topology optimization process and has gone some way towards enhancing our understanding of the theoretical maximal performance of porous reactors. Further investigation is required to determine how other transport phenomena, such as heat and electric charge transfer, could impact optimization and interactions between the coupled driving forces of the system.

Abbreviations

BC	Boundary condition
EoEP	Equipartition of entropy production
EoF	Equipartition of force
NET	Non-equilibrium thermodynamics
PDE	Partial differential equation
RD	Reaction-diffusion

Nomenclature

C	Concentration	$\mathrm{mol\,m^{-3}}$
C_0	Characteristic concentration	$\mathrm{mol\,m^{-3}}$
D	Diffusion coefficient	$\mathrm{m^2\,s^{-1}}$
F_{obj}	Objective function	$\mathrm{mol\,m^{-1}\,s^{1}}$
$\mathbf{J}_{\mathrm{s}}$	Entropy flux	$\mathrm{W\,K^{-1}\,m^{-2}}$
k	Reaction kinetics	$\mathrm{s^{-1}}$
L	Characteristic length	m
N	Number of moles	mol
p	Pressure	Pa
P	Total entropy production	$\mathrm{W\,K^{-1}\,m^{-1}}$
R	Reaction rate / Filter radius	$\mathrm{mol\,m^{-3}\,s^{-1}}$ / m
s	Entropy density	$\mathrm{J\,K^{-1}\,m^{-3}}$
S	Entropy	$\mathrm{J\,K^{-1}}$
T	Temperature	K

t	Time	s
U	Internal energy	J
V	Volume	m^3

Greek symbols

β	Projection steepness	$-$
δ	Move limit	$-$
ε	Porosity	$-$
η	Diffusivity correction exponent	$-$
γ	Reaction correction exponent	$-$
ν	Chemical potential	$\mathrm{J\,mol^{-1}}$
ρ	Density function	$-$
ρ_β	Projection point	$-$
ψ	Dimensionless group	$-$
σ	Entropy source term	$\mathrm{W\,K^{-1}\,m^{-3}}$
τ	Characteristic time	s

Subscripts/superscripts

b	Backward
eff	Effective
f	Forward
ref	Reference

Bibliography

[1] G. Palmisano, S. Jitan, and C. Garlisi, *Heterogeneous Catalysis: Fundamentals, Engineering and Characterizations (with accompanying presentation slides and instructor's manual)*. Elsevier Science, 2022.

[2] A. A. Ingle, S. Z. Ansari, D. Z. Shende, K. L. Wasewar, and A. B. Pandit, "Progress and prospective of heterogeneous catalysts for h2o2 production via anthraquinone process," *Environmental Science and Pollution Research*, pp. 1–17, 2022.

[3] K. Nantasaksiri, P. Charoen-amornkitt, T. Machimura, and K. Hayashi, "Multidisciplinary assessment of napier grass plantation on local energetic, environmental and socioeconomic industries: A watershed-scale study in southern thailand," *Sustainability*, vol. 13, no. 24, p. 13520, 2021.

[4] K. Nantasaksiri, P. Charoen-amornkitt, and T. Machimura, "Integration of multicriteria decision analysis and geographic information system for site suitability assessment of napier grass-based biogas power plant in southern thailand," *Renewable and Sustainable Energy Transition*, vol. 1, p. 100011, 2021.

[5] K. Nantasaksiri, P. Charoen-Amornkitt, and T. Machimura, "Land potential assessment of napier grass plantation for power generation in thailand using swat model. model validation and parameter calibration," *Energies*, vol. 14, no. 5, p. 1326, 2021.

[6] P.-C. Sui, X. Zhu, and N. Djilali, "Modeling of pem fuel cell catalyst layers: status and outlook," *Electrochemical Energy Reviews*, vol. 2, no. 3, pp. 428–466, 2019.

[7] P. Charoen-Amornkitt, T. Suzuki, and S. Tsushima, "Determination of constant phase element parameters under cyclic voltammetry conditions using a semitheoretical equation," *Electrochemistry*, vol. 87, no. 4, pp. 204–213, 2019.

[8] P. Charoen-Amornkitt, T. Suzuki, and S. Tsushima, "Determination of constant phase element parameters under cyclic voltammetry conditions using a semitheoretical equation," *Electrochemistry*, vol. 87, no. 4, pp. 204–213, 2019.

[9] P. Charoen-amornkitt, T. Suzuki, and S. Tsushima, "Ohmic resistance and constant phase element effects on cyclic voltammograms using a combined model of mass transport and equivalent circuits," *Electrochimica Acta*, vol. 258, pp. 433–441, 2017.

[10] R. Aris, *The Mathematical Theory of Diffusion and Reaction in Permeable Catalysts: The theory of the steady state*. The Mathematical Theory of Diffusion and Reaction in Permeable Catalysts, Clarendon Press, 1975.

[11] N. Limjeerajarus and P. Charoen-Amornkitt, "Effect of different flow field designs and number of channels on performance of a small pefc," *International Journal of Hydrogen Energy*, vol. 40, no. 22, pp. 7144–7158, 2015.

[12] J. Wu, O. Sigmund, and J. P. Groen, "Topology optimization of multi-scale structures: a review," *Structural and Multidisciplinary Optimization*, vol. 63, no. 3,

pp. 1455–1480, 2021.

[13] M. P. Bendsøe, "Optimal shape design as a material distribution problem," *Structural optimization*, vol. 1, no. 4, pp. 193–202, 1989.

[14] J. Alexandersen and C. S. Andreasen, "A review of topology optimisation for fluid-based problems," *Fluids*, vol. 5, no. 1, p. 29, 2020.

[15] D. Bhattacharjee and A. Atta, "Topology optimization of a packed bed microreactor involving pressure driven non-newtonian fluids," *Reaction Chemistry & Engineering*, vol. 7, no. 3, pp. 609–618, 2022.

[16] F. Dugast, Y. Favennec, and C. Josset, "Reactive fluid flow topology optimization with the multi-relaxation time lattice boltzmann method and a level-set function," *Journal of Computational Physics*, vol. 409, p. 109252, 2020.

[17] S. Kubo, K. Yaji, T. Yamada, K. Izui, and S. Nishiwaki, "A level set-based topology optimization method for optimal manifold designs with flow uniformity in plate-type microchannel reactors," *Structural and Multidisciplinary Optimization*, vol. 55, no. 4, pp. 1311–1327, 2017.

[18] Y. Demirel and V. Gerbaud, *Nonequilibrium Thermodynamics: Transport and Rate Processes in Physical, Chemical and Biological Systems*. Elsevier Science, 2018.

[19] D. Jiang, W. Yang, and K. J. Chua, "Entropy generation analysis of h2/air premixed flame in micro-combustors with heat recuperation," *Chemical engineering science*, vol. 98, pp. 265–272, 2013.

[20] A. Bejan, *Entropy Generation Minimization: The Method of Thermodynamic Optimization of Finite-Size Systems and Finite-Time Processes*. Mechanical and Aerospace Engineering Series, CRC Press, 2013.

[21] Z. Dong and Q. Du, "The local distribution of temperatures and entropy generation rate in an ideal counterflow heat exchanger," *Coatings*, vol. 11, no. 8, p. 970, 2021.

[22] J. Avellaneda, F. Bataille, A. Toutant, and G. Flamant, "Variational entropy generation minimization of a channel flow: Convective heat transfer in a gas flow," *International Journal of Heat and Mass Transfer*, vol. 160, p. 120168, 2020.

[23] R. Dormohammadi, M. Farzaneh-Gord, A. Ebrahimi-Moghadam, and M. H. Ahmadi, "Heat transfer and entropy generation of the nanofluid flow inside

sinusoidal wavy channels," *Journal of Molecular Liquids*, vol. 269, pp. 229–240, 2018.

[24] G. Giangaspero and E. Sciubba, "Application of the entropy generation minimization method to a solar heat exchanger: A pseudo-optimization design process based on the analysis of the local entropy generation maps," *Energy*, vol. 58, pp. 52–65, 2013.

[25] J. Guo, L. Cheng, and M. Xu, "Optimization design of shell-and-tube heat exchanger by entropy generation minimization and genetic algorithm," *Applied Thermal Engineering*, vol. 29, no. 14-15, pp. 2954–2960, 2009.

[26] E. Johannessen, L. Nummedal, and S. Kjelstrup, "Minimizing the entropy production in heat exchange," *International Journal of Heat and Mass Transfer*, vol. 45, no. 13, pp. 2649–2654, 2002.

[27] M. Taherkhani and R. Safabakhsh, "A novel stability-based adaptive inertia weight for particle swarm optimization," *Applied Soft Computing*, vol. 38, pp. 281–295, 2016.

[28] P. Charoen-amornkitt, M. Alizadeh, T. Suzuki, and S. Tsushima, "Entropy generation analysis during adjoint variable-based topology optimization of porous reaction-diffusion systems under various design dimensionalities," *International Journal of Heat and Mass Transfer*, vol. 202, p. 123725, 2023.

[29] F. Hecht, "New development in freefem++," *J. Numer. Math.*, vol. 20, no. 3-4, pp. 251–265, 2012.

[30] V. Mendez, S. Fedotov, and W. Horsthemke, *Reaction-transport systems: mesoscopic foundations, fronts, and spatial instabilities*. Springer Science & Business Media, 2010.

[31] Y. Li, M. Zhao, C. Li, and W. Ge, "Concentration fluctuation due to reaction-diffusion coupling near an isolated active site on catalyst surfaces," *Chemical Engineering Journal*, vol. 373, pp. 744–754, 2019.

[32] M. Gao, H. Li, M. Yang, J. Zhou, X. Yuan, P. Tian, M. Ye, and Z. Liu, "A modeling study on reaction and diffusion in mto process over sapo-34 zeolites," *Chemical Engineering Journal*, vol. 377, p. 119668, 2019.

[33] F. Wang, X. Li, J. Tan, X. Hao, and B. Xiong, "Pore-scale prediction of the oxygen effective diffusivity in porous battery electrodes using the random walk theory," *International Journal of Heat and Mass Transfer*, vol. 183, p. 122085, 2022.

[34] P. García-Salaberri, "Modeling diffusion and convection in thin porous transport layers using a composite continuum-network model: Application to gas diffusion layers in polymer electrolyte fuel cells," *International Journal of Heat and Mass Transfer*, vol. 167, p. 120824, 2021.

[35] Z. Bao, Y. Li, X. Zhou, F. Gao, Q. Du, and K. Jiao, "Transport properties of gas diffusion layer of proton exchange membrane fuel cells: Effects of compression," *International Journal of Heat and Mass Transfer*, vol. 178, p. 121608, 2021.

[36] L. Maier, M. Scherle, M. Hopp-Hirschler, and U. Nieken, "Effective transport parameters of porous media from 2d microstructure images," *International Journal of Heat and Mass Transfer*, vol. 175, p. 121371, 2021.

[37] F. Tsutsui, T. Suzuki, and S. Tsushima, "Measurement and analysis of gas transport properties in catalyst layers of polymer electrolyte fuel cells with different ionomer to carbon ratio," *ECS Transactions*, vol. 98, no. 9, p. 49, 2020.

[38] A. Rajora and J. Haverkort, "An analytical multiphase flow model for parallel plate electrolyzers," *Chemical Engineering Science*, vol. 260, p. 117823, 2022.

[39] J. Cho, J. Marquis, P. Trogadas, T. Neville, D. Brett, and M.-O. Coppens, "Optimizing the architecture of lung-inspired fuel cells," *Chemical Engineering Science*, vol. 215, p. 115375, 2020.

[40] J. Liang, Y. Li, R. Wang, and J. Jiang, "Cross-dimensional model of the oxygen transport behavior in low-pt proton exchange membrane fuel cells," *Chemical Engineering Journal*, vol. 400, p. 125796, 2020.

[41] B. Tjaden, S. J. Cooper, D. J. Brett, D. Kramer, and P. R. Shearing, "On the origin and application of the bruggeman correlation for analysing transport phenomena in electrochemical systems," *Current opinion in chemical engineering*, vol. 12, pp. 44–51, 2016.

[42] Y.-l. Fu, B. Zhang, X. Zhu, D.-d. Ye, P.-C. Sui, N. Djilali, and Q. Liao, "Pore-scale modeling of mass transport in the air-breathing cathode of membraneless microfluidic fuel cells," *International Journal of Heat and Mass Transfer*, vol. 188, p. 122590, 2022.

[43] B. Tjaden, D. J. Brett, and P. R. Shearing, "Tortuosity in electrochemical devices: a review of calculation approaches," *International Materials Reviews*, vol. 63, no. 2, pp. 47–67, 2018.

[44] P. Salamon, K. H. Hoffmann, S. Schubert, R. S. Berry, and B. Andresen, "What conditions make minimum entropy production equivalent to maximum power production?," *Journal of Non-Equilibrium Thermodynamics*, vol. 26, no. 1, pp. 73–83, 2001.

[45] S. Kjelstrup, D. Bedeaux, E. Johannessen, and J. Gross, *Non-equilibrium Thermodynamics For Engineers (Second Edition)*. World Scientific Publishing Company, 2017.

[46] G. Watanabe and Y. Minami, "Finite-time thermodynamics of fluctuations in microscopic heat engines," *Physical Review Research*, vol. 4, no. 1, p. L012008, 2022.

[47] W. Muschik and K. H. Hoffmann, "Modeling, simulation, and reconstruction of 2-reservoir heat-to-power processes in finite-time thermodynamics," *Entropy*, vol. 22, no. 9, p. 997, 2020.

[48] A. Bejan, "Entropy generation minimization: The new thermodynamics of finite-size devices and finite-time processes," *Journal of Applied Physics*, vol. 79, no. 3, pp. 1191–1218, 1996.

[49] D. Tondeur and E. Kvaalen, "Equipartition of entropy production. an optimality criterion for transfer and separation processes," *Industrial & engineering chemistry research*, vol. 26, no. 1, pp. 50–56, 1987.

[50] E. Sauar, S. Kjelstrup Ratkje, and K. M. Lien, "Equipartition of forces: a new principle for process design and optimization," *Industrial & engineering chemistry research*, vol. 35, no. 11, pp. 4147–4153, 1996.

[51] E. Magnanelli, E. Johannessen, and S. Kjelstrup, "Entropy production minimization as design principle for membrane systems: Comparing equipartition results to numerical optima," *Industrial & Engineering Chemistry Research*, vol. 56, no. 16, pp. 4856–4866, 2017.

[52] M. Alizadeh and F. Torabi, "Precise pem fuel cell parameter extraction based on a self-consistent model and sccsa optimization algorithm," *Energy Conversion and Management*, vol. 229, p. 113777, 2021.

[53] G. Jing, J. Jia, and J. Xiang, "Level set-based bem topology optimization method for maximizing total potential energy of thermal problems," *International Journal of Heat and Mass Transfer*, vol. 182, p. 121921, 2022.

[54] S. Kubo, A. Koguchi, K. Yaji, T. Yamada, K. Izui, and S. Nishiwaki, "Level set-based topology optimization for two dimensional turbulent flow using an immersed boundary method," *Journal of Computational Physics*, vol. 446, p. 110630, 2021.

[55] J. C. Maxwell, "I.—on reciprocal figures, frames, and diagrams of forces," *Earth and Environmental Science Transactions of the Royal Society of Edinburgh*, vol. 26, no. 1, pp. 1–40, 1870.

[56] A. G. M. Michell, "Lviii. the limits of economy of material in frame-structures," *The London, Edinburgh, and Dublin Philosophical Magazine and Journal of Science*, vol. 8, no. 47, pp. 589–597, 1904.

[57] M. P. Bendsøe and N. Kikuchi, "Generating optimal topologies in structural design using a homogenization method," *Computer methods in applied mechanics and engineering*, vol. 71, no. 2, pp. 197–224, 1988.

[58] O. Sigmund and K. Maute, "Topology optimization approaches," *Structural and Multidisciplinary Optimization*, vol. 48, no. 6, pp. 1031–1055, 2013.

[59] H. Antil, D. Kouri, M. Lacasse, and D. Ridzal, *Frontiers in PDE-Constrained Optimization*. The IMA Volumes in Mathematics and its Applications, Springer New York, 2018.

[60] B. S. Lazarov and O. Sigmund, "Filters in topology optimization based on helmholtz-type differential equations," *International Journal for Numerical Methods in Engineering*, vol. 86, no. 6, pp. 765–781, 2011.

[61] A. Kawamoto, T. Matsumori, S. Yamasaki, T. Nomura, T. Kondoh, and S. Nishiwaki, "Heaviside projection based topology optimization by a pde-filtered scalar function," *Structural and Multidisciplinary Optimization*, vol. 44, no. 1, pp. 19–24, 2011.

[62] X. Huang and Y. Xie, "Convergent and mesh-independent solutions for the bi-directional evolutionary structural optimization method," *Finite elements in analysis and design*, vol. 43, no. 14, pp. 1039–1049, 2007.

[63] J. V. Carstensen and J. K. Guest, "Projection-based two-phase minimum and maximum length scale control in topology optimization," *Structural and multidisciplinary optimization*, vol. 58, no. 5, pp. 1845–1860, 2018.

[64] D. Frank-Kamenetskii, *Diffusion and Heat Transfer in Chemical Kinetics*. Plenum Press, 1969.

[65] S. Dong, C. Zhang, Z. Yue, F. Zhang, H. Zhao, Q. Cheng, G. Wang, J. Xu, C. Chen, Z. Zou, *et al.*, "Overall design of anode with gradient ordered structure with low iridium loading for proton exchange membrane water electrolysis," *Nano Letters*, vol. 22, no. 23, pp. 9434–9440, 2022.

[66] M. D. R. Batista, S. Chandrasekaran, B. D. Moran, M. S. de Troya, A. Pinongcos, Z. Wang, R. Hensleigh, A. Carleton, M. Zeng, T. Roy, *et al.*, "Design and additive manufacturing of optimized electrodes for energy storage applications," *Carbon*, vol. 205, pp. 262–269, 2023.

Chapter 3

A numerical simulation of evolution processes and entropy generation for optimal architecture of an electrochemical reaction-diffusion system: comparison of two optimization strategies

Abstract

Employment of electrochemical energy devices is being expanded as the world is shifting toward more sustainable power resources. To meet the required cost efficiency standards for commercialization, there is a need for optimal design of the electrodes. In this study, a topology optimization method is proposed to increase the performance of an electrochemical reaction-diffusion system. A dimensionless model is developed to characterize the transport and rate processes in the system. Two optimization strategies are introduced to improve system performance using a heterogeneous distribution of constituents. In addition, an entropy generation model is proposed to evaluate the system irreversibilities quantitatively. The findings show that the system performance could be enhanced up to 116.7% with an optimal tree-root-like structure. Such a heterogeneous material distribution provides a balance among various competing transport and rate processes. The proposed methodology could be employed in optimal design of electrodes for various electrochemical devices. This study also offers a fundamental comprehension of optimal designs by showing the connection between the optimal designs and the entropy generation. It is revealed that a less dissipating system corresponds to a more uniform current and entropy generation.

This chapter is published as:

M. Alizadeh, P. Charoen-amornkitt, T. Suzuki, and S. Tsushima. "A numerical simulation of evolution processes and entropy generation for optimal architecture of an electrochemical reaction-diffusion system: comparison of two optimization strategies", *Journal of The Electrochemical Society*, **170**.11 (2023): 114520.
https://doi.org/10.1149/1945-7111/ad0a7c

3.1 Introduction

Using renewable energies is a shortcut to combating environmental and energy security issues [1, 2]. Electrochemical energy conversion and storage devices, including secondary batteries and fuel cells (FCs), play an essential role in the transition from fossil fuel-based societies to ones that rely heavily on renewable resources to respond human energy needs [3, 4]. Despite recent advancements in the research and development of these technologies [5, 6], more work has to be done before they can be widely commercialized. Electrodes are vital components of any electrochemical device since they facilitate the electrochemical reactions that produce electricity. They serve as a bed for several transport and rate processes, and play a significant role in determination of the performance and efficiency of the electrochemical devices. Electrodes are typically porous medium that are made of an electrically conductive material, such as carbon, and coated with a catalyst. The catalyst promotes the desired electrochemical reaction at the electrode by increasing the reaction rate. In FC applications, for instance, the fuel and oxidant are supplied to the cell through channels in the electrodes. As the fuel and oxidant react at the electrodes, the released electrons flow through the external circuit to power an electrical load. The movement of reactant species and electric charges is essential for generating power in these systems. The performance of an electrochemical cell is mainly determined by the processes that are occurring at the electrode. Several research works [7–9] addressed these processes via electroanalytical methods. These transport processes (including mass diffusion, electric charges transfer, and heat transfer) and rate process (electrochemical reaction) are competing with each other. From an electrochemical standpoint, catalytic activity of the catalyst material and the electrochemical surface area are crucial factors that specify the rate of reactant consumption. However, the overall rate of an electrochemical reaction depends on the transport characteristics of the system as well. In other words, the speed of reactant delivery and product discharge are likewise influential in electrode performance. Hence, the design of the electrodes is an important consideration in the development of electrochemical technologies, and researchers are constantly working to improve the efficiency and durability of this component [10].

The electrochemical factors are dominantly hinged on the choice of catalyst material (or electrochemically-active material). Various catalysts come with different catalytic activity. However, the transport properties and effective utilization of the catalyst material strongly depend on the structural design of the porous electrode [11, 12].

A better design solution might improve the transport phenomena and consequently lead to a more effective utilization of the catalyst material. Modifying the composition of an electrode is an approach used by previous researchers [13–15] to get an appropriate compromise between various processes. Depending on the application, composition modification includes, but is not limited to, changing the porosity, catalyst loading, and electrolyte loading. Mathematical optimization can be utilized to search for the optimal composition. So far, the studies in the literature focused on controlling the composition in a global level. A heterogeneous design, however, can provide a superior control of the transport and rate processes by extending the degree of freedom to a local level. In this regard, topology optimization (TO) [16] is a mathematical technique that can provide innovative design solutions for a variety of engineering applications. In this approach, the goal is to find the best shape and layout of structure or system that improves one or several performance criteria. This is typically conducted by using iterative mathematical procedures to test different material distribution until finding the one that best meets the desired performance criteria. TO outperforms other categories of mathematical optimization, such as parametric optimization, thanks to its higher degree of freedom. It has been successfully applied to a wide range of engineering applications, including mechanical [17], chemical [18, 19], thermal [20], and fluid [21] systems. In electrochemical devices, TO can be used to design efficient and high-performing electrodes [22–24], flow channels [25, 26], and other components. To date, only a few studies addressed the employment of TO for designing electrodes with heterogeneous structures. For instance, Roy et al. [22] used this technique to find the best porosity distribution layout in the electrode of a redox flow battery. Their results show that a non-uniform distribution of porosity could increase the cell performance by reducing the ohmic losses in the system. However, this study does not account for the effect of concentration depletion. Reviewing the literature shows that TO has a significant potential for designing better porous reactors for electrochemical applications. It is worth noting that recent advancements in additive manufacturing and 3D printing technologies have made it possible to fabricate complex structures [27]. For instance, in a recent study [28], researchers introduced a grooved electrode structure for FCs, which improved cell performance by enhancing ionic conductivity and mass diffusion. As a result, the development of innovative designs necessitates the application of rigorous mathematical approaches, such as TO.

In power generating electrochemical devices (e.g., a fuel cell), a better design is referred to the increment in the output power. In this sense, design enhancement might

be gained by controlling either the current density or the system overpotential. This give a rise to two strategies in optimization of electrochemical systems: (1) maximizing the current density at a given overpotential and (2) minimizing the total overpotential at a given current density. Both these approaches will lead to a higher output power in the case of power generating system. The same approaches could be applied for a power consuming electrochemical system (e.g., electrolyzers). However, in such devices, optimization will reduce the power consumption or increase the output products. From a physicochemical standpoint, however, the above-mentioned approaches are different. Despite promising results reported by previous researchers in the employment of TO for designing better system, they usually overlook investigation of optimization process from a physical basis. Such elucidation is crucial because it might open new room for further improvement of system performance beyond the capabilities of existing mathematical schemes. To obtain a physical understanding, one can investigate the changes in system irreversibilities over the course of optimization. The irreversibilities of a system could be expressed quantitatively in the form of entropy generation. Non-equilibrium thermodynamics (NET) [29, 30], a branch of thermodynamics that deals with the systems that are not in a global equilibrium conditions, could be used to determine the local and global rate of entropy generation in a system. Previously, it has been extensively used for analysis of thermofluid systems [31–41]. In a recent study by Charoen-amornkitt et al. [18], the authors used NET to describe entropy generation in a chemical reactor. The entropy production approach based on NET of physical processes at the interfaces has been applied for efficiency improvement in PEM fuel cells with porous electrodes [42]. Entropy generation is known as an index of power dissipation in a system. Therefore, it is desirable to reduce the rate of entropy generation (if and only if the system duty is not changed). This idea led to a so-called Entropy Generation Minimization (EGM) principle [43]. It is noteworthy that EGM only works when a certain system duty is guaranteed. Since under a finite time/size condition, any system is doomed to generate some amount of entropy, the two aforementioned optimization strategies may have different behaviors in terms of entropy production. These differences will be comprehensively discussed in the subsequent sections.

3.1.1 Research objectives and gaps

In this study, a mathematical optimization process is employed to seek the optimal architecture for a porous electrochemical reactor. Such an engineered structure obtained by TO is shown to be capable of enhancing the system performance substantially. This enhancement is obtained by improving the utilization of the constituents materials that is achieved thanks to a heterogeneous layout. This research work introduced a general framework for optimization of constituents placement in an electrochemical reactor. Hence, similar procedure might be used for real applications, such as catalyst layer of a FC. By revisiting the definition of performance enhancement in an electrochemical system, the present work compares two different strategies in optimizing electrochemical systems.

While previous optimization studies (e.g. [13, 14, 22]) predominantly concentrated on the comparative analysis of designs pre- and post-optimization, this research takes a deeper dive into the physical aspects driving design improvements. To achieve this, the entire course of optimization is thoroughly explored, rather than just looking at the starting and ending designs. Furthermore, this study introduces two distinct electrode optimization strategies and examines their physicochemical differences. To the best of the authors' knowledge, such distinctions have not been observed in prior research. As previously highlighted, the full-scale commercialization of electrochemical energy devices hinges on advancing their performance and cost efficiency. In this context, the application of topological optimization to electrode structures may yield highly efficient designs. Furthermore, a more comprehensive understanding of the optimization process through NET analysis could pave the way for uncovering the upper limits of performance achievable with current materials. This insight could also shed light on areas ripe for further improvement through research and development efforts.

3.2 Methods

In this study, a 2D electrochemical porous reactor involving reactant diffusion, electric charges transport, and a redox reaction is inspected. The porous reactor is considered being composed of three phases. A reactant is diffused into the system according to the Fick's law of diffusion. This reactant is converted to the products through an electrochemical reaction in the presence of a catalyst material. The rate of this reaction is described using the Butler-Volmer relationship. A non-dimensional mathematical model is developed to characterize the performance of this system.

Two sets of boundary conditions are assumed to analyze the system, including a given current density and a given total overpotential. By solving the governing equations together with a given current density as the boundary condition (B.C.), the total overpotential of the reactor is calculated. On the other hand, when the total overpotential is given as the B.C., the numerical simulation provides the system current density. An entropy generation model is also developed to evaluate the rate of irreversibilities in the system by various mechanisms. The entropy generation rate is also non-dimensionalized to generalize the applicability of the results and discussions. Next, a TO method is used to find the optimal distribution of constituents in a given design domain. The local volume fractions of constituents are controlled to obtain the best performance. For this purpose, two different optimizations, including maximization of current density and minimization of total overpotential, are performed. The local and global entropy production is calculated in each iteration. The trend of entropy generation is compared for the two optimization approaches to explain the differences from a physical viewpoint. The methods are described in details as follows.

3.3 Mathematical modeling

In the present study, a continuum model is employed to describe the behavior of various rate and transport phenomena occurring in a 2D electrochemical reactor. The schematic of the representative porous reactor is depicted in Fig. 3.1. As it can be seen in this figure, the reactor is assumed to consist of three phases, including void, electrolyte, and solid phases. This reactor design with triple phases is not common in electrochemical systems. For instance, in lithium-ion batteries and redox flow batteries, the pore is filled with electrolyte solution, resulting in a double-phase system (solid and electrolyte). In this study, however, we modeled the system in a way to be applicable to both double- or triple-phase systems, with the aims of covering FCs that are triple-phase systems. The reactant species is diffused through pores and the produced ion is transferred by the electrolyte material. The solid phase is responsible not only for transport of exchanged electrons but also for increase in reaction rate. In electrochemical energy devices, such as FCs, the solid phase is typically composed of a catalyst material (e.g., platinum) and a supporting material (e.g., carbon). In this study, it is assumed that the reactant species $\mathrm{A_{red}}$ is oxidized in the presence of a solid phase (catalyst material) as follows:

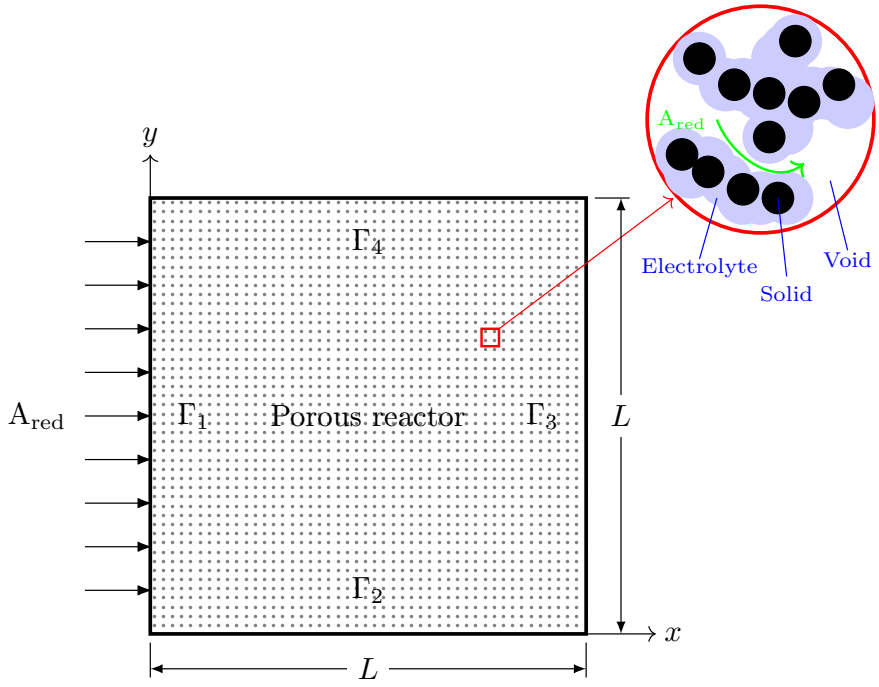

Figure 3.1: Schematic of electrochemical porous reactor

$$A_{red} \rightarrow A_{ox} + ne^{-} \tag{3.1}$$

where A_{red} and A_{ox} are reducing and oxidizing agents, respectively, and n is the number of electrons involved in this reaction. For simplicity, n is assumed to be unity ($n = 1$). It is noteworthy that choice of an oxidation reaction over a reduction reaction may not affect the generality of methods and discussions drawn in this study. In fact, a reversed redox reaction, i.e. reduction reaction, might be obtained by using the same formulations proposed in the present study and a slightly different choice of B.C.s. This issue is explained in the subsequent parts, where B.C.s are discussed. It is assumed that the investigated system in this study is working under a steady-state and isothermal conditions. The equations governing the transport and production/consumption of reacting agent and electric charges are given in the following subsection.

3.3.1 Governing equations

The governing equations presented here are based on a volume-averaged approach. The generic differntial form of any balance equation (e.g., mass, energy, and charge) on a control volume is expressed as:

$$\frac{\partial \rho}{\partial t} = \nabla \cdot \mathbf{f} + S \tag{3.2}$$

where ρ is any quantity of interest, such as mass, energy, and charge. Moreover, $\mathbf{f}$ and S represent the flux and source terms of the relevant quantity. In the present study, it is assumed that the distribution of the reactant concentration throughout the porous reactor is controlled by the Fick's second law of diffusion [44–46] and electrochemical reaction rate. Therefore, conservation of species in this ERD system reads as [44]:

$$\frac{\partial C}{\partial t} = \nabla \cdot (D^{\text{eff}} \nabla C) + R_{\text{C}} \tag{3.3}$$

in which C is reactant species concentration ($\text{mol}\,\text{m}^{-3}$), D^{eff} is effective diffusivity ($\text{m}^2\,\text{s}^{-1}$), and R_{C} is the reaction source term ($\text{mol}\,\text{m}^{-3}\,\text{s}^{-1}$). This source term is defined as $R_{\text{C}} = -\frac{a^{\text{eff}} j_{\text{src}}}{F}$ for an oxidation reaction and $R_{\text{C}} = \frac{a^{\text{eff}} j_{\text{src}}}{F}$ for a reduction reaction. Also, j_{src} is current density source ($\text{A}\,\text{m}^{-2}$), a^{eff} is effective active specific surface area ($\text{m}^2\,\text{m}^{-3}$), and F is Faraday constant ($96485\,\text{C}\,\text{mol}^{-1}$). Under a steady-state condition, the term on the left-hand side of Eq. (3.3) is zero. Therefore, in the calculations of the present study, the species accumulation term is disregarded. However, since the unsteady form of this equation is used for derivation of entropy production rate in the subsequent section, it is shown in this form. The conservation of electric charges in electrolyte and solid phases follows Ohm's law and is expressed as follows for an electroneutral system [47]:

$$\frac{\partial q^{+}}{\partial t} = \nabla \cdot (\sigma_{\text{l}}^{\text{eff}} \nabla \phi_{\text{l}}) + a^{\text{eff}} j_{\text{src}} \tag{3.4}$$

$$\frac{\partial q^{-}}{\partial t} = \nabla \cdot (\sigma_{\text{s}}^{\text{eff}} \nabla \phi_{\text{s}}) - a^{\text{eff}} j_{\text{src}} \tag{3.5}$$

where q^{+} and q^{-} are positive and negative charge densities ($\text{C}\,\text{m}^{-3}$), $\sigma_{\text{l}}^{\text{eff}}$ and $\sigma_{\text{s}}^{\text{eff}}$ are effective electrolyte and solid phases charge conductivity ($\text{S}\,\text{m}^{-1}$), and ϕ_{l} and ϕ_{s} are electrolyte and solid phases potentials (V), respectively. It should be emphasized that the left-hand side of Eqs. (3.4) and (3.5) represent accumulation rate of electric charge in the system. In electrochemical reactors (e.g., electrode of batteries or FCs), no charge is accumulated and therefore, this term is usually not shown in the literature. Moreover, since this study assumes a steady-state condition, these terms are zero (similar to what exists in the literature). However, as aforementioned, the unsteady form of governing equations is used for derivation of local entropy generation rate.

The current density source, j_{src}, might be expressed by well-known Butler-Volmer equation as follows [47].

$$j_{\mathrm{src}} = i_0 \left(\frac{C}{C^{\mathrm{ref}}} \right) \left\{ \exp\left[\frac{\alpha_{\mathrm{a}} F \eta}{RT} \right] - \exp\left[\frac{-\alpha_{\mathrm{c}} F \eta}{RT} \right] \right\} \tag{3.6}$$

In Eq. (3.6), i_0, C^{ref}, α_{a}, α_{c}, η, R, and T are exchange current density ($\mathrm{A\,m^{-2}}$), reference concentration ($\mathrm{mol\,m^{-3}}$), anodic charge transfer coefficient, cathodic charge transfer coefficient, activation overpotential (V), gas constant ($8.3145\,\mathrm{J\,mol^{-1}\,K^{-1}}$), and temperature (K). The correction term $\left(\frac{C}{C^{\mathrm{ref}}}\right)$ is considered to include the effect of mass transport limitations. In this study, one of the terms on the right-hand-side of Eq. (3.6) is neglected by assuming a largely-polarized condition. The activation overpotential is measured based on the local electrolyte and solid phases potentials as follows [47]:

$$\eta = \phi_{\mathrm{s}} - \phi_{\mathrm{l}} - E_{\mathrm{eq}} \tag{3.7}$$

where E_{eq} is equilibrium potential (V). As indicated in Eq. (3.6), in such an ERD system, current density and overpotential are correlated through two rate mechanisms, including: (1) charge transfer rate and (2) mass transport rate. The former mechanism dictates how fast the reactant species is consumed (or likewise, the speed at which the products are produced). On the other hand, the mass transport rate determines the pace of reactant supply and products discharge from the reaction site. The overall process kinetics depends on the slowest mechanism. In electrochemical applications, sluggish mass transport is a serious challenge when the device is working at a high current density and causes a huge drop in output power. Therefore, not only sufficient supply of reactant species but also adequate discharge of products is vital to improve the performance. This issue is elaborated in Section 3.4. While thanks to previous experimental studies, the bulk magnitude of mass diffusivity and electric charges conductivity are known for many substances, estimating the effective values of these transport properties in porous media is a long-running dispute among researchers [48–50]. The Bruggeman equation is an enduring correlation relating the effective properties to the material volume fraction through a power-law. Despite numerous arguments around its validity [51, 52], the simplicity of the Bruggeman equation led to frequent utilization and recognition of this model in various disciplines, including electrochemistry applications [53–57]. Therefore, in this study, the effective properties are computed based on the Bruggeman model with a different exponent from that of the original equation as follows:

$$D^{\text{eff}} = D^0 \varepsilon_{\text{v}}^{\beta_1}; \quad \sigma_{\text{l}}^{\text{eff}} = \sigma_{\text{l}}^0 \varepsilon_{\text{l}}^{\beta_2}; \quad \sigma_{\text{s}}^{\text{eff}} = \sigma_{\text{s}}^0 \varepsilon_{\text{s}}^{\beta_3}; \quad a^{\text{eff}} = a^0 \varepsilon_{\text{s}}^{\beta_4} \tag{3.8}$$

in which D^0, σ_{l}^0, σ_{s}^0, and a^0 are bulk mass diffusivity ($\text{m}^2\,\text{s}^{-1}$), bulk electrolyte ionic conductivity ($\text{S}\,\text{m}^{-1}$), bulk solid phase electric conductivity ($\text{S}\,\text{m}^{-1}$), and bulk active specific surface area ($\text{m}^2\,\text{m}^{-3}$), respectively. These bulk values are corrected according to the volume fractions of void (ε_{v}), electrolyte phase (ε_{l}), and solid phase (ε_{s}) together with the relevant given penalty exponents, β_1 to β_4.

3.3.2 Boundary conditions

The system of partial differential equations (PDEs) given by Eqs. (3.3) to (3.5) might be solved in the calculation domain, Ω, if sufficient B.C.s are provided on the boundary of the domain, $\partial\Omega$. While the proposed model could work with any set of sufficient B.C.s, two of them are our interest in this study. The chosen B.C.s, according to Fig. 3.1, are given by:

$$\begin{aligned}
C &= C^{\text{bnd}} \quad \text{on}\,\Gamma_1 \quad \text{and} \quad -D^{\text{eff}}\nabla C \cdot \hat{\mathbf{n}} = 0 \quad \text{on}\,\partial\Omega\backslash\Gamma_1 \\
\phi_{\text{l}} &= \phi_{\text{l}}^{\text{bnd}} \quad \text{on}\,\Gamma_3 \quad \text{and} \quad -\sigma_{\text{l}}^{\text{eff}}\nabla \phi_{\text{l}} \cdot \hat{\mathbf{n}} = 0 \quad \text{on}\,\partial\Omega\backslash\Gamma_3 \\
\phi_{\text{s}} &= \phi_{\text{s}}^{\text{bnd}} \quad \text{on}\,\Gamma_1 \quad \text{and} \quad -\sigma_{\text{s}}^{\text{eff}}\nabla \phi_{\text{s}} \cdot \hat{\mathbf{n}} = 0 \quad \text{on}\,\partial\Omega\backslash\Gamma_1
\end{aligned} \tag{3.9}$$

and

$$\begin{aligned}
C &= C^{\text{bnd}} \quad \text{on}\,\Gamma_1 \quad \text{and} \quad -D^{\text{eff}}\nabla C \cdot \hat{\mathbf{n}} = 0 \quad \text{on}\,\partial\Omega\backslash\Gamma_1 \\
-\sigma_{\text{l}}^{\text{eff}}\nabla \phi_{\text{l}} \cdot \hat{\mathbf{n}} &= j^{\text{bnd}} \quad \text{on}\,\Gamma_3 \quad \text{and} \quad -\sigma_{\text{l}}^{\text{eff}}\nabla \phi_{\text{l}} \cdot \hat{\mathbf{n}} = 0 \quad \text{on}\,\partial\Omega\backslash\Gamma_3 \\
\phi_{\text{s}} &= \phi_{\text{s}}^{\text{bnd}} \quad \text{on}\,\Gamma_1 \quad \text{and} \quad -\sigma_{\text{s}}^{\text{eff}}\nabla \phi_{\text{s}} \cdot \hat{\mathbf{n}} = 0 \quad \text{on}\,\partial\Omega\backslash\Gamma_1
\end{aligned} \tag{3.10}$$

where C^{bnd}, $\phi_{\text{l}}^{\text{bnd}}$, $\phi_{\text{s}}^{\text{bnd}}$, and j^{bnd} are constant concentration ($\text{mol}\,\text{m}^{-3}$), electrolyte potential (V), solid potential (V), and ionic current density ($\text{A}\,\text{m}^{-2}$) on boundary, respectively. Also, $\hat{\mathbf{n}}$ denotes the outward unit normal vector. In the first set specified by Eqs. (3.9), a combination of Dirichlet and homogeneous Neumann B.C.s are introduced for all variables. The values of all variables (concentration, electrolyte potential, and solid potential) are given on one of the system boundaries. This means that the system total overpotential (i.e., the difference of solid and electrolyte phases potentials on the boundaries that the current density is flowing) is given. Based on

these settings, the total electric current that passes the system boundaries is computed by solving the system of PDEs. This current represents the total electrochemical reaction rate that is taking place within the ERD system. In Eq. (3.10), the B.C.s for reactant concentration and solid phase potential are kept the same as in previous conditions. In contrast, the ionic current density passing Γ_3 is prescribed. Accordingly, the total electrochemical reaction rate, that is happening the entire porous reactor, is known. As a result, in such kind of setup, the system overpotential would be determined as a solution of governing equations.

The reason behind these choices for B.C.s are explained as follows. As stated previously, one of the aims of this study is to elucidate the best material distribution (structure) in the porous reactor that enhances the system performance. Hence, it is essential to clearly interpret the meaning of "performance". In electrochemical systems, performance enhancement is achieved either by: (1) maximization of total reaction rate (or likewise, the current that is flowing through the system boundaries) at a given overpotential level or, (2) minimization of system overpotential (which represents the energy loss) for a given total reaction rate. Although the combination of both these strategies might be a third alternative for performance improvement, it is out of the scope of this study. Based on the given definitions of "performance" in an ERD system, the optimization is formulated as both maximization and minimization problems. The B.C.s given by Eqs. (3.9) and (3.10) are chosen in a way to fulfill the aforementioned optimization goals. Using the first set of B.C.s, the solution of governing equations (i.e., total current density flowing the system boundaries), might be used as the objective function for the maximization problem. On the other hand, by employment of B.C.s given in Eq. (3.10), the system overpotential could be used as the objective function for minimization formulation. The details of maximization and minimization problems are comprehensively discussed in Section 3.4. To distinguish the two formulations described above, hereinafter, the governing equations (Eqs. (3.3) to (3.5)) together with B.C.s of Eq. (3.9) are called "overpotential-based ERD system" and the combination of the governing equations and B.C.s of Eq. (3.10) are called "current-based ERD system". The names are assigned based on the electrolyte phase condition on boundary Γ_3 that is given as the model input. Thus, "overpotential-based ERD system" is associated with the maximization optimization and "current-based ERD system" is associated with the minimization optimization. It is also noteworthy that by a proper choice of values for B.C.s given in Eqs. (3.9) and (3.10), the electrochemical reaction might be switched between oxidation and reduction. For instance, a positive value for j^{bnd} in B.C.s of Eq. (3.10),

provides an oxidation reaction. A negative value will result in a reduction reaction.

3.3.3 Entropy generation model

A system is at an equilibrium state if all macroscopic flows, such as heat or mass fluxes, are zero within its boundaries. Equilibrium thermodynamics, as part of contemporary thermodynamics, successfully handles the systems at an equilibrium state as well as those involving low equilibrium, relatively slow, quasiequilibrium processes. NET extends conventional equilibrium thermodynamics to characterize the systems which are not in an equilibrium state [29, 30]. The concept has been widely used in the literature to analyze the entropy generation in various engineering applications and thermofluid systems [58–64]. Since the ERD system in this study is in a non-equilibrium condition from a global standpoint, the concept of NET is recruited to develop a model for evaluation of local and global entropy generation rate. A lower entropy production is only favorable if the output of the system (in ERD system, the total reaction rate) is kept at a certain amount. If a system is working under a finite time/size thermodynamics, doing more (i.e. a higher electrochemical reaction rate in the case of ERD system) will inevitably result in a higher amount of entropy production. Therefore, maximization of current in the "overpotential-based ERD system" is expected to increase the total amount of entropy generation rate. However, at a same level of reaction rate (i.e. happening in "current-based ERD system"), an optimized design solution will minimize the system losses and consequently reduce the total entropy generation of the system. The difference between the two optimization approaches, including maximization and minimization formulations, might be recognized in terms of entropy generation. This contrast is highlighted in Section 3.5 where the results of both strategies are discussed. Development of entropy generation model starts with the extended form of Gibbs equation, which is a fundamental thermodynamics equation and reads as follows [29, 65, 66]:

$$dU = TdS - pdV + \mu dN + \phi_{\mathrm{l}} dQ^{+} + \phi_{\mathrm{s}} dQ^{-} \tag{3.11}$$

where U, S, V, N, Q^{+} and Q^{-} are internal energy (J), entropy ($\mathrm{J\,K^{-1}}$), volume ($\mathrm{m^3}$), the number of moles (mol), positive electric charge (C), and negative electric charge (C) respectively. Also, T, p, and μ are temperature (K), pressure (Pa), and chemical potential ($\mathrm{J\,mol^{-1}}$), respectively. It is assumed that the reactant substance is an ideal gas, and the system is working under a constant temperature (isothermal) condition. Since the internal energy of an ideal gas is a function of temperature and the volume

of the porous reactor is not changing, dU and pdV are zero. By dividing Eq. (3.11) by the volume, it is simplified into:

$$Tds = -\mu dC - \phi_{\mathrm{l}} dq^{+} - \phi_{\mathrm{s}} dq^{-} \tag{3.12}$$

where $s = S/V$ is the entropy density ($\mathrm{J\,k^{-1}\,m^{-3}}$). Given the fact that the system does not have any convective flow, the time derivative of the entropy is given by:

$$\frac{\partial s}{\partial t} = -\frac{1}{T}\left(\mu \frac{\partial C}{\partial t} + \phi_{\mathrm{l}} \frac{\partial q^{+}}{\partial t} + \phi_{\mathrm{s}} \frac{\partial q^{-}}{\partial t}\right) \tag{3.13}$$

By substituting the partial derivatives on the right-hand-side of Eq. (3.13) with Eqs. (3.3) to (3.5), the rate of entropy accumulation is as follows:

$$\begin{aligned}\frac{\partial s}{\partial t} = -\nabla \cdot \left[\frac{\mu D^{\mathrm{eff}} \nabla C + \phi_{\mathrm{l}} \sigma_{\mathrm{l}}^{\mathrm{eff}} \nabla \phi_{\mathrm{l}} + \phi_{\mathrm{s}} \sigma_{\mathrm{s}}^{\mathrm{eff}} \nabla \phi_{\mathrm{s}}}{T}\right] + \frac{1}{T}(D^{\mathrm{eff}} \nabla C \cdot \nabla \mu \\ + \sigma_{\mathrm{l}}^{\mathrm{eff}} \nabla \phi_{\mathrm{l}} \cdot \nabla \phi_{\mathrm{l}} + \sigma_{\mathrm{s}}^{\mathrm{eff}} \nabla \phi_{\mathrm{s}} \cdot \nabla \phi_{\mathrm{s}} \pm \frac{\mu a^{\mathrm{eff}} j_{\mathrm{src}}}{F} - \phi_{\mathrm{l}} a^{\mathrm{eff}} j_{\mathrm{src}} + \phi_{\mathrm{s}} a^{\mathrm{eff}} j_{\mathrm{src}})\end{aligned} \tag{3.14}$$

in which plus and minus signs of term $\pm\frac{\mu a^{\mathrm{eff}} j_{\mathrm{src}}}{F}$ are related to oxidation and reduction reactions, respectively. By comparing the general form of entropy balance ($\frac{\partial s}{\partial t} = -\nabla \cdot \mathbf{J}_{\mathrm{s}} + \sigma$) [29, 30] with Eq. (3.14), the entropy flux ($\mathrm{W\,K^{-1}\,m^{-2}}$) and entropy generation rate per unit volume ($\mathrm{W\,K^{-1}\,m^{-3}}$) are respectively given by:

$$\mathbf{J}_{\mathrm{s}} = \frac{\mu D^{\mathrm{eff}} \nabla C + \phi_{\mathrm{l}} \sigma_{\mathrm{l}}^{\mathrm{eff}} \nabla \phi_{\mathrm{l}} + \phi_{\mathrm{s}} \sigma_{\mathrm{s}}^{\mathrm{eff}} \nabla \phi_{\mathrm{s}}}{T} \tag{3.15}$$

and

$$\begin{aligned}\sigma = \frac{1}{T}(D^{\mathrm{eff}} \nabla C \cdot \nabla \mu + \sigma_{\mathrm{l}}^{\mathrm{eff}} \nabla \phi_{\mathrm{l}} \cdot \nabla \phi_{\mathrm{l}} + \sigma_{\mathrm{s}}^{\mathrm{eff}} \nabla \phi_{\mathrm{s}} \cdot \nabla \phi_{\mathrm{s}} \\ \pm \frac{\mu a^{\mathrm{eff}} j_{\mathrm{src}}}{F} - \phi_{\mathrm{l}} a^{\mathrm{eff}} j_{\mathrm{src}} + \phi_{\mathrm{s}} a^{\mathrm{eff}} j_{\mathrm{src}})\end{aligned} \tag{3.16}$$

The first three terms on right-hand-side of entropy generation rate equation, σ, are related to the entropy produced by the transport processes. The other three terms correspond to the source terms in the governing equations (Eqs. (3.3) to (3.5)). To

quantify the individual contribution of each process to the entropy generation rate, the terms are split into four contributions as follows:

$$\begin{aligned}
\sigma_{\mathrm{mt}} &= \tfrac{1}{T} D^{\mathrm{eff}} \nabla C \cdot \nabla \mu \\
\sigma_{\mathrm{it}} &= \tfrac{1}{T} \sigma_{\mathrm{l}}^{\mathrm{eff}} \nabla \phi_{\mathrm{l}} \cdot \nabla \phi_{\mathrm{l}} \\
\sigma_{\mathrm{et}} &= \tfrac{1}{T} \sigma_{\mathrm{s}}^{\mathrm{eff}} \nabla \phi_{\mathrm{s}} \cdot \nabla \phi_{\mathrm{s}} \\
\sigma_{\mathrm{rx}} &= \tfrac{1}{T} (\pm \tfrac{\mu a^{\mathrm{eff}} j_{\mathrm{src}}}{F} - \phi_{\mathrm{l}} a^{\mathrm{eff}} j_{\mathrm{src}} + \phi_{\mathrm{s}} a^{\mathrm{eff}} j_{\mathrm{src}})
\end{aligned} \tag{3.17}$$

where σ_{mt}, σ_{it}, σ_{et}, and σ_{rx} correspond to the entropy production by mass diffusion, ion transport, electron transport, and reaction ($\mathrm{W\,K^{-1}\,m^{-3}}$), respectively. Moreover, to evaluate the total amount of entropy production throughout the entire system ($\mathrm{W\,K^{-1}\,m^{-1}}$), the local entropy generation rate, σ, should be integrated as:

$$P = \int_{\Omega} \sigma d\Omega \tag{3.18}$$

Likewise, the total entropy production is also broken into four parts, including $P_{\mathrm{mt}} = \int_{\Omega} \sigma_{\mathrm{mt}} d\Omega$, $P_{\mathrm{it}} = \int_{\Omega} \sigma_{\mathrm{it}} d\Omega$, $P_{\mathrm{et}} = \int_{\Omega} \sigma_{\mathrm{et}} d\Omega$, and $P_{\mathrm{rx}} = \int_{\Omega} \sigma_{\mathrm{rx}} d\Omega$, each of which is associated with the integral of corresponding local term over the entire domain. The chemical potential of an ideal gas at a constant temperature is computed by [29]:

$$\mu = \mu^{\mathrm{ref}} + RT \ln \left(\frac{C}{C^{\mathrm{ref}}} \right) \tag{3.19}$$

in which μ^{ref} and R are chemical potential at the reference point ($\mathrm{J\,mol^{-1}}$) and universal gas constant (8.314 $\mathrm{J\,K^{-1}\,mol^{-1}}$), respectively. For a given electrochemical reaction, the reference chemical potential correlated to the equilibrium potential by the following equation [67].

$$E_{\mathrm{eq}} = \frac{\mu^{\mathrm{ref}}}{F} \tag{3.20}$$

3.3.4 Non-dimensional analysis

To generalize the applicability of this study, the governing equations are converted into a dimensionless form. Non-dimensionalization might reduce the number of

model parameters, expand the applicability of the obtained results, increase the stability and accuracy of the simulated results, and make the comparison between various scenarios easier [68, 69]. The system of governing equations, as well as the B.C.s, are non-dimensionalized by substitution of proper dimensionless variables to remove the units. The dimensionless form of Eqs. (3.3) to (3.5) at a steady-state condition reads as:

$$\nabla^* \cdot \left(\theta_1 \varepsilon_{\mathrm{v}}^{\beta_1} \nabla^* C^*\right) \mp \varepsilon_{\mathrm{s}}^{\beta_4} j_{\mathrm{src}}^* = 0 \tag{3.21}$$

$$\nabla^* \cdot \left(\frac{\theta_2}{1+\theta_3} \varepsilon_{\mathrm{l}}^{\beta_2} \nabla^* \phi_{\mathrm{l}}^*\right) + \varepsilon_{\mathrm{s}}^{\beta_4} j_{\mathrm{src}}^* = 0 \tag{3.22}$$

$$\nabla^* \cdot \left(\frac{\theta_2 \theta_3}{1+\theta_3} \varepsilon_{\mathrm{s}}^{\beta_3} \nabla^* \phi_{\mathrm{s}}^*\right) - \varepsilon_{\mathrm{s}}^{\beta_4} j_{\mathrm{src}}^* = 0 \tag{3.23}$$

in which C^*, ϕ_{l}^*, and ϕ_{s}^* are dimensionless concentration, electrolyte potential, and solid potential, respectively. Moreover, ∇^* is differentiation with respect to dimensionless coordinates x^* and y^*. The dimensionless dependent and independent variables are given by:

$$\begin{aligned} x^* &= \tfrac{x}{L}; \quad y^* = \tfrac{y}{L}; \quad C^* = \tfrac{C}{C_0}; \quad \mu^* = \tfrac{\mu}{RT} \\ \phi_{\mathrm{l}}^* &= \tfrac{\phi_{\mathrm{l}}}{\phi_0}; \quad \phi_{\mathrm{s}}^* = \tfrac{\phi_{\mathrm{s}}}{\phi_0}; \quad a^* = \tfrac{a^{\mathrm{eff}}}{a_0}; \quad j_{\mathrm{src}}^* = \tfrac{j_{\mathrm{src}}}{i_0} \end{aligned} \tag{3.24}$$

In addition, the dimensionless groups are expressed as:

$$\begin{aligned} \theta_1 &= \tfrac{D^0}{L^2 a^0 i_0/(C_0 F)} = \tfrac{D^0}{D^{\mathrm{exchange}}} \\ \theta_2 &= \tfrac{(\sigma_{\mathrm{l}}^0+\sigma_{\mathrm{s}}^0)}{L^2 a^0 i_0/\phi_0} = \tfrac{(\sigma_{\mathrm{l}}^0+\sigma_{\mathrm{s}}^0)}{\sigma_{\mathrm{ohm}}^{\mathrm{exchange}}} \\ \theta_3 &= \tfrac{\sigma_{\mathrm{s}}^0}{\sigma_{\mathrm{l}}^0} \end{aligned} \tag{3.25}$$

where L, C_0 and ϕ_0 are the characteristic length (m), characteristic concentration ($\mathrm{mol\,m^{-3}}$), and characteristic potential (V) of the system, respectively. Based on these definitions, θ_1 is the dimensionless conductivity. This dimensionless number could be interpreted as the ratio of species intrinsic diffusivity and system exchange diffusivity ($D^{\mathrm{exchange}} = L^2 a^0 i_0/(C_0 F)$). From another perspective, θ_1 is attributed to

inverse of Damköhler number (or inverse square Thiele modulus) in chemical engineering literature [70–73], which indicates the ratio of the bulk diffusion rate and reaction rate. Moreover, θ_2 represents the ratio of intrinsic conductivity and system exchange ohmic conductivity ($\sigma_{\text{ohm}}^{\text{exchange}} = L^2 a^0 i_0/\phi_0$). In electrochemistry literature, dimensionless parameter θ_2 is known as Wagner number [47, 67], which shows the proportion of kinetic resistance to ohmic resistance. Finally, θ_3 represents the ratio of solid and electrolyte phases conductivity. In many real electrochemical applications, such as polymer electrolyte membrane fuel cell (PEMFC), this ratio is relatively large ($\theta_3 \gg 1$). While there might be different alternatives for the characteristic parameters of the system, a reasonable choice is given:

$$C_0 = C^{\text{bnd}}; \quad \phi_0 = \frac{RT}{F} \tag{3.26}$$

Based on Eq. (3.26), the characteristic concentration is assumed to be the constant concentration on the inlet boundary. This way, the concentration B.C. would be easily scaled to unity. Also, characteristic potential is chosen to be the thermal voltage of the system that is correlated to the temperature at which the system is working. The characteristic length is considered to be equal to the length of the domain, as shown in Fig. 3.1, for the sake of simplicity. Using the dimensionless parameters introduced before, the B.C.s of "overpotential-based ERD system" and "current-based ERD system" are non-dimensionalized as follows:

$$\begin{aligned}
C^* &= 1 \quad \text{on}\,\Gamma_1 \quad \text{and} \quad -D^*\nabla^* C^* \cdot \hat{\mathbf{n}} = 0 \quad \text{on}\,\partial\Omega\backslash\Gamma_1 \\
\phi_{\text{l}}^* &= \phi_{\text{l}}^{\text{bnd},*} \quad \text{on}\,\Gamma_3 \quad \text{and} \quad -\sigma_{\text{l}}^*\nabla^*\phi_{\text{l}}^* \cdot \hat{\mathbf{n}} = 0 \quad \text{on}\,\partial\Omega\backslash\Gamma_3 \\
\phi_{\text{s}}^* &= \phi_{\text{s}}^{\text{bnd},*} \quad \text{on}\,\Gamma_1 \quad \text{and} \quad -\sigma_{\text{s}}^*\nabla^*\phi_{\text{s}}^* \cdot \hat{\mathbf{n}} = 0 \quad \text{on}\,\partial\Omega\backslash\Gamma_1
\end{aligned} \tag{3.27}$$

and

$$\begin{aligned}
C^* &= 1 \quad \text{on}\,\Gamma_1 \quad \text{and} \quad -D^*\nabla^* C^* \cdot \hat{\mathbf{n}} = 0 \quad \text{on}\,\partial\Omega\backslash\Gamma_1 \\
-\sigma_{\text{l}}^*\nabla^*\phi_{\text{l}}^* \cdot \hat{\mathbf{n}} &= j^{\text{bnd},*} \quad \text{on}\,\Gamma_3 \quad \text{and} \quad -\sigma_{\text{l}}^*\nabla^*\phi_{\text{l}}^* \cdot \hat{\mathbf{n}} = 0 \quad \text{on}\,\partial\Omega\backslash\Gamma_3 \\
\phi_{\text{s}}^* &= \phi_{\text{s}}^{\text{bnd},*} \quad \text{on}\,\Gamma_1 \quad \text{and} \quad -\sigma_{\text{s}}^*\nabla^*\phi_{\text{s}}^* \cdot \hat{\mathbf{n}} = 0 \quad \text{on}\,\partial\Omega\backslash\Gamma_1
\end{aligned} \tag{3.28}$$

in which, the boundary values are converted to a dimensionless form according to:

$$\phi_{\mathrm{l}}^{\mathrm{bnd},*} = \frac{\phi_{\mathrm{l}}^{\mathrm{bnd}}}{\phi_0}; \quad \phi_{\mathrm{s}}^{\mathrm{bnd},*} = \frac{\phi_{\mathrm{s}}^{\mathrm{bnd}}}{\phi_0}; \quad j^{\mathrm{bnd},*} = \frac{j^{\mathrm{bnd}}}{i_0} \tag{3.29}$$

Furthermore, the dimensionless entropy generation rate, σ^* might be determined through diving the left-hand-side of Eq. (3.16) by the exchange entropy generation rate ($\mathrm{W\,K^{-1}m^{-3}}$) and is formulated as:

$$\begin{aligned}\sigma^* = \frac{\sigma}{a^0 i_0 \phi_0 / T} = \frac{\sigma}{\sigma^{\mathrm{exchange}}} = \theta_1 \varepsilon_{\mathrm{v}}^{\beta_1} \nabla^* C^* \cdot \nabla^* \mu^* + \frac{\theta_2}{1+\theta_3} \varepsilon_{\mathrm{l}}^{\beta_2} \nabla^* \phi_{\mathrm{l}}^* \cdot \nabla^* \phi_{\mathrm{l}}^* \\ + \frac{\theta_2 \theta_3}{1+\theta_3} \varepsilon_{\mathrm{s}}^{\beta_3} \nabla^* \phi_{\mathrm{s}}^* \cdot \nabla^* \phi_{\mathrm{s}}^* \pm \varepsilon_{\mathrm{s}}^{\beta_4} \mu^* j_{\mathrm{src}}^* - \varepsilon_{\mathrm{s}}^{\beta_4} \phi_{\mathrm{l}}^* j_{\mathrm{src}}^* + \varepsilon_{\mathrm{s}}^{\beta_4} \phi_{\mathrm{s}}^* j_{\mathrm{src}}^*\end{aligned} \tag{3.30}$$

in which the exchange entropy generation rate is defined as $\sigma^{\mathrm{exchange}} = a^0 i_0 \phi_0 / T$. The individual contributions, σ_{mt}, σ_{it}, σ_{et}, and σ_{rx}, could be non-dimensionalized to σ_{mt}^*, σ_{it}^*, σ_{et}^*, and σ_{rx}^* after dividing by the exchange entropy production. Finally, the total dimensionless entropy generation is computed as:

$$P^* = \int_{\Omega^*} \sigma^* d\Omega^* \tag{3.31}$$

where Ω^* represents the non-dimensional domain. The related dimensionless breakdowns, P_{mt}^*, P_{it}^*, P_{et}^*, and P_{rx}^*, are evaluated by a similar integration.

3.4 Optimization algorithm

In the present study, a TO technique is used to seek the best spatial distribution of constituent, including solid phase, electrolyte phase, and voids, in the given design domain. By controlling the local volume fraction of each constituent, the local effective properties of the system (i.e., diffusivity, ionic conductivity, electric conductivity, and active specific surface area) might be adjusted in a way that provides the best compromise between the transport and rate processes. Such a balance could result in a better system performance. As aforementioned, a better performance might be interpreted in two ways: (1) in an "overpotential-based ERD system", an optimized system should have a higher total electrochemical reaction rate and (2) in a "current-based ERD system", an optimized system should lead into a lower energy loss (or lower total overpotential). Hence, for each system setting, a unique formulation is used as the optimization objective. However, the optimization procedure for both

problem formulations are same. Therefore, in this section, first, the two problem formulations are described and next the common TO algorithm is briefly explained.

TO outperforms other mathematical optimization methods, such as parametric optimization, because of higher degrees of freedom provided by this technique [74–76]. Although such a substantial increase in degrees of freedom makes the algorithm more sophisticated, it possibly allows obtaining a much better result. Advantages of TO over conventional optimization methods are comprehensively studied in the literature and interested readers may refer to a previous publication of our group [77] or the works of other research groups [22, 78, 79]. According to TO formalism, the optimization is defined as a material allocation problem in a prescribed design domain. A so called "density method" [16] is used to describe the local volume fractions. Pursuant to this method, at any position, $\mathbf{x}$, in the design domain, Ω, the volume fraction of each constituent is a continuous function changing between 0 and 1 ($0 \leq \varepsilon_\mathrm{l}(\mathbf{x}) \,\mathrm{and}\, \varepsilon_\mathrm{s}(\mathbf{x}) \,\mathrm{and}\, \varepsilon_\mathrm{v}(\mathbf{x}) \leq 1$) with the restriction that $\varepsilon_\mathrm{l}(\mathbf{x}) + \varepsilon_\mathrm{s}(\mathbf{x}) + \varepsilon_\mathrm{v}(\mathbf{x}) = 1$.

3.4.1 Problem formulation: Current-based ERD system

Since the current density that passes the system boundaries is given in a "current-based ERD system", the total rate of electrochemical reaction is prescribed in this system setting as an input. In this formulation, the goal is to minimize the system total overpotential for a certain reaction rate. Total overpotential indicates the excess required potential to drive a Faradaic reaction at a specific current density. Hence, it is favorable to reduce the total overpotential in an electrochemical system for a given current density. Minimization of total overpotential will lead to maximization of output power for a power generating system and will reduce the input power for a power consuming system. Based on these explanations, the optimization problem is defined as:

$$
\begin{aligned}
\min_{\varepsilon_\mathrm{l},\varepsilon_\mathrm{s}} \quad & F_{\mathrm{obj},1} = |\eta^{\mathrm{tot},*}| = \left|(\phi_\mathrm{s}^*|_{\Gamma_1} - \phi_\mathrm{l}^*|_{\Gamma_3} - E_\mathrm{eq}^*)\right| \\
\text{s.t.} \quad & \text{Eqs. (3.21) to (3.23)} \\
& \varepsilon_\mathrm{l}^{\min} \leq \varepsilon_\mathrm{l}(\mathbf{x}^*) \leq \varepsilon_\mathrm{l}^{\max} \quad \forall \mathbf{x}^* \in \Omega^* \\
& \varepsilon_\mathrm{s}^{\min} \leq \varepsilon_\mathrm{s}(\mathbf{x}^*) \leq \varepsilon_\mathrm{s}^{\max} \quad \forall \mathbf{x}^* \in \Omega^* \\
& \varepsilon_\mathrm{l}(\mathbf{x}^*) + \varepsilon_\mathrm{s}(\mathbf{x}^*) + \varepsilon_\mathrm{v}(\mathbf{x}^*) = 1 \quad \forall \mathbf{x}^* \in \Omega^*
\end{aligned}
\tag{3.32}
$$

in which $F_{\mathrm{obj},1}$ is the objective function and $E^*_{\mathrm{eq}} = \frac{E_{\mathrm{eq}}}{\phi_0}$ is non-dimensional equilibrium potential. Knowing that the total overpotential for a reduction reaction is negative, the absolute value of overpotential is used in the objective function definition. It is noteworthy that in an ideal condition, the reactor potential (i.e., $\phi^*_{\mathrm{s}}|_{\Gamma_1} - \phi^*_{\mathrm{l}}|_{\Gamma_3}$) should be as close as possible to the thermodynamic equilibrium potential (E^*_{eq}). Volume fractions of electrolyte and solid phases are considered as design variables in this optimization problem. These volume fractions are the system parameters that are required for solving the system of governing equations. Since the summation of all volume fractions should be equal to unity, by knowing two of them, the third one might be calculated automatically. Hence, the porosity (volume fraction of voids) is calculated based on the values of two design variables. Moreover, the optimization problem is constrained by the governing equations of the system. As an additional constraint, it is assumed that the local volume fractions of the electrolyte and solid phases could only alter within a predefined range. These ranges are given by $\varepsilon_{\mathrm{l}}^{\min}$, $\varepsilon_{\mathrm{l}}^{\max}$, $\varepsilon_{\mathrm{s}}^{\min}$, and $\varepsilon_{\mathrm{s}}^{\max}$ that are minimum and maximum allowed volume fractions of electrolyte and solid phases, respectively.

3.4.2 Problem formulation: Overpotential-based ERD system

In an "overpotential-based ERD system", the total overpotential ($\eta^{\mathrm{tot}} = \phi_{\mathrm{s}}|_{\Gamma_1} - \phi_{\mathrm{l}}|_{\Gamma_3}$) is given as the problem input through the B.C.s and the total electrochemical reaction rate might be calculated by solving the governing equations. Total electrochemical reaction rate is equivalent to the total current that passes the system boundary. Since the system is electroneutral, the total amount of negative and positive electric charges that leaves (or come into) the system is equal. Hence, in this system setting, the aim is to maximize the total electrochemical reaction rate. Increasing the electrochemical reaction rate (or system current) at a given overpotential is equivalent to maximizing the output power of the system (for a power generating system). Improving the active specific surface area and discharge of products from the reaction sites will boost the reaction rate. This could be obtained by increasing the volume fractions of electrolyte and solid phases. However, to keep the reaction rate high, it is necessary to assure sufficient reactant delivery to the reaction sites through pores. By increasing the volume fractions of electrolyte and solid phases, the volume fraction of voids will consequently be reduced. This means that the mass transport resistance will be increased and the delivery of reactant spices will be more complicated. Therefore, there should be a trade-off between reactant consumption and delivery rates. This trade-off leads to an optimization problem that might be addressed by

controlling the local composition of the porous reactor. This optimization problem is mathematically indicated in a non-dimensional form as:

$$\begin{aligned}
\max_{\varepsilon_{\mathrm{l}},\varepsilon_{\mathrm{s}}} \quad & F_{\mathrm{obj},2} = \int_{\Omega^*} \left| \varepsilon_{\mathrm{s}}^{\beta_4} j_{\mathrm{src}}^* \right| d\Omega^* \\
\text{s.t.} \quad & \text{Eqs. (3.21) to (3.23)} \\
& \varepsilon_{\mathrm{l}}^{\min} \leq \varepsilon_{\mathrm{l}}(\mathbf{x}^*) \leq \varepsilon_{\mathrm{l}}^{\max} \quad \forall \mathbf{x}^* \in \Omega^* \\
& \varepsilon_{\mathrm{s}}^{\min} \leq \varepsilon_{\mathrm{s}}(\mathbf{x}^*) \leq \varepsilon_{\mathrm{s}}^{\max} \quad \forall \mathbf{x}^* \in \Omega^* \\
& \varepsilon_{\mathrm{l}}(\mathbf{x}^*) + \varepsilon_{\mathrm{s}}(\mathbf{x}^*) + \varepsilon_{\mathrm{v}}(\mathbf{x}^*) = 1 \quad \forall \mathbf{x}^* \in \Omega^*
\end{aligned} \tag{3.33}$$

where $F_{\mathrm{obj},2}$ is the objective function. Given the fact that j_{src}^* is negative in case of a reduction reaction, the absolute value of reaction rate is used in this equation to generalize the applicability of the objective function for any kind of electrochemical reaction. As represented in Eq. (3.33), the goal is to maximize the overall dimensionless rate of electrochemical reaction over the entire domain. The term $a^* j_{\mathrm{src}}^*$ is the local dimensionless rate of reaction and by integrating it over the non-dimensional domain, the overall value might be computed. Evidently, this objective function could be expressed in a dimensional form with the corresponding dimensional parameters. However, since this study focuses on a non-dimensional analysis of the ERD system, the objective function is also expressed in a dimensionless form.

3.4.3 Numerical implementation

In this research work, COMSOL Multiphysics ® (version 5.6) is used to solve the governing equations and to implement the optimization procedure. The calculation domain, system parameters, governing equations, and B.C.s are specified in the software. In the first step of the optimization process, the design variables are initialized and Eqs. (3.21) to (3.23) are solved using a finite element method. By solving these equations, the distribution of concentration, electrolyte potential, and solid potential are obtained. Next, the objective function is evaluated according to $F_{\mathrm{obj},1}$ or $F_{\mathrm{obj},2}$. The choice of objective function depends on the system of interest. Afterward, the sensitivity (or gradient) of objective function is computed with respect to the design variables using an adjoint state method [80]. Since the adjoint method is independent of the number of the design variables, it is computationally much cheaper than other approaches, such as the forward method. Therefore, it is very useful for optimization problems which contain numerous decision variables. Next, the design solutions are regularized using a Helmholtz filter [81] and hyperbolic tangent project [82]. These

regularization helps to prevent checkerboard pattern [16], which is a common challenge in TO. This problem has been addressed in the literature comprehensively and the readers are referred to the papers in this field, such as [81, 83, 84], for further information. In the next step, the design variables are updated locally in throughout the entire calculation domain. The updating procedure is conducted using a globally convergent method of moving asymptotes (GCMMA) algorithm [85]. GCMMA is an efficient algorithm for handling problems with abundant design variables. As a post-processing step, the local and total entropy production rate are also calculated. This step is separate from the optimization process and the entropy generation is assessed in each iteration of optimization to track the changes. The explained process is repeated until the convergence criterion (in this case, maximum number of iteration) is reached. The optimization procedure is summarized as follows:

Step 1: The calculation domain, governing equations, and B.C.s are defined and the design variables are initialized.

Step 2: The ERD system is solved based on Eqs. (3.21) to (3.23) and the objective function is evaluated using Eq. (3.32) or (3.33).

Step 3: The gradient of objective function with respect to the design variables is evaluated using the adjoint method.

Step 4: The design solutions are regularized using a Helmholtz filter and a hyperbolic tangent projection to obtain smoothed solutions.

Step 5: The design variables are updated using the GCMMA algorithm.

Step 6: The local and global entropy generation rates are evaluated using Eqs. (3.30) and (3.31).

Step 7: If the convergence criteria are met, the iteration is stopped. Otherwise, steps 2 to 6 are repeated.

3.5 Results and discussion

This section presents the results of numerical calculations. The design domain is a square with a 1×1 non-dimensional size (see Fig. 3.1). The optimization process is conducted under several conditions, as indicated in Table 3.1 for both minimization and maximization problems. $10,000$ structured quad meshes are used for numerical calculations. A mesh dependency assessment was conducted prior to optimization to ensure that the finite element method results were independent of the chosen

Table 3.1: Values/ranges of system dimensionless parameters

Parameter	Value/Range	Parameter	Value/Range
θ_1	2 - 5	E^*_{eq}	0
θ_2	20 - 50	$\phi_{\text{s}}^{\text{bnd},*}$	0
θ_3	5 - 10	$\phi_{\text{l}}^{\text{bnd},*}$	1 - 9
$\beta_1, \beta_2, \beta_3$	2	$j^{\text{bnd},*}$	5 - 30
β_4	1	$\varepsilon_{\text{l}}^{\text{min}}, \varepsilon_{\text{s}}^{\text{min}}$	0
α	1	$\varepsilon_{\text{l}}^{\text{max}}, \varepsilon_{\text{s}}^{\text{max}}$	0.5

mesh size. Given that the volume fractions of electrolyte and solid phases are controlled at each grid in the optimization process, the total number of design variables is $20,000$. Each optimization is carried out for 300 iterations and necessary measures are taken to guarantee sufficient convergence with this number of iterations.

3.5.1 Current-based ERD system

As explained before, in this problem setting, the objective is to reduce the total overpotential of the system. The total overpotential refers to the amount of energy necessary for an electrochemical reaction to proceed at a given conversion rate (current density). Figs. 3.2 and 3.3 depict the optimized distribution of constituents under various system settings. The optimal spatial distribution of electrolyte, solid, and void phases are illustrated for two different dimensionless current densities ($j^{\text{bnd},*}$). In each figure, the optimized results for four different combinations of dimensionless numbers (θ_1 to θ_3) are shown to reflect the impact of each number on the final optimization outcome. Analyzing and contrasting the results from each system configuration elucidates the impact of diverse transport, rate, and characteristic parameters on the ultimate optimal structure. Under all conditions, the optimization process led to complex tree-root-like shapes. Comparing the final objective function values of each scenario across Figs. 3.2 and 3.3 shows that in general, a higher working current density corresponds to a higher total overpotential. For instance, as $j^{\text{bnd},*}$ is changed from 30 to 5 at the first θs settings (Fig. 3.2a vs. Fig. 3.3a), the non-dimensional total overpotential is altered from 4.64 to 0.589. This is due to the intrinsic relationship between current density and overpotential in an electrochemical system. The higher the working current density of the system, the higher total overpotential. The initial layout used for all the cases reported in these two figures are the same (uniform $\varepsilon_{\text{l}} = 0.25$ and $\varepsilon_{\text{s}} = 0.25$). However, it is evident that the solid volume fraction in final layouts of Fig. 3.3 ($j^{\text{bnd},*} = 5$) is higher than those of Fig. 3.2 ($j^{\text{bnd},*} = 30$). At a

low current density, the activation overpotential is the major contributor to the total overpotential. Therefore, it is favorable to increase the average volume fraction of the solid phase. On the contrary, at a high current density ($j^{\mathrm{bnd},*} = 30$), where sluggish mass transport is dominant, larger diffusion channels are preferred to assure a sufficient reactant delivery. As it can be understood from Eq. (3.25), the system mass transport is controlled by dimensionless number θ_1. Therefore, changing the value of this parameter should affect the optimized distribution of voids. As it can be seen in Fig. 3.2, decreasing the value of this parameter influences the optimized porosity distribution in the ERD system. However, this impact is more significant at a high current density because of a serious mass transport limitation under this operational condition. The same changes in θ_1 at a low current density cause a slight change in the final void distribution. This is due to the fact that at $j^{\mathrm{bnd},*} = 5$, the concentration overpotential is small and a variation of θ_1 could be compensated by a tiny change in the optimized layout (see Figs. 3.3a and 3.3b).

In addition, dimensionless number θ_2 dictates the ohmic conductivity of the system. Hence, diminishing this parameter is associated with new layouts (Figs. 3.2c and 3.3c) which provide a better pathway for conduction of electric charges. Finally, decreasing parameter θ_3 boosts the ionic conductivity of the system in comparison to the electric conductivity. In many real applications, the electrochemical devices suffer from a high ionic resistance, but not electric one. Therefore, decreasing θ_3 (by keeping θ_2 constant) improves the balance between electron and cation transport in the ERD system. Consequently, a lower total overpotential could be achieved after optimization with a smaller θ_3. For $j^{\mathrm{bnd},*} = 5$, this means a less requirement for the electrolyte phase (see Fig. 3.3d). The optimized layouts shown in Figs. 3.2 and 3.3 reduce the overpotential of the ERD system between 39.6% and 64.2% compared to the initial uniform configuration (before optimization). The improvements owe to the heterogeneous structures obtained from TO. These tree-root-like structures facilitate diffusion of reactant species and electric charges while augmenting the reaction rate throughout the system. For instance, in the case of mass diffusion, all optimized structures involve some primary diffusion channels together with secondary channels. The primary channels are extended throughout the system in x-direction, which facilitates the delivery of the reactant material to the regions far from the inlet boundary ($\partial\Omega_1$). Evidently, the system of interest in this study is symmetrical with respect to the y-axis (see Fig. 3.1). Therefore, it is necessary to direct the reactant in x-direction, especially at a high $j^{\mathrm{bnd},*}$, which mass transport limitation is more severe. Additionally, the secondary channels connected to the primary ones help a better

dissemination of the reactant over the entire porous reactor. On a similar note, the electrolyte and solid phases are also arranged in a way that give a greater access to electric charge currents. Since the left boundary is isolated to the transport of ions, the electrolyte phase is more concentrated on the right half of the reactor. It is notable that the solid phase not only transfers the produced electrons to the outside but also provides the necessary surface area for the reaction. Therefore, both these roles are reflected in the optimal layout. The heterogeneous distribution of materials within the ERD system strikes a balance between multiple transport and rate processes, consequently leading to enhanced overall performance.

To further analyze the optimization process, the scenario with $\theta_1 = 5$, $\theta_2 = 50$, and $\theta_3 = 10$ is assessed in details. The convergence history of the optimization process is plotted in Fig. 3.4a along with the system layout at two intermediate iterations (iteration number 20 and 70). As expected, during the optimization, the objective function monotonically decreased. A sharp decline is observed at the beginning, which is due to the higher sensitivity (or gradient) of the objective function in these iterations. As the optimization proceeds, the change rate slows down. The objective function (total overpotential) reaches a constant value of 4.64 after around 125 iterations, where the changes in objective function drops under 0.01% afterwards. This assures a confident convergence. Fig. 3.4b demonstrates the current density-overpotential (I-V) relationship of the system before and after optimization. Indeed, an I-V curve shows the performance of the system for a wide range of current densities. To demonstrate how the results of optimization at various current densities are different, the I-V curves are plotted for two structures obtained from optimization at $j^{\mathrm{bnd},*}$ equal to 30 (point A on the plot) and 5 (point A on the plot). From the first optimization, point A is shifted to A' and the structure shown in Fig. 3.2a is obtained. Then, this optimal layout is used to plot the I-V curve over a range of $5 \leq j^{\mathrm{bnd},*} \leq 30$. A similar procedure has been conducted for optimization at point B. In both cases, the optimal I-V curve is vertically shifted downward (vertical optimization). However, the final I-V characteristics of the two optimal structures are different. Evidently, at medium and high current densities ($j^{\mathrm{bnd},*} \geq 15$), I-V curve of A' is superior. However, in low current density regions ($j^{\mathrm{bnd},*} \leq 5$), the I-V characteristics of B' surpasses that of the other optimization. The reason for this difference is when the optimization is performed at a high current density, the optimal layout comes with large diffusion channels (see Fig. 3.2a). At $j^{\mathrm{bnd},*} \geq 15$, the concentration depletion is the prevailing mechanism. Hence, larger diffusion channels (higher average porosity) is beneficial to make a compromise between the competing processes. On the other hand, at

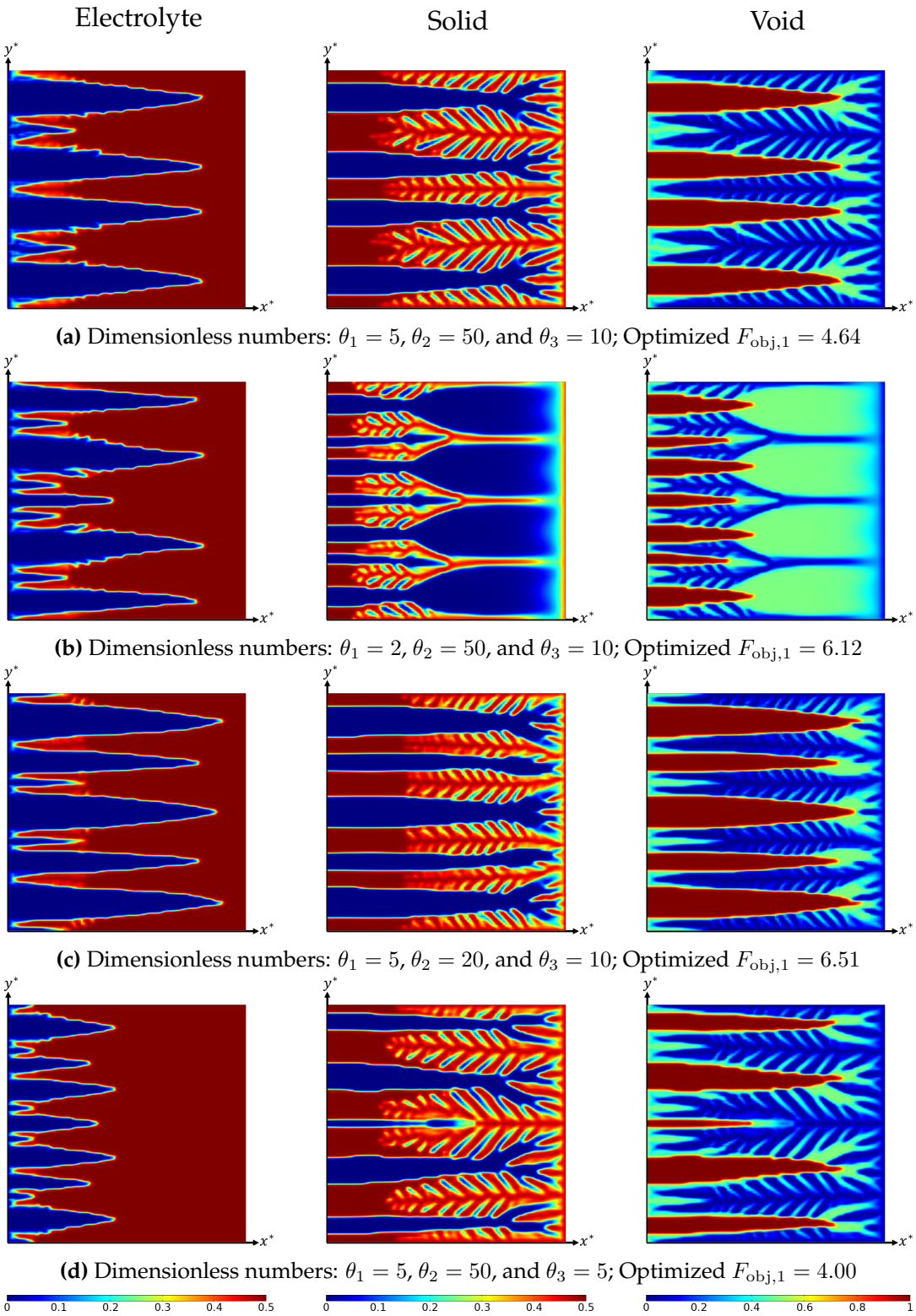

(a) Dimensionless numbers: $\theta_1 = 5$, $\theta_2 = 50$, and $\theta_3 = 10$; Optimized $F_{\text{obj},1} = 4.64$

(b) Dimensionless numbers: $\theta_1 = 2$, $\theta_2 = 50$, and $\theta_3 = 10$; Optimized $F_{\text{obj},1} = 6.12$

(c) Dimensionless numbers: $\theta_1 = 5$, $\theta_2 = 20$, and $\theta_3 = 10$; Optimized $F_{\text{obj},1} = 6.51$

(d) Dimensionless numbers: $\theta_1 = 5$, $\theta_2 = 50$, and $\theta_3 = 5$; Optimized $F_{\text{obj},1} = 4.00$

Figure 3.2: Optimized volume fraction distribution of electrolyte, solid, and void phases under various system settings at $j^{\text{bnd},*} = 30$; Improvement of optimized layout compared to initial uniform distribution is: (a) 49.5%, (b) 52.5%, (c) 64.2%, and (d) 39.6%

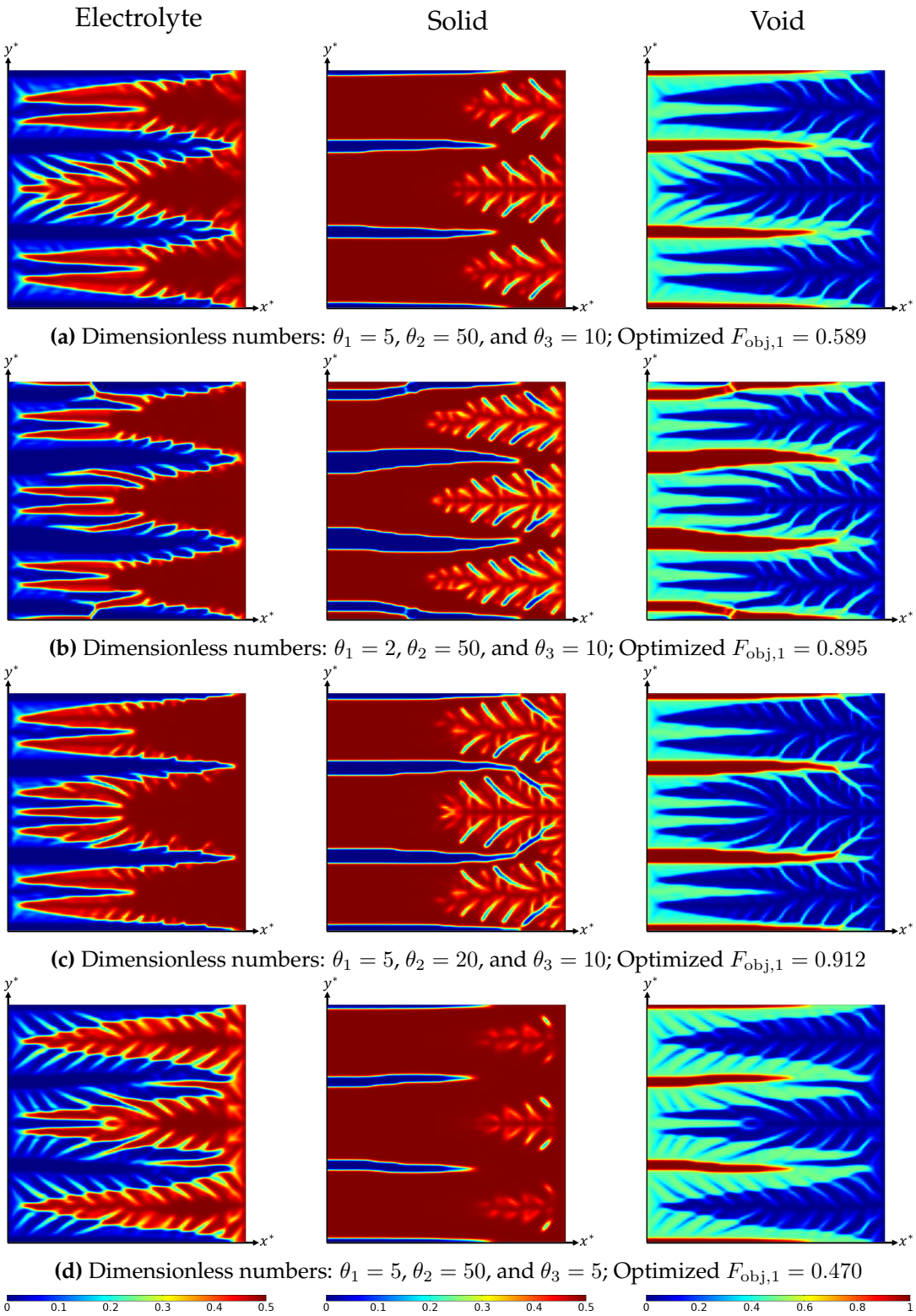

(a) Dimensionless numbers: $\theta_1 = 5$, $\theta_2 = 50$, and $\theta_3 = 10$; Optimized $F_{\text{obj},1} = 0.589$

(b) Dimensionless numbers: $\theta_1 = 2$, $\theta_2 = 50$, and $\theta_3 = 10$; Optimized $F_{\text{obj},1} = 0.895$

(c) Dimensionless numbers: $\theta_1 = 5$, $\theta_2 = 20$, and $\theta_3 = 10$; Optimized $F_{\text{obj},1} = 0.912$

(d) Dimensionless numbers: $\theta_1 = 5$, $\theta_2 = 50$, and $\theta_3 = 5$; Optimized $F_{\text{obj},1} = 0.470$

Figure 3.3: Optimized volume fraction distribution of electrolyte, solid, and void phases under various system settings at $j^{\text{bnd},*} = 5$; Improvement of optimized layout compared to initial uniform distribution is: (a) 59.1%, (b) 48.8%, (c) 57.6%, and (d) 61.4%

$j^{\mathrm{bnd},*} \leq 10$, sufficient reactant is supplied to the reaction site. Hence, a higher volume fraction of the solid phase is needed to increase the effective electrochemical surface area and consequently decrease the system total overpotential. What stands out in this figure is that when optimizing an electrochemical system at a specific working point, the optimal result might not be equally good over the entire I-V curve. Therefore, the optimization point should be adjusted according to the application and purposes. The average effective transport coefficients of the system before and after optimization are compared in Table 3.2. The transport properties after optimization are divided by the relevant exchange properties (D^{exchange} and $\sigma_{\mathrm{ohm}}^{\mathrm{exchange}}$) to obtain the dimensionless properties. As it can be seen in this table, all transport properties are considerably enhanced after optimization. The only exception is average diffusivity after optimization at $j^{\mathrm{bnd},*} = 5$. Since the overall reaction rate is low at $j^{\mathrm{bnd},*} = 5$, the reactant delivery is sufficient even at a relatively lower effective diffusivity. Therefore, TO favors to reduce the porosity (effective diffusivity) and instead increases the volume fraction of solid phase to augment the electrochemical surface area.

To clarify the benefits of a heterogeneous structure, the optimal layout (obtained from optimization of $\theta_1 = 5$, $\theta_2 = 50$, and $\theta_3 = 10$ at $j^{\mathrm{bnd},*} = 30$) is compared to two uniform distributions. As aforementioned, the optimization process started with a homogeneous material distribution in which volume fractions of both electrolyte and solid phases were 0.25. In this case, the non-dimensional total overpotential is 9.18. After optimization, this value is declined to 4.64, which shows a 49.5% reduction in system losses. Such a substantial improvement proves the advantage of the topologically-optimized layout over the uniform distribution. In the final optimum layout, the average volume fraction of various phases are $\varepsilon_{\mathrm{l}}^{\mathrm{ave}} = 0.264$, $\varepsilon_{\mathrm{s}}^{\mathrm{ave}} = 0.313$, and $\varepsilon_{\mathrm{v}}^{\mathrm{ave}} = 0.423$ as shown in Table 3.2. Considering these average values with a uniform distribution gives a total overpotential of $|\eta^{\mathrm{tot},*}| = 9.83$, which is considerably higher than 4.64. In fact, it is even higher than that of before optimization. This reveals that the placement of constituents is as important as their overall average amounts. In other words, TO adjusts the overall volume fraction of constituents as well as their distribution in a manner to reduce the total overpotential.

A closer inspection of system evolution is required to obtain a deeper grasp about how TO lead to a better design solution. To do so, some of the system parameters are traced during optimization. Since the system is symmetrical, the parameters of interest are projected on x-axis to reduce their distribution to 1D for the sake of simplicity. The projected dimensionless concentration (C^*) and current source ($|a^* j_{\mathrm{src}}^*|$) along with entropy production evolution are set out in Fig. 3.5. What stands out in

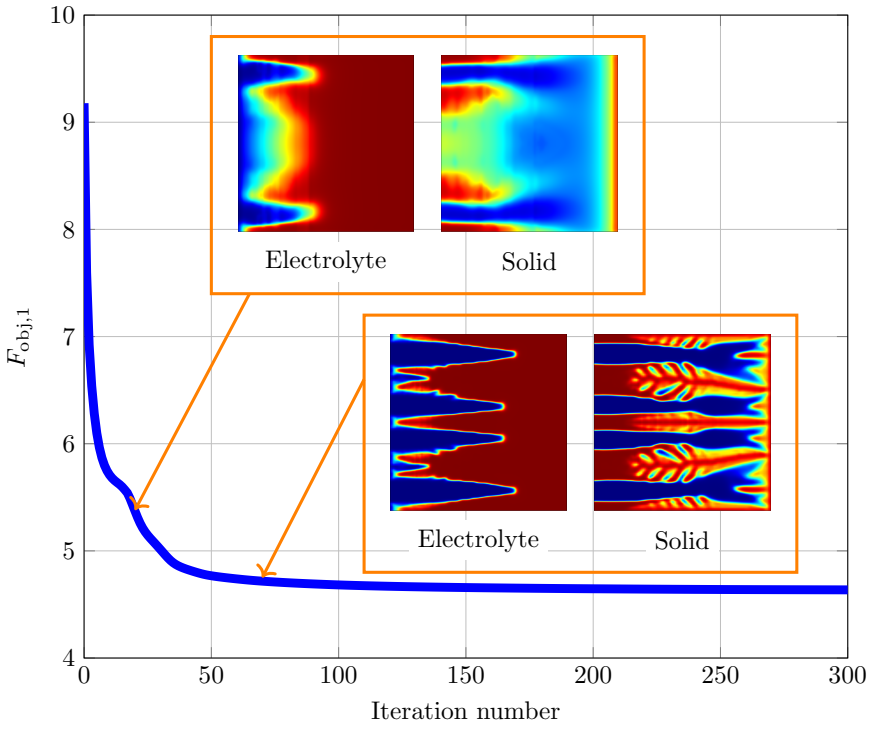

(a) Convergence history of optimization at $j^{\mathrm{bnd},*} = 30$

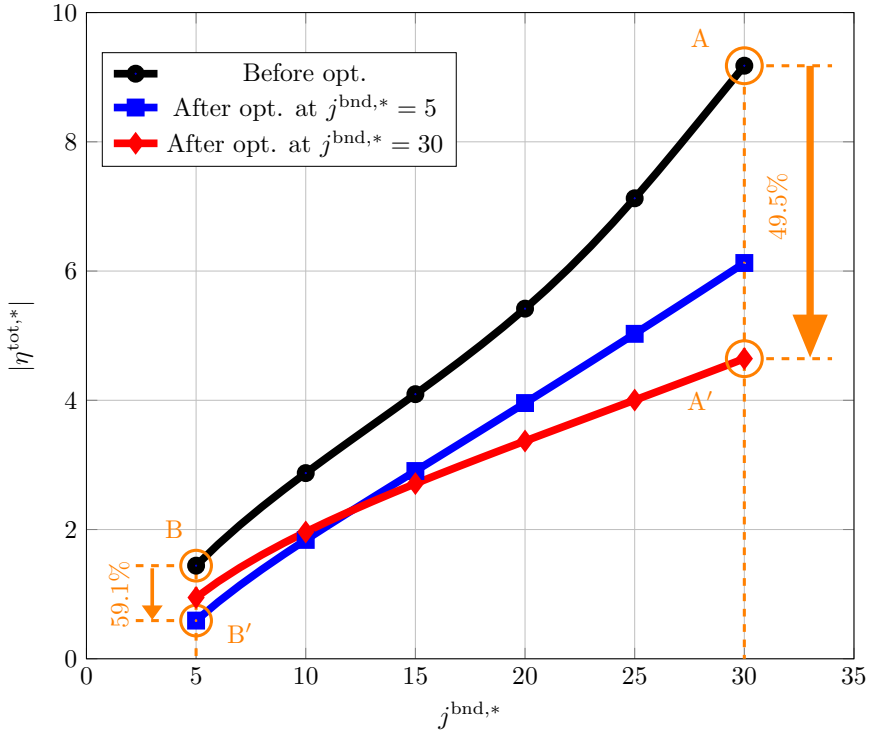

(b) System I-V curves before and after optimization

Figure 3.4: (a) Convergence history and (b) I-V curves for $\theta_1 = 5$, $\theta_2 = 50$, and $\theta_3 = 10$

Table 3.2: Average values of dimensionless transport properties and volume fractions before and after optimization for $\theta_1 = 5$, $\theta_2 = 50$, and $\theta_3 = 10$; the values in parentheses shows the changes with respect to the before optimization case

Optimization	$D^{*,\text{ave}}$	$\sigma_\text{l}^{*,\text{ave}}$	$\sigma_\text{s}^{*,\text{ave}}$	$\varepsilon_\text{l}^{\text{ave}}$	$\varepsilon_\text{s}^{\text{ave}}$	$\varepsilon_\text{v}^{\text{ave}}$
Before	1.25 (-)	0.284 (-)	2.84 (-)	0.25	0.25	0.5
After - $j^{\text{bnd},*} = 30$	1.62 (+29.6%)	0.679 (+139%)	5.05 (+77.8%)	0.264	0.313	0.423
After - $j^{\text{bnd},*} = 5$	0.766 (-38.7%)	0.537 (+89.1%)	9.78 (+244%)	0.274	0.446	0.280

Fig. 3.5a is during the optimization process, the reactant concentration is elevated in the system. The concentration at $x^* = 1$ is increased by two orders of magnitude after the optimization. This is attributed to a better porosity distribution that assist delivery of reactant to the regions far from the system inlet. The emerged diffusion channels in x-direction prevent significant concentration overpotential. This is especially essential for high operational current densities where mass transport limitation is dominant. What is striking about these results is that the increase in concentration occurs in a condition where the average porosity in the optimal structure (0.423) is lower than the initial one (0.5). Checking the general trend of projected current source, that is depicted in Fig. 3.5b, shows that the optimization algorithm favors design solutions with a more uniform current source distribution. This means that to lessen the total overpotential, it is necessary to scatter the electrochemical reaction all over the ERD system. From a global standpoint, spreading the reaction throughout the design domain assists to reduce the entropy that is generated in the system. Fig. 3.5c illustrates the changing progress of dimensionless total entropy generation, P^*, in the course of optimization along with local distribution at some selected iteration numbers. As it can be confirmed by both local and global analysis, the total entropy generation rate is decreasing as the optimization proceeds. This observation is in full agreement with the principle of EGM [43]. Hence, for a minimization problem set-up, the total overpotential could be substituted with the total entropy generation as an objective function. It will be later discussed that this replacement does not hold for a maximization formulation. Since the entropy generation rate is reduced after optimization, it can be concluded that the second law efficiency of the system is increased. To understand how the entropy production reduced by TO, the distribution of projected entropy is plotted in Fig. 3.5d for some iterations. It can be seen that the entropy curve at iteration zero is at a higher level than other iterations. After some early changes in the system layout, the entropy curve shifted

downward considerably. This huge drop in entropy generation happened thanks to an improvement in transport processes. In the subsequent steps, the optimization algorithm attempted to further reduce entropy generation rate by providing a more uniform distribution of entropy production throughout the system (see the curves for iterations 35, 50, and 300 in Fig. 3.5d). A more uniform distribution of entropy production might (but not necessarily) be helpful in reducing the total entropy production and consequently increasing the system efficiency. This principle is known as Equipartition of Entropy Production (EoEP) [86, 87] in the literature. It has been applied to many heat exchanger and membrane systems [88–95].

These behaviors can be observed in the individual entropy contribution by each process. Fig. 3.6 illustrates the breakdown of entropy production by various processes, including mass diffusion, ion transfer by electrolyte phase, electron transfer by solid phase, and electrochemical reaction. The projected distribution of entropy production by each mechanism is shown in this figure. From these breakdowns, one can understand that the entropy curves of transport processes (Fig. 3.6a to 3.6c) lay quickly down hinged at one boundary. Especially, the entropy production by ion transport (Fig. 3.6b) shows a significant drop. This is because of the enhanced pathways formed by TO for transport of reactant, ion, and electron. Meanwhile, the flattening of these entropy curves causes a sharp decrease in total entropy production, as shown in Fig. 3.5c. The behavior of entropy contribution by the electrochemical reaction is, however, different from that of transport phenomena. According to the curves of Fig. 3.6d, the entropy production distribution becomes more equipartitioned during the optimization. This is mainly because of a more uniform distribution of the current source that is discussed before. To achieve this flatness, the entropy production in part of the system is reduced, while it is increased in the other part. Therefore, the total amount of entropy production by the reaction does not change very much. This could be confirmed from the column chart demonstrated in Fig. 3.6e. This chart compares the total entropy production by each process. It can be seen that the contribution by electrochemical reaction stays almost constant during the optimization process. The slight reduction is related to the more equipartitioned distribution of entropy generation, which prevents excess dissipation caused by non-uniformity of thermodynamics driving force in the system [86, 87]. Since the total reaction rate is given by the system current density, most entropy production by the reaction is the inevitable entropy generation that cannot be prevented in a finite time/size context [18, 77]. Based on the data of Fig. 3.6e, the electron transport has

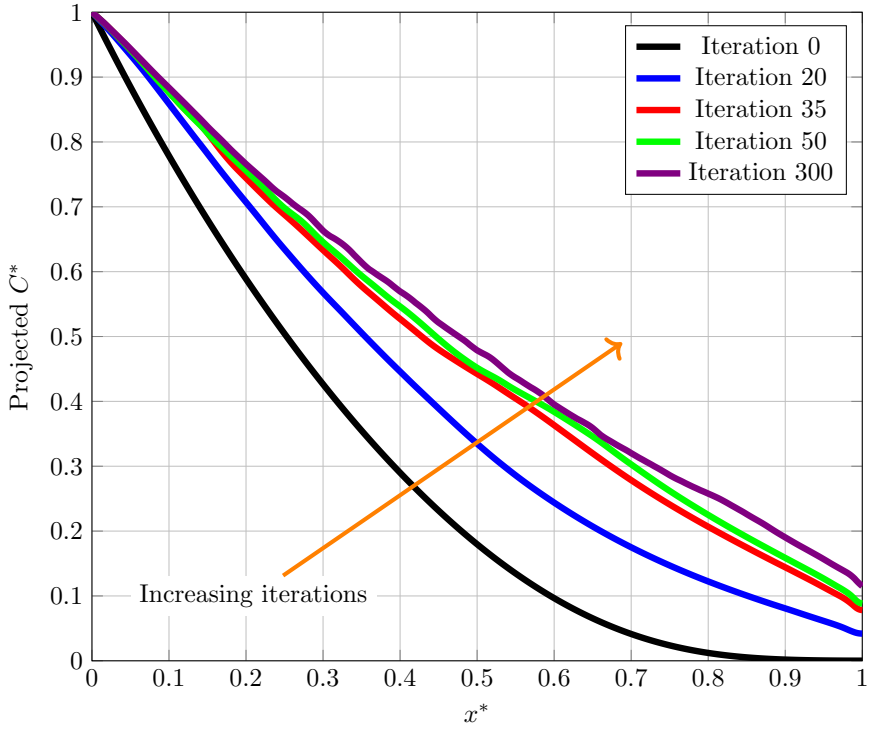

(a) Evolution of projected concentration

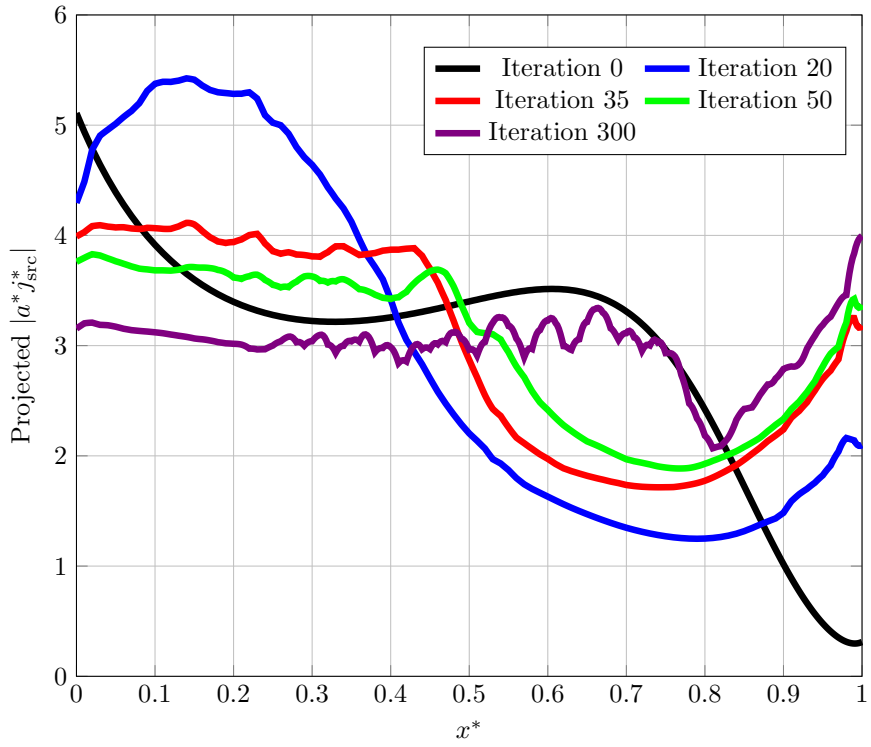

(b) Distribution of projected current source

the smallest contribution to the total entropy compared to other transport phenomena. This is because of the high intrinsic electronic conductivity of the system.

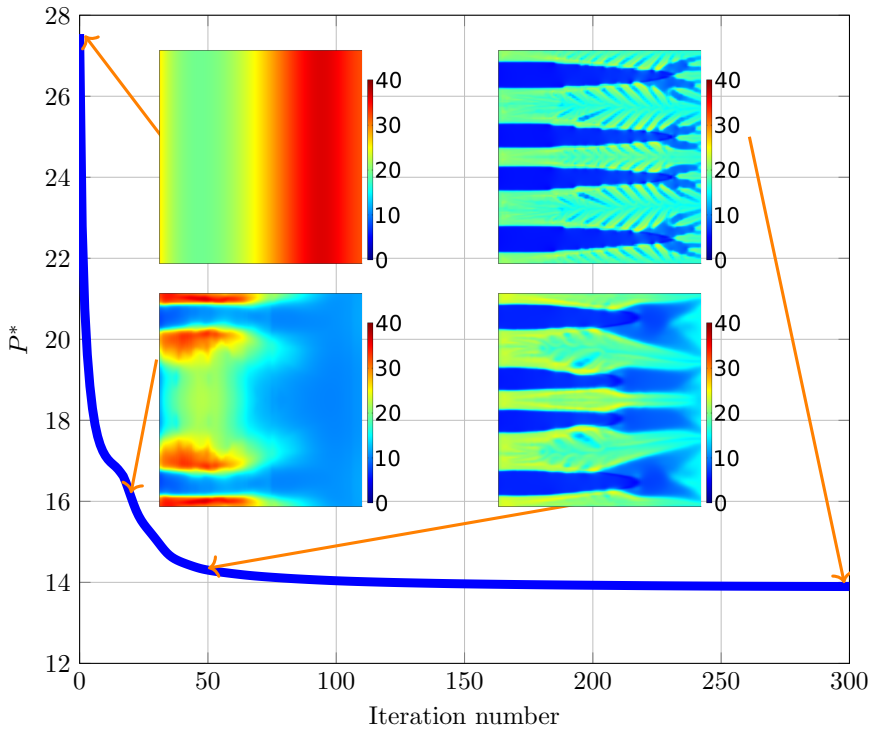

(c) Convergence history of dimensionless local and global entropy

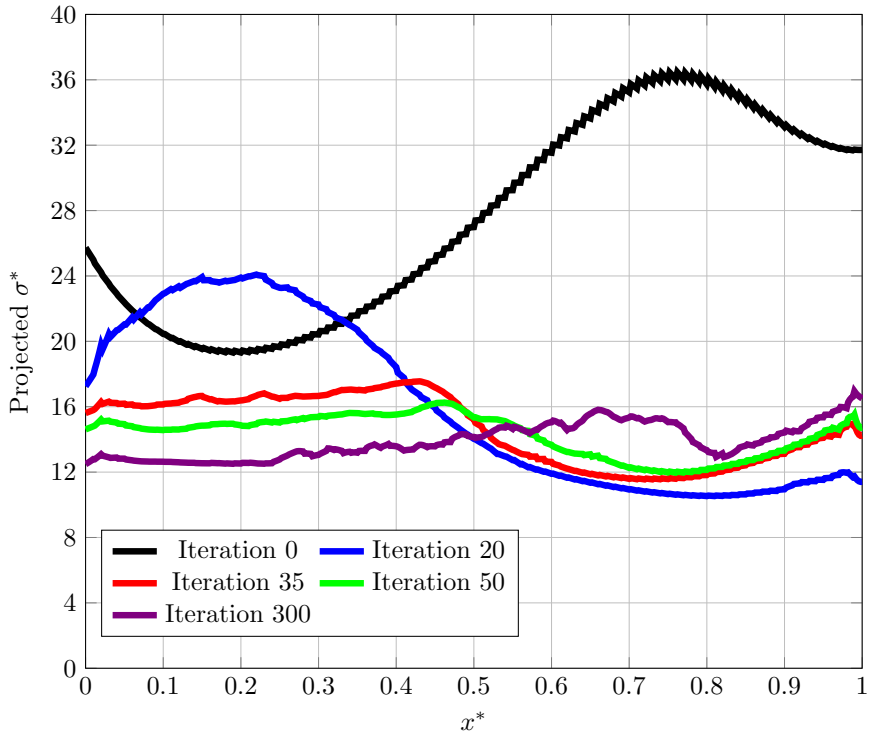

(d) Distribution of projected dimensionless entropy generation

Figure 3.5: (a) Projected concentration, (b) projected current source, (c) entropy convergence history, and (d) projected entropy during optimization process for $\theta_1 = 5$, $\theta_2 = 50$, and $\theta_3 = 10$ at $j^{\mathrm{bnd},*} = 30$

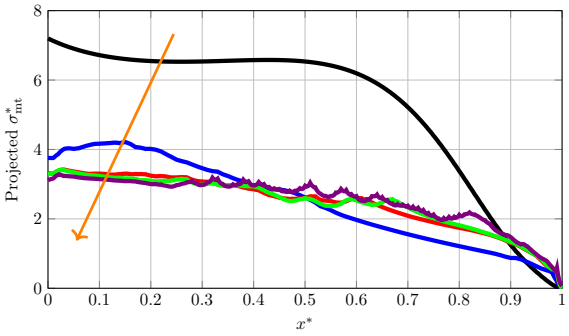

(a) Distribution of entropy generation by mass transport

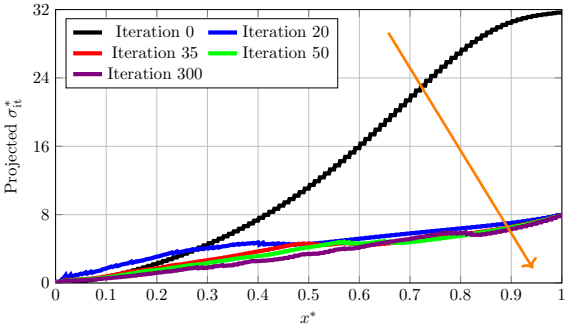

(b) Distribution of entropy generation by ion transport

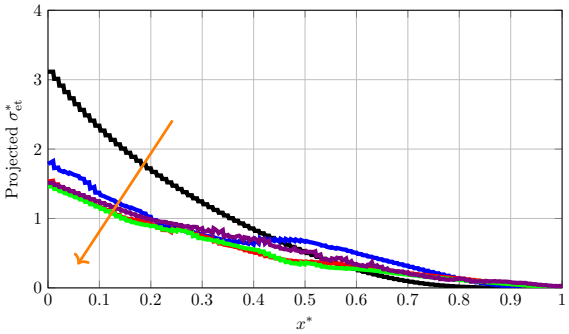

(c) Distribution of entropy generation by electron transport

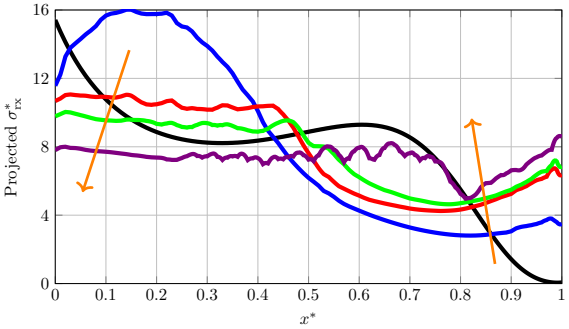

(d) Distribution of entropy generation by reaction

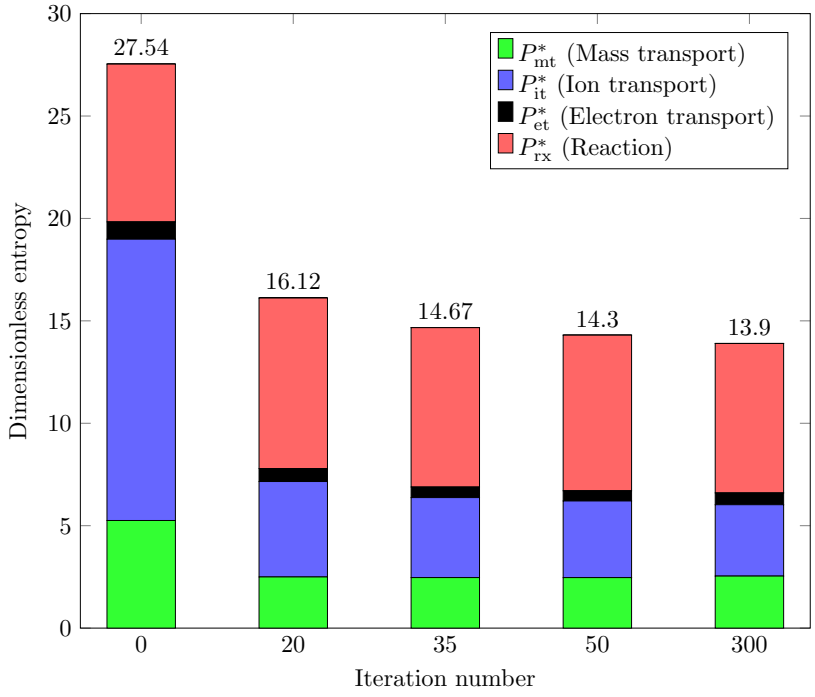

(e) Breakdown of entropy generation

Figure 3.6: (a)-(d) Distribution of entropy generation by various processes and (e) total entropy breakdown during optimization for $\theta_1 = 5$, $\theta_2 = 50$, and $\theta_3 = 10$ at $j^{\mathrm{bnd},*} = 30$

3.5.2 Overpotential-based ERD system

In this subsection, the optimization results of the overpotential-based ERD system are briefly discussed. In contrast to the previous strategy, the goal of this optimization is to increase the current density that is passing the system boundary at a given overpotential level. The optimized system layout for an ERD system with $\theta_1 = 5$, $\theta_2 = 50$, and $\theta_3 = 10$ are demonstrated in Fig. 3.7 for two different overpotentials ($\phi_{\mathrm{l}}^{\mathrm{bnd},*} = 1$ and 9). The structure obtained for $\phi_{\mathrm{l}}^{\mathrm{bnd},*} = 9$ (Fig. 3.7a) increased the system current density by 116.7%. A closer look at this optimal layout reveals that it is pretty similar to Fig. 3.2b. While the exact distributions are different in the two figures, the overall shapes look alike. However, the system settings (θ_1) are different. The reason for this similarity is as follows. The value of θ_1 in the optimized system of Fig. 3.2b has a small value, meaning that the system is diffusion-controlled (diffusion-limited) by nature. Therefore, the optimization algorithm attempts to compensate for the weak reactant delivery by forming a distributed high porosity region in half of the reactor (far from the inlet boundary). On the other hand, the system in Fig. 3.7a is not diffusion-limited by nature. However, increasing the current density necessitates a faster reactant delivery to the reaction sites. As stated before, the output power of a power-generating electrochemical system could be increased in two ways, including reduction of total overpotential and increment of current density. The latter comes at the cost of a higher overall electrochemical reaction rate. To increase the reaction rate, it is required to supply more reactant. This explains why the optimized layouts in Fig. 3.2b and Fig. 3.7a are similar despite their different settings (different θ_1). The results of optimization at a lower overpotential ($\phi_{\mathrm{l}}^{\mathrm{bnd},*} = 1$) are presented in Fig. 3.7a. At a lower overpotential level, the activation overpotential prevails. As a result, a higher volume fraction of the solid phase is beneficial to increase the current density.

From the convergence diagram shown in Fig. 3.8a, it is understandable that the objective function reaches a constant maximum value after around 115 iterations. The insets in Fig. 3.8a illustrate how the distributions of decision variables are changing over the optimization course before fully converging. The I-V curves obtained from the optimized systems for the two cases ($\phi_{\mathrm{l}}^{\mathrm{bnd},*} = 1$ and 9) are plotted in Fig. 3.8b. Opposed to a minimization problem, this optimization approach shifted the initial I-V curve horizontally to the right (horizontal optimization). Performing an optimization at a high overpotential point ($\phi_{\mathrm{l}}^{\mathrm{bnd},*} = 9$, point C in Fig. 3.8b) leads to a

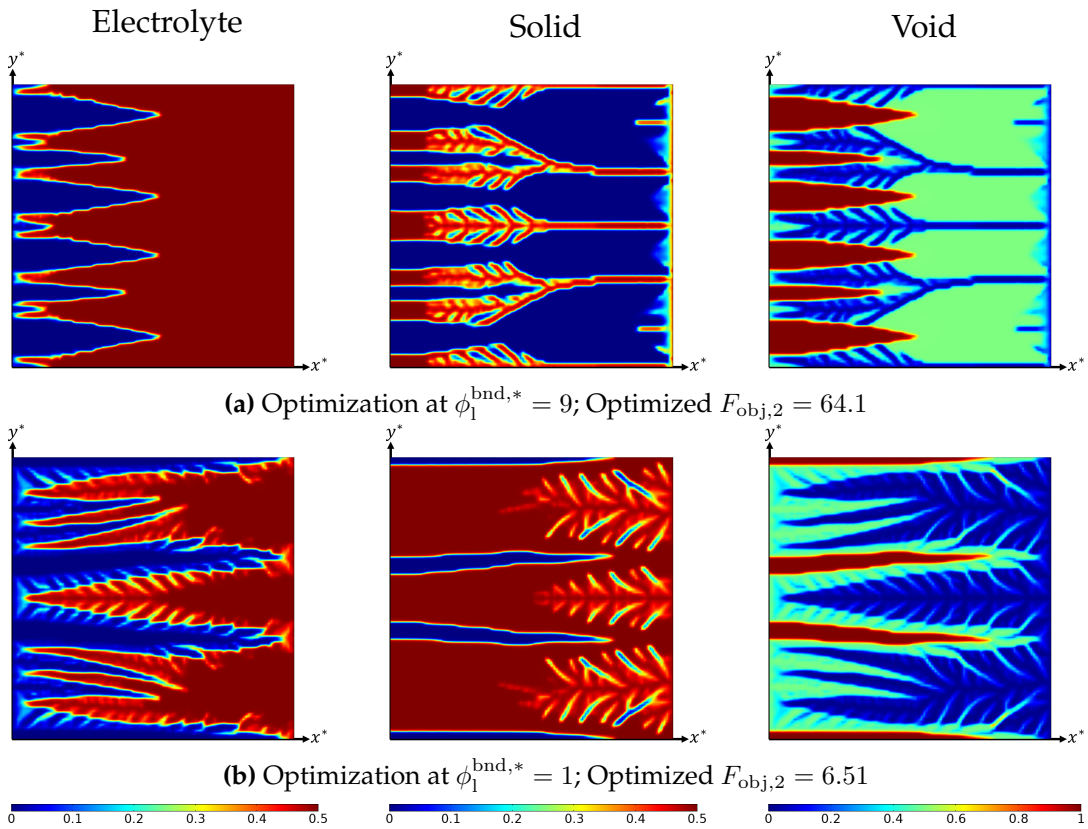

(a) Optimization at $\phi_{\mathrm{l}}^{\mathrm{bnd},*} = 9$; Optimized $F_{\mathrm{obj},2} = 64.1$

(b) Optimization at $\phi_{\mathrm{l}}^{\mathrm{bnd},*} = 1$; Optimized $F_{\mathrm{obj},2} = 6.51$

Figure 3.7: Optimized volume fraction distribution of electrolyte, solid, and void phases for $\theta_1 = 5$, $\theta_2 = 50$, and $\theta_3 = 10$ at different overpotential levels; Improvement of optimized layout compared to initial uniform distribution is: (a) 116.7% and (b) 70.5%

significant improvement in terms of I-V characteristics for medium and high overpotentials ($\phi_{\mathrm{l}}^{\mathrm{bnd},*} \geq 5$). However, this optimization is mainly focused on the improvement of reactant deficit as a result of increased reaction rate. Since the volume fraction of solid phase is relatively low in the optimized structure, the I-V performance of this structure is comparatively weak at low overpotentials ($\phi_{\mathrm{l}}^{\mathrm{bnd},*} \leq 3$). In addition, optimizing the system at a lower overpotential ($\phi_{\mathrm{l}}^{\mathrm{bnd},*} = 1$) increases the current density by 70.5%. However, it is not as beneficial when the system is working at a high overpotential level.

To obtain some insight about maximization approach and identify the differences with the previous formulation, the evolution of projected concentration and convergence of entropy production are investigated for optimization at $\phi_{\mathrm{l}}^{\mathrm{bnd},*} = 9$. As it can be seen in Fig. 3.8c, the concentration changes non-monotonically during the optimization process. In the primary iterations, when there is an increase in the reaction rate as a result of an increase in ionic conductivity, the reactant concentration

suddenly drops. To compensate for the concentration depletion and raise the reaction rate, TO forms some diffusion channels, which helped the concentration to be almost retrieved to the value before optimization. Increasing the concentration through facilitated mass transport helps the system to work at a higher reaction rate without experiencing any reactant shortage. The behavior of dimensionless entropy generation differs from that of the minimization approach. As shown in Fig. 3.8d, the total entropy production is increasing during the optimization. Before the optimization, the local distribution of entropy generation was relatively uniform and its quantity was also low. However, the final optimized solution comes with a higher entropy generation rate, especially in areas with a high volume fraction of the solid phase. This behavior might be assigned to the fact that the electrochemical reaction occurs in those areas. In a finite time/size thermodynamics context, any system that is "doing" something is doomed to produce some amount of entropy. Therefore, when the "doing" of a system is increased (in this case the reaction rate is increased), it is expected that total entropy production to rise. As discussed in [18, 77], this increase is associated with the "inevitable entropy production". Another striking point in Fig. 3.8d is that despite the objective function shows a monotonic convergence behavior (see Fig. 3.8a), the convergence curve of total entropy production shows some noises. This means that the maximization formulation may produce some design solutions that are desirable in terms of objective function but are not completely favorable from the perspective of the second law of thermodynamics. Hence, maximization of current density is not equivalent to the maximization entropy production and the objective function cannot be substituted. To rephrase it, a lower entropy production corresponds to a lower dissipation; nonetheless, a higher entropy production does not imply a higher reaction rate. This is the major difference between the two optimization strategies. A vertical optimization attempts to reduce the losses in the system; however, a horizontal optimization aims to increase the conversion capacity of the system. Therefore, the results obtained from the latter approach might not have the highest possible second law efficiency. In summary, the findings of this study proves that introducing a heterogeneous material distribution within an electrode can effectively enhance material utilization, thereby improving overall performance. This enhancement is achieved through a balance among competing transport and rate processes. Unlike parametric optimization, which primarily controls design variables globally, TO fine-tunes material distribution locally, thus surpassing conventional optimization methods. Moreover, the results of this study show that a proper choice of optimization approach depends on the application of interest. In principle, both strategies might be used for any application by sufficient

considerations. Yet, a vertical optimization may be recommended in power generating systems (e.g., FCs) where there is a need to reduce the energy losses. Moreover, a horizontal optimization may be employed for power consuming systems (e.g., electrolyzers) in which the conversion rate is a major challenge. It is also important to choose the optimization point on I-V curve in accordance with the practical working conditions. Although the optimized design enhances the performance at the chosen optimization point, it might not be beneficial for other working conditions. In the case of an ERD system, the I-V characteristic does not improve equally over a wide operating range.

3.6 Conclusions

The present study investigates a 2D electrochemical porous reactor that involved mass transport, electric charge transfer, and a redox reaction. A dimensionless mathematical model is developed to describe the performance of the system, and a TO method is employed to find the optimal distribution of constituents in the reactor. Since any mathematical optimization algorithm, including TO, is confined to some extent by their tuning parameters and employed mathematical schemes, a more fundamental understanding of optimal design may pave a path beyond the computational limitations. With this goal, the present study also proposes an entropy generation model to evaluate the rate of irreversibilities in the system. Hence, the methodology presented in this study holds potential appeal for researchers engaged in electrode design and optimization as well as those seeking a deeper, fundamental comprehension of optimal designs. Two different optimization approaches, including minimization and maximization formulations, are used to enhance the system performance. The final optimal layouts are complex root-like structures that facilitate the transport processes while improving the conversion rate. The optimized structures are obtained for various combinations of dimensionless numbers and the differences are discussed. The process that leads into a better design solution is explained using the proposed entropy generation model. By comparing the entropy generation trends for two different optimization approaches, this study provided a framework for optimizing the distribution of constituents in porous electrochemical reactors and offered insight into the relationship between TO and the entropy generation rate. The results are shown to be in line with the EGM and EoEP principles. The findings of this study could have potential applications in the optimization of the electrode structure for various electrochemical technologies, such as FCs and electrolyzers. Moreover, the two optimization approaches (vertical and horizontal

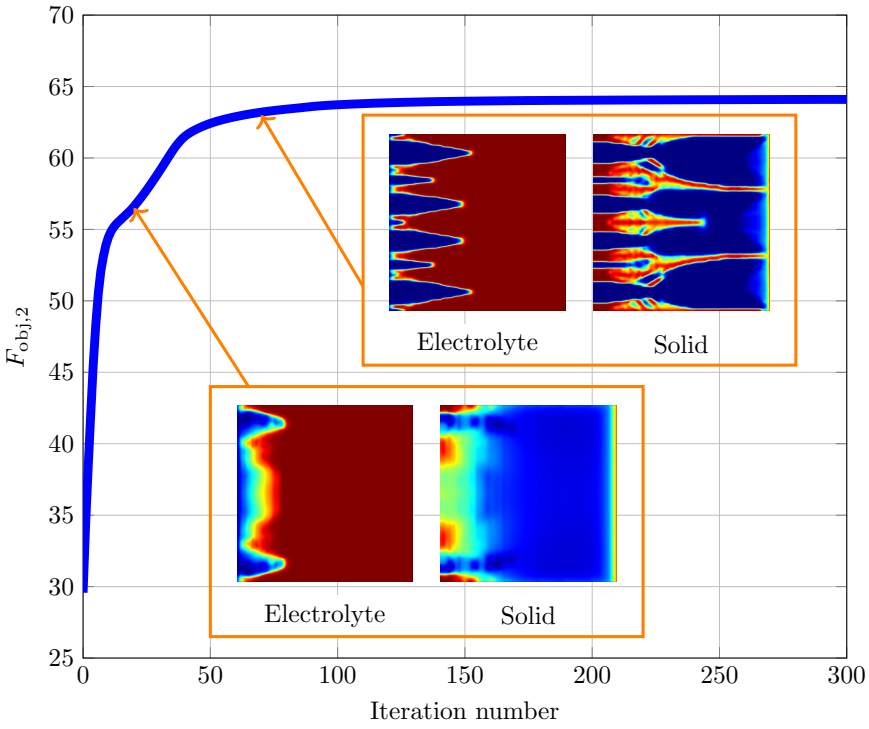

(a) Convergence history of optimization at $\phi_{\mathrm{l}}^{\mathrm{bnd},*} = 9$

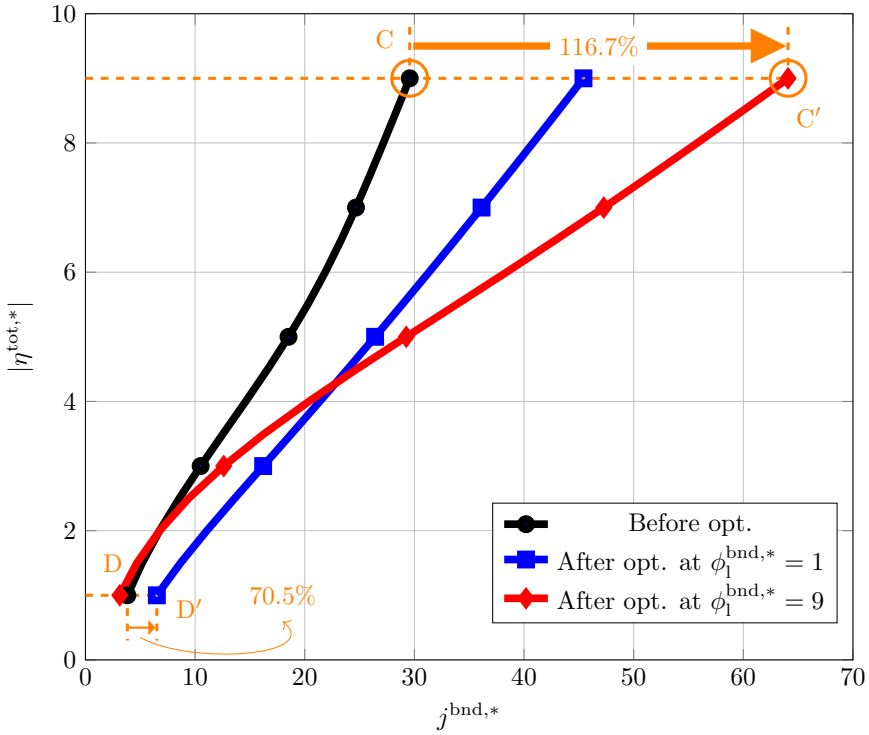

(b) System I-V curves before and after optimization

optimizations) are compared. It is shown that the choice of proper optimization approach and optimization point depends on the practical application. There is, therefore, a definite need for more studies on real devices. Given the generic form of the

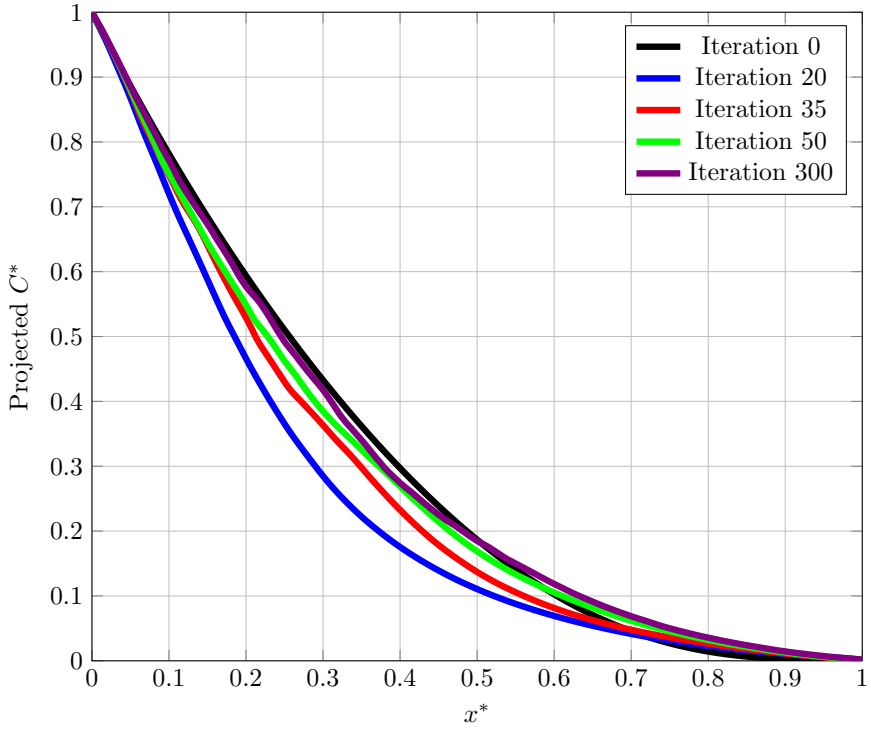

(c) Evolution of projected concentration during optimization at $\phi_1^{\text{bnd},*} = 9$

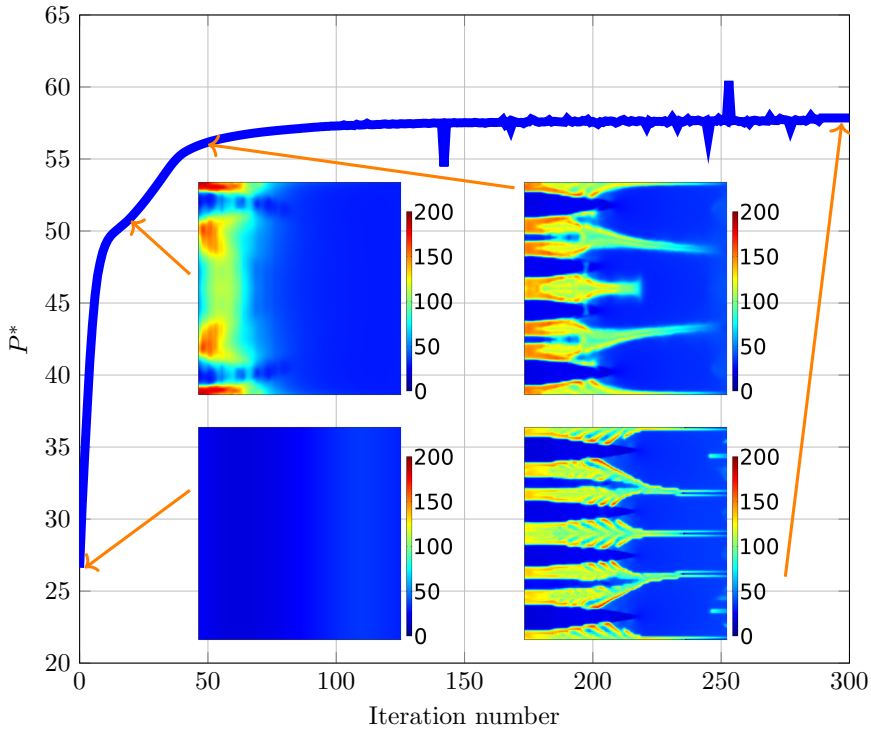

(d) Convergence history of dimensionless local and global entropy at $\phi_1^{\text{bnd},*} = 9$

Figure 3.8: (a) Convergence history of objective function, (b) I-V curves, (c) projected concentration, and (d) convergence history of entropy for optimization of system with $\theta_1 = 5$, $\theta_2 = 50$, and $\theta_3 = 10$

presented optimization and entropy generation analysis, the proposed framework may be applied to other electrochemical systems. This research sheds new insights on how topology optimization relates to the reduction of entropy generation, offering promising pathways for the development of optimization strategies that are both more efficient and firmly rooted in theoretical principles. Future research might also explore a mixed optimization strategy that is a combination of vertical and horizontal ones. In this study, entropy generation analysis was performed as a post-processing step to clarify the characteristics of the optimized design. However, further research is needed to establish a stronger link between entropy generation and performance optimization. One possible direction could involve optimizing the uniformity of entropy generation as an objective function to examine whether this leads to enhanced performance and to determine if the relationship is reciprocal.

Abbreviations

BC	Boundary condition
EGM	Entropy generation minimization
EoEP	Equipartition of entropy production
FC	Fuel cell
GCMMA	Globally convergent method of moving asymptotes
NET	Non-equilibrium thermodynamics
PDE	Partial differential equation
PEMFC	Polymer electrolyte membrane fuel cell
TO	Topology optimization

Nomenclature

a	Active specific surface area	$\mathrm{m^2\,m^{-3}}$
C	Concentration	$\mathrm{mol\,m^{-3}}$
C_0	Characteristic concentration	$\mathrm{mol\,m^{-3}}$
D	Diffusivity	$\mathrm{m^2\,s^{-1}}$
E_{eq}	Equilibrium potential	V
F	Faraday's constant	$\mathrm{C\,mol^{-1}}$
F_{obj}	Objective function	$-$
i_0	Exchange current density	$\mathrm{A\,m^{-2}}$
j	Current density	$\mathrm{A\,m^{-2}}$
$\mathbf{J}_{\mathrm{s}}$	Eentropy flux	$\mathrm{W\,K^{-1}\,m^{-2}}$

L	Characteristic length	m
n	Number of electron	$-$
N	Number of moles	mol
p	Pressure	Pa
P	Total entropy production	$\mathrm{W\,K^{-1}\,m^{-1}}$
q	Charge density	$\mathrm{C\,m^{-3}}$
Q	Electric charge	C
R	Gas constant	$\mathrm{J\,mol^{-1}\,K^{-1}}$
R_{C}	Reaction source term	$\mathrm{mol\,m^{-3}\,s^{-1}}$
S	Entropy	$\mathrm{J\,K^{-1}}$
s	Entropy density	$\mathrm{J\,K^{-1}\,m^{-3}}$
t	Time	s
T	Temperature	K
U	Internal energy	J
V	Volume	$\mathrm{m^3}$

Greek symbols

α	Charge transfer coefficient	$-$
β	Penalty exponent	$-$
η	Overpotential	V
μ	Chemical potential	$\mathrm{J\,mol^{-1}}$
ϕ	Potential	V
ϕ_0	Characteristic potential	V
σ	Charge conductivity / Entropy generation rate	$\mathrm{S\,m^{-1}}/\mathrm{W\,K^{-1}\,m^{-3}}$
θ	Dimensionless group	$-$
ε	Volume fraction	$-$

Subscripts/superscripts

bnd	Boundary
eff	Effective
et	Electron transport
it	Ion transport
l	Electrolyte
mt	Mass transfer
ox	Oxidizing

red	Reducing
rx	Reaction
s	Solid
src	Source
v	Void

Bibliography

[1] K. Nantasaksiri, P. Charoen-amornkitt, T. Machimura, and K. Hayashi, "Multidisciplinary assessment of napier grass plantation on local energetic, environmental and socioeconomic industries: A watershed-scale study in southern thailand," *Sustainability*, vol. 13, no. 24, p. 13520, 2021.

[2] K. Nantasaksiri, P. Charoen-amornkitt, and T. Machimura, "Integration of multicriteria decision analysis and geographic information system for site suitability assessment of napier grass-based biogas power plant in southern thailand," *Renewable and Sustainable Energy Transition*, vol. 1, p. 100011, 2021.

[3] N. Limjeerajarus and P. Charoen-Amornkitt, "Effect of different flow field designs and number of channels on performance of a small pefc," *International Journal of Hydrogen Energy*, vol. 40, no. 22, pp. 7144–7158, 2015.

[4] M. Alizadeh and F. Torabi, "Precise pem fuel cell parameter extraction based on a self-consistent model and sccsa optimization algorithm," *Energy Conversion and Management*, vol. 229, p. 113777, 2021.

[5] J. Ma, Y. Li, N. S. Grundish, J. B. Goodenough, Y. Chen, L. Guo, Z. Peng, X. Qi, F. Yang, L. Qie, *et al.*, "The 2021 battery technology roadmap," *Journal of Physics D: Applied Physics*, vol. 54, no. 18, p. 183001, 2021.

[6] A. Olabi, T. Wilberforce, and M. A. Abdelkareem, "Fuel cell application in the automotive industry and future perspective," *Energy*, vol. 214, p. 118955, 2021.

[7] P. Charoen-amornkitt, T. Suzuki, and S. Tsushima, "Effects of voltage-dependence of the constant phase element and ohmic parameters in the modeling and simulation of cyclic voltammograms," *Journal of The Electrochemical Society*, vol. 167, no. 16, p. 166506, 2020.

[8] P. Charoen-Amornkitt, T. Suzuki, and S. Tsushima, "Determination of constant phase element parameters under cyclic voltammetry conditions using a semi-theoretical equation," *Electrochemistry*, vol. 87, no. 4, pp. 204–213, 2019.

[9] P. Charoen-amornkitt, T. Suzuki, and S. Tsushima, "Ohmic resistance and constant phase element effects on cyclic voltammograms using a combined model of mass transport and equivalent circuits," *Electrochimica Acta*, vol. 258, pp. 433–441, 2017.

[10] Y. Wang, D. F. R. Diaz, K. S. Chen, Z. Wang, and X. C. Adroher, "Materials, technological status, and fundamentals of pem fuel cells–a review," *Materials today*, vol. 32, pp. 178–203, 2020.

[11] F. Tsutsui, T. Suzuki, and S. Tsushima, "Measurement and analysis of gas transport properties in catalyst layers of polymer electrolyte fuel cells with different ionomer to carbon ratio," *ECS Transactions*, vol. 98, no. 9, p. 49, 2020.

[12] T. Suzuki, Y. Nakata, F. Tsutsui, and S. Tsushima, "Investigation of gas transport properties of pemfc catalyst layers using a microfluidic device," *Journal of The Electrochemical Society*, vol. 167, no. 12, p. 124519, 2020.

[13] Y. Guo, F. Pan, W. Chen, Z. Ding, D. Yang, B. Li, P. Ming, and C. Zhang, "The controllable design of catalyst inks to enhance pemfc performance: A review," *Electrochemical Energy Reviews*, vol. 4, no. 1, pp. 67–100, 2021.

[14] Z. Yang, Y. Wei, Y. Zeng, and Y. Yuan, "Effects of in-situ bismuth catalyst electrodeposition on performance of vanadium redox flow batteries," *Journal of Power Sources*, vol. 506, p. 230238, 2021.

[15] J. Lee, P. Srimuk, S. Fleischmann, X. Su, T. A. Hatton, and V. Presser, "Redox-electrolytes for non-flow electrochemical energy storage: A critical review and best practice," *Progress in Materials Science*, vol. 101, pp. 46–89, 2019.

[16] O. Sigmund and K. Maute, "Topology optimization approaches," *Structural and Multidisciplinary Optimization*, vol. 48, no. 6, pp. 1031–1055, 2013.

[17] J. Wu, O. Sigmund, and J. P. Groen, "Topology optimization of multi-scale structures: a review," *Structural and Multidisciplinary Optimization*, vol. 63, no. 3, pp. 1455–1480, 2021.

[18] P. Charoen-amornkitt, M. Alizadeh, T. Suzuki, and S. Tsushima, "Entropy generation analysis during adjoint variable-based topology optimization of porous

reaction-diffusion systems under various design dimensionalities," *International Journal of Heat and Mass Transfer*, vol. 202, p. 123725, 2023.

[19] M. Long, P. Charoen-Amornkitt, M. Alizadeh, T. Suzuki, and S. Tsushima, "Effect of reaction and diffusion parameters on optimized porosity distribution in a reaction-diffusion system," in *AIP Conference Proceedings*, vol. 3086, AIP Publishing, 2024.

[20] J. S. Lee, S. Y. Yoon, B. Kim, H. Lee, M. Y. Ha, and J. K. Min, "A topology optimization based design of a liquid-cooled heat sink with cylindrical pin fins having varying pitch," *International Journal of Heat and Mass Transfer*, vol. 172, p. 121172, 2021.

[21] J. Alexandersen and C. S. Andreasen, "A review of topology optimisation for fluid-based problems," *Fluids*, vol. 5, no. 1, p. 29, 2020.

[22] T. Roy, M. A. Salazar de Troya, M. A. Worsley, and V. A. Beck, "Topology optimization for the design of porous electrodes," *Structural and Multidisciplinary Optimization*, vol. 65, no. 6, pp. 1–21, 2022.

[23] M. Alizadeh, P. Charoen-amornkitt, T. Suzuki, and S. Tsushima, "Mixed topology optimization: A self-guided boundary-independent approach for power sources," *Energy Conversion and Management*, vol. 294, p. 117567, 2023.

[24] P. Charoen-amornkitt, M. Alizadeh, T. Suzuki, and S. Tsushima, "Topologically optimized anode catalyst layers of proton exchange membrane water electrolyzers," *ECS Transactions*, vol. 111, no. 4, p. 87, 2023.

[25] C.-H. Chen, K. Yaji, S. Yamasaki, S. Tsushima, and K. Fujita, "Computational design of flow fields for vanadium redox flow batteries via topology optimization," *Journal of Energy Storage*, vol. 26, p. 100990, 2019.

[26] K. Yaji, S. Yamasaki, S. Tsushima, T. Suzuki, and K. Fujita, "Topology optimization for the design of flow fields in a redox flow battery," *Structural and multidisciplinary optimization*, vol. 57, no. 2, pp. 535–546, 2018.

[27] M. D. R. Batista, S. Chandrasekaran, B. D. Moran, M. S. de Troya, A. Pinongcos, Z. Wang, R. Hensleigh, A. Carleton, M. Zeng, T. Roy, *et al.*, "Design and additive manufacturing of optimized electrodes for energy storage applications," *Carbon*, vol. 205, pp. 262–269, 2023.

[28] C. Lee, W. J. Kort-Kamp, H. Yu, D. A. Cullen, B. M. Patterson, T. A. Arman, S. Komini Babu, R. Mukundan, R. L. Borup, and J. S. Spendelow, "Grooved electrodes for high-power-density fuel cells," *Nature Energy*, pp. 1–10, 2023.

[29] Y. Demirel and V. Gerbaud, *Nonequilibrium Thermodynamics: Transport and Rate Processes in Physical, Chemical and Biological Systems*. Elsevier Science, 2018.

[30] S. Kjelstrup, D. Bedeaux, E. Johannessen, and J. Gross, *Non-equilibrium Thermodynamics For Engineers (Second Edition)*. World Scientific Publishing Company, 2017.

[31] Z. Dong and Q. Du, "The local distribution of temperatures and entropy generation rate in an ideal counterflow heat exchanger," *Coatings*, vol. 11, no. 8, p. 970, 2021.

[32] J. Avellaneda, F. Bataille, A. Toutant, and G. Flamant, "Variational entropy generation minimization of a channel flow: Convective heat transfer in a gas flow," *International Journal of Heat and Mass Transfer*, vol. 160, p. 120168, 2020.

[33] R. Dormohammadi, M. Farzaneh-Gord, A. Ebrahimi-Moghadam, and M. H. Ahmadi, "Heat transfer and entropy generation of the nanofluid flow inside sinusoidal wavy channels," *Journal of Molecular Liquids*, vol. 269, pp. 229–240, 2018.

[34] S. A. Khan, T. Hayat, A. Alsaedi, and B. Ahmad, "Melting heat transportation in radiative flow of nanomaterials with irreversibility analysis," *Renewable and Sustainable Energy Reviews*, vol. 140, p. 110739, 2021.

[35] M. I. Khan, S. Ahmad Khan, T. Hayat, M. Waqas, and A. Alsaedi, "Modeling and numerical simulation for flow of hybrid nanofluid (sio2/c3h8o2) and (mos2/c3 h 8o2) with entropy optimization and variable viscosity," *International Journal of Numerical Methods for Heat & Fluid Flow*, vol. 22, no. 8, pp. 3939–3955, 2020.

[36] T. Hayat, S. A. Khan, A. Alsaedi, and H. M. Fardoun, "Heat transportation in electro-magnetohydrodynamic flow of darcy-forchheimer viscous fluid with irreversibility analysis," *Physica Scripta*, vol. 95, no. 10, p. 105214, 2020.

[37] S. A. Khan, T. Hayat, and A. Alsaedi, "Thermal conductivity performance for ternary hybrid nanomaterial subject to entropy generation," *Energy Reports*, vol. 8, pp. 9997–10005, 2022.

[38] S. A. Khan, T. Hayat, and A. Alsaedi, "Simultaneous features of soret and dufour in entropy optimized flow of reiner-rivlin fluid considering thermal radiation," *International Communications in Heat and Mass Transfer*, vol. 137, p. 106297, 2022.

[39] S. A. Khan, T. Hayat, and A. Alsaedi, "Entropy optimization for nanofluid flow with radiation subject to a porous medium," *Journal of Petroleum Science and Engineering*, vol. 217, p. 110864, 2022.

[40] S. A. Khan, T. Hayat, and A. Alsaedi, "Numerical study for entropy optimized radiative unsteady flow of prandtl liquid," *Fuel*, vol. 319, p. 123601, 2022.

[41] S. A. Khan, T. Hayat, A. Alsaedi, and M. Alhodaly, "Thermal analysis for radiative flow of darcy–forchheimer nanomaterials subject to entropy generation," *Journal of Computational Design and Engineering*, vol. 9, no. 5, pp. 1756–1764, 2022.

[42] M. Sauermoser, G. Fossati, N. Kizilova, and S. Kjelstrup, "Modelling electrochemical cells with porous electrodes. the proton exchange membrane fuel cell," *ECS Transactions*, vol. 92, no. 8, p. 279, 2019.

[43] A. Bejan, *Entropy Generation Minimization: The Method of Thermodynamic Optimization of Finite-Size Systems and Finite-Time Processes*. Mechanical and Aerospace Engineering Series, CRC Press, 2013.

[44] S. Wan, L. Qiu, G. Tang, W. Chen, Y. Li, B. Gao, and F. He, "Ultrafast sequestration of cadmium and lead from water by manganese oxide supported on a macro-mesoporous biochar," *Chemical Engineering Journal*, vol. 387, p. 124095, 2020.

[45] C. Wedler and R. Span, "A pore-structure dependent kinetic adsorption model for consideration in char conversion–adsorption kinetics of co2 on biomass chars," *Chemical Engineering Science*, vol. 231, p. 116281, 2021.

[46] T. G. Tranter, P. Stogornyuk, J. T. Gostick, A. Burns, and W. F. Gale, "A method for measuring relative in-plane diffusivity of thin and partially saturated porous media: An application to fuel cell gas diffusion layers," *International Journal of Heat and Mass Transfer*, vol. 110, pp. 132–141, 2017.

[47] T. Fuller and J. Harb, *Electrochemical Engineering*. Wiley, 2018.

[48] F. Wang, X. Li, J. Tan, X. Hao, and B. Xiong, "Pore-scale prediction of the oxygen effective diffusivity in porous battery electrodes using the random walk theory," *International Journal of Heat and Mass Transfer*, vol. 183, p. 122085, 2022.

[49] Z. Bao, Y. Li, X. Zhou, F. Gao, Q. Du, and K. Jiao, "Transport properties of gas diffusion layer of proton exchange membrane fuel cells: Effects of compression," *International Journal of Heat and Mass Transfer*, vol. 178, p. 121608, 2021.

[50] L. Maier, M. Scherle, M. Hopp-Hirschler, and U. Nieken, "Effective transport parameters of porous media from 2d microstructure images," *International Journal of Heat and Mass Transfer*, vol. 175, p. 121371, 2021.

[51] B. Tjaden, S. J. Cooper, D. J. Brett, D. Kramer, and P. R. Shearing, "On the origin and application of the bruggeman correlation for analysing transport phenomena in electrochemical systems," *Current opinion in chemical engineering*, vol. 12, pp. 44–51, 2016.

[52] D.-W. Chung, M. Ebner, D. R. Ely, V. Wood, and R. E. García, "Validity of the bruggeman relation for porous electrodes," *Modelling and Simulation in Materials Science and Engineering*, vol. 21, no. 7, p. 074009, 2013.

[53] A. Rajora and J. Haverkort, "An analytical multiphase flow model for parallel plate electrolyzers," *Chemical Engineering Science*, vol. 260, p. 117823, 2022.

[54] E. Chehrazi, "Determination of the thickness of interfacial voids in a spherical nanoparticles-polymer membrane: Fundamental insight from the gas permeation modeling," *Chemical Engineering Research and Design*, vol. 177, pp. 56–64, 2022.

[55] J. Cho, J. Marquis, P. Trogadas, T. Neville, D. Brett, and M.-O. Coppens, "Optimizing the architecture of lung-inspired fuel cells," *Chemical Engineering Science*, vol. 215, p. 115375, 2020.

[56] J. Liang, Y. Li, R. Wang, and J. Jiang, "Cross-dimensional model of the oxygen transport behavior in low-pt proton exchange membrane fuel cells," *Chemical Engineering Journal*, vol. 400, p. 125796, 2020.

[57] G. Ye, W. Tong, X. Liu, X. Song, J. Zhou, and X. Zhou, "An analytical method for the optimization of pore network in lithium-ion battery electrodes," *Chemical Engineering Research and Design*, vol. 149, pp. 226–234, 2019.

[58] L. E. Paniagua-Guerra and B. Ramos-Alvarado, "Efficient hybrid microjet liquid cooled heat sinks made of photopolymer resin: thermo-fluid characteristics and entropy generation analysis," *International Journal of Heat and Mass Transfer*, vol. 146, p. 118844, 2020.

[59] Z. Wan, W. Quan, C. Yang, H. Yan, X. Chen, T. Huang, X. Wang, and S. Chan, "Optimal design of a novel m-like channel in bipolar plates of proton exchange membrane fuel cell based on minimum entropy generation," *Energy Conversion and Management*, vol. 205, p. 112386, 2020.

[60] Z. H. Khan, W. A. Khan, J. Tang, and M. A. Sheremet, "Entropy generation analysis of triple diffusive flow past a horizontal plate in porous medium," *Chemical Engineering Science*, vol. 228, p. 115980, 2020.

[61] Z. Guo, S. Deng, Y. Zhu, L. Zhao, X. Yuan, S. Li, and L. Chen, "Non-equilibrium thermodynamic analysis of adsorption carbon capture: Contributors, mechanisms and verification of entropy generation," *Energy*, vol. 208, p. 118348, 2020.

[62] C. E. Damian-Ascencio, A. Saldaña-Robles, A. Hernandez-Guerrero, and S. Cano-Andrade, "Numerical modeling of a proton exchange membrane fuel cell with tree-like flow field channels based on an entropy generation analysis," *Energy*, vol. 133, pp. 306–316, 2017.

[63] G. Kefayati and H. Tang, "Simulation of natural convection and entropy generation of mhd non-newtonian nanofluid in a cavity using buongiorno's mathematical model," *International Journal of Hydrogen Energy*, vol. 42, no. 27, pp. 17284–17327, 2017.

[64] L. Duan, X. Wu, Z. Ji, and Q. Fang, "Entropy generation analysis on cyclone separators with different exit pipe diameters and inlet dimensions," *Chemical Engineering Science*, vol. 138, pp. 622–633, 2015.

[65] M. Alizadeh, P. Charoen-Amornkitt, T. Suzuki, and S. Tsushima, "Structural topology optimization and irreversibility analysis in an electrochemical reaction-diffusion system," in *AIP Conference Proceedings*, vol. 3086, AIP Publishing, 2024.

[66] M. Alizadeh, P. Charoen-amornkitt, T. Suzuki, and S. Tsushima, "Analysis of local-global entropy generation in an electrochemical system," in *International Heat Transfer Conference Digital Library*, Begel House Inc., 2023.

[67] J. Newman and K. Thomas-Alyea, *Electrochemical Systems*. The ECS Series of Texts and Monographs, Wiley, 2012.

[68] T. Nazghelichi, F. Torabi, and V. Esfahanian, "Non-dimensional analysis of electrochemical governing equations of lead-acid batteries," *Journal of Energy Storage*, vol. 27, p. 101120, 2020.

[69] G. Kreysa, K. Ota, and R. Savinell, *Encyclopedia of Applied Electrochemistry*. Encyclopedia of Applied Electrochemistry, Springer New York, 2014.

[70] T. Salmi, V. Russo, and A. F. Aguilera, "Modelling of the interaction of kinetics and external transport phenomena in structured catalysts: The effect of reaction kinetics, mass transfer and channel size distribution in solid foams," *Chemical Engineering Science*, vol. 244, p. 116815, 2021.

[71] M. Moghaddam, A. Abbassi, J. Ghazanfarian, and S. Jalilian, "Investigation of microstructure effects on performance of hierarchically structured porous catalyst using a novel pore network model," *Chemical Engineering Journal*, vol. 388, p. 124261, 2020.

[72] A. Pietschak, M. Kaiser, and H. Freund, "Tailored catalyst pellet specification for improved fixed-bed transport characteristics: A shortcut method for the model-based reactor design," *Chemical Engineering Research and Design*, vol. 137, pp. 60–74, 2018.

[73] X. Wang, M. Liu, and Z. Yang, "Coupled model based on radiation transfer and reaction kinetics of gas–liquid–solid photocatalytic mini-fluidized bed," *Chemical Engineering Research and Design*, vol. 134, pp. 172–185, 2018.

[74] G. Wautischer, C. Abert, F. Bruckner, F. Slanovc, and D. Suess, "A topology optimization algorithm for magnetic structures based on a hybrid fem–bem method utilizing the adjoint approach," *Scientific Reports*, vol. 12, no. 1, pp. 1–11, 2022.

[75] G. Jing, J. Jia, and J. Xiang, "Level set-based bem topology optimization method for maximizing total potential energy of thermal problems," *International Journal of Heat and Mass Transfer*, vol. 182, p. 121921, 2022.

[76] S. Kubo, A. Koguchi, K. Yaji, T. Yamada, K. Izui, and S. Nishiwaki, "Level set-based topology optimization for two dimensional turbulent flow using an immersed boundary method," *Journal of Computational Physics*, vol. 446, p. 110630, 2021.

[77] M. Alizadeh, P. Charoen-amornkitt, T. Suzuki, and S. Tsushima, "Investigation of transport-reaction dynamics and local/global entropy production in topology optimization of two-species reaction-diffusion systems," *Chemical Engineering Science*, vol. 275, p. 118739, 2023.

[78] N. M. Patel, D. Tillotson, J. E. Renaud, A. Tovar, and K. Izui, "Comparative study of topology optimization techniques," *AIAA journal*, vol. 46, no. 8,

pp. 1963–1975, 2008.

[79] B. Wang, "Topology optimization of electric machines: A review," in *2022 IEEE Energy Conversion Congress and Exposition (ECCE)*, pp. 1–8, IEEE, 2022.

[80] M. Bendsoe and O. Sigmund, *Topology Optimization: Theory, Methods, and Applications*. Springer Berlin Heidelberg, 2013.

[81] B. S. Lazarov and O. Sigmund, "Filters in topology optimization based on helmholtz-type differential equations," *International Journal for Numerical Methods in Engineering*, vol. 86, no. 6, pp. 765–781, 2011.

[82] J. V. Carstensen and J. K. Guest, "Projection-based two-phase minimum and maximum length scale control in topology optimization," *Structural and multidisciplinary optimization*, vol. 58, no. 5, pp. 1845–1860, 2018.

[83] A. Kawamoto, T. Matsumori, S. Yamasaki, T. Nomura, T. Kondoh, and S. Nishiwaki, "Heaviside projection based topology optimization by a pde-filtered scalar function," *Structural and Multidisciplinary Optimization*, vol. 44, no. 1, pp. 19–24, 2011.

[84] X. Huang and Y. Xie, "Convergent and mesh-independent solutions for the bi-directional evolutionary structural optimization method," *Finite elements in analysis and design*, vol. 43, no. 14, pp. 1039–1049, 2007.

[85] C. Zillober, "A globally convergent version of the method of moving asymptotes," *Structural optimization*, vol. 6, no. 3, pp. 166–174, 1993.

[86] D. Tondeur and E. Kvaalen, "Equipartition of entropy production. an optimality criterion for transfer and separation processes," *Industrial & engineering chemistry research*, vol. 26, no. 1, pp. 50–56, 1987.

[87] E. Magnanelli, E. Johannessen, and S. Kjelstrup, "Entropy production minimization as design principle for membrane systems: Comparing equipartition results to numerical optima," *Industrial & Engineering Chemistry Research*, vol. 56, no. 16, pp. 4856–4866, 2017.

[88] L. Van der Ham, J. Gross, and S. Kjelstrup, "Two performance indicators for the characterization of the entropy production in a process unit," *Energy*, vol. 36, no. 6, pp. 3727–3732, 2011.

[89] E. Johannessen and A. Røsjorde, "Equipartition of entropy production as an approximation to the state of minimum entropy production in diabatic distillation," *Energy*, vol. 32, no. 4, pp. 467–473, 2007.

[90] E. Johannessen and S. Kjelstrup, "A highway in state space for reactors with minimum entropy production," *Chemical engineering science*, vol. 60, no. 12, pp. 3347–3361, 2005.

[91] F. Balkan, "Application of eoep principle with variable heat transfer coefficient in minimizing entropy production in heat exchangers," *Energy conversion and management*, vol. 46, no. 13-14, pp. 2134–2144, 2005.

[92] F. Balkan, "Comparison of entropy minimization principles in heat exchange and a short-cut principle: Eotd," *International journal of energy research*, vol. 27, no. 11, pp. 1003–1014, 2003.

[93] E. Johannessen, L. Nummedal, and S. Kjelstrup, "Minimizing the entropy production in heat exchange," *International Journal of Heat and Mass Transfer*, vol. 45, no. 13, pp. 2649–2654, 2002.

[94] L. Nummedal and S. Kjelstrup, "Equipartition of forces as a lower bound on the entropy production in heat exchange," *International Journal of Heat and Mass Transfer*, vol. 44, no. 15, pp. 2827–2833, 2001.

[95] S. K. Ratkje, E. Sauar, E. M. Hansen, K. M. Lien, and B. Hafskjold, "Analysis of entropy production rates for design of distillation columns," *Industrial & engineering chemistry research*, vol. 34, no. 9, pp. 3001–3007, 1995.

Chapter 4

A hierarchical design solution for structure of PEMFC catalyst layer based on a two-phase flow model

Abstract

Proton exchange membrane fuel cells (PEMFCs) have emerged as a promising solution as the world is moving toward sustainable energy resources. However, in order to compete economically with existing technologies, further improvements in performance are necessary. Mathematical modeling and optimization are viable tools for designing better PEMFCs. This study aims to provide a framework for topological optimization of the electrode structure, with the ultimate goal of enhancing cell performance. To achieve this, a two-phase flow model of PEMFC is developed to characterize the cell performance. The model is then coupled with a topology optimization technique, which is the main focus of the present work, to seek an optimized constituent distribution in the catalyst layer. Results indicate that an electrode with a heterogeneous structure can enhance the overall cell performance by balancing various transport and rate processes. The optimized designs are investigated for various key factors, including effective diffusivity, effective conductivity, and liquid water management, to demonstrate how an optimized design can be advantageous.

This chapter is published as:

M. Alizadeh, P. Charoen-amornkitt, T. Suzuki, and S. Tsushima. "A mathematically optimized design solution for structure of PEMFC catalyst layer based on a two-phase flow model", *Journal of The Electrochemical Society*, **171**.11 (2024): 114506. https://doi.org/10.1149/1945-7111/ad8efe

4.1 Introduction

As the world is moving toward carbon-free energy resources, electrochemical energy conversion and storage technologies, such as secondary batteries and fuel cells, received much attention [1, 2]. In particular, proton exchange membrane fuel cells (PEMFCs) have attracted significant attention due to their high efficiency, high power density, and low startup time, as well as their scalability and ability to operate at low temperatures. These characteristics make PEMFCs suitable for a wide range of applications, from stationary power generation [3, 4] to transportation [5, 6]. Although they offer various advantages, their manufacturing cost remains high due to the use of precious metals such as platinum as catalysts, which poses a significant obstacle to their widespread commercial adoption [7–10]. Therefore, it is crucial to focus on further enhancing their performance and reducing costs to make these energy devices more feasible for extensive deployment. This goal might be achieved by enhancement of a vital component called catalyst layer (CL), which is shown in Fig. 4.1a.

The significance of CL is twofold: (1) it is the largest cost contributor, and (2) the electrochemical reaction is taking place in this component. As previously mentioned, the former is attributed to the usage of costly noble metals as catalysts to increase the electrochemical reaction rate. CL is a crucial determinant of the overall performance of a PEMFC, as it facilitates several coupled transport phenomena, including mass and electric charge transfer, alongside electrochemical reactions. As a result, any improvement in CL not only reduces system costs but also enhances cell performance. The CL of a PEMFC is a thin, porous medium consisting of a catalyst supported by a support material (such as carbon-supported platinum), a polymeric binder material (ionomer), and voids. This triple-phase layer serves as the bed for redox reactions, where the fuel and oxidant undergo reduction and oxidation, respectively, on the catalyst material's surface. The electrochemical reaction involves chemical substances, electrons, and protons. In the CL, carbon-supported platinum (PtC) and ionomer phases are responsible for transporting electrons and protons, respectively. In addition, the reactant is delivered to the reaction site through the pores.

Several approaches have been attempted in previous research works to address the performance-cost challenge of CL. For instance, some studies explored the use of cheaper catalyst materials, such as non-platinum group metals, to reduce fabrication costs [11–16]. However, substituting platinum group metals (PGMs) with other elements in the fabrication of PGM-free catalyst layers can pose new challenges, such as

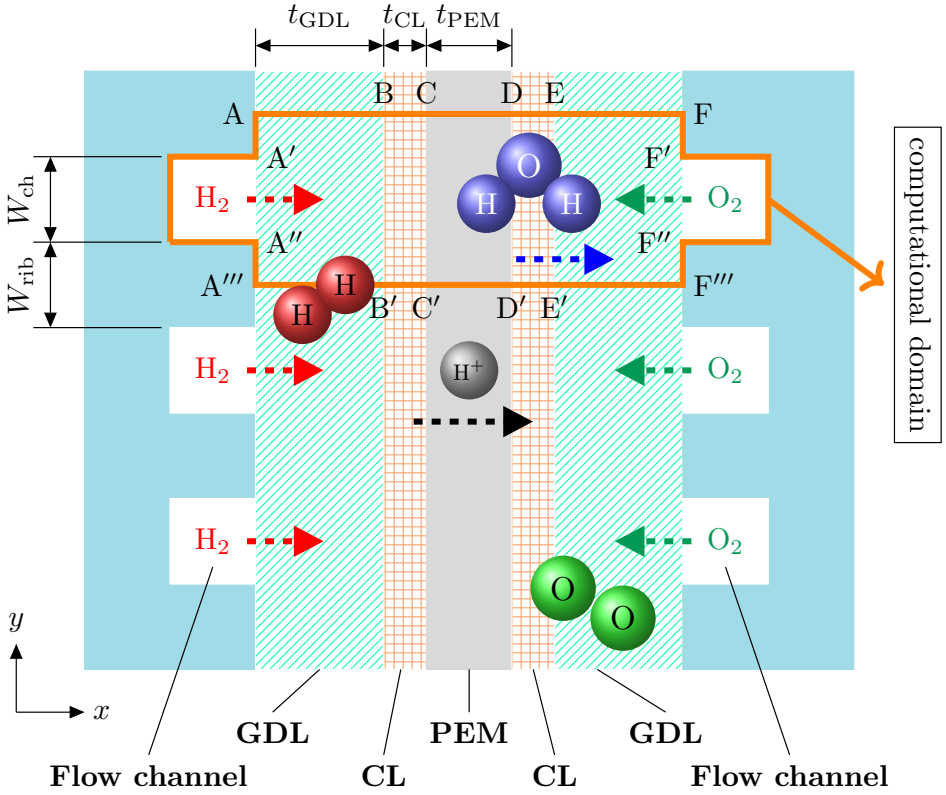

(a) 2D schematic diagram of a PEMFC cell

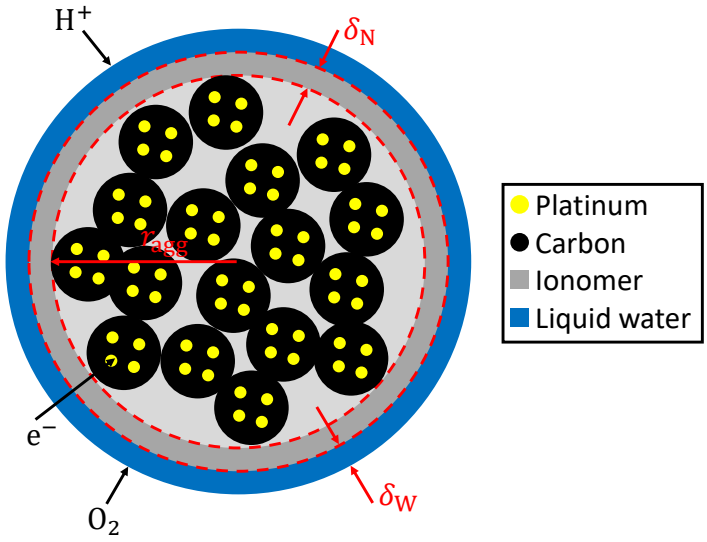

(b) Sketch of an agglomerate

Figure 4.1: Schematic representation of (a) a single PEMFC cell and (b) a CCL agglomerate.

low durability and reduced oxygen reduction reaction (ORR) activity. Thicker electrodes can be used to overcome the low ORR activity issue, but this can increase mass transport resistance and degrade liquid water discharge [17]. In another attempt, a number of studies [18–21] employed electroanalytical methods to assess and obtain a deeper understanding of electrode modification. Moreover, over the last three decades, remarkable dedication and substantial advancements have been devoted to improving PEMFCs performance by focusing on modeling of CL with the goal of optimizing its structure and composition [22–31]. A summary of some selected past research works on this topic is presented in Table 4.1. Numerical methods are efficient approaches in designing superior CL and have been vastly used in the literature [32–36]. This strategy is based on mathematical modeling and optimization of CL structure. Mathematical modeling provides a powerful tool for simulation of cell characteristics under various structural and operational conditions. By changing any structural or operational parameter, the impacts of these changes might be determined. When integrated with mathematical optimization algorithms, the best set of parameters might be identified within a given bound [37]. As aforementioned, several coupled transport phenomena, including mass, heat, and electric charge transfer, and a rate process (i.e., electrochemical reaction) are happening simultaneously in CL. The cell performance is mainly dictated by two mechanisms in CL: (1) charge transfer rate, and (2) reactant supply/product discharge rate. Charge transfer rate represents how fast the reactant species are consumed (or likewise, product species are produced). On the other hand, the latter mechanism specifies the pace of reactant delivery to the reaction site (or product discharge from reaction site). This mechanism is also known as mass transport resistance and becomes dominant when a PEMFC is working at a high current density. At higher current densities, the rate of the chemical reaction increases, causing the reactant substance to be consumed more rapidly. To maintain the desired reaction rate, it is necessary to compensate the available amount of reactant accordingly. Insufficient reactant delivery leads to a substantial performance drop at high current densities. Moreover, excess liquid water production at these current density regions blocks the pores and makes the reactant delivery more complicated. This phenomenon is known as flooding [38, 39]. In a porous medium, like CL, the effective transport and electrochemical properties depend on its microstructure. For instance, the effective ionic conductivity of CL is related to the volume fraction of ionomer. However, enhanced ionic conductivity (at a constant PtC volume fraction) translates into lower porosity, which lessens the effective reactant diffusivity. Therefore, an appropriate CL composition might provide a balance between the transport and rate processes, which consequently results

in an elevated overall cell performance. The described trade-off between different mechanisms gives a rise to an optimization problem.

The aim of this optimization problem is to maximize the membrane electrode assembly (MEA) performance by providing a compromise between the processes occurring in CL. A proper balance between dynamics of these phenomena is obtainable by controlling the composition of CL. In other words, an appropriate adjustment of volume fractions of constituent materials would improve the performance. As a result, the volume fraction of PtC, volume fraction of ionomer, and porosity could be considered as the decision variables of this optimization problem. Several previous studies in the literature focused on parametric optimization of CL composition. For instance, He et al. [33] investigated the impact of five parameters of the cathode catalyst layer (CCL) on the current-voltage (I-V) relationship of a mathematically modeled PEMFC. These parameters include platinum loading, platinum to carbon (Pt/C) mass ratio, ionomer to carbon (I/C) ratio, carbon particle radius, and electrochemical surface area (ECSA). Their results revealed that platinum loading substantially affects the cell performance. Also, according to their findings, contrary to limiting current density that might be increased by a smaller I/C ratio, a higher value of this parameter is beneficial for enhancing maximum power density. Some other studies [40, 42–46] tried to expand parametric analysis by dividing CL into several sub-domains and finding the best composition of CL in a double- or multi-layer configuration. These studies proposed that the cell performance improvement can be achieved with a functionally graded multi-layer design for the catalyst layer [45]. The composition of each sub-layer is controlled independently of other ones with the aim of amplifying the output power. In a more advanced form, Havaej et al. [35], for instance, compared several non-uniform catalyst loading distribution based on a set of predefined functions. They found that by introducing a non-uniform distribution of catalyst in the longitudinal direction, the cell current density could be increased by 3.1% at a voltage level of 0.2 V. In a recent work, Fan and colleagues [47] used a 1D two-phase model to investigate the impact of graded CL designs on output power and current density distribution of a PEMFC. Despite some improvement in current density uniformity and the output performance, their study is only limited to a linear distribution of ionomer and catalyst within CL. Reviewing the literature clearly shows that a graded or multi-layer design of CL outperforms the simple parametric optimization due to a relatively higher degree of freedom achieved thanks to the heterogeneous distribution of design parameters. However, in graded CL designs,

Table 4.1: Summary of some selected papers from the literature

Ref.	Year	Summary of approaches and results
[40]	2000	The impact of catalyst gradients on the performance of the active layer in a PEMFC has been verified through both experimentation and modeling, encompassing both porous and non-porous active layers. The modeling of diffusion and ionic ohmic drop in the cathode's active layer further corroborated the experimental findings, demonstrating that the graded distribution of platinum nanoparticles enhances performance.
[23]	2004	The study employs mathematical modeling and simulation to investigate transport and reaction kinetics in two types of CCL agglomerates: ionomer-filled and water-filled. It reveals that ionomer-filled agglomerates display more consistent reaction rate distributions, while water-flooded agglomerates exhibit high catalyst utilization due to significant proton penetration under specific conditions. The findings highlight the importance of designing an idealized CL composite with hydrophobic secondary pores for effective macroscopic reactant transport and water removal, along with hydrophilized primary micropores for optimal wettability and proton accessibility.
[24]	2006	A model linking spatial distributions, water handling capabilities, and performance is developed using statistical theories and a macro-homogeneous model. The simulation results reveal the sensitivity of CCL operation to various factors, such as porous structure, thickness, wetting angle, and gas pressure. Notably, the findings propose that with favorable parameters (i.e., $10\,\mu\mathrm{m}$ thickness, $5\,\mathrm{atm}$ cathode gas pressure, and 89° wetting angle in case of this study), the flooding current density could reach as high as 2 to $3\,\mathrm{A\,cm^{-2}}$.
[25]	2007	The paper introduces a numerical framework for optimizing cathode electrodes under different operating conditions. By coupling an agglomerate model with a gradient-based optimization algorithm, the study determines the ideal parameters setting. The results highlight that higher platinum loading and moderate electrolyte volume fraction improve performance at low current densities, while reduced platinum loading and increased electrolyte volume fraction and porosity enhance performance at higher current densities. The research also suggests that reducing the solid phase volume fraction in the CL could lead to improved electrode performance.
[41]	2008	The study presents a model for the CCL, incorporating considerations of random porous morphology, transport properties, and electrochemical conversion. A feedback mechanism triggers a transition from low saturation, which leads to high voltage efficiency, to excessive water accumulation, affecting reaction rate distributions and causing voltage losses. Optimizing the critical current density during this transition enhances both voltage efficiency and power density, with optimal conditions favoring high porosity, a significant fraction of secondary pores, an approximate 90° wetting angle, high gas pressure, and elevated temperature.
[27]	2012	This research explores the oxygen gain in hydrogen fuel cells, which refers to the performance difference observed between cathode fuel streams with varying oxygen levels (depleted and oxygen-rich). The study develops mathematical models to distinguish between mass-transport resistances in CL and GDL medium. Two extreme scenarios are examined: cases where mass transfer limitations occur solely within CL and those external to it, in GDL. In the former situation, oxygen gain values are confined to a finite range, while in the latter, they are unrestricted. The paper proposes a diagnostic technique aimed at identifying the primary source of mass transfer degradation.
[28]	2014	The study develops a model to investigates voltage losses and to explore how agglomerate size and ionomer distribution influence the effectiveness of platinum utilization and the distribution of reaction rates during ORR. The results indicate that smaller agglomerates with higher oxygen pressure at their surface exhibit higher effectiveness factors. Moreover, it is shown that the impact of pore diameter on effectiveness factor is less significant compared to agglomerate size. While the variation of effectiveness factor with ionomer coverage is insignificant within the range of 0.125 to 0.5, higher coverage reduces the effectiveness factor due to increased resistance to oxygen diffusion. Ultimately, the study suggests that a high effectiveness factor is achieved by combining high oxygen pressure, small agglomerate size, and medium ionomer coverage.

the material distribution function should be usually prescribed in advance. Topology optimization (TO) is a rigorous mathematical optimization technique which provides a high degree of freedom in controlling distribution of decision variables in a given design domain [48–50]. TO can automatically generate spatially graded electrode designs with gradual variations in microstructural topology to achieve favorable MEA performance. In contrast to parametric optimization, which is restricted to adjusting decision variables at a global level while maintaining a uniform distribution, TO allows for control of decision variables values at a local scale [51–53]. Moreover, contrary to the graded designs, TO does not require any material distribution function prior to the optimization. Thus, it is capable of providing various heterogeneous distribution of decision variables while maintaining their global average constant. TO was initially emerged in the field of structural mechanics [54]; however, its application has been then extended to other disciplines, such as fluid-based problems [55] and reaction-diffusion systems [56, 57]. To date, the implementation of TO for electrochemical energy devices has been mainly limited to the flow field design [58–60] and thermal management [61, 62]. However, there are only a few number of studies that have investigated the employment of TO for designing innovative electrodes with heterogeneous structures [63–66]. In a recent study, Beck et al. [63] proposed a pioneer non-uniform structure design procedure for electrodes of redox flow batteries based on mathematical optimization. Their findings show that, as compared to conventional electrodes with uniform porosity distribution, using an engineered electrode with varying porosity can increase the efficiency of the battery under various operating conditions. In another study conducted by Deng and Lu [64], the authors used an optimization algorithm integrated with self-directed online machine learning to obtain the optimal topology of the porous electrode of a lithium-ion battery. By controlling the distribution of solid volume fraction in a 2D electrode, they successfully found a pattern for the structure of the electrode, which leads to 18% increment in the cell's maximum specific energy. For the purpose of optimization, they used a 5×5 grid, which is coarser than the mesh used for finite element calculations. Moreover, Lamb and Andrei [65] implemented a gradient-based topology optimization method to achieve the best configuration for the spatial distribution of constituent materials in the catalyst layer of a PEMFC. Unlike [64], which only considered porosity or solid volume fraction as a decision variable, the researchers in [65] conducted a multi-variable optimization of catalyst, electrolyte, carbon, and void volume fractions. They reported that in the case of PEMFC, it is desired to increase the volume fraction of catalyst and electrolyte in the region close to the membrane and increase the volume fraction of carbon and voids in the region

near the gas diffusion layer (GDL) to obtain higher output voltage. While the study presented in [65] shows promising results, it is important to note that the use of a single-phase model for simulating the behavior of PEMFC means that the liquid water transport mechanism was not accounted for. Since liquid water has a significant impact on PEMFC characteristics, particularly at high current densities, it is crucial to incorporate a multi-phase model to obtain a more comprehensive understanding and more robust results in the optimization process.

Reviewing the existing research works on optimal design of CL composition shows that there is a relatively small body of literature that is concerned with implementation of powerful mathematical optimization methods, like TO, to find novel electrodes with heterogeneous distribution of constituent materials. The objectives of the present study are to establish a framework for topology optimization of PEMFC electrode and to explore the optimal CL structure that provides an appropriate balance between dynamics of transport and rate processes, which as a result might enhance the overall cell performance. To accomplish this goal, first, a 2D two-phase model of PEMFC is developed that captures major electrochemical and transport phenomena of PEMFC. By considering the liquid water transfer in PEMFC, the proposed model is capable of accurately simulating the cell behavior even at high current densities. The model is then validated against experimental data to ensure the precision of the proposed mathematical formulation. Next, a topology optimization algorithm based on density model [67] is used to obtain the best structure of CCL in a given design domain with the aim of increasing the output current density at a constant cell voltage. Whilst the models that were used in the previous TO studies, such as [65], dominantly suffered from a lack of two-phase flow effects, this gap is filled by adoption of a robust mathematical description of PEMFC performance that considers those mechanisms. Hence, the findings of this research are more reliable and consistent than those reported in the literature. However, it is noteworthy that the primary aim of this study is establishment of an optimization procedure that seeks optimized structure for CL of PEMFC rather than overstated claims. The readers should bear in mind that some limitations are present in the current cell-scale modeling of PEMFC in the literature. For instance, the electrode properties (e.g., porosity) vary between the regions beneath the rib and beneath the channel due to differences in compression during the cell assembly process. However, most modeling studies in the literature assume uniform properties across these regions. Those details are beyond the scope of this study, as the current work primarily focuses on applying TO to achieve optimized material distribution in the CL. Finally, PEMFC performance

improvement as a result of the optimized CL structure will be discussed in terms of electrochemical aspects and transport phenomena.

The following parts of this chapter is divided into five sections. Section 4.2 deals with modeling of PEMFC, where the governing equations used in the present work are described. In addition, a brief explanation of various categories of PEMFC modeling that exists in the literature is provided. All the processes considered in this model are descried and their relevant mathematical correlations are provided. Section 4.3 reviews the topology optimization procedure and presents the optimization problem formulation with an explanation of the objective function and constraints. In Section 4.4, first, the developed model is validated against experimental results. Afterwards, the results obtained from the optimization process are given together with a comprehensive discussion of electrochemical and transport phenomena. Finally, the conclusion of this chapter is drawn in Section 4.5.

4.2 Mathematical modeling

In the present study, a two-phase flow, non-isothermal model is developed to simulate the performance of the PEMFC. The computational domain is shown in Fig. 4.1a. The model considers the flow channel as well as five layers of the cell, including two GDLs, two CLs, and a proton exchange membrane (PEM). The governing equations are given as follows.

Conservation of mass and species:

The conservation of species and mass for gaseous are described by the Maxwell-Stefan and Brinkman equations, respectively [68, 69]. The Maxwell-Stefan, mass continuity, and Brinkman equations are given as:

$$\rho \mathbf{u} \cdot \nabla \omega_{\mathrm{i}} - \nabla \cdot \left(\rho \omega_{\mathrm{i}} \sum_{\mathrm{k}} D_{\mathrm{ik}} \left[\nabla x_{\mathrm{k}} + (x_{\mathrm{k}} - \omega_{\mathrm{i}}) \frac{\nabla p}{p} \right] + D_{\mathrm{i}}^{\mathrm{T}} \frac{\nabla T}{T} \right) = M_{\mathrm{i}} R_{\mathrm{i}} \tag{4.1}$$

$$\nabla \cdot (\rho \mathbf{u}) = Q_{\mathrm{m}} \tag{4.2}$$

$$\frac{\rho}{\varepsilon_{\text{void}}}\left(\mathbf{u}\cdot\nabla\frac{\mathbf{u}}{\varepsilon_{\text{void}}}\right)=-\nabla p+\nabla\cdot\left[\frac{\mu}{\varepsilon_{\text{void}}}\left\{\left(\nabla\mathbf{u}+(\nabla\mathbf{u})^{\top}\right)-\frac{2}{3}(\nabla\cdot\mathbf{u})\mathbf{I}\right\}\right]-\left(\mu\kappa^{-1}+\frac{Q_{\text{m}}}{\varepsilon_{\text{void}}^{2}}\right)\mathbf{u} \quad (4.3)$$

in which $\mathbf{u}$ is velocity ($\mathrm{m\,s^{-1}}$), p is pressure (Pa), T is temperature (K), ρ is density ($\mathrm{kg\,m^{-3}}$), and μ is viscosity ($\mathrm{Pa\,s}$) of the gaseous mixture. In addition, ω, x, D^{T}, M, ε_{v}, and κ are mass fraction, mole fraction, thermal diffusion coefficient ($\mathrm{kg\,m^{-1}\,s^{-1}}$), molecular weight ($\mathrm{kg\,mol^{-1}}$), porosity, and permeability ($\mathrm{m^2}$), respectively. D_{ik} is multi-component diffusivity ($\mathrm{m^2\,s^{-1}}$). The subscripts i and k denotes the gas species. Also, R and Q_{m} represent the source terms.

Liquid water transport:

The liquid water transport equation is expressed by:

$$-\nabla\cdot(D_{\text{cap}}\nabla C_{\text{lw}})+\mathbf{u}\nabla C_{\text{lw}}=R_{\text{lw}} \quad (4.4)$$

where C_{lw} is liquid water concentration ($\mathrm{mol\,m^{-3}}$) and D_{cap} is capillary diffusivity ($\mathrm{m^2\,s^{-1}}$). The source term, R_{lw}, is determined by the rate of water condensation and evaporation in the cell. However, in CCL, where ORR is taking place, the produced liquid water is also contributing to this source term. The water saturation, s_{lw}, is correlated to the liquid water concentration through the following relationship.

$$s_{\text{lw}}=\frac{M_{\text{H}_2\text{O}}}{\varepsilon_{\text{void}}\rho_{\text{lw}}}C_{\text{lw}} \quad (4.5)$$

Dissolved water transport:

The transport of dissolved water through membrane/ionomer in ACL, PEM, and CCL is given by:

$$-\nabla\cdot(D_{\text{dw}}C_{\text{dw}})=S_{\text{d}} \quad (4.6)$$

In Eq. (4.6), D_{dw} and C_{dw} are dissolved water diffusivity ($\mathrm{m^2\,s^{-1}}$) and dissolved water concentration ($\mathrm{mol\,m^{-3}}$), respectively. The boundary conditions required for solving this equation are calculated based on the relative humidity level (RH) at the interface

Table 4.2: Source terms

Source terms	Domain
$Q_{\mathrm{m}} = M_{\mathrm{H_2}} S_{\mathrm{H_2}} + M_{\mathrm{O_2}} S_{\mathrm{O_2}} + M_{\mathrm{H_2O}} S^{\mathrm{v}}_{\mathrm{H_2O}}$	GDLs and CLs
$S_{\mathrm{H_2}} = \frac{i^{\mathrm{a}}_{\mathrm{src}}}{2F}$	ACL
$S_{\mathrm{O_2}} = \frac{i^{\mathrm{c}}_{\mathrm{src}}}{4F}$	CCL
$S^{\mathrm{v}}_{\mathrm{H_2O}} = \begin{cases} h_{\mathrm{cond}} \frac{\varepsilon_{\mathrm{void}}(1-s_{\mathrm{lw}}) x^{\mathrm{v}}_{\mathrm{H_2O}}}{RT} (x^{\mathrm{v}}_{\mathrm{H_2O}} p - p^{\mathrm{sat}}) & \text{if } x^{\mathrm{v}}_{\mathrm{H_2O}} p \geq p^{\mathrm{sat}} \\ h_{\mathrm{evp}} C_{\mathrm{lw}} (p^{\mathrm{sat}} - x^{\mathrm{v}}_{\mathrm{H_2O}} p) & \text{if } x^{\mathrm{v}}_{\mathrm{H_2O}} p < p^{\mathrm{sat}} \end{cases}$	GDLs and CLs
$R^{\mathrm{rxn}}_{\mathrm{lw}} = \frac{i^{\mathrm{a}}_{\mathrm{src}}}{2F}$	CCL
$S_{\mathrm{d}} = h_{\mathrm{mass}} (C_{\mathrm{H_2O}} - C_{\mathrm{wp}})$	CLs
$S^{\mathrm{electric}}_{\mathrm{T,joule}} = \frac{j^2_{\mathrm{electric}}}{\sigma^{\mathrm{eff}}_{\mathrm{s}}}$	GDLs and CLs
$S^{\mathrm{ionic}}_{\mathrm{T,joule}} = \frac{j^2_{\mathrm{ionic}}}{\sigma^{\mathrm{eff}}_{\mathrm{m}}}$	CLs and PEM
$S^{\mathrm{a}}_{\mathrm{T,rxn}} = \lvert i^{\mathrm{a}}_{\mathrm{src}} \rvert (\lvert \eta^{\mathrm{a}} \rvert - \frac{T\Delta S^{\mathrm{a}}}{2F})$	ACL
$S^{\mathrm{c}}_{\mathrm{T,rxn}} = \lvert i^{\mathrm{c}}_{\mathrm{src}} \rvert (\lvert \eta^{\mathrm{c}} \rvert - \frac{T\Delta S^{\mathrm{c}}}{4F})$	CCL
$S_{\mathrm{T,phase}} = M_{\mathrm{H_2O}} S^{\mathrm{v}}_{\mathrm{H_2O}} \Delta h_{\mathrm{H_2O}}$	GDLs and CLs

between CL and GDL. The dissolved water concentration at this interface is formulated as [69]:

$$C_{\mathrm{dw}}|_{\mathrm{CL/GDL}} = \left(0.043 + 17.81\mathrm{RH} - 39.85\mathrm{RH}^2 + 36.0\mathrm{RH}^3\right) \frac{\rho_{\mathrm{m}}}{EW} \tag{4.7}$$

where ρ_{m} is density of ionomer/membrane ($\mathrm{kg\,m^{-3}}$) and EW is the equivalent weight of ionomer/membrane ($\mathrm{kg\,mol^{-1}}$).

Conservation of energy:

Given the assumption that all phases are in thermal equilibrium, the energy conservation is governed by [62, 68]:

$$\nabla \cdot \left(\sum_{\mathrm{i=g,l}} [\rho c_{\mathrm{p}} \mathbf{u}]_{\mathrm{i}} T \right) - \nabla \cdot \left(\sum_{\mathrm{i=g,l,s}} k_{\mathrm{i}} \nabla T \right) = S_{\mathrm{T}} \tag{4.8}$$

where c_{p} and k are specific heat capacity ($\mathrm{J\,mol^{-1}\,K^{-1}}$) and thermal conductivity ($\mathrm{W\,m^{-1}\,K^{-1}}$), respectively. The subscript i denotes the gas mixture, liquid water, and solid phase. It is noteworthy that the energy source term, S_{T}, is a summation of heat generation/consumption by electrochemical reaction, Joule heating, and the water phase change process. All source terms are listed in Table 4.2.

Conservation of charge:

The electrons and protons are transferred through carbon-supported platinum and ionomer, respectively. The electron transport in GDLs and CLs of both anode and cathode sides, as well as proton transport in CLs and PEM, is modeled by Ohm's law. The conservation of charges are expressed by:

$$\nabla \cdot (-\sigma_{\mathrm{s}}^{\mathrm{eff}} \nabla \phi_{\mathrm{s}}) = -i_{\mathrm{src}} \tag{4.9}$$

$$\nabla \cdot (-\sigma_{\mathrm{m}}^{\mathrm{eff}} \nabla \phi_{\mathrm{m}}) = i_{\mathrm{src}} \tag{4.10}$$

in which $\sigma_{\mathrm{s}}^{\mathrm{eff}}$ and $\sigma_{\mathrm{m}}^{\mathrm{eff}}$ are effective electric and ionic conductivities ($\mathrm{S\,m^{-1}}$), respectively. Moreover, ϕ_{s} and ϕ_{m} are solid and electrolyte phases potentials (V), respectively, and i_{src} is volumetric current density source ($\mathrm{A\,m^{-3}}$). The current density source is zero within both the GDLs and PEM. The calculation of i_{src} within the CLs is addressed in the next subsection.

4.2.1 Agglomerate model

A spherical agglomerate sub-model (see Fig. 4.1b), adopted from [68–71], is utilized to determine the electrochemical kinetics. It is assumed that the agglomerate is covered with a thin ionomer film. Moreover, owing to the hydrophilic properties of the ionomer, the liquid water produced during the electrochemical reaction is considered to form an additional layer, overlaying the ionomer film [69]. The ionomer film thickness is treated as an input for the model, whereas the water film thickness is calculated based on the liquid water saturation, as described in a subsequent equation. Previous experimental and numerical studies reported various values for the thickness of ionomer film, spanning from a few nanometers to as much as $100\,\mathrm{nm}$ [72–75]. Moreover, although microscopy studies [76, 77] reported a value between 50 to 170 nm for the agglomerate radius, numerical studies typically reported larger values in a range between 50 and 5000 nm [68, 73, 75, 78]. This occurs because, in cell-scale modeling, the intricate microstructure of CL is substituted with volume-averaged characteristics, like porosity. Consequently, certain adjustments or fittings are necessary to mimic the experimental performance results. The summation of constituent volume fractions in CL is as follows:

$$\varepsilon_{\mathrm{PtC}} + \varepsilon_{\mathrm{l}} + \varepsilon_{\mathrm{void}} = 1 \tag{4.11}$$

where $\varepsilon_{\mathrm{PtC}}$ and ε_{l} are volume fractions of carbon-supported platinum and ionomer, respectively. The volume fraction of platinum and carbon might be separated according to Eqs. (4.12) and (4.13).

$$\varepsilon_{\mathrm{Pt}} = \frac{m_{\mathrm{Pt}}}{t_{\mathrm{CL}}\rho_{\mathrm{Pt}}} \tag{4.12}$$

$$\varepsilon_{\mathrm{C}} = \frac{m_{\mathrm{Pt}}(1-\gamma_{\mathrm{PtC}})}{\gamma_{\mathrm{PtC}}t_{\mathrm{CL}}\rho_{\mathrm{C}}} \tag{4.13}$$

in which m_{Pt} is platinum loading ($\mathrm{kg\,m^{-2}}$), t_{CL} is thickness of CL (m), ρ_{Pt} and ρ_{C} are platinum and carbon densities ($\mathrm{kg\,m^{-3}}$), and γ_{PtC} is platinum mass fraction. Knowing the carbon loading m_{C} ($\mathrm{kg\,m^{-2}}$), the platinum mass fraction is expressed as:

$$\gamma_{\mathrm{PtC}} = \frac{m_{\mathrm{Pt}}}{m_{\mathrm{Pt}} + m_{\mathrm{C}}} \tag{4.14}$$

The radius of agglomerate r_{agg} and thickness of ionomer film δ_{N} (m) are given as model input. The agglomerate density, which is defined as the number of agglomerates per unit volume of CL, reads as:

$$N_{\mathrm{agg}} = \frac{1-\varepsilon_{\mathrm{void}}}{\frac{4}{3}\pi(r_{\mathrm{agg}}+\delta_{\mathrm{N}})^3} \tag{4.15}$$

The specific surface area of agglomerate with water coating is given by:

$$a'_{\mathrm{agg}} = a_{\mathrm{agg}}\left(\frac{r_{\mathrm{agg}}+\delta_{\mathrm{N}}+\delta_{\mathrm{W}}}{r_{\mathrm{agg}}+\delta_{\mathrm{N}}}\right)^2 \tag{4.16}$$

where a_{agg} and a'_{agg} are specific surface area of agglomerate without and with water coating ($\mathrm{m^{-1}}$), respectively, and δ_{W} is the thickness of liquid water coating (m) covering the agglomerate. The value of a_{agg} is computed by:

$$a_{\mathrm{agg}} = 4\pi N_{\mathrm{agg}}(r_{\mathrm{agg}}+\delta_{\mathrm{N}})^2 \tag{4.17}$$

Knowing that Nafion ionomer is hydrophilic, it is assumed that the generated water by the electrochemical reaction forms a liquid water coating on the ionomer film [69]. The thickness of liquid water coating is estimated by [69]:

$$\delta_{\mathrm{W}} = \sqrt[3]{(r_{\mathrm{agg}} + \delta_{\mathrm{N}})^3 + \frac{s_{\mathrm{lw}}\varepsilon_{\mathrm{void}}}{\frac{4}{3}\pi N_{\mathrm{agg}}}} - (r_{\mathrm{agg}} + \delta_{\mathrm{N}}) \tag{4.18}$$

For CCL, the volumetric current density source is expressed by [69, 70]:

$$i_{\mathrm{src}}^{\mathrm{c}} = 4F\frac{P_{\mathrm{O_2}}}{H_{\mathrm{O_2}}}\left[\frac{1}{E_{\mathrm{r}}k_{\mathrm{c}}\frac{r_{\mathrm{agg}}^3 a_{\mathrm{agg}}}{(r_{\mathrm{agg}}+\delta_{\mathrm{N}})^2}} + \frac{(r_{\mathrm{agg}}+\delta)}{\xi r_{\mathrm{agg}}}\right]^{-1} \tag{4.19}$$

in which

$$\delta = \delta_{\mathrm{N}} + \delta_{\mathrm{W}} \tag{4.20}$$

and

$$\xi = \frac{\xi_{\mathrm{N}}\xi_{\mathrm{W}}}{\xi_{\mathrm{N}} + \xi_{\mathrm{W}}} \tag{4.21}$$

$$\xi_{\mathrm{N}} = \frac{a_{\mathrm{agg}} D_{\mathrm{O_2-N}}}{\delta_{\mathrm{N}}} \tag{4.22}$$

$$\xi_{\mathrm{W}} = \frac{a'_{\mathrm{agg}} D_{\mathrm{O_2-W}}}{\delta_{\mathrm{W}}} \tag{4.23}$$

where $D_{\mathrm{O_2-N}}$ and $D_{\mathrm{O_2-W}}$ are diffusivity of oxygen in ionomer and water ($\mathrm{m^2\,s^{-1}}$), respectively. In Eq. (4.19), $P_{\mathrm{O_2}}$ is oxygen partial pressure (Pa) and $H_{\mathrm{O_2}}$ is Henry's constant for oxygen dissolution ($\mathrm{Pa\,m^3\,mol^{-1}}$). In addition, the reaction rate coefficient (k_{c}) and effectiveness factor (E_{r}) in this equation are calculated as follows [69]:

$$k_{\mathrm{c}} = \frac{A_{\mathrm{Pt}}}{4F(1-\varepsilon_{\mathrm{void}})}\left(\frac{i_{0,\mathrm{c}}}{C_{\mathrm{O_2}}^{\mathrm{ref}}}\right)\left[-\exp\left(\frac{(1-\alpha_{\mathrm{c}})F\eta_{\mathrm{c}}}{RT}\right) + \exp\left(\frac{-\alpha_{\mathrm{c}}F\eta_{\mathrm{c}}}{RT}\right)\right] \tag{4.24}$$

$$E_{\mathrm{r}} = \frac{1}{Th}\left[\frac{1}{\tanh(Th)} - \frac{1}{Th}\right] \tag{4.25}$$

in which A_{Pt} is total reaction area per unit volume of agglomerate ($\mathrm{m^{-1}}$), $i_{0,\mathrm{c}}$ is exchange current density for oxygen reduction reaction ($\mathrm{A\,m^{-2}}$), $C_{\mathrm{O_2}}^{\mathrm{ref}}$ is oxygen reference concentration ($\mathrm{mol\,m^{-3}}$), α_{c} is cathode charge transfer coefficient, η_{c} is cathode overpotential (V), R is gas constant ($\mathrm{J\,mol^{-1}\,K^{-1}}$), and Th is Thiele modulus. It is noteworthy that the dependence of ORR rate on the local concentration (pressure) of

oxygen is considered in Eq. (4.19). The temperature dependence of exchange current density is expressed using an Arrhenius relationship as [79]:

$$i_{0,\mathrm{c}} = i_{0,\mathrm{c}}^{\mathrm{ref}} \exp\left[-\frac{E_{\mathrm{a}}}{RT}\left(1-\frac{T}{T^{\mathrm{ref}}}\right)\right] \tag{4.26}$$

where $i_{0,\mathrm{c}}^{\mathrm{ref}}$, E_{a}, and T^{ref} are reference exchange current density ($\mathrm{A\,m^{-2}}$), activation energy ($\mathrm{J\,mol^{-1}}$), and reference temperature (K). The activation energy of ORR on platinum is $66000\,\mathrm{J\,mol^{-1}}$ [79]. In addition, A_{Pt} reads as [69]:

$$A_{\mathrm{Pt}} = A_0 \frac{m_{\mathrm{Pt}}}{t_{\mathrm{CL}}} \tag{4.27}$$

where A_0 ($\mathrm{m^2\,kg^{-1}}$) is given by the following empirical relationship as a function of platinum mass fraction [69, 70].

$$A_0 = \left[2.2779\gamma_{\mathrm{PtC}}^3 - 1.5857\gamma_{\mathrm{PtC}}^2 - 2.0153\gamma_{\mathrm{PtC}} + 1.5950\right] \times 10^5 \tag{4.28}$$

Additionally, Thiele modulus is evaluated as:

$$Th = r_{\mathrm{agg}} \sqrt{\frac{k_{\mathrm{c}}}{D_{\mathrm{agg}}^{\mathrm{eff}}}} \tag{4.29}$$

where $D_{\mathrm{agg}}^{\mathrm{eff}}$ is effective diffusivity of oxygen within agglomerate ($\mathrm{m^2\,s^{-1}}$) and is computed based on Bruggeman equation as follows:

$$D_{\mathrm{agg}}^{\mathrm{eff}} = D_{\mathrm{O_2-N}} \times \varepsilon_{\mathrm{agg}}^{1.5} \tag{4.30}$$

In Eq. (4.30), $\varepsilon_{\mathrm{agg}}$ is fraction of agglomerate volume filled with ionomer and might be evaluated as:

$$\varepsilon_{\mathrm{agg}} = 1 - \left(\frac{\varepsilon_{\mathrm{PtC}}}{\frac{4}{3}\pi N_{\mathrm{agg}} r_{\mathrm{agg}}^3}\right) \tag{4.31}$$

For ACL, the hydrogen reduction kinetics follows the well-known Butler-Volmer relationship as [69]:

$$i_{\mathrm{src}}^{\mathrm{a}} = A_{\mathrm{Pt}} i_{0,\mathrm{a}}^{\mathrm{ref}} \left(\frac{1-\varepsilon_{\mathrm{void}}}{\varepsilon_{\mathrm{PtC}}}\right) \left(\frac{P_{\mathrm{H_2}}}{H_{\mathrm{H_2}} C_{\mathrm{H_2}}^{\mathrm{ref}}}\right)^{0.5} \left[\exp\left(\frac{\alpha_{\mathrm{a}} F \eta_{\mathrm{a}}}{RT}\right) - \exp\left(\frac{-(1-\alpha_{\mathrm{a}}) F \eta_{\mathrm{a}}}{RT}\right)\right] \tag{4.32}$$

in which $i_{0,\mathrm{a}}^{\mathrm{ref}}$ is anode exchange current density, $P_{\mathrm{H_2}}$ is hydrogen partial pressure (Pa), $H_{\mathrm{H_2}}$ is Henry's constant for hydrogen dissolution ($\mathrm{Pa\,m^3\,mol^{-1}}$), and $C_{\mathrm{H_2}}^{\mathrm{ref}}$ is hydrogen reference concentration ($\mathrm{mol\,m^{-3}}$). Moreover, α_{a} is anode charge transfer coefficient and η_{a} is anode overpotential (V). Since anode charge transfer coefficient and anode exchange current density exhibit weak dependence on temperature, they are considered constant across various operating temperatures [69]. However, considering the relatively greater influence of temperature on the cathode charge transfer coefficient, this parameter was fine-tuned during the validation process to achieve results that effectively replicate the experimental data [69]. For both anode and cathode CLs, activation overpotential is given by:

$$\eta = \phi_{\mathrm{s}} - \phi_{\mathrm{m}} - E^{\mathrm{eq}} \tag{4.33}$$

where E^{eq} is equilibrium potential (V). A list of additional relationships and physical properties are given in Tables 4.3 and 4.4.

4.2.2 Boundary conditions

The electric potential on the anode rib ($\mathrm{A} - \mathrm{A}'$ and $\mathrm{A}'' - \mathrm{A}'''$) and cathode rib ($\mathrm{F} - \mathrm{F}'$ and $\mathrm{F}'' - \mathrm{F}'''$) are defined as Dirichlet boundary conditions. The value on anode side is set to be zero and on the cathode side corresponds to the cell voltage. The dissolved water concentration at the CL/GDL interface for both anode and cathode sides ($\mathrm{B} - \mathrm{B}'$ and $\mathrm{D} - \mathrm{D}'$) are defined as Dirichlet boundary condition according to Eq. (4.7). The conditions at anode inlet ($\mathrm{A}' - \mathrm{A}''$) and anode rib ($\mathrm{A} - \mathrm{A}'$ and $\mathrm{A}'' - \mathrm{A}'''$) are given by:

$$p = p_{\mathrm{a}};\; x_{\mathrm{H_2O},a}^{0} = \frac{P^{\mathrm{sat}} \mathrm{RH}_{\mathrm{a}}}{p_{\mathrm{a}}};\; x_{\mathrm{H_2},a}^{0} = 1 - x_{\mathrm{H_2O},a}^{0};\; T = T_{\mathrm{a}}^{0} \tag{4.34}$$

in which x represents the mole fraction. Likewise, the boundary condition at cathode inlet ($\mathrm{F}' - \mathrm{F}''$) and cathode rib ($\mathrm{F} - \mathrm{F}'$ and $\mathrm{F}'' - \mathrm{F}'''$) are expressed as:

Table 4.3: Additional relationships and definitions

Description	Equation	Unit
Ionic conductivity [68]	$\sigma_{\mathrm{m}}^{0} = (0.514\lambda - 0.326)\exp\left[1268(\frac{1}{303} - \frac{1}{T})\right]$	$\mathrm{S\,m^{-1}}$
Effective ionic conductivity [68]	$\sigma_{\mathrm{m}}^{\mathrm{eff}} = \sigma_{\mathrm{m}}^{0}\varepsilon_{\mathrm{l}}^{1.5}$	$\mathrm{S\,m^{-1}}$
Effective electric conductivity [68]	$\sigma_{\mathrm{s}}^{\mathrm{eff}} = \sigma_{\mathrm{s}}^{0}\varepsilon_{\mathrm{PtC}}^{1.5}$, $\sigma_{\mathrm{s}}^{\mathrm{eff}} = \sigma_{\mathrm{s}}^{0}(1-\varepsilon_{\mathrm{void}}^{\mathrm{GDL}})^{1.5}$	$\mathrm{S\,m^{-1}}$
Water content [80]	$\lambda = \frac{EW}{\rho_{\mathrm{m}}}C_{\mathrm{dw}}$	-
Dissolved water diffusivity [68]	$D_{\mathrm{dw}} = 10^{-10}\exp\left[2416(\frac{1}{303} - \frac{1}{T})\right]\begin{cases} 2.05\lambda - 3.25 & \text{for } 2 \le \lambda < 3 \\ 6.65 - 1.25\lambda & \text{for } 3 \le \lambda < 4 \\ 2.563 - 0.33\lambda + 0.0264\lambda^2 - 0.000671\lambda^3 & \text{for } \lambda \ge 4 \end{cases}$	$\mathrm{m^2\,s^{-1}}$
Effective porosity	$\varepsilon_{\mathrm{void}}^{\mathrm{eff}} = \varepsilon_{\mathrm{void}}(1 - s_{\mathrm{lw}})$	-
Leverett function [69]	$J = \begin{cases} 1.417(1-s_{\mathrm{lw}}) - 2.120(1-s_{\mathrm{lw}})^2 + 1.263(1-s_{\mathrm{lw}})^3 & \text{for } \theta < 90^\circ \\ 1.417s_{\mathrm{lw}} - 2.120s_{\mathrm{lw}}^2 + 1.263s_{\mathrm{lw}}^3 & \text{for } \theta > 90^\circ \end{cases}$	-
Capillary pressure [68]	$P_{\mathrm{cap}} = \sigma_{\mathrm{lw}}\cos(\theta)\left(\frac{\varepsilon_{\mathrm{void}}}{\kappa}\right)^{0.5}J$	Pa
Saturation pressure [69]	$P^{\mathrm{sat}} = 10^{\left[-2.1794+0.02953(T-273.15)-9.1837\times10^{-5}(T-273.15)^2+1.4454\times10^{-7}(T-273.15)^3\right]}$	Pa
Relative permeability [68]	$\kappa_{\mathrm{l}}^{\mathrm{rel}} = \kappa s_{\mathrm{lw}}^{3}$	$\mathrm{m^2}$
Capillary diffusivity [68]	$D_{\mathrm{cap}} = -\frac{\kappa_{\mathrm{l}}^{\mathrm{rel}}}{\mu_{\mathrm{lw}}}\left(\frac{\partial P_{\mathrm{cap}}}{\partial s_{\mathrm{lw}}}\right)$	$\mathrm{m^2\,s^{-1}}$
Cathode equilibrium potential [69]	$E_{\mathrm{c}}^{\mathrm{eq}} = 1.482 - 8.45\times10^{-4}T + 4.31\times10^{-5}T\ln\left(p_{\mathrm{H_2}}p_{\mathrm{O_2}}^{0.5}\right)$	V
Equilibrium vapor concentration [81]	$C_{\mathrm{wp}} = \frac{P^{\mathrm{sat}}}{RT}a$	$\mathrm{mol\,m^{-3}}$

Table 4.4: Physical and transport properties

Parameter	Symbol	Value/Expression	Unit
Platinum density [69]	ρ_{Pt}	21450	$\mathrm{kg\,m^{-3}}$
Carbon density [69]	ρ_{C}	2000	$\mathrm{kg\,m^{-3}}$
Ionomer density [69]	ρ_{m}	1800	$\mathrm{kg\,m^{-3}}$
Ionomer equivalent weight [69]	EW	1.1	$\mathrm{kg\,mol^{-1}}$
Permeability (GDL, CL) [69]	κ	4.97×10^{-13}, $4.97\times10^{-13}(\varepsilon_{\mathrm{void}}^{\mathrm{CL}}/\varepsilon_{\mathrm{void}}^{\mathrm{GDL}})^{1.5}$	$\mathrm{m^2}$
Agglomerate radius [75]	r_{agg}	7×10^{-7}	m
Ionomer film thickness [72]	δ_{N}	7×10^{-9}	m
Oxygen reference concentration [82]	$C_{\mathrm{O_2}}^{\mathrm{ref}}$	3.39	$\mathrm{mol\,m^{-3}}$
Hydrogen reference concentration [82]	$C_{\mathrm{H_2}}^{\mathrm{ref}}$	56.4	$\mathrm{mol\,m^{-3}}$
Water surface tension coefficient [82]	σ_{lw}	0.0625	$\mathrm{N\,m^{-1}}$
Evaporation rate constant [69]	h_{evp}	100	$\mathrm{atm^{-1}\,s^{-1}}$
Condensation rate constant [69]	h_{cond}	100	$\mathrm{s^{-1}}$
Electric conductivity [69]	σ_{s}^{0}	1250	$\mathrm{S\,m^{-1}}$
Latent heat of condensation/evaporation [69]	$\Delta h_{\mathrm{H_2O}}$	2.308×10^{6}	$\mathrm{J\,kg^{-1}}$
Entropy of hydrogen oxidation [69]	ΔS^{a}	161.2	$\mathrm{J\,mol^{-1}\,K^{-1}}$
Entropy of oxygen reduction [69]	ΔS^{a}	-324	$\mathrm{J\,mol^{-1}\,K^{-1}}$

$$p = p_{\mathrm{c}};\ x^0_{\mathrm{H_2O},c} = \frac{P^{\mathrm{sat}}\mathrm{RH_c}}{p_{\mathrm{c}}};\ x^0_{\mathrm{O_2},c} = 0.21(1 - x^0_{\mathrm{H_2O},c});$$
$$x^0_{\mathrm{N_2},c} = 0.79(1 - x^0_{\mathrm{H_2O},c});\ T = T^0_{\mathrm{c}} \quad (4.35)$$

The liquid water saturation at the cathode inlet ($\mathrm{F}' - \mathrm{F}''$) is set to be zero. A symmetry boundary condition is considered for all other boundaries.

4.3 Topology optimization

TO is a relatively more advanced method compared to other conventional optimization techniques, such as shape and size optimizations. Compared to other optimization approaches that usually focus on globally tuning a set of decision variables to maximize or minimize one or more objective functions, TO stands out for its ability to finely control those variables at a local level. From this standpoint, the higher degree of freedom provided by TO makes it a robust and strong optimization tool. TO considers optimization process as a material distribution problem and seeks to generate creative layouts within a defined design domain to either maximize or minimize a specified objective function. In this sense, a material allocation problem might mathematically read as:

$$\theta(\mathbf{x}) = \begin{cases} 1 & \text{if } \mathbf{x} \in \Omega_{\mathrm{M}} \\ 0 & \text{if } \mathbf{x} \in \Omega \backslash \Omega_{\mathrm{M}} \end{cases} \quad (4.36)$$

in which $\mathbf{x}$ is any position in the given design domain (Ω) and θ is a material distribution function. The distribution θ takes a value of one ($\theta = 1$) in regions where material exists (Ω_{M}), while it is set to zero ($\theta = 0$) in void regions. Given the fact that working with a discontinuous function is mathematically troublesome, a "density method" [67] is usually used in real applications. This method replaces the discontinuous function, θ, with an analogous continuous density function, θ_{C}, which can take any value between zero and one ($0 \leq \theta_{\mathrm{C}}(\mathbf{x}) \leq 1$). In structural mechanics problem, where any intermediate value for the density function (other than zero or one) is physically meaningless, some additional considerations, such as "Simplified Isotropic Material with Penalization" (SIMP) method [67], are taken into account to obtain a more accurate correlation between density value and material

properties. However, in this study, as we are working with volume fraction of constituent materials (rather than Boolean-type distribution of materials), the effective material properties are correlated to the volume fraction of corresponding materials through power-law relationships as expressed in Table 4.3. In other words, a power-law (Bruggeman equation) penalization scheme is utilized to reflect the effect of TO homogenization on the material parameters in the governing equations. Standard regularization methods are implemented on optimization solutions to prevent the checkerboard pattern problem. It is a well-studied problem in the field of TO [83–85] and has been resolved by utilization of solution filtering and projection. This research exploits a Helmholtz-type filter [83] as well as a hyperbolic tangent projection [86] to address this problem. Helmholtz filter is expressed as a solution to the following partial differential equation (PDE).

$$\begin{aligned} -R_{\mathrm{f}}^2\nabla^2\tilde{\theta_{\mathrm{C}}}(\mathbf{x}) + \tilde{\theta_{\mathrm{C}}}(\mathbf{x}) &= \theta_{\mathrm{C}}(\mathbf{x}) \\ \nabla\tilde{\theta_{\mathrm{C}}}\cdot\hat{\mathbf{n}} &= 0 \quad \text{on}\,\Gamma \end{aligned} \tag{4.37}$$

In Eq. (4.37), $\tilde{\theta_{\mathrm{C}}}$ and R_{f} are filtered density function and the filter radius, respectively. To obtain filtered density function, Helmholtz PDE should be solved based on a homogeneous Neumann boundary condition, as shown in the above equation (Γ is the boundary of the design domain). Additionally, a hyperbolic tangent projection [86] is used to further regulate the optimization solutions, as follows:

$$\tilde{\tilde{\theta}}_{\mathrm{C}} = \frac{\tanh\Big(\beta(\tilde{\theta_{\mathrm{C}}} - \theta_\beta)\Big) + \tanh(\beta\theta_\beta)}{\tanh(\beta(1-\theta_\beta)) + \tanh(\beta\theta_\beta)} \tag{4.38}$$

where $\tilde{\tilde{\theta}}_{\mathrm{C}}$ is the density function after projection, and β and θ_β are projection tuning parameters. In the literature, β is called projection steepness and θ_β is known as projection point. Next, "globally convergent method of moving asymptotes" (GCMMA) algorithm [87] is used to update the decision variables. GCMMA is a gradient-based algorithm; as a consequence, the sensitivity of objective function with respect to the decision variables should be calculated. Sensitivity analysis is performed using the adjoint state method [88]. Contrary to other approaches, like forward method, which are computationally expensive, the adjoint method is independent of the number of the decision variables. Hence, it is a very efficient technique from the computational perspective, which makes it especially suitable for TO problems that typically include numerous decision variables. According to this method, the total derivative of an objective function (F_{obj}) with respect to each decision variable, ζ_{i}, is indicated as:

$$\frac{dF_{\mathrm{obj}}}{d\zeta_{\mathrm{i}}} = \frac{\partial F_{\mathrm{obj}}}{\partial \zeta_{\mathrm{i}}} + \boldsymbol{\lambda}^{\intercal} \frac{\partial \mathbf{G}}{\partial \zeta_{\mathrm{i}}} \tag{4.39}$$

in which $\boldsymbol{\lambda}$ is the vector of adjoint variables and $\mathbf{G}$ is the system of governing PDEs. As this study deals with CL structure optimization, the decision variables (ζ) are considered being volume fractions of PtC ($\varepsilon_{\mathrm{PtC}}$) and ionomer ($\varepsilon_{\mathrm{l}}$). The adjoint variables are given as the solution to the following adjoint equation:

$$\left(\frac{\partial \mathbf{G}}{\partial \mathbf{U}}\right)^{\intercal} \boldsymbol{\lambda} = -\left(\frac{\partial F_{\mathrm{obj}}}{\partial \mathbf{U}}\right)^{\intercal} \tag{4.40}$$

where $\mathbf{U}$ is a vector of state variables that are determined from the governing equations.

4.3.1 Problem formulation

As previously mentioned, the performance of PEMFC depends on several coupled transport and rate processes that are taking place in the cell. In such a situation, the overall cell performance is dictated by the slowest process. For instance, the rate of an electrochemical reaction not only depends on charge transfer rate but also is affected by the rate at which reactant species are supplied (or product species are removed). The effective transport and rate properties of CL might be controlled by the volume fraction of constituent materials. For example, a very high volume fraction of PtC is beneficial to increase the rate of reactant consumption. On the other hand, this means a lower porosity, which in return causes sluggish gas transport. A huge drop in reactant delivery might deteriorate the overall cell performance. Hence, the composition of CL should be adjusted in a way that a compromise would be obtained between various processes. The output power density of PEMFC, which indicates the cell performance, could be estimated knowing the cell voltage and current density. At any specific current density, the cell voltage can be calculated using the governing equations expressed in Section 4.2. Therefore, at any given current density, a superior performance might be achieved if the overpotential is decreased and consequently, the cell voltage is increased. The optimization problem at a given current density ($I_{\mathrm{cell}}^{\mathrm{in}}$) is defined as:

$$\begin{aligned}
\max_{\varepsilon_{\mathrm{PtC}},\varepsilon_{\mathrm{l}}} \quad & F_{\mathrm{obj}} = V_{\mathrm{cell}}\Big|_{@\, I_{\mathrm{cell}}^{\mathrm{in}}} \\
\text{s.t.} \quad & \varepsilon_{\mathrm{PtC}}(\mathbf{x}) + \varepsilon_{\mathrm{l}}(\mathbf{x}) + \varepsilon_{\mathrm{void}}(\mathbf{x}) = 1 \quad \forall \mathbf{x} \in \Omega_{\mathrm{CCL}} \\
& 0 \leq \varepsilon_{\mathrm{PtC}}(\mathbf{x}) \text{ and } \varepsilon_{\mathrm{l}}(\mathbf{x}) \leq 1 \quad \forall \mathbf{x} \in \Omega_{\mathrm{CCL}} \\
& 0 \leq m_{\mathrm{Pt}}^{\mathrm{avg}} \leq m_{\mathrm{Pt}}^{\mathrm{max}} \\
& 0 \leq \varepsilon_{\mathrm{l}}^{\mathrm{avg}} \leq \varepsilon_{\mathrm{l}}^{\mathrm{max}}
\end{aligned} \tag{4.41}$$

where Ω_{CCL} is the CCL domain. Since the overpotential in CCL is greater than that of the anode catalyst layer (ACL), this study only focuses on the spatial structure of this component. However, the described procedure might be applied to any other component of PEMFC by considering appropriate decision variables. Furthermore, according to the formulation of Eq. (4.41), the optimization objective is defined as maximization of the cell voltage at a specific current density $I_{\mathrm{cell}}^{\mathrm{in}}$. The optimization problem is subject to some physical and design constraint as shown in Eq. (4.41). First, at the local level, a physical constraint applies to any position $\mathbf{x}$ in the CCL domain, which requires that the summation of volume fractions of constituents adds up to one. Additionally, by definition, the volume fraction of each decision variable cannot be more than unity at a local level. In practical implementation, the optimization algorithm updates the value of decision variables ($\varepsilon_{\mathrm{PtC}}$ and ε_{l}) in each iteration while calculating the porosity automatically through $\varepsilon_{\mathrm{void}} = 1-(\varepsilon_{\mathrm{PtC}}+\varepsilon_{\mathrm{l}})$. At a global level, the optimization problem might be subject to some additional constraints. In the present study, the problem is formulated so that the average mass loading of platinum ($m_{\mathrm{Pt}}^{\mathrm{avg}}$) and average ionomer volume fraction ($\varepsilon_{\mathrm{l}}^{\mathrm{avg}}$) over the entire CCL do not exceed a maximum value ($m_{\mathrm{Pt}}^{\mathrm{max}}$ and $\varepsilon_{\mathrm{l}}^{\mathrm{max}}$). A major difference between parametric and TO rises from the fact that parametric optimization can only control the average mass loading (or average volume fraction) of constituent materials; however, TO not only controls the average mass loading but also adjusts their distribution. When performing parametric optimization, a higher loading of platinum or ionomer may lead to enhanced output power. Nevertheless, it should be noted that a higher platinum (or ionomer) loading implies more expensive cell as well. Opposed to conventional parametric optimization, TO does not necessarily improve CL design by using more amount of platinum or ionomer. However, it promotes the cell performance through more effective distribution of the available materials. It is also noteworthy that while the previously introduced density function (θ_{C}) does not appear explicitly in the optimization problem Eq. (4.41), a unique density function is assigned for determination of each decision variable during the optimization process. In this regard, the

decision variables ($\varepsilon_{\mathrm{PtC}}$ and ε_{l}) are updated according to the value of their relevant density function after regularization.

4.3.2 Numerical implementation

The numerical procedure used in the present study to find the optimal CL design is as follows. The mathematical model developed in the previous section is implemented in COMSOL Multiphysics ® (version 5.6) software to solve the governing equations by a finite element method. The parameters used in this study are tabulated in Table 4.5. By solving these equations for a wide range of current densities, polarization characteristics of the PEMFC are obtained. The obtained I-V is then compared to an experimental data set to confirm the validity of the proposed model. Next, an optimization is conducted to obtain the optimal distribution of material in CCL. TO process begins with initialization of the design variables and evaluation of the objective function according to Eq. (4.41). Next, the sensitivity (gradient) of objective function with respect to the design variables is computed. By regularization of the design variables using a Helmholtz filtering and hyperbolic tangent projection schemes, the optimization process is continued. In the subsequent step, the GCMMA algorithm is used to update the design variables. As the measured sensitivity has a different value at each position in the calculation domain, the design variables are updated at a local level accordingly. Hence, the updated values of design variables vary with the position, which gives a rise to a heterogeneous layout. TO favors non-uniform distribution of design variables in order to maximize the objective function. In other words, it enhances utilization of the constituent materials by placing them in areas that they are needed more. This iterative procedure is repeated till the maximum number of iterations is reached. In summary, the optimization process is described as follows:

Step 1: The PEMFC model, related parameters, and the design variables are initialized.

Step 2: The mathematical model is solved at a given current density and the objective function is computed according to Eq. (4.41).

Step 3: A sensitivity analysis is performed using the adjoint variable method to calculate the gradient of objective function with respect to the design variables.

Step 4: A regularization process is conduced to smooth the design solutions over the calculation domain.

Table 4.5: Operational and structural parameters of the cell

Parameter	Validation	Base case	Unit
Relative humidity (RH)	100 [69]	100	%
Cell temperature (T)	80/60 [69]	80	°C
Cell pressure (P)	1.0 [69]	1.0	atm
Channel width (W_{ch})	1 [69]	1	mm
Rib width (W_{rib})	1.5 [69]	1.5	mm
GDL thickness (t_{GDL})	300 [69]	300	μm
CL thickness (t_{CL})	15 [69]	8	μm
PEM thickness (t_{PEM})	55 [69]	55	μm
Pt/C mass ratio (γ_{PtC})	0.2 [69]	0.4	-
Cathode platinum loading ($m_{\mathrm{Pt,c}}$)	0.4 [69]	0.25	$\mathrm{mg\,cm^{-2}}$
Anode platinum loading ($m_{\mathrm{Pt,a}}$)	0.1 [69]	0.1	$\mathrm{mg\,cm^{-2}}$
Cathode ionomer volume fraction ($\varepsilon_{\mathrm{m,c}}$)	0.133 [69]	0.2	-
Anode ionomer volume fraction ($\varepsilon_{\mathrm{m,a}}$)	0.133 [69]	0.1	-
GDL porosity ($\varepsilon_{\mathrm{void,GDL}}$)	0.8	0.8	-
Cathode charge transfer coefficient (α_{c})	$1(80°\mathrm{C})$ $0.95(60°\mathrm{C})$	1	-
Anode charge transfer coefficient (α_{a})	1	1	-
Cathode exchange current density ($i_{0,\mathrm{c}}^{\mathrm{ref}}$)	10^{-4} [68]	10^{-4}	$\mathrm{A\,m^{-2}}$
Anode exchange current density ($i_{0,\mathrm{a}}^{\mathrm{ref}}$)	10^{4} [69]	10^{4}	$\mathrm{A\,m^{-2}}$
Anode equilibrium potential ($E_{\mathrm{a}}^{\mathrm{eq}}$)	0	0	V

Step 5: Using the GCMMA method, the design variables are updated.

Step 6: If the maximum number of iterations is reached, the optimization process is terminated. Otherwise, steps 2 to 5 are repeated.

4.4 Results and discussion

4.4.1 Mathematical model validation

To verify validity of the developed model, the simulated I-V curves are compared with the experimental ones adopted from [69] for a single cell with an active electrode area of $1 \times 1\,\mathrm{cm}^2$. The mathematical model of Section 4.2 is solved using the values reported in Table 4.5 for two different cell temperatures. The values of these structural and operational parameters are according to those reported in [69] for the experimental condition. It is noteworthy to note that, similar to [69] where the experimental data was adopted from, the model in the present work is based on parallel

straight channels. This results in mass transport within the catalyst layer being primarily driven by molecular diffusion rather than convection. Other flow channel configurations, such as serpentine or interdigitated designs, warrant further investigation, which lies beyond the scope of this study. The simulation and experimental curves are plotted in Fig. 4.2. Comparison of the experimental and simulated polarization curves reveals good agreement across different operating temperatures. At low current densities, a sharp decline could be observed in the cell voltage due to the activation losses. This overpotential is followed by Ohmic and concentration voltage drops at higher current densities. The former is caused by transport of electrons and protons through PtC and ionomer, which becomes considerable at medium current densities. The concentration overpotential, however, is dominant at high current density regions. The observed phenomenon is the result of slow transport of oxygen through the water and the ionomer films that surround the agglomerates. This sluggishness creates an oxygen delivery rate that is outpaced by the rate at which oxygen is consumed, leading to an imbalance in the cell performance. Furthermore, at high current densities, liquid water formation accelerates, leading to an excessive accumulation of liquid water in the CCL. This surplus of liquid water can block the pores that are responsible for oxygen delivery. This is included in the developed model by introducing an effective porosity. Fig. 4.2 confirms that the present model well follows the polarization trend of a real PEMFC over a range of current densities and operating conditions.

4.4.2 Optimization of electrode structure

This study focuses on the optimization of CCL structure at high current density levels. Under such working condition, the excess liquid water generated as a result of high electrochemical reaction rate blocks the pores. This makes the reactant delivery complicated and results in considerable oxygen depletion. Moreover, a thicker water film formed around the agglomerates at a relatively high current density increases the resistance against diffusion of oxygen into the agglomerate, where could react in the presence of platinum particles. Therefore, an optimal distribution of the constituents could enhance the utilization of available materials and provide a compromise between various transport and rate processes. The optimization is performed on a base case with a uniform material distribution. The parameters of this reference cell is reported in Table 4.5. At a current density of $1.69\,(\mathrm{A\,cm^{-2}})$ the base case corresponds to a voltage of $0.1\,(\mathrm{V})$, which is computed by solving the governing equations. This is the operating point at which the optimization is conducted.

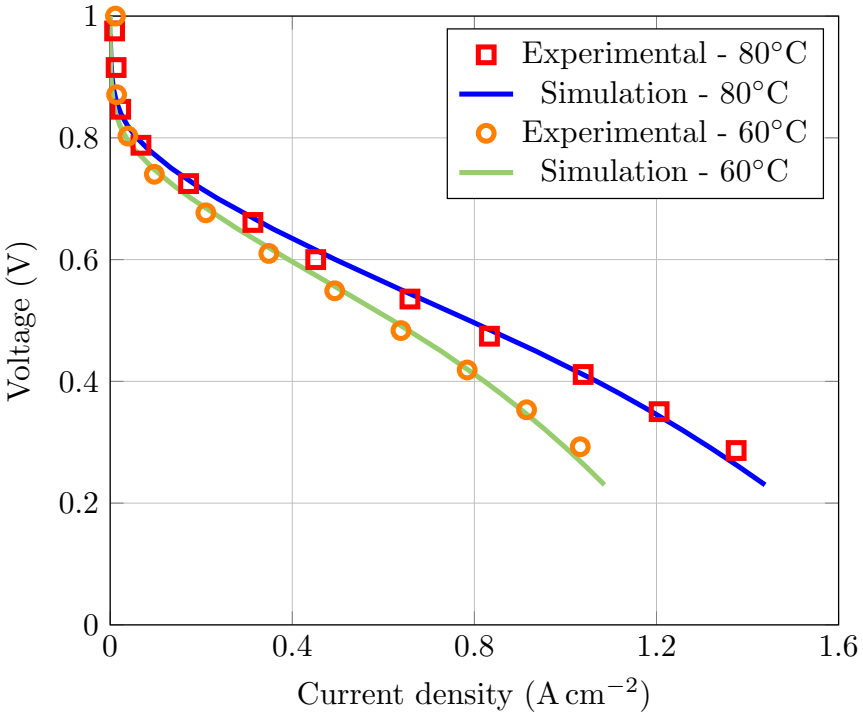

Figure 4.2: Validation of the simulation results against experimental ones [69]

Table 4.6: Optimization scenarios

Optimization scenario	Decision variable(s)	$m_{\mathrm{Pt}}^{\max}$ (mg cm^{-2})	$\varepsilon_{\mathrm{l}}^{\max}$
OPT-I	$\varepsilon_{\mathrm{PtC}}$ and ε_{l}	0.25	0.2
OPT-II	$\varepsilon_{\mathrm{PtC}}$	0.25	-
OPT-III	ε_{l}	-	0.2

Moreover, the generic form of the designated optimization problem in Eq. (4.41), considers two decision variables, including volume fractions of PtC and ionomer, as well as two global constraints. To extend the analysis scope of this study, various possible combinations of decision variables are considered in form of three different optimization scenarios as summarised in Table 4.6. As indicated in this table, scenario OPT-I represents the formulation of Eq. (4.41). This scenario includes simultaneous optimization of volume fractions of both PtC and ionomer. In this case, the average mass loading of platinum and volume fraction of ionomer are kept the same as the base case to obtain a fair comparison between the results. In scenario OPT-II, only the volume fraction of PtC is considered as the decision variable and the average platinum loading is restricted to that of the base case. In the final scenario (OPT-III), the volume fraction of the ionomer is the only decision variable and the average of this variable cannot exceed that of the base case.

Fig. 4.3 demonstrates the optimization history of material distribution for OPT-I. The volume fractions of PtC, ionomer, and void (i.e., porosity) are shown at initial, intermediate, and optimized steps. Although the optimization process started with a uniform distribution of various phases, the optimal design shows a heterogeneous distribution of materials over the CCL domain. As can be seen in this figure, the optimized design solution exhibits high porosity in regions underneath the rib, while areas closer to the channel have relatively higher PtC and ionomer concentrations. This is because of the significant depletion of oxygen concentration in the regions farther away from the channel, specifically beneath the rib where oxygen delivery is insufficient. Closer examination of the optimal design depicted in Fig. 4.3 shows that the spatial distribution of materials remains uniform in the through-plane direction, which is attributed to the low thickness of CCL. Therefore, the optimization favors a heterogeneous distribution in lateral direction rather than through-plane direction. A similar behavior is observed in other optimization scenarios as well. Hence, for other cases, only the projected distributions on the lateral direction (y-direction) are plotted as shown in Fig. 4.4. According to the findings of this figure, materials distribution for various optimization scenarios is different. However, in any case, the optimal design shows a complicated heterogeneous material allocation, which provides a balance between different transport process and the electrochemical reaction. While the exact optimum solution depends on the cell characteristics and problem settings, analyzing the outcomes of Fig. 4.4 provides some useful qualitative information. What is striking about the optimized designs in this figure is that the porosity increases when getting farther from the channel. In the areas under the rib, oxygen concentration drops due to the sluggish mass transport. This causes a significant concentration overpotential. To overcome this problem, the optimization algorithm favors designs with higher porosity in those regions to compensate for the insufficient oxygen delivery through a higher effective diffusivity. Moreover, an increment in porosity might improve discharge of liquid water generated in those areas as a result of ORR. In addition, distribution of both PtC and ionomer have a local minimum in the middle of CCL, followed by symmetrical maxima close to the border of the regions under the channel and rib. Such a structure further facilitates dispersion of oxygen from areas under the channel, where oxygen concentration is relatively higher, and assures an improved proton transport and an escalated ECSA, where there is a potential for a higher reaction rate. The topologically-optimized distribution of PtC in our study shares similarities with the layout proposed by Havaej et al. [35]. In their work, they achieved improved cell performance by employing a predefined parabolic distribution of catalyst material in the lateral direction. However,

their approach relied on trial and error, searching for the optimal catalyst loading distribution through prescribed functions. In contrast, the present study introduces a novel optimization framework that offers a more robust and informed procedure for discovering such functionality. Our method does not depend on any prior information regarding the distribution and allows for a high degree of freedom to conduct multi-variable optimization. This advancement ensures greater accuracy and efficiency in identifying the best material distribution, ultimately leading to enhanced cell performance. Also of note is that achieving a finely graded design for CL in practice may not be possible at a high precision. Nevertheless, recent progress in additive manufacturing and 3D printing technologies has introduced new opportunities for realizing topologically optimized microstructures [89–91].

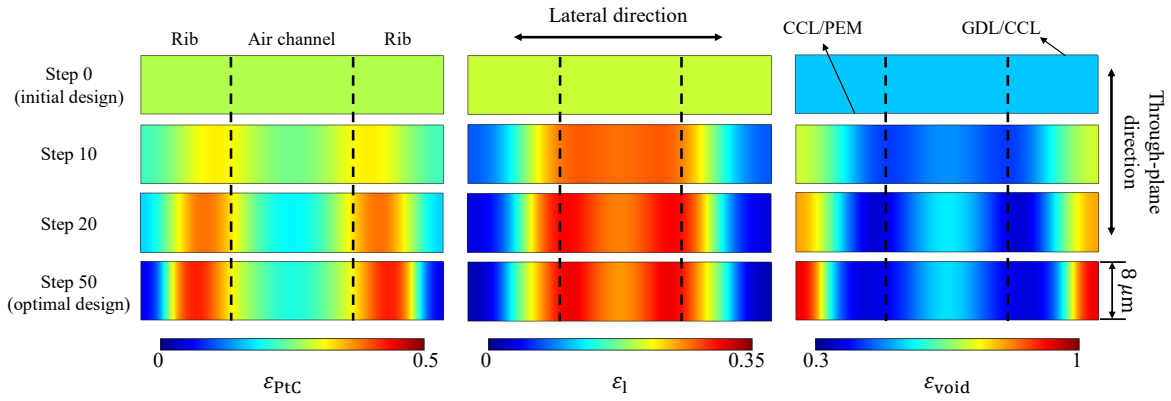

Figure 4.3: Optimization history of material distribution in CCL for scenario OPT-I (contour plots are not to scale)

Table 4.7 compares the cell voltage (objective function) of optimized designs with that of the base case. The objective function increased between 18% and 42% after different optimization scenarios. From the data in this table, it is apparent that scenario OPT-I outperforms the two other ones thanks to its higher freedom in material arrangement provided by simultaneous optimization of two decision variables. While the cell voltage is enhanced considerably in all optimizations, the overpotential improvement is relatively lower. However, it is anticipated that optimization of a 3D model, in which longitudinal effects are also included, may result in further enhancement. Evidently, such an optimization would require a significant amount of computational resources and it falls outside the scope of the present study. The total overpotential is decomposed using an applied-voltage breakdown (AVB) method proposed by Gerhardt et al. [92], which made it possible to separate contribution of each process quantitatively. Fig. 4.5 provides an overview of total overpotential

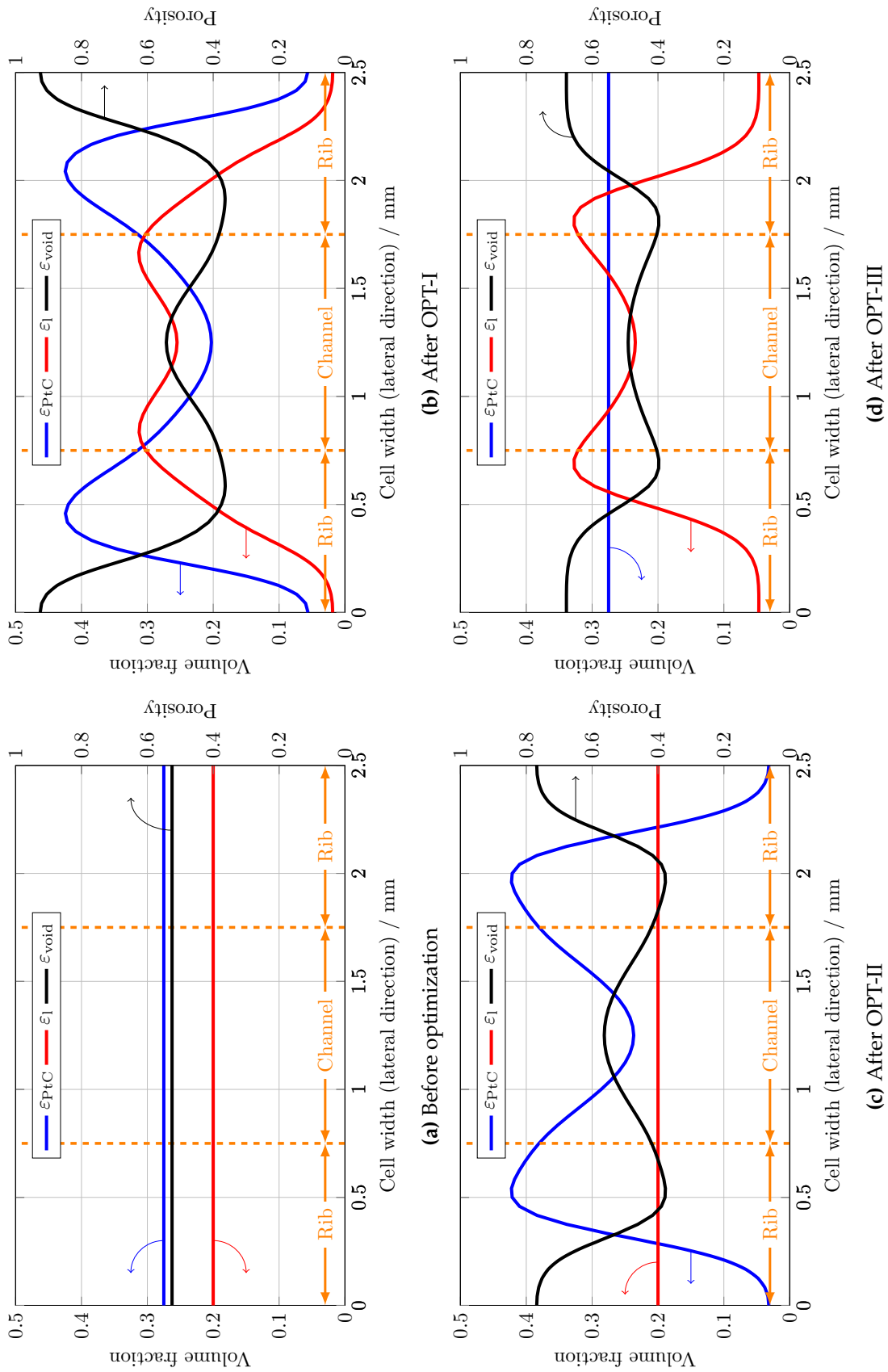

Figure 4.4: Spatial distribution of constituents in lateral direction of CCL (a) before optimization, and after optimization with scenario (b) OPT-I, (c) OPT-II, and (d) OPT-III

Table 4.7: Performance enhancement for various optimization scenarios

Scenario	Base case	OPT-I	OPT-II	OPT-III
Cell voltage (V)	0.1	0.142	0.118	0.133
Voltage change (%)	-	42	18	33
Overpotential change (%)	-	−3.89	−1.67	−3.06
Activation	-	0.47	0.46	0.52
Ohmic	-	4.94	3.03	4.50
Concentration	-	−19.78	−9.89	−16.43

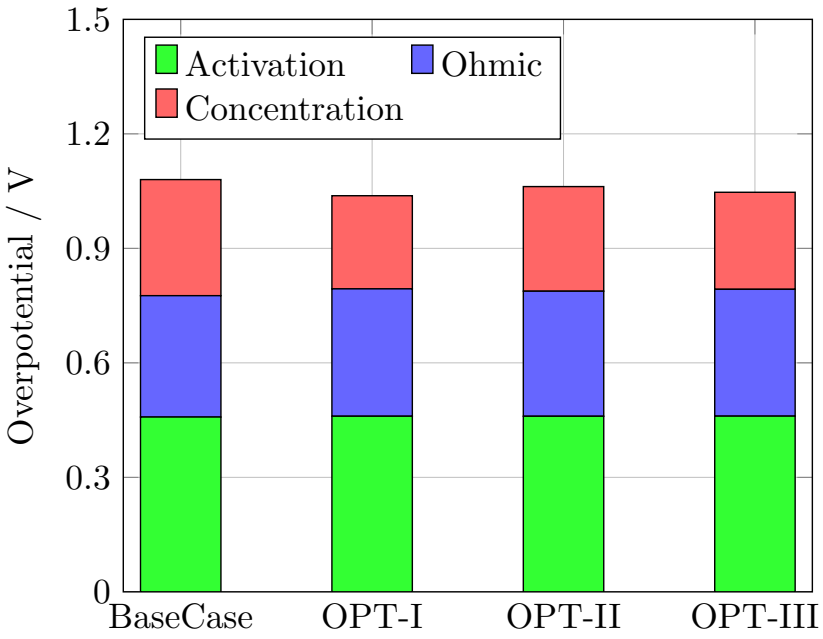

Figure 4.5: Overpotential breakdown analysis for various scenarios at current density of 1.69 ($\mathrm{A\,cm^{-2}}$)

breakdown, including activation, ohmic, and concentration losses for different scenarios. Moreover, the changes of overpotential components with respect to the base case are given in Table 4.7. These findings suggest that, in all optimization scenarios, there is a slight increase in both activation and ohmic overpotentials. Despite these factors at play, the reduction in concentration overpotential ultimately proves to have the greatest impact on overall performance improvement.

According to the problem formulation of Eq. (4.41), the optimization algorithm favors those topological structures that maximize the cell voltage. This aim may be accomplished by obtaining a proper balance among transport and rate processes,

such as oxygen diffusion, liquid water discharge, proton transport, and electrochemical reaction. To elucidate how an optimized design enhances the overall cell performance from a physical standpoint, some key parameters are inspected more in detail. To do so, first, the distributions of oxygen concentration are compared before and after optimization. Investigation of oxygen concentration shows that the gradient of this parameter along CL thickness (through-plane direction) is mainly negligible with a maximum difference of 10% in some limited parts. This variance is significantly smaller than that of lateral direction. Similar to what was mentioned before, the small thickness of CCL is the reason that makes the concentration gradient insignificant in this direction. Therefore, for the sake of clarity, the projected concentration along the cell width is presented in Fig. 4.6. As shown in Fig. 4.6a, all optimized designs have a higher average concentration compared to the base case. Significant improvements have been made, particularly in the concentration under the rib, which previously suffered from oxygen starvation in the base case. The observed increase in average concentration could be attributed to the more effective distribution of porosity, which augmented effective diffusivity in the areas under the rib. It could also be related to an enhanced product discharge which prevents pores blockage with the liquid water. This is discussed in a later part. Moreover, it can be clearly confirmed that such heterogeneous porosity distributions do not adversely affect the concentration in the rest of CCL, where the optimized porosity is lower than that of the uniform base case (see Fig. 4.4). Fig. 4.6b illustrates the changes of concentration over the course of optimization OPT-I, as a representative scenario. According to this figure, at the initial step, the oxygen concentration shows a large drop in the lateral direction. As the optimization algorithm modifies the material distribution (see Fig. 4.3), it gradually compensates for oxygen depletion. In the final optimized design (step 50), the concentration at the two ends of CCL is almost two times higher than the initial uniform configuration. Interestingly, this significant improvement is achieved because of a better material distribution, despite the fact that the average porosity remains consistent in both the initial and final stages.

Water management is a critical issue in the design of low temperature PEMFCs since the water exists in the liquid phase. The liquid water accumulation increases the gas transport resistance in the secondary pores. Moreover, due to the hydrophilic nature of the ionomer, a greater amount of water results in a thicker liquid water film around the agglomerates. This, in turn, leads to an additional resistance against the delivery of oxygen to the platinum particles. Fig. 4.7 compares distribution of

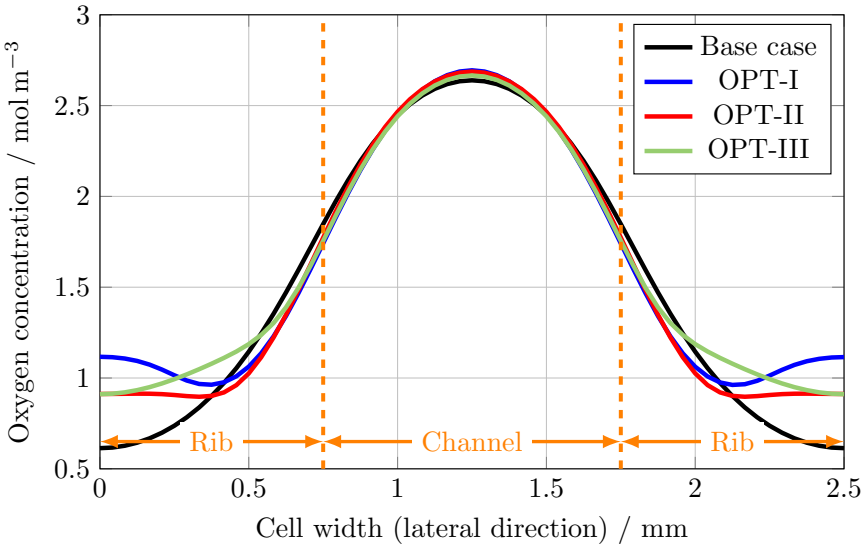

(a) Oxygen concentration distribution before and after optimization

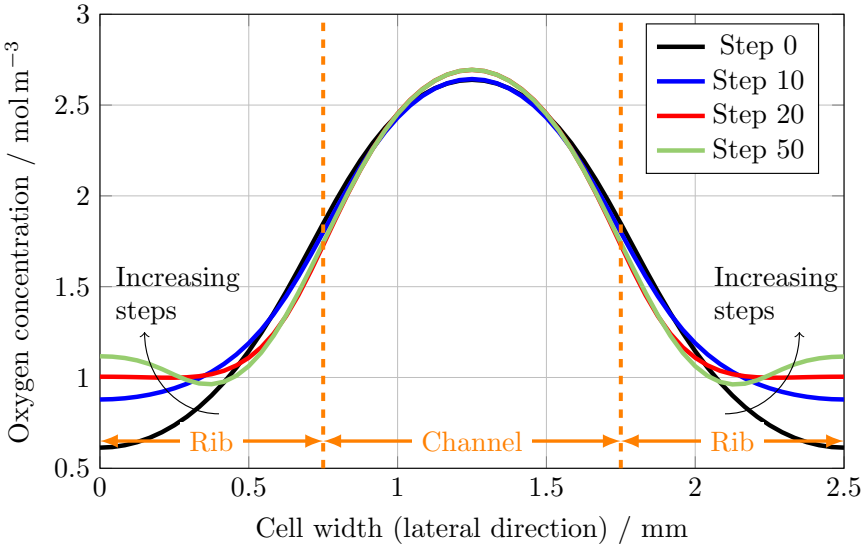

(b) Evolution of oxygen concentration distribution during optimization OPT-I

Figure 4.6: Spatial distribution of oxygen concentration: (a) compression of base case with three optimal designs and (b) optimization history for scenario OPT-I

water concentration, saturation, and capillary diffusivity before and after optimizations. According to Fig. 4.7a, the overall amount of accumulated water is decreased in CCL after all optimizations. This decline is more significant in areas under the rib. As discussed before, the oxygen concentration is low in those areas due to the sluggish mass transport. A decrease in the liquid water accumulation may facilitate the oxygen delivery process. This has been already confirmed by inspection of oxygen concentration distribution (see Fig. 4.6). Liquid water saturation, that represents the ratio of water volume to void volume, is another critical index. Despite the decrease in local water concentration in the CCL after optimization, as depicted in Fig. 4.7b, the saturation exhibits a non-monotonic trend. Since saturation is related to both water volume and porosity, this behavior is attributed to the non-uniform porosity distribution after optimization. Optimization favored low porosity in certain areas, which, in turn, led to an increase in saturation within those regions. The capillary diffusivity is correlated to the water saturation through Leverett J-function. A higher saturation in some part of the CCL improved the capillary diffusivity in those areas as illustrated in Fig. 4.7c. This higher diffusivity is the reason behind the enhanced water management in optimized designs.

As previously mentioned, during the process of hydrogen oxidation in ACL, hydrogen ions (protons) are produced. These ions are then transported across a polymeric membrane to the CCL, where they participate in ORR. These protons are transported through the ionomer phase within CCL. Therefore, ionic conductivity of CCL is another crucial factor in determining the overall cell performance. The intrinsic ionic conductivity of the ionomer is much lower than the electric conductivity of PtC. Hence, electron transport is not a limiting phenomenon. The effective ionic conductivity depends on water content as well as volume fraction of ionomer. While excess water generation at high current densities can have negative impacts on oxygen delivery, it may have a positive effect on ionic conductivity. Since in this study it is assumed that the cell is working at a high current density and RH level, the ionomer is fully hydrated. In such a case, the ionomer volume fraction becomes the determining factor. The distribution of effective ionic conductivity is depicted in Fig. 4.8a. Because the ionomer distribution is kept unchanged during OPT-II, as expected, the conductivity plot of this scenario coincide that of the base case. The conductivity distribution after OPT-I and OPT-III follows the trend of the ionomer volume fraction distribution. A heterogeneous distribution of ionomer leads into a non-uniform conductivity. Although the ionic conductivity in the two ending parts far from the channel is reduced compared to the base case, it is considerably enhanced in the

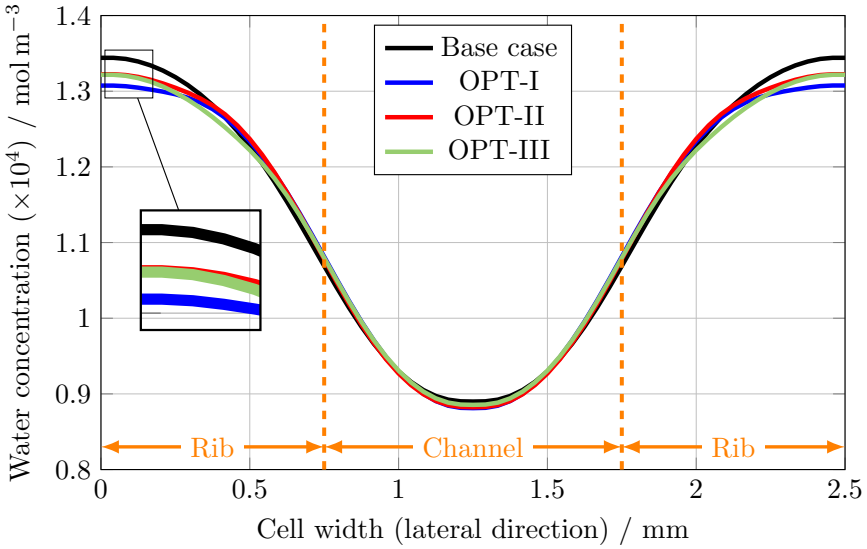

(a) Liquid water concentration

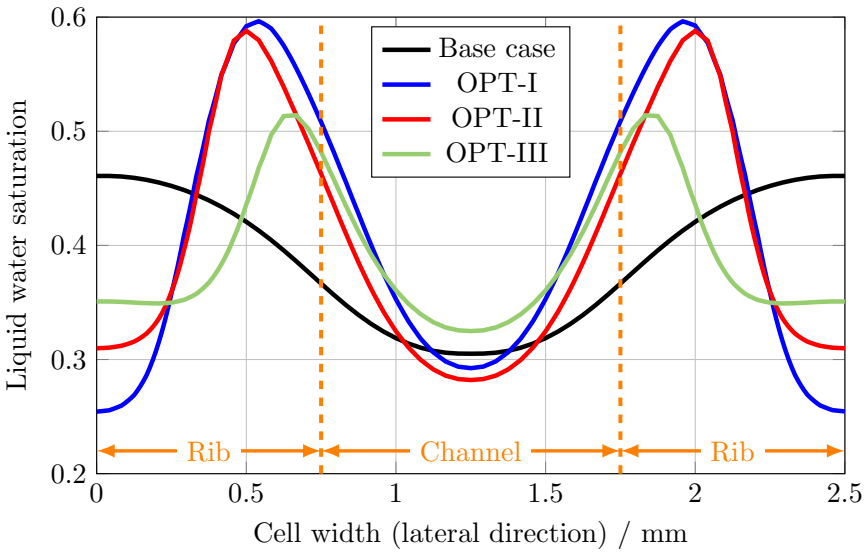

(b) Liquid water saturation

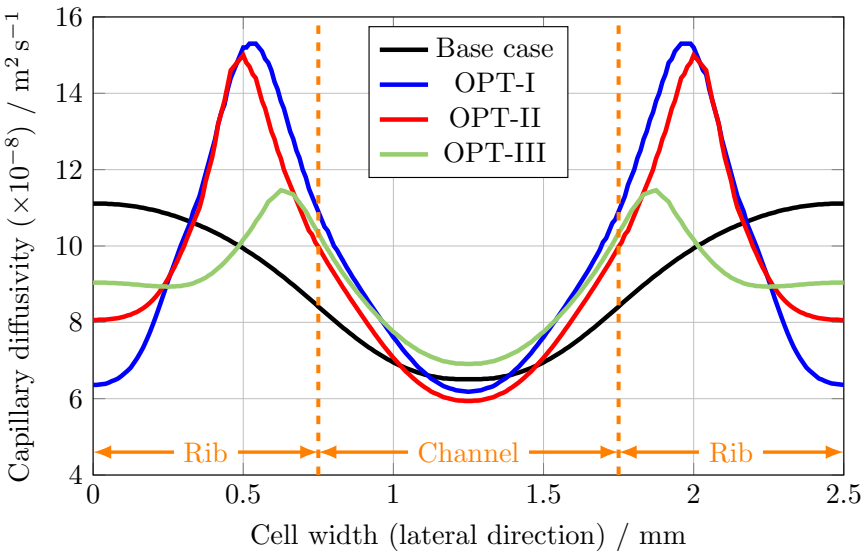

(c) Capillary diffusivity

Figure 4.7: Spatial distribution of (a) liquid water concentration, (b) liquid water saturation, and (c) capillary diffusivity before and after optimizations

rest of CCL. The average effective conductivity throughout CCL is increased from a value of $1.19\,\mathrm{S\,m^{-1}}$ for the base case to $1.33\,\mathrm{S\,m^{-1}}$ and $1.32\,\mathrm{S\,m^{-1}}$ for OPT-I and OPT-III, respectively. This 11% enhancement is achieved thanks to an uneven ionomer distribution. According to Fig. 4.8b, which shows the distributions of current source, overpotential, and power loss, a higher reaction rate can be observed in the areas beneath rib/channel border before optimization. Also, in a through-plane direction, the regions close to the CCL/PEM interface show a higher potential for ORR. As a result, instead of distributing the ionomer phase uniformly, the optimization algorithm places more ionomer in areas with a high possibility for reaction. Increasing the ionic conductivity in regions where there is a high potential for reaction may further improve the conversion rate in those areas thanks to an improved proton transport. Thus, this variation in ionomer distribution made the ionic conductivity to match the reaction rate and consequently enhanced the material utilization. It is noteworthy that, since the optimization is performed at a constant current density, the average current density in all current source contour plots ($|i^{\mathrm{c}}_{\mathrm{src}}|$) are the same. However, its distribution is changed so that the overall performance is enhanced. Investigating the overpotential magnitude ($|\eta_{\mathrm{c}}|$) presented in Fig. 4.8b shows a local increase in some parts of the CCL after optimization. However, this increase in overpotential is accompanied by a decrease in the current source in those regions as well. The combined effect of these two changes resulted in a lower power loss ($|i^{\mathrm{c}}_{\mathrm{src}} \times \eta_{\mathrm{c}}|$) over the entire CCL that has been confirmed before through the overall

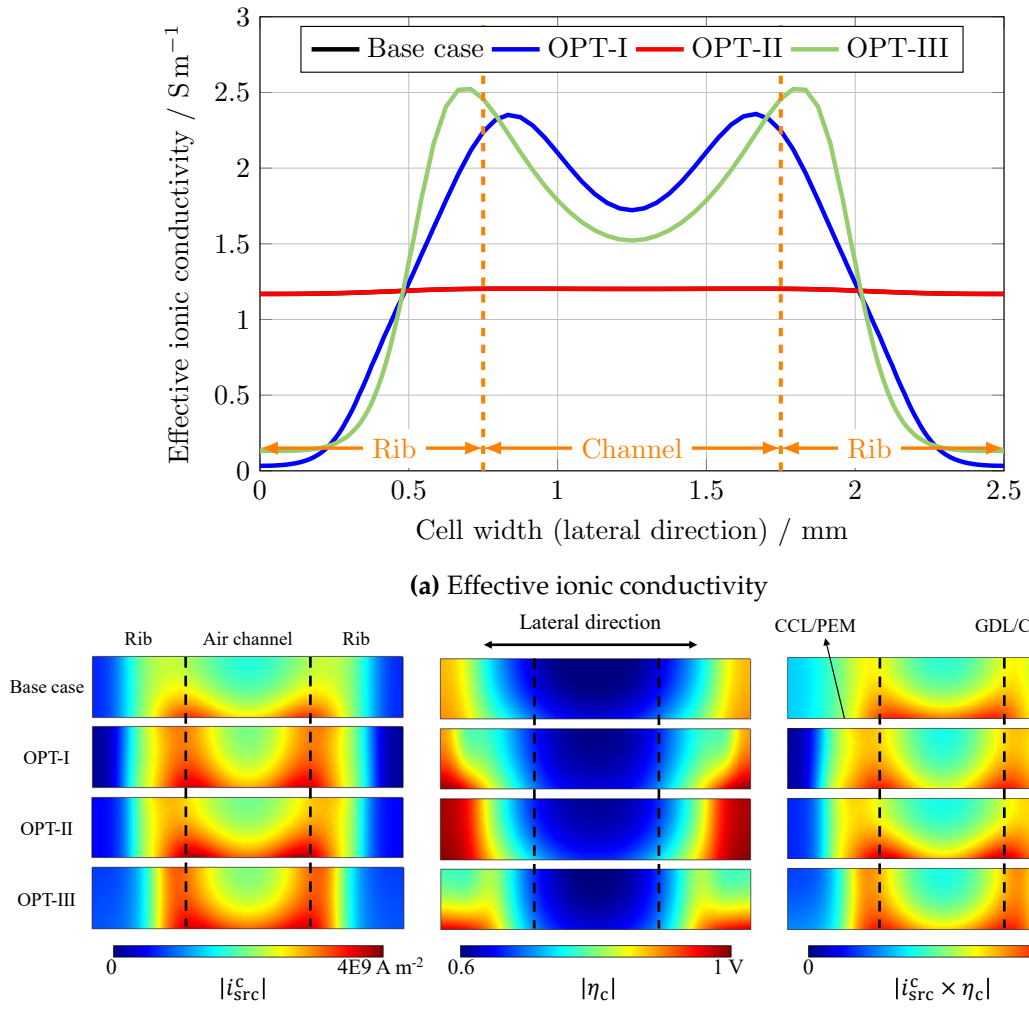

(a) Effective ionic conductivity

(b) Current source and overpotential distribution

Figure 4.8: (a) Projected distribution of effective ionic conductivity and (b) distribution of current source and overpotential before and after optimizations

cell performance. The power loss contour plots ($|i^c_{src} \times \eta_c|$) are compared for all scenarios in Fig. 4.8b. For instance, after OPT-I, the average power loss decreases by 8% compared to the base case, from an initial value of $1.59 \times 10^9\,\mathrm{W\,m^{-3}}$ to a final value of $1.46 \times 10^9\,\mathrm{W\,m^{-3}}$.

4.5 Conclusions

This research provides a mathematical optimization approach for the mathematically optimized design of material distribution in CL of PEMFC based on TO. First, a two-phase flow model of PEMFC is developed to simulate the cell performance. The model is validated against experimental data. Next, TO is employed to optimize the

material distribution in CCL with the objective of increasing the cell performance. While a mathematical model is an essential part of any optimization, this work primarily focuses on applying TO to PEMFC, rather than on the model itself. The performance enhancement is formulated as a higher voltage at a given current density. The optimization is performed with various decision variables. Under a high working current density, the excess liquid water generated in CCL may cause significant mass transport losses. An optimal design can reduce the concentration overpotential through an improved distribution of materials within the electrode. In general, an optimal CL design showed a higher volume fraction of PtC and ionomer in areas under the channel compared to those under the rib. The optimization results are further investigated through the breakdown of overpotential contributions. It is confirmed that the concentration overpotential is considerably decreased after optimization. Moreover, inspecting the oxygen distribution in the CCL proves the improvement in oxygen delivery to those areas under the rib that suffer from oxygen starvation. This improvement in oxygen transport is achieved thanks to a better porosity distribution, which in return increases the effective gas diffusivity and enhances the liquid water discharge. A better ionomer placement in accordance to reaction rate also positively affected the cell performance. In the application of TO for electrode design, reliable design solutions require validating the models against experimental data to ensure real-world performance improvements. While existing models of PEMFC, including the present work, have been validated under varying operational conditions, their applicability to different structural designs remains uncertain. To enhance the robustness of TO applications for electrode design and ensure the practical relevance of the results, future PEMFC modeling efforts should prioritize validation across a wider range of structural conditions, which is currently less common compared to validation under operational conditions. Furthermore, continuum models must accurately capture the relationship between local microstructure and overall performance. In this regard, structural optimization based on alternative modeling approaches, such as the lattice Boltzmann method [93] or pore network modeling [94], may offer valuable insights. Subsequent studies may explore the optimization of a 3D model, which is expected to provide additional benefits after introducing the effects of concentration depletion in longitudinal direction. However, solving a 3D multiphysics finite element model of a PEMFC at high current densities requires substantial computational resources. Furthermore, incorporating this into an optimization process, which involves repeated simulations, significantly increases the computational burden.

Abbreviations

ACL	Anode catalyst layer
AVB	Applied-voltage breakdown
CCL	Cathode catalyst layer
CL	Catalyst layer
ECSA	Electrochemical surface area
GCMMA	Globally convergent method of moving asymptotes
GDL	Gas diffusion layer
MEA	Membrane electrode assembly
ORR	Oxygen reduction reaction
PDE	Partial differential equation
PEM	Proton exchange membrane
PEMFC	Proton exchange membrane fuel cell
PGM	Platinum group metals
PtC	Carbon-supported platinum
RH	Relative humidity
SIMP	Simplified Isotropic Material with Penalization
TO	Topology optimization

Nomenclature

a_{agg}	Specific surface area of agglomerate without water	m^{-1}
A_{Pt}	Total reaction area per unit volume of agglomerate	m^{-1}
a'_{agg}	Specific surface area of agglomerate with water	m^{-1}
C	Concentration	$\mathrm{mol\,m}^{-3}$
c_{p}	Specific heat capacity	$\mathrm{J\,mol}^{-1}\,\mathrm{K}^{-1}$
D	Diffusivity	$\mathrm{m}^2\,\mathrm{s}^{-1}$
D^{T}	Thermal diffusion coefficient	$\mathrm{kg\,m}^{-1}\,\mathrm{s}^{-1}$
E_{r}	Effectiveness factor	$-$
E^{eq}	Equilibrium potential	V
EW	Equivalent weight of ionomer	$\mathrm{kg\,mol}^{-1}$
F	Faraday's constant	$\mathrm{C\,mol}^{-1}$
F_{obj}	Objective function	V
$H_{\mathrm{O_2}}$	Henry's constant for oxygen dissolution	$\mathrm{Pa\,m}^3\,\mathrm{mol}^{-1}$
h_{cond}	Condensation rate constant	s^{-1}

h_{evp}	Evaporation rate constant	s^{-1}
i_{src}	Volumetric current density source	$\mathrm{A\,m}^{-3}$
i_0	Exchange current density	$\mathrm{A\,m}^{-2}$
k	Thermal conductivity	$\mathrm{W\,m}^{-1}\,\mathrm{K}^{-1}$
k_{c}	Reaction rate coefficient	s^{-1}
M	Molecular weight	$\mathrm{kg\,mol}^{-1}$
m_{Pt}	Platinum loading	$\mathrm{kg\,m}^{-2}$
N_{agg}	Agglomerate density	–
p	Pressure	Pa
$P_{\mathrm{O_2}}$	Oxygen partial pressure	Pa
Q_{m}	Mass source term	$\mathrm{kg\,s}^{-1}\,\mathrm{m}^{-3}$
R	Gas constant	$\mathrm{J\,mol}^{-1}\,\mathrm{K}^{-1}$
R	Species source term	$\mathrm{mol\,s}^{-1}\,\mathrm{m}^{-3}$
r_{agg}	Agglomerate radius	m
R_{f}	Filter radius	m
s	Saturation	–
S_{T}	Heat Source term	$\mathrm{W\,m}^{-3}$
T	Temperature	K
t	Thickness	m
Th	Thiele modulus	–
$\mathbf{u}$	Velocity	$\mathrm{m\,s}^{-1}$
W	width	m
x	Mole fraction	–
Δh	Latent heat of condensation/evaporation	$\mathrm{J\,kg}^{-1}$
ΔS	Reaction entropy	$\mathrm{J\,mol}^{-1}\,\mathrm{K}^{-1}$

Greek symbols

α	Charge transfer coefficient	–
β	Projection steepness	–
θ_β	Projection point	–
δ_{N}	Thickness of ionomer film	m
δ_{W}	Thickness of liquid water coating	m
η	Overpotential	V
γ_{PtC}	Platinum mass fraction	–
κ	Permeability	m^2
λ	Water content	–

μ	Viscosity	$\mathrm{Pa\,s}$
ω	Mass fraction	$-$
ϕ	Potential	V
ρ	Density	$\mathrm{kg\,m^{-3}}$
σ	Electric charge conductivity	$\mathrm{S\,m^{-1}}$
θ	Material distribution function	$-$
ε	Volume fraction	$-$
ε_v	Porosity	$-$

Subscripts/superscripts

agg	Agglomerate
c	Cathode
cap	Capillary
ch	Channel
CL	Catalyst layer
dw	Dissolved water
l	Electrolyte phase
lw	Liquid
m	Membrane
phase	Phase change
ref	Reference
rel	Relative
rib	Rib
rxn	Reaction
s	Solid phase
sat	Saturation
src	Source

Bibliography

[1] Y. Matsui, M. Kawase, T. Suzuki, and S. Tsushima, "Electrochemical cell recharging by solvent separation and transfer processes," *Scientific reports*, vol. 12, no. 1, pp. 1–8, 2022.

[2] N. Limjeerajarus and P. Charoen-Amornkitt, "Effect of different flow field designs and number of channels on performance of a small pefc," *International Journal of Hydrogen Energy*, vol. 40, no. 22, pp. 7144–7158, 2015.

[3] T. Capurso, M. Stefanizzi, M. Torresi, and S. Camporeale, "Perspective of the role of hydrogen in the 21st century energy transition," *Energy Conversion and Management*, vol. 251, p. 114898, 2022.

[4] J. St-Pierre, "Perspective—oxygen-based fuel cell and reversible systems for heavy-duty motive and stationary applications," *Journal of The Electrochemical Society*, vol. 169, no. 4, p. 044506, 2022.

[5] E. Pahon, D. Bouquain, D. Hissel, A. Rouet, and C. Vacquier, "Performance analysis of proton exchange membrane fuel cell in automotive applications," *Journal of Power Sources*, vol. 510, p. 230385, 2021.

[6] G. Wang, Y. Yu, H. Liu, C. Gong, S. Wen, X. Wang, and Z. Tu, "Progress on design and development of polymer electrolyte membrane fuel cell systems for vehicle applications: A review," *Fuel Processing Technology*, vol. 179, pp. 203–228, 2018.

[7] B. M. Stühmeier, R. J. Schuster, L. Hartmann, S. Selve, H. A. El-Sayed, and H. A. Gasteiger, "Modification of the electrochemical surface oxide formation and the hydrogen oxidation activity of ruthenium by strong metal support interactions," *Journal of The Electrochemical Society*, vol. 169, no. 3, p. 034519, 2022.

[8] X. Chen, J. Xu, C. Yang, Y. Fang, W. Li, Y. Zhang, Z. Wan, and X. Wang, "Thermodynamic and economic study of pemfc stack considering degradation characteristic," *Energy Conversion and Management*, vol. 235, p. 114016, 2021.

[9] K. Talukdar, M. A. Ripan, T. Jahnke, P. Gazdzicki, T. Morawietz, and K. A. Friedrich, "Experimental and numerical study on catalyst layer of polymer electrolyte membrane fuel cell prepared with diverse drying methods," *Journal of Power Sources*, vol. 461, p. 228169, 2020.

[10] O. B. Rizvandi and S. Yesilyurt, "A transient pseudo-3d model of the pem fuel cell for the analysis of dead-ended anode and anode bleeding operation modes," *Electrochimica Acta*, vol. 324, p. 134866, 2019.

[11] M. E. Abdelrahman, H. Zhang, G. Wu, X. Li, and S. Litster, "Half-cell electrode assessments of a crossover-tolerant direct methanol fuel cell with a platinum group metal-free cathode," *Electrochimica Acta*, vol. 416, p. 140262, 2022.

[12] L. Osmieri and Q. Meyer, "Recent advances in integrating platinum group metal-free catalysts in proton exchange membrane fuel cells," *Current Opinion in Electrochemistry*, vol. 31, p. 100847, 2022.

[13] X. Qu, Y. Li, G. Li, R. Ji, S. Yin, X. Cheng, C. Wang, J. Yang, Y. Jiang, and S. Sun, "Boosting the orr performance of fe-n/c catalyst via increasing the density and modifying the electronic structure of fe-nx active sites," *Electrochimica Acta*, vol. 403, p. 139604, 2022.

[14] T. Reshetenko, G. Randolf, M. Odgaard, B. Zulevi, A. Serov, and A. Kulikovsky, "The effect of proton conductivity of fe–n–c–based cathode on pem fuel cell performance," *Journal of The Electrochemical Society*, vol. 167, no. 8, p. 084501, 2020.

[15] D. Banham, J.-Y. Choi, T. Kishimoto, and S. Ye, "Integrating pgm-free catalysts into catalyst layers and proton exchange membrane fuel cell devices," *Advanced Materials*, vol. 31, no. 31, p. 1804846, 2019.

[16] S. Stariha, K. Artyushkova, M. J. Workman, A. Serov, S. Mckinney, B. Halevi, and P. Atanassov, "Pgm-free fe-nc catalysts for oxygen reduction reaction: Catalyst layer design," *Journal of Power Sources*, vol. 326, pp. 43–49, 2016.

[17] L. Dunsmore, A. Uddin, H. Zhang, G. Wu, and S. Litster, "Non-planar platinum group metal-free fuel cell cathodes for enhanced oxygen transport and water rejection," *Journal of Power Sources*, vol. 506, p. 230188, 2021.

[18] P. Charoen-amornkitt, T. Suzuki, and S. Tsushima, "Effects of voltage-dependence of the constant phase element and ohmic parameters in the modeling and simulation of cyclic voltammograms," *Journal of The Electrochemical Society*, vol. 167, no. 16, p. 166506, 2020.

[19] P. Charoen-Amornkitt, T. Suzuki, and S. Tsushima, "Determination of constant phase element parameters under cyclic voltammetry conditions using a semi-theoretical equation," *Electrochemistry*, vol. 87, no. 4, pp. 204–213, 2019.

[20] P. Charoen-amornkitt, T. Suzuki, and S. Tsushima, "Ohmic resistance and constant phase element effects on cyclic voltammograms using a combined model of mass transport and equivalent circuits," *Electrochimica Acta*, vol. 258, pp. 433–441, 2017.

[21] P. Charoen-amornkitt, W. Pholauyphon, T. Suzuki, and S. Tsushima, "An approach to unify capacitance measurements of electric double layer capacitors using sinusoidal potential scan," *Journal of Energy Storage*, vol. 66, p. 107522, 2023.

[22] M. L. Perry, J. Newman, and E. J. Cairns, "Mass transport in gas-diffusion electrodes: a diagnostic tool for fuel-cell cathodes," *Journal of the Electrochemical Society*, vol. 145, no. 1, p. 5, 1998.

[23] Q. Wang, M. Eikerling, D. Song, and Z. Liu, "Structure and performance of different types of agglomerates in cathode catalyst layers of pem fuel cells," *Journal of Electroanalytical Chemistry*, vol. 573, no. 1, pp. 61–69, 2004.

[24] M. Eikerling, "Water management in cathode catalyst layers of pem fuel cells: a structure-based model," *Journal of The Electrochemical Society*, vol. 153, no. 3, p. E58, 2006.

[25] M. Secanell, K. Karan, A. Suleman, and N. Djilali, "Multi-variable optimization of pemfc cathodes using an agglomerate model," *Electrochimica Acta*, vol. 52, no. 22, pp. 6318–6337, 2007.

[26] A. Kulikovsky, "The regimes of catalyst layer operation in a fuel cell," *Electrochimica acta*, vol. 55, no. 22, pp. 6391–6401, 2010.

[27] K. O'Neil, J. P. Meyers, R. M. Darling, and M. L. Perry, "Oxygen gain analysis for proton exchange membrane fuel cells," *international journal of hydrogen energy*, vol. 37, no. 1, pp. 373–382, 2012.

[28] E. Sadeghi, A. Putz, and M. Eikerling, "Effects of ionomer coverage on agglomerate effectiveness in catalyst layers of polymer electrolyte fuel cells," *Journal of Solid State Electrochemistry*, vol. 18, pp. 1271–1279, 2014.

[29] M. Sabharwal and M. Secanell, "Microstructural analysis of electrode performance in fuel cells at varying water contents," *ECS Transactions*, vol. 86, no. 13, p. 51, 2018.

[30] M. Moore, S. Shukla, S. Voss, K. Karan, A. Weber, I. Zenyuk, and M. Secanell, "A numerical study on the impact of cathode catalyst layer loading on the open circuit voltage in a proton exchange membrane fuel cell," *Journal of The Electrochemical Society*, vol. 168, no. 4, p. 044519, 2021.

[31] M. Sabharwal and M. Secanell, "Understanding the effect of porosity and pore size distribution on low loading catalyst layers," *Electrochimica Acta*, vol. 419, p. 140410, 2022.

[32] B. Prince Abraham and M. Kalidasa, "Influence of catalyst layer and gas diffusion layer porosity in proton exchange membrane fuel cell performance," *Electrochim Acta*, vol. 389, p. 138793, 2021.

[33] P. He, Y.-T. Mu, J. W. Park, and W.-Q. Tao, "Modeling of the effects of cathode catalyst layer design parameters on performance of polymer electrolyte membrane fuel cell," *Applied Energy*, vol. 277, p. 115555, 2020.

[34] E. Carcadea, M. Varlam, A. Marinoiu, M. Raceanu, M. Ismail, and D. Ingham, "Influence of catalyst structure on pem fuel cell performance–a numerical investigation," *International Journal of Hydrogen Energy*, vol. 44, no. 25, pp. 12829–12841, 2019.

[35] P. Havaej, M. Kermani, M. Abdollahzadeh, H. Heidary, and A. Moradi, "A numerical modeling study on the influence of catalyst loading distribution on the performance of polymer electrolyte membrane fuel cell," *international journal of hydrogen energy*, vol. 43, no. 21, pp. 10031–10047, 2018.

[36] R. Friedmann and T. Van Nguyen, "Optimization of the microstructure of the cathode catalyst layer of a pemfc for two-phase flow," *Journal of the Electrochemical Society*, vol. 157, no. 2, p. B260, 2009.

[37] M. Alizadeh and F. Torabi, "Precise pem fuel cell parameter extraction based on a self-consistent model and sccsa optimization algorithm," *Energy Conversion and Management*, vol. 229, p. 113777, 2021.

[38] J. Shen, L. Xu, H. Chang, Z. Tu, and S. H. Chan, "Partial flooding and its effect on the performance of a proton exchange membrane fuel cell," *Energy Conversion and Management*, vol. 207, p. 112537, 2020.

[39] X. Wang and B. Zhou, "Liquid water flooding process in proton exchange membrane fuel cell cathode with straight parallel channels and porous layer," *Journal of Power Sources*, vol. 196, no. 4, pp. 1776–1794, 2011.

[40] O. Antoine, Y. Bultel, P. Ozil, and R. Durand, "Catalyst gradient for cathode active layer of proton exchange membrane fuel cell," *Electrochimica Acta*, vol. 45, no. 27, pp. 4493–4500, 2000.

[41] J. Liu and M. Eikerling, "Model of cathode catalyst layers for polymer electrolyte fuel cells: The role of porous structure and water accumulation," *Electrochimica Acta*, vol. 53, no. 13, pp. 4435–4446, 2008.

[42] W. Li, R. Lin, and Y. Yang, "Investigation on the reaction area of pemfc at different position in multiple catalyst layer," *Electrochimica Acta*, vol. 302, pp. 241–248, 2019.

[43] G.-Y. Chen, C. Wang, Y.-J. Lei, J. Zhang, Z. Mao, Z.-Q. Mao, J.-W. Guo, J. Li, and M. Ouyang, "Gradient design of pt/c ratio and nafion content in cathode catalyst layer of pemfcs," *International Journal of Hydrogen Energy*, vol. 42, no. 50, pp. 29960–29965, 2017.

[44] M. Srinivasarao, D. Bhattacharyya, and R. Rengaswamy, "Optimization studies of a polymer electrolyte membrane fuel cell with multiple catalyst layers," *Journal of Power Sources*, vol. 206, pp. 197–203, 2012.

[45] Q. Wang, M. Eikerling, D. Song, Z. Liu, T. Navessin, Z. Xie, and S. Holdcroft, "Functionally graded cathode catalyst layers for polymer electrolyte fuel cells: I. theoretical modeling," *Journal of the Electrochemical Society*, vol. 151, no. 7, p. A950, 2004.

[46] Z. Xie, T. Navessin, K. Shi, R. Chow, Q. Wang, D. Song, B. Andreaus, M. Eikerling, Z. Liu, and S. Holdcroft, "Functionally graded cathode catalyst layers for polymer electrolyte fuel cells: Ii. experimental study of the effect of nafion distribution," *Journal of the Electrochemical Society*, vol. 152, no. 6, p. A1171, 2005.

[47] R. Fan, G. Chang, Y. Xu, and J. Xu, "Multi-objective optimization of graded catalyst layer to improve performance and current density uniformity of a pemfc," *Energy*, vol. 262, p. 125580, 2023.

[48] P. Charoen-amornkitt, M. Alizadeh, T. Suzuki, and S. Tsushima, "Topologically optimized anode catalyst layers of proton exchange membrane water electrolyzers," *ECS Transactions*, vol. 111, no. 4, p. 87, 2023.

[49] M. Alizadeh, P. Charoen-amornkitt, T. Suzuki, and S. Tsushima, "Mixed topology optimization: A self-guided boundary-independent approach for power sources," *Energy Conversion and Management*, vol. 294, p. 117567, 2023.

[50] D. Yang, Y. Hao, B. Li, P. Ming, and C. Zhang, "Topology optimization design for the lightweight endplate of proton exchange membrane fuel cell stack clamped with bolts," *International Journal of Hydrogen Energy*, vol. 47, no. 16, pp. 9680–9689, 2022.

[51] M. Alizadeh, P. Charoen-Amornkitt, T. Suzuki, and S. Tsushima, "Structural topology optimization and irreversibility analysis in an electrochemical reaction-diffusion system," in *AIP Conference Proceedings*, vol. 3086, AIP Publishing, 2024.

[52] S. Mukherjee, D. Lu, B. Raghavan, P. Breitkopf, S. Dutta, M. Xiao, and W. Zhang, "Accelerating large-scale topology optimization: State-of-the-art and challenges," *Archives of Computational Methods in Engineering*, pp. 1–23, 2021.

[53] M. Long, T. Suzuki, M. Alizadeh, S. Tsushima, and P. Charoen-amornkitt, "The influence of rib and porous reactor thickness on topologically optimized structure in reaction-diffusion systems," in *2023 IEEE Transportation Electrification Conference and Expo, Asia-Pacific (ITEC Asia-Pacific)*, pp. 1–7, IEEE, 2023.

[54] M. P. Bendsøe, "Optimal shape design as a material distribution problem," *Structural optimization*, vol. 1, no. 4, pp. 193–202, 1989.

[55] J. Alexandersen and C. S. Andreasen, "A review of topology optimisation for fluid-based problems," *Fluids*, vol. 5, no. 1, p. 29, 2020.

[56] P. Charoen-amornkitt, M. Alizadeh, T. Suzuki, and S. Tsushima, "Entropy generation analysis during adjoint variable-based topology optimization of porous reaction-diffusion systems under various design dimensionalities," *International Journal of Heat and Mass Transfer*, vol. 202, p. 123725, 2023.

[57] M. Alizadeh, P. Charoen-amornkitt, T. Suzuki, and S. Tsushima, "Investigation of transport-reaction dynamics and local/global entropy production in topology optimization of two-species reaction-diffusion systems," *Chemical Engineering Science*, vol. 275, p. 118739, 2023.

[58] R. Behrou, A. Pizzolato, and A. Forner-Cuenca, "Topology optimization as a powerful tool to design advanced pemfcs flow fields," *International Journal of Heat and Mass Transfer*, vol. 135, pp. 72–92, 2019.

[59] C.-H. Chen, K. Yaji, S. Yamasaki, S. Tsushima, and K. Fujita, "Computational design of flow fields for vanadium redox flow batteries via topology optimization," *Journal of Energy Storage*, vol. 26, p. 100990, 2019.

[60] K. Yaji, S. Yamasaki, S. Tsushima, T. Suzuki, and K. Fujita, "Topology optimization for the design of flow fields in a redox flow battery," *Structural and multidisciplinary optimization*, vol. 57, no. 2, pp. 535–546, 2018.

[61] F. Chen, J. Wang, and X. Yang, "Topology optimization design and numerical analysis on cold plates for lithium-ion battery thermal management," *International Journal of Heat and Mass Transfer*, vol. 183, p. 122087, 2022.

[62] Z. Liu, X. Zeng, W. Zhao, Y. Gao, Y. Sun, and P. Yan, "A topology optimization design of three-dimensional cooling plate for the thermal homogeneity of

lithium-ion batteries," *Energy Conversion and Management: X*, vol. 14, p. 100215, 2022.

[63] V. A. Beck, J. J. Wong, C. F. Jekel, D. A. Tortorelli, S. E. Baker, E. B. Duoss, and M. A. Worsley, "Computational design of microarchitected porous electrodes for redox flow batteries," *Journal of Power Sources*, vol. 512, p. 230453, 2021.

[64] C. Deng and W. Lu, "Geometry optimization of porous electrode for lithium-ion batteries," *Ecs Transactions*, vol. 97, no. 7, p. 249, 2020.

[65] J. Lamb and P. Andrei, "Optimizing the composition of the pemfc catalyst layer," *ECS Transactions*, vol. 98, no. 9, p. 67, 2020.

[66] M. Alizadeh, P. Charoen-amornkitt, T. Suzuki, and S. Tsushima, "A numerical simulation of evolution processes and entropy generation for optimal architecture of an electrochemical reaction-diffusion system: comparison of two optimization strategies," *Journal of The Electrochemical Society*, vol. 170, no. 11, p. 114520, 2023.

[67] O. Sigmund and K. Maute, "Topology optimization approaches," *Structural and Multidisciplinary Optimization*, vol. 48, no. 6, pp. 1031–1055, 2013.

[68] S. Li and B. Sundén, "Effects of gas diffusion layer deformation on the transport phenomena and performance of pem fuel cells with interdigitated flow fields," *International Journal of Hydrogen Energy*, vol. 43, no. 33, pp. 16279–16292, 2018.

[69] L. Xing, X. Liu, T. Alaje, R. Kumar, M. Mamlouk, and K. Scott, "A two-phase flow and non-isothermal agglomerate model for a proton exchange membrane (pem) fuel cell," *Energy*, vol. 73, pp. 618–634, 2014.

[70] F. C. Cetinbas, S. G. Advani, and A. K. Prasad, "An improved agglomerate model for the pem catalyst layer with accurate effective surface area calculation based on the sphere-packing approach," *Journal of the Electrochemical Society*, vol. 161, no. 6, p. F803, 2014.

[71] B. K. Kanchan, P. Randive, and S. Pati, "Implications of non-uniform porosity distribution in gas diffusion layer on the performance of a high temperature pem fuel cell," *International Journal of Hydrogen Energy*, vol. 46, no. 35, pp. 18571–18588, 2021.

[72] M. Moore, P. Wardlaw, P. Dobson, J. Boisvert, A. Putz, R. Spiteri, and M. Secanell, "Understanding the effect of kinetic and mass transport processes in

cathode agglomerates," *Journal of the Electrochemical Society*, vol. 161, no. 8, p. E3125, 2014.

[73] F. C. Cetinbas, S. G. Advani, and A. K. Prasad, "A modified agglomerate model with discrete catalyst particles for the pem fuel cell catalyst layer," *Journal of The Electrochemical Society*, vol. 160, no. 8, p. F750, 2013.

[74] W. Yoon and A. Z. Weber, "Modeling low-platinum-loading effects in fuel-cell catalyst layers," *Journal of The Electrochemical Society*, vol. 158, no. 8, p. B1007, 2011.

[75] S. Kamarajugadda and S. Mazumder, "Numerical investigation of the effect of cathode catalyst layer structure and composition on polymer electrolyte membrane fuel cell performance," *Journal of Power Sources*, vol. 183, no. 2, pp. 629–642, 2008.

[76] T. Suzuki, S. Okada, and S. Tsushima, "Analysis of ionomer distribution and pt/c agglomerate size in catalyst layers by two-stage ion-beam processing," *Journal of The Electrochemical Society*, vol. 167, no. 12, p. 124513, 2020.

[77] Y.-T. Mu, P. He, Z.-L. Gu, Z.-G. Qu, and W.-Q. Tao, "Modelling the reactive transport processes in different reconstructed agglomerates of a pefc catalyst layer," *Electrochimica Acta*, vol. 404, p. 139721, 2022.

[78] K. Broka and P. Ekdunge, "Modelling the pem fuel cell cathode," *Journal of Applied Electrochemistry*, vol. 27, pp. 281–289, 1997.

[79] F. Barbir, *PEM Fuel Cells: Theory and Practice*. Elsevier Science, 2012.

[80] H. Wu, P. Berg, and X. Li, "Modeling of pemfc transients with finite-rate phase-transfer processes," *Journal of The Electrochemical Society*, vol. 157, no. 1, p. B1, 2009.

[81] M. Sahraoui, Y. Bichioui, and K. Halouani, "Three-dimensional modeling of water transport in pemfc," *International journal of hydrogen energy*, vol. 38, no. 20, pp. 8524–8531, 2013.

[82] G. Zhang, J. Wu, Y. Wang, Y. Yin, and K. Jiao, "Investigation of current density spatial distribution in pem fuel cells using a comprehensively validated multi-phase non-isothermal model," *International Journal of Heat and Mass Transfer*, vol. 150, p. 119294, 2020.

[83] B. S. Lazarov and O. Sigmund, "Filters in topology optimization based on helmholtz-type differential equations," *International Journal for Numerical Methods in Engineering*, vol. 86, no. 6, pp. 765–781, 2011.

[84] A. Kawamoto, T. Matsumori, S. Yamasaki, T. Nomura, T. Kondoh, and S. Nishiwaki, "Heaviside projection based topology optimization by a pde-filtered scalar function," *Structural and Multidisciplinary Optimization*, vol. 44, no. 1, pp. 19–24, 2011.

[85] X. Huang and Y. Xie, "Convergent and mesh-independent solutions for the bi-directional evolutionary structural optimization method," *Finite elements in analysis and design*, vol. 43, no. 14, pp. 1039–1049, 2007.

[86] J. V. Carstensen and J. K. Guest, "Projection-based two-phase minimum and maximum length scale control in topology optimization," *Structural and multidisciplinary optimization*, vol. 58, no. 5, pp. 1845–1860, 2018.

[87] C. Zillober, "A globally convergent version of the method of moving asymptotes," *Structural optimization*, vol. 6, no. 3, pp. 166–174, 1993.

[88] M. Bendsoe and O. Sigmund, *Topology Optimization: Theory, Methods, and Applications*. Springer Berlin Heidelberg, 2013.

[89] M. D. R. Batista, S. Chandrasekaran, B. D. Moran, M. S. de Troya, A. Pinongcos, Z. Wang, R. Hensleigh, A. Carleton, M. Zeng, T. Roy, *et al.*, "Design and additive manufacturing of optimized electrodes for energy storage applications," *Carbon*, vol. 205, pp. 262–269, 2023.

[90] V. Muñoz-Perales, M. van der Heijden, P. A. García-Salaberri, M. Vera, and A. Forner-Cuenca, "Engineering lung-inspired flow field geometries for electrochemical flow cells with stereolithography 3d printing," *ACS Sustainable Chemistry & Engineering*, vol. 11, no. 33, pp. 12243–12255, 2023.

[91] C. Lee, W. J. Kort-Kamp, H. Yu, D. A. Cullen, B. M. Patterson, T. A. Arman, S. Komini Babu, R. Mukundan, R. L. Borup, and J. S. Spendelow, "Grooved electrodes for high-power-density fuel cells," *Nature Energy*, pp. 1–10, 2023.

[92] M. R. Gerhardt, L. M. Pant, J. C. Bui, A. R. Crothers, V. M. Ehlinger, J. C. Fornaciari, J. Liu, and A. Z. Weber, "Method—practices and pitfalls in voltage breakdown analysis of electrochemical energy-conversion systems," *Journal of the Electrochemical Society*, vol. 168, no. 7, p. 074503, 2021.

[93] Y. Su, "An improved weighted topology optimization lattice boltzmann model for porous structures of advection–diffusion chemical reaction systems," *Chemical Engineering Journal*, vol. 495, p. 153267, 2024.

[94] M. Alizadeh, J. Gostick, T. Suzuki, and S. Tsushima, "Topological optimization for tailored designs of advection–diffusion-reaction porous reactors based on pore scale modeling and simulation: A pnm-nsga framework," *Computers & Structures*, vol. 301, p. 107452, 2024.

Chapter 5

Topological optimization for tailored designs of advection-diffusion-reaction porous reactors based on pore scale modeling and simulation: A PNM-NSGA framework

Abstract

Reactive transport within porous reactors is crucial to many diverse applications, and the efficacy of these reactors hinges on their microstructure. Mathematical modeling and optimization play a pivotal role in the exploration of efficient designs, enabling the generation of structures that may not be achievable through random realizations of packings. In this study, we propose a framework for high-resolution topological optimization of porous flow-through reactors based on pore-scale simulations using a non-dominated sorting genetic algorithm II. A pore network model for an advection-diffusion-reaction system is developed to simulate reactor performance. This model is integrated with a mathematical optimization algorithm, incorporating a background grid and Delaunay tessellation. The optimization framework generates enhanced porous structures, simultaneously maximizing conversion rates while minimizing pumping costs. Striking a balance between permeability and reactive surface area, the final designs yield a set of Pareto optimal solutions, encompassing diverse non-dominated designs with varying reaction rates and hydraulic requirements. The results demonstrate that optimal pore configurations lead to a 280% increase in conversion rates and a 6% reduction in pumping costs at one end, while on the opposite end of the Pareto front, a 15.2% increase in reaction rates and an 11.3% reduction in pumping costs are observed.

This chapter is published as:

M. Alizadeh, J. Gostick, T. Suzuki, and S. Tsushima. "Topological optimization for tailored designs of advection-diffusion-reaction porous reactors based on pore scale modeling and simulation: A PNM-NSGA framework", *Computers & Structures*, **301** (2024): 107452. https://doi.org/10.1016/j.compstruc.2024.107452

5.1 Introduction

Porous reactors are found in a variety of applications, including redox batteries, fuel cells, and catalytic reactors [1–3]. The reactive transport occurring within these porous media includes advection and diffusion of reactive species in single- or multi-phase fluids, as well as singular or multiple (electro-) chemical reactions. The porous matrix provides the active surface area on which heterogeneous catalytic reactions occur and also facilitates the flow of heat and charge. The void space provides pathways for the flow of reactive and product species, and carrier fluids. Consequently, reactor performance, hydraulic efficiency, operational costs, and durability of porous reactors are intertwined with the microstructural characteristics. For instance, achieving a higher reaction rate can be accomplished by increasing the surface area, which is most readily achieved by incorporation of smaller pores, but this generally hinders flow and diffusion of reactant. Hence, optimizing overall performance entails balancing between maximizing surface area and minimizing mass transport resistance. An ideal porous reactor should consist of pores of varying size and appropriate distribution to enhance both surface area and mass transfer concurrently. Recent progress in additive manufacturing and 3D printing technologies has unlocked fresh prospects for the fabrication of porous reactors featuring complex microarchitectures, offering promising advances in fields such as catalysis [4], electrochemistry [5, 6], and pharmaceuticals [7]. However, leveraging the full potential of these fabrication methods requires a finely tuned design of the porous microstructure. Several experimental investigations have explored tailored reactors with engineered structures to enhance performance [8–10]. For instance, Xu et al. [8] proposed an electrospinning method to fabricate a free-standing carbon nano-fibrous web with ultra-large pores for vanadium redox flow batteries (VRFBs). Their findings showed that the new design reduces concentration polarization, resulting in a VRFB with 10.3% higher voltage efficiency and double the electrolyte utilization efficiency compared to traditional electrodes at a current density of $60\,\mathrm{mA\,cm^{-2}}$. Despite these promising results, performing comprehensive parametric studies to pinpoint the optimal structural parameters (e.g., pore size) remains challenging due to the cost and time associated with experiments. Evidently, achieving a fully optimal topology (including factors like the ideal pore size and spatial distribution) through experimental trial and error appears to be a daunting task. Alternatively, mathematical modeling and optimization offer a systematic approach to investigate the structure-performance relationship and generate more efficient designs [11–16]. For instance, topology optimization using continuum macroscale models has been successfully

utilized for optimizing reactive transport in porous media. In a recent study by Roy et al. [17], researchers employed a density-based topology optimization method to automatically optimize the distribution of porosity throughout the electrode of VRFBs. Their optimized designs reduced losses caused by overpotentials by up to 84%. Additionally, Mitchell and Ortiz [18] employed density-based topology optimization to enhance the anode electrode structure of a lithium-ion battery. By improving the sluggish electron transport caused by the low intrinsic electrical conductivity of silicon, they significantly enhanced the electrode performance. While these approaches provide a powerful tool for optimizing macroscopic material properties (e.g., porosity), they are typically unable to optimize the porous microstructure at the pore level. Particularly, since the interactions between the aforementioned transport and rate processes happen at a pore level, a pore-scale mathematical model becomes imperative for precise simulation of reactor behavior under varying structural and operational conditions. Moreover, in advection-diffusion-reaction (ADR) systems, around which this study revolves, several conflicting objectives must be met simultaneously, namely high conversion rate, low mass transport resistance, and low pumping cost. The absence of trade-offs among these objectives gives rise to a multi-objective optimization (MOO) problem, wherein a set of Pareto optimal (non-dominated) solutions can be attained. Another emerging trend is the utilization of particle-scale models, such as the lattice Boltzmann method (LBM), together with topology optimization algorithms. In a paper published in 2024, Zheng et al. [19] utilized LBM coupled with level-set topology optimization to generate optimized porous diffusion-reaction systems with hierarchical structures. Their optimization yielded structures with enhanced reaction rates and material utilization. However, their study only considers diffusion and reaction processes, without incorporating any convective flow. Currently, integration of LBM and topology optimization in the literature is limited and does not encompass various complicated transport and rate processes.

Mathematical models for reactive transport can be broadly classified into two primary categories: (1) macro-scale continuum models and (2) pore-scale models. In practical applications, porous reactors exhibit a diverse and heterogeneous structure. However, macro-scale continuum models assume uniform, averaged properties –

such as flow resistance, thermal resistance, and reaction activity – within a representative elementary volume (REV). These models typically describe porous media using multiple isotropic and anisotropic properties (e.g. porosity, tortuosity, permeability coefficient). Although this approach offers valuable insights into reactive transport phenomena, it falls short in capturing the impact of the detailed microstructure at a high resolution – a necessity for precise simulation and design of porous reactors. In contrast, pore-scale models offer a geometrically resolved simulation of the system, addressing flow, transport, and reactions at a pore level. While this approach comes with increased computational requirements, it enables a thorough and dependable insight into the 3D morphology of porous reactors, resulting in a more robust comprehension of the structure-performance relationship. Numerous studies in the literature have introduced pore-scale models aimed at analyzing transport and rate processes within porous media across a range of applications [19–27]. For example, Zhan et al. [21] employed a 3D pore-scale lattice Boltzmann method (LBM) to simulate transport mechanisms and electrochemical processes within VRFB electrodes. Their investigation revealed a critical link between the microstructure of the electrode and its electrochemical performance. They concluded that an optimal microstructure with a single dominant pore size peak (around $10 - 20\,\mu\mathrm{m}$) and some large pores is essential for achieving both superior electrochemical performance and low-pressure drop, which are crucial for reducing operational costs. In another application, Kočí et al. [22] introduced a novel methodology for pore-scale simulation of flow, diffusion, and reaction in coated catalytic filters. They accomplished this using 3D reconstructions of porous structures based on X-ray tomography (XRT). The reconstructed medium was then used for simulation in OpenFOAM using the finite volume method (FVM). Their results highlight that gas primarily flows through cracks in the coated layer and remaining free pores in the filter wall, with mass transport driven by diffusion. The results also underscored that compact catalytic coatings lead to a significant increase in pressure drop due to reduced local permeability.

While geometrically resolved models offer valuable insights into reactive transport phenomena, it is well-known that direct numerical simulation (DNS) demands substantial computational resources and is often limited to unreasonably small calculation domains [28]. Therefore, modeling an entire component (e.g., an electrode of a battery) or device (e.g., a battery cell) with a realistic length scale remains a challenge through these approaches. Also, the majority of these studies have concentrated on

existing materials and structures [29], while pursuit of a systematic technique in generating novel optimal designs is not yet well studied. This is partly because mathematical optimization algorithms usually involve iterative model solutions, requiring extensive computational resources to seek even a single local optimum solution. In light of these constraints, it becomes evident that topological optimizing using geometrically resolved pore scale models is not yet feasible, at least with reasonable computational resources.

Pore network modeling (PNM) [30–32] represents an alternative approach to DNS, simplifying the intricate microstructure of porous media into a network of interconnected pores and straight tubes (throats). This abstraction accelerates simulations by several orders of magnitude (typically >10000 times faster) compared to conventional pore-scale DNS models while maintaining an acceptable level of pore-scale accuracy. The computational efficiency of PNM positions it as a viable alternative for large-scale mathematical optimization of porous microstructures at a geometrically resolved level. PNM has been successfully employed to investigate various physical phenomena in different systems—diffusion in fuel cells [33], electrochemical reactive transport in battery electrodes [1], dispersion in porous media [34], and two-phase flow [35] to name a few. For example, in a recent publication, Misaghian et al. [1] extended PNM to include multiple coupled physical processes to assess the influence of heterogeneous electrode structures on a VRFB cell performance, solving the advection-diffusion and Nernst-Planck equations for ion transport coupled with Butler-Volmer kinetics and solid-liquid mass transfer films. Their findings demonstrated that multi-layer structures with higher permeability near the membrane and lower permeability near the channel substantially increased current density, resulting in a remarkable 57% performance enhancement compared to the opposite layer arrangement.

Furthermore, Sadeghi et al. [28] introduced a PNM-based framework to investigate reactive transport within hierarchical porous catalyst particles, emphasizing the generation of optimal microstructures rather than exclusively modeling existing porous media. Notably, the study finds that increasing macroporosity does not always enhance catalytic activity, and particles with lower pore size ratios exhibit higher reactivity. Subsequently, another research group extended this study into 3D [36], incorporating pore interconnections as an adjustable parameter. It has been found that particle performance exhibits distinct trends, influenced by macroporosity and other factors, depending on the average pore Damköhler number. Also of note is that the advantages of hierarchical structures are most pronounced in systems where the

reaction-controlled process is absent, and species diffusivity is the limiting factor for reactive transport. Following these earlier research endeavors, Huang et al. [30] investigates the influence of adding channels to a porous reactor with a first-order chemical reaction. After validating their PNM model against a finite element method (FEM), they showed that the addition of channels in these structures significantly enhances mass transport, making multi-channel featured porous systems desirable for catalyst applications. Nevertheless, although these studies yielded valuable results, their proposed frameworks lack a comprehensive mathematical scheme for generating innovative microstructures automatically. Instead, they often presuppose certain characteristics of the optimal microstructure, such as the presence of macroporosity or extended channels, primarily conducting parametric analysis on various parameters. In a more rigorous approach, van Gorp et al. [29] integrated a genetic algorithm (GA) with PNM to design highly efficient electrodes for VRFBs. Their optimized design effectively reduced pumping costs by 73% and improved electrochemical performance by 42% compared to a randomly generated initial structure. Although that study provided a valuable proof-of-concept, it was limited in several regards. The pores were confined to a cubic lattice with a relatively limited number of pores (a total of 676 pores), which also limited the size distribution that could be attained. Their model did not account for the influence of local convective flow (local Reynolds number) when estimating the mass transfer coefficient for the transport of species from the bulk solution to the solid-liquid interface. Instead, a uniform Reynolds number was assumed throughout the domain, based on the superficial velocity. Additionally, they manually maintained overall porosity at a constant value during the optimization process. As such, their framework did not encompass the capacity to generate entirely distinct pore network (PN) topologies.

The primary objective of this study is to present a framework for the large-scale optimization of porous reactors by integrating PNM and a non-dominated sorting genetic algorithm II (NSGA-II). This framework specifically addresses advection, diffusion, and chemical reaction phenomena within a porous network, which is generated using a Delaunay tessellation of random base points [37]. By employing a Delaunay tessellation, the optimization algorithm gained the flexibility to distribute pores in arbitrary spatial configurations, in contrast to previous efforts which were limited to a cubic lattice. The network generation and simulations are conducted using OpenPNM, a Python-based open-source package developed for PN simulations [38]. Moreover, the optimization process is carried out through NSGA-II, allowing for theres simultaneous optimization of multiple objectives. In this study,

the focus is on two key objectives: conversion rate and pumping cost. However, it is worth noting that this framework is versatile and capable of accommodating any number of objectives as needed.

5.2 Modeling and optimization

In many practical applications, diverse and concurrent processes (e.g., advection, diffusion, and reaction) compete within porous reactors, collectively shaping their overall performance. Should any one of these processes impose limitations, it may degrade the overall performance. Given the significant influence of porous microstructure on these processes, the topology of porous networks should seek a balance among different processes without imposing severe limitations on any of them [39–41]. Furthermore, such systems frequently necessitate the simultaneous optimization of multiple conflicting objectives. For instance, in the context of ADR porous reactors, it is favorable to maximize the overall conversion rate while minimizing the hydraulic power requirements (pumping cost). Therefore, a MOO algorithm becomes a requisite tool to concurrently satisfy these diverse and contradictory requirements. In the present study, a designated set of points is provided as input for the network generation algorithm to create the PN. This constructed PN is subsequently used to solve flow and reaction in accordance with predetermined boundary conditions (BCs). The PNM simulation is in turn incorporated into an optimization algorithm, enabling the systematic refinement of the porous topology through an iterative process. Further details on these steps are provided in the following subsections.

5.2.1 Network generation

Transport through the PN depends not only on the pore size distribution, but also on the spatial and topological arrangement of the pores. Recent work by van Gorp et al [29] demonstrated the ability of genetic algorithm-based optimization to generate improve electrode performance by adjusting the pore size distribution and their spatial distribution on a cubic lattice. Confining the pore centers to a cubic lattice restricted the possible designs in several ways: the maximum pore size could not exceed the lattice spacing (lest pores overlap), the connectivity distribution was limited to 6 neighbors, and all connections between pores were oriented along the principal

axis of the lattice. The present work aimed to overcome these limitations by developing a procedure for using random PNs based on Delaunay tessellations. Generating a PN from a Delaunay tessellation has been described in detail previously [37].

The communication between PNM and NSGA-II lies in the network generation process. On the PNM side, network generation is performed using a Delaunay tessellation in OpenPNM. It receives the coordinates of some base points to generate a network. The background grid specifies the coordinates of all possible pores in the design domain. The optimizer, NSGA-II, tries to improve the structural design by selecting these possible coordinates from the background grid. It does this by including or excluding them in an algorithmic way, to enhance the objective functions (maximizing reaction rate and minimizing pumping requirements).

Generating random network topology

The main challenge when coupling random networks to genetic optimization is the incompatibility between having a fixed number of genes in each individual and each generation, and the infinite possible locations of pores. To address this, we defined a grid of possible locations and setup the genetic algorithm to optimize which of these locations were activated (described in section 5.2.4). The grid of possible location essentially adds a lower limit to the resolution of the pore locations. A resolution of $40\,\mu\mathrm{m}$ was chosen meaning that the smallest pores size and smallest pore-to-pore space cannot be less than this if no other operator is applied. Fig. 5.1a shows the result of applying a Delaunay tessellation on a grid, which yields a standard cubic lattice, while Fig. 5.1b shows the result after randomly activating 30% of the sites on the grid. In this case the pore centers still lie on the grid, but the connectivity of the pores is more diverse than on a fixed lattice. The pore size distribution, shown in Fig. 5.1e, is also wider than a cubic lattice (Fig. 5.1e) because the pore diameters were able to grow up the distance of the nearest pore rather than the fixed lattice spacing. The randomized network shown in Fig. 5.1b was further enhanced by applying a relaxation of the pore centers after the tessellation. A rigorous relaxation as described by Lloyd [42] uses the geometric centroid of each Voronoi cell, which requires computing many convex hulls and is time consuming. An alternative, less computationally demanding, relaxation method was performed here such that new pore locations were computed as the distance-weighted average of each neighbor pore. This relaxation was applied iteratively by moving the pore centers halfway to the new locations to avoid overcorrecting, then repeated N times by recomputing the weighted average after each step. It was found that $N = 3$ provided a good

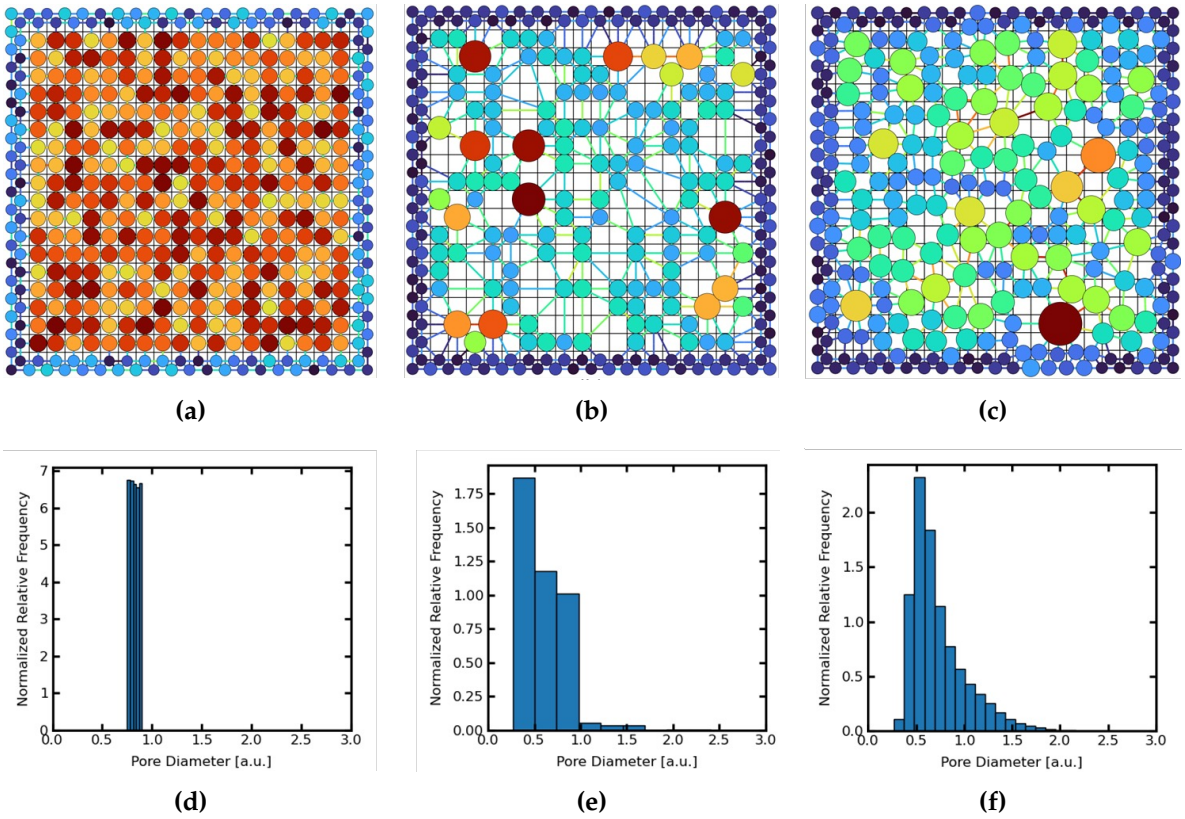

Figure 5.1: 2D schematic of random network generation on a grid. The subfigures show results (a) when all possible locations are used, (b) with using only 30% of possible locations, and (c) using 30% possible location with relaxation of the base points. The bottom row shows the corresponding pore size distributions (in arbitrary units) attained by assuming all pore diameters are between 90 to 100% of the distance to their nearest neighbor.

balance between stable results and efficient computation. The final result is shown in Fig. 5.1c where it can be seen that most pore centers no longer lie on the grid and the distribution of the pores fills space. The pore size distribution in Fig. 5.1f is even broader than the case in Fig. 5.1e. The sites along the edges and faces of the domain were always included to ensure that the internal pores were confined to a fixed domain size. The pores on the inlet and outlet faces were used to apply boundary conditions so did not affect the flow through the domain. The layer of small pores on the other surfaces can be considered as physically compacted or compressed so not relevant to the flow. All simulation results reported below were obtained on a 3D network, and the 2D representation shown in Fig. 5.1 is only to aid visualization.

Assigning geometric properties

Once the spatial locations of the pores and their connectivity was established, the geometric properties of the pores and throats were calculated. Pore radii were assigned by finding the maximum possible size of each pore that just touched its nearest neighbor, then multiplying this value by a random number between 0.75 and 0.9. Throat diameters were assigned by finding the minimum diameter of the two neighboring pores, then multiplying this value by a random number between 0.5 and 0.7 to create constrictions. The aforementioned ranges are chosen arbitrarily but they fall within the range of previously reported values in the literature [29, 30]. Pores were treated as spheres and throats as cylinders for all subsequent geometry calculations such as surface areas and volumes. Throat lengths were computed by assigning the overlap between the spherical pore bodies and cylindrical throats to the throat. This is illustrated in Fig. 5.2.

Adding throat nodes

As will be discussed in section 5.2.2, it was necessary to incorporate local mass transfer coefficients in the reaction term. Mass transfer coefficients are a function of local fluid velocity, which is only known in the throats, while the reaction is also a function of concentration, which is only known in the pores. It was therefore necessary to incorporate throat nodes into the network, as described by Misaghian et al. [1]. Each throat was divided into two segments and a new "node" (i.e., a pore) was inserted at the junction. The fluid velocity through this node could then be found from the upstream throat segment. The reaction term was only enabled in these throat nodes. This process increased the number of degrees of freedom so increased the computational time required to solve the transport problem, but this was unavoidable. The geometric properties of the throat nodes were chosen such that they had no impact on the hydraulic and diffusive conductance of the conduit, which were calculated before the throat nodes were added.

5.2.2 Modeling of dilute solution transport

Transport through the domain was modeled as advective-diffusive transport of a reactive solute. The pressure in each pore (and throat node) was first found by solving the flow problem assuming a fixed pressure drop across the domain (boundary conditions are outlined in section 5.2.3). The velocity in each throat was found using the computed pressures, then used to compute the advective-diffusive conductance values using the power-law scheme [34]. Finally, the advection-diffusion problem was

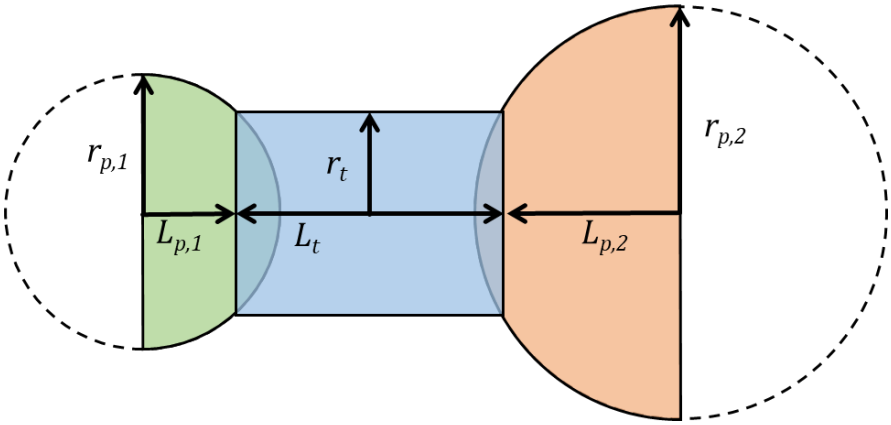

Figure 5.2: Schematic diagram showing the assumed shape and pertinent dimensions for calculating transport conductance values.

solved to determine the concentration distribution in the domain in the presence of a reaction.

The conductance values were computed assuming cylindrical throats and spherical pore bodies, as shown in Fig. 5.2. The length of the pores, L_p, was found by subtracting the length of the intersection between a sphere and a cylinder from the radius of the pore. Due to the way that pore sizes were assigned they never overlapped, which helped to ensure the throat node procedure remained viable.

Given these assumptions, the total hydraulic conductance, G^{h}, of each pore-throat-pore conduit was computed as:

$$\frac{1}{G^{\mathrm{h}}} = \frac{1}{g^{\mathrm{h}}_{p,1}} + \frac{1}{g^{\mathrm{h}}_{t}} + \frac{1}{g^{\mathrm{h}}_{p,2}} \tag{5.1}$$

where $g^{\mathrm{h}}_{p,i}$ for a sphere is [43, 44]:

$$\frac{1}{g^{\mathrm{h}}_{p,i}} = \frac{4\mu}{\pi r_p^3}\left(\frac{r_p L_p}{(r_p^2 - L_p^2)} + \tanh^{-1}\left(\frac{L_p}{r_p}\right)\right) \tag{5.2}$$

and g^{h}_{t} for a cylindrical throat is:

$$\frac{1}{g^{\mathrm{h}}_{t}} = \frac{8\mu L_t}{\pi^2 r_t^4} \tag{5.3}$$

Similarly, the diffusive conductance, G^{d}, was found from:

$$\frac{1}{G^{\mathrm{d}}} = \frac{1}{g^{\mathrm{d}}_{p,1}} + \frac{1}{g^{\mathrm{d}}_{t}} + \frac{1}{g^{\mathrm{d}}_{p,2}} \tag{5.4}$$

where:

$$\frac{1}{g^{\mathrm{d}}_{p}} = \frac{1}{D_A \pi r_p} \tanh^{-1}\left(\frac{L_p}{r_p}\right) \tag{5.5}$$

and:

$$\frac{1}{g^{\mathrm{d}}_{t}} = \frac{L_t}{\pi r_t^2 D_A} \tag{5.6}$$

And the advective-diffusive conductance, G^{ad}, was found using the following power-law formulation [34]:

$$G^{\mathrm{ad}} = \frac{q_{ij}}{e^{Pe_{ij}} - 1} \tag{5.7}$$

Pe_{ij} is the pore-scale Peclet number defined as:

$$Pe_{ij} = \frac{Q_{ij}}{A_t}\left(\frac{L_t}{D_A}\right) \tag{5.8}$$

where Q_{ij} is the volumetric flow between pores i and j. L_t and A_t are the length and cross-sectional area of the element, respectively, and D_A s the diffusion coefficient of the solute. Inserting the definition of the diffusive conductance and the fact that $Q_{ij} = G^{\mathrm{h}}_{ij}\Delta P_{ij}$ yields the Peclet number for a conduit in terms of pre-computed conductance values and the calculated pressure values in each pore:

$$Pe_{ij} = \frac{G^{\mathrm{h}}_{ij}}{G^{\mathrm{d}}_{ij}}\Delta P_{ij} \tag{5.9}$$

The system was modeled at steady state so the mass balance around each node i can be expressed as:

$$\sum_j \left(Q_{ij}C_{A,j} + G^{ad}(C_{A,j} - C_{A,i})\right) = r_A \tag{5.10}$$

Writing Eq. (5.10) for every pore in the network yields a system of linear equations which must be solved simultaneously to determine the concentration in every pore.

The value of r_A in Eq. (5.10) was set to zero for pores where no reaction was occurring. In the throat nodes, the solute was consumed in a first-order heterogeneous reaction occurring at the solid-liquid interface in the throat nodes according to the standard rate expression:

$$r_A = k_r A_s C_{A,\text{surf}} \tag{5.11}$$

where k_r is the kinetic constant per unit area, A_s is the wetted surface area, and $C_{A,\text{surf}}$ is the concentration of the reactant at the surface. Only the bulk concentration is known after solving the system of equation defined by Eq. (5.10); however, since the reaction was assumed to occur at the solid-liquid interface the rate of mass transfer between the bulk fluid and the wall can be expressed as:

$$r_A = -k_L A_s (C_A - C_{A,\text{surf}}) \tag{5.12}$$

noting that the diffusion from the bulk to the surface corresponds to a consumption of A and hence a negative reaction rate. In Eq. (5.12), k_L is mass transfer coefficient. Equating these two expressions for the reaction rate and solving for r_A in terms of C_A yields:

$$r_A = \frac{k_r k_L}{k_L - k_r} A_s C_A \tag{5.13}$$

which provides the required expression for the rate of consumption of A in terms of the known concentration. The kinetic constant, k_r, was taken from Misaghian et al. [1] for consumption of vanadium in a redox flow battery, while the mass transfer coefficient was computed from:

$$Sh = \frac{k_L D_t}{D_A} = 1.0\, Re^{0.7}\, Sc^{0.33} \tag{5.14}$$

Sh was computed for each throat node and the throat diameter D_t was taken as the characteristic length. The surface area of each throat node was taken as the sum of the internal surface areas of the two neighboring throat segments which comprised the original throat. As mentioned above the velocity is not known in pores, yet this is where the mass balances and reactions are applied. Dividing throats into two segments separated by a "throat node" means that the velocity from the neighboring throat segment can be adopted as the velocity in each throat node. Finally, the total

rate of reaction in the network was found by summing up the rate of consumption of species A in each pore using Eq. (5.10).

5.2.3 Boundary conditions

Constant pressure conditions were assigned to the inlet and outlet nodes of the network to solve for the pressure distribution and throat velocity. This is translated as a fixed pressure drop (ΔP) across the domain. Additionally, at the inlet, the concentration (C_{in}) remained fixed, while an outflow boundary condition was imposed at the outlet pores, ensuring a zero gradient for the reactant species concentration. The specific values of boundary conditions used in this study are discussed in section 5.2.5 (System parameters).

5.2.4 Optimization algorithm

GA is a well-established optimization technique that draws inspiration from the principles of biological evolution, which find application in a wide range of fields, including optimization problems, machine learning, scheduling, and parameter tuning for machine learning models, among others. GA is a part of a broader class of algorithms known as evolutionary algorithms, which are designed to mimic the process of natural selection by adopting operators such as crossover, mutation, and selection to address computationally difficult or time-consuming problems. The sophisticated, nonlinear nature of reactive transport within porous media at the pore-level necessities the employment of gradient-free metaheuristic algorithms, such as GA, to seek the optimal PN morphology. In this work, a binary NSGA-II algorithm, a MOO variant of GA, is used to improve the conversion rate while concurrently minimizing pumping costs. NSGA-II is a mainstream choice for multi-objective optimization problems and has been successfully employed for various problems [45–48]. In this work, we opted for NSGA-II because of its robust and efficient algorithm for MOO problems. We acknowledge that other metaheuristic algorithms that might be advantageous for topological optimization of porous reactors, such as sailfish optimization (SFO) [49], whale optimization algorithm (WOA) [50], particle swarm optimization (PSO) [51], and multi-objective imperialist competitive algorithm (MOICA) [52] could be explored. However, a thorough comparison of these algorithms would require a comprehensive investigation that falls outside the scope of the present work.

As previously explained, the PN is generated based on a set of points residing on a background grid, forming the initial coordinates for potential pores. These initial coordinates undergo a relaxation function to determine the final pore coordinates within the PN. Each point in the problem grid corresponds to a potential pore within the PN, with the optimization problem controlling the presence or absence of these potential pores. Consequently, a Boolean value is assigned to each point, indicating whether the corresponding pore exists or not, and the optimization solutions are encoded as a Boolean vector, representing the existence or absence of candidate pores. Eliminating one pore may lead to the expansion of nearby pores, which facilitates the transportation of reactant species. Nevertheless, this action simultaneously affects the available reactive surface area. The algorithm begins with the Initialization step, wherein a set of n_{pop} initial solutions, referred to as the population or chromosomes, is randomly generated. Each individual within the population represents distinct combinations of potential pore existence, yielding a binary vector of length n_{g}, where n_{g} denotes the total number of points in the problem grid. The size of the grid is determined based on the number of points in each direction and the voxel size, which defines the spacing between neighboring grid points. Subsequently, the initial population undergoes iterative evolution, generating increasingly improved solutions over successive generations until convergence or a predefined termination criterion is satisfied. This study uses the maximum number of iterations as the termination criterion. The optimization problem is formulated as:

$$\begin{aligned} \max_{V_{\mathrm{g}}} \quad & F^1_{\mathrm{obj}} = \sum_{i=1}^{N_{\text{throat node}}} r_{A,i} \\ \min_{V_{\mathrm{g}}} \quad & F^2_{\mathrm{obj}} = Q \times \Delta p \\ \text{s.t.} \quad & V_{\mathrm{g},j} \in \{0,1\} \quad \text{for} \quad j = 1, 2, \ldots, n_{\mathrm{g}} \end{aligned} \tag{5.15}$$

In which, F^1_{obj} and F^2_{obj} represents the total conversion rate and pumping power, respectively. As previously mentioned, F^1_{obj} is computed by summing the reaction rates in all throat nodes where reactions occur. Moreover, F^2_{obj} is determined by multiplying the overall reactor flow rate (Q) and the pressure drop (ΔP). Q is evaluated by summing up the flow rate of fluid moving through the inlet pores, while ΔP is dictated by the specified boundary condition. Also, the solution vector, denoted as V_{g}, represents the status of each pore in the problem grid. Following the initialization, NSGA-II proceeds to the fitness evaluation step. In this phase, the performance of each individual is assessed, by generating the corresponding PN, solving

the governing equations, and calculating the conversion rate and pumping cost. It is worth noting that, in this study, population fitness evaluation is executed in parallel on several CPU cores. This parallelization significantly accelerates the calculation speed, allowing the algorithm to explore a wide search space and find high-quality solutions more rapidly. Subsequent to fitness evaluation, the algorithm performs a ranking process. It categorizes the population into different non-dominated fronts based on their fitness and dominance relationships. The first front contains Pareto optimal solutions, which are the best trade-offs between conversion rate and pumping cost and are not dominated by any other solution. In the crossover and mutation step, NSGA-II selects a pool of parent population via a binary tournament selection process for reproduction. These selected parents undergo a uniform crossover as well as mutation process to produce a new set of offspring. The crossover process combines data from two parent solutions, enabling the offspring to inherit their distinctive attributes, while the mutation operation makes random modifications to a single parent, thereby enriching exploration of the search space. Finally, in the selection and truncation step, the current population and offspring are merged to form a combined pool. Here, the algorithm applies ranking operation once again to select fittest individuals from the combined pool according to their ranking and crowding distance for the next generation. An overview of the optimization procedure is depicted in Fig. 5.3, with the primary operators briefly described as follows.

Initialization

In the initialization step, n_{pop} distinct PNs are generated randomly using Delaunay tessellation. As previously mentioned, each PN is represented by a solution vector, V_{g}, comprising n_{g} Boolean values that indicate presence or absence of each candidate pore in the final PN. To generate each V_{g}, first, a vector of random numbers between 0 and 1, with the same size (n_{g}), is produced using a uniform random distribution. Subsequently, each element in this vector is compared to a chosen threshold value. Values below the threshold indicate the existence of the corresponding pore, while values exceeding the threshold signify the absence of the potential pore. As the initial random numbers (between 0 and 1) were generated using a uniform random distribution, tuning the threshold value approximately determines the overall percentage of pores that exist in the final PN. For instance, choosing a threshold with an extreme value of one will lead to the presence of all potential pores from the background in the final PN (see Fig. 5.1a). It is well-known that the efficiency of GA is significantly influenced by the quality and diversity of the initial population [53]. To ensure appropriate diversity, a range of threshold values is considered based on

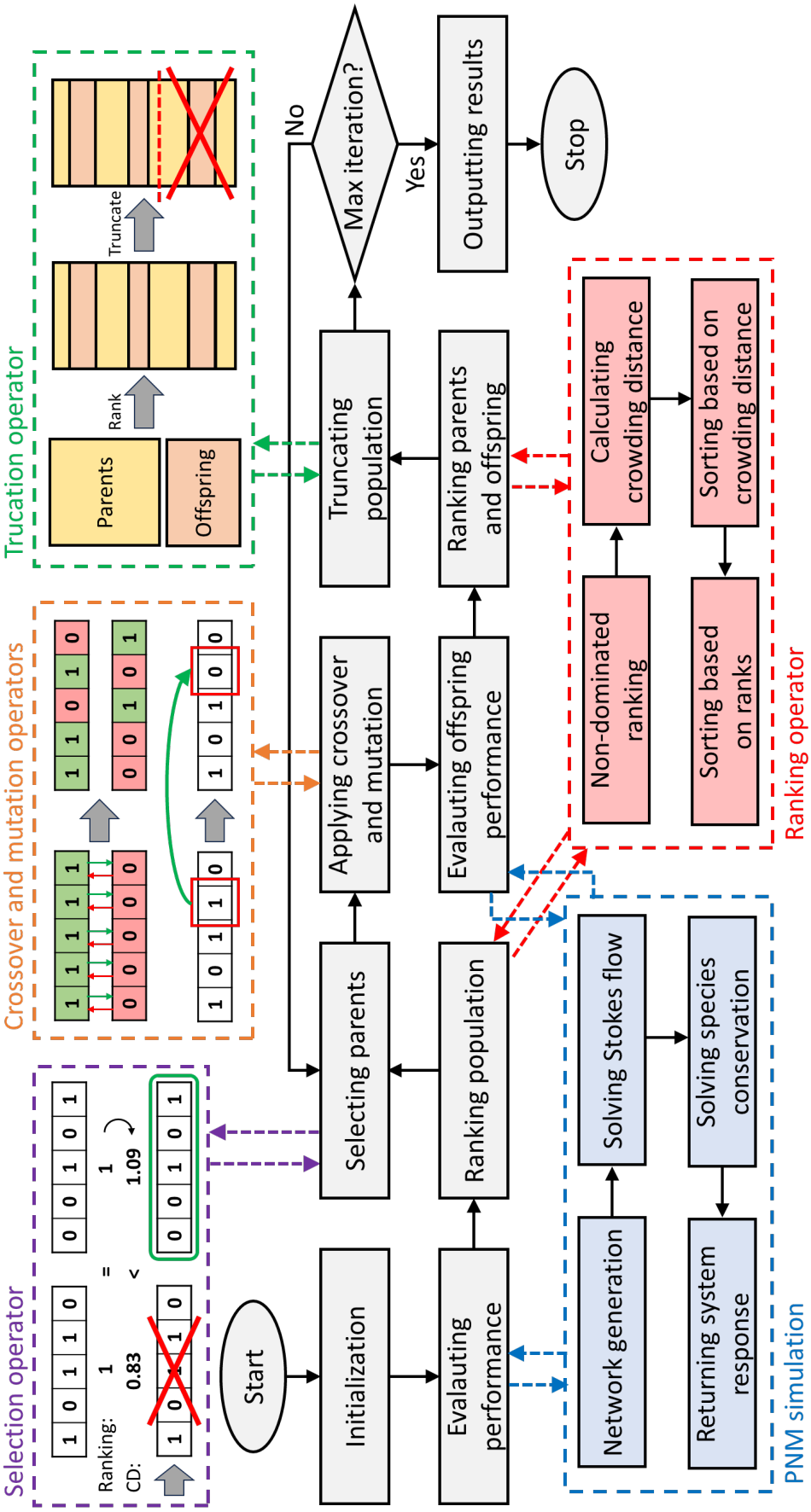

Figure 5.3: Flowchart of optimization and simulation algorithms.

linear spacing between 0 and 1, in accordance with n_{pop}. This initialization strategy ensures the presence of a diverse range of design solutions in the initial population, encompassing configurations with low, medium, and high numbers of pores. In other words, out of the entire intial populations generated in this study, the threshold value for each one was different, ranging linearly from 0 to 1. Hence, among the initial populations, there existed design solutions with various numbers of pores. From this perspective, we started with generating populations with a "vector of random continuous variables", but then converted this to a "binary vector" using the threshold value.

Population ranking front

NSGA-II [54, 55] employs a non-dominated sorting operator to rank the individuals of a population in a case with multiple objectives. The initial step in this operator is non-dominated sorting, which classifies individuals into distinct fronts based on their dominance relationships. Dominance is determined by comparing the objective function values of two individuals. If one individual is superior in at least one objective and not worse in any other, it is considered dominant. For instance, in this study, conversion rate and pumping cost are treated as two conflicting objectives. A solution exhibiting a higher conversion rate and lower pumping cost consistently dominates any alternative solutions characterized by lower conversion rates and higher pumping costs. However, in scenarios where both the conversion rate and pumping cost of two solutions are either simultaneously higher or lower compared to each other, mutual domination does not occur, and these solutions are categorized within the same class (or front). This process organizes individuals into a series of fronts, where the first front consists of non-dominated individuals, the second front contains individuals dominated only by those in the first front, and so on. After non-dominated sorting, the next step is to calculate the crowding distance (CD) for each individual within a front. CD reflects the density of individuals in the objective space, helping to maintain diversity in the population. It is calculated by considering the distances between an individual and its neighboring individuals along each objective dimension. Individuals with higher CDs are preferred as they contribute to a more evenly distributed Pareto front. The final sorting of the entire population is a two-step process: first, individuals are sorted based on their crowding distance in descending order, ensuring that individuals with greater CDs are prioritized. The second sorting is the front ranking, arranging individuals based on their front ranking. This sequential sorting based on CD and front ranking guarantees a systematic arrangement of population according to dominance. In tied rankings, priority is

assigned by considering their CD values. This dual-criteria sorting mechanism ensures a meticulous organization of individuals within the population, promoting a comprehensive and balanced exploration of the solution space. In each generation, following the arrangement of the merged parent and offspring populations through the previously outlined procedure, the top n_{pop} individuals survive and advance to the subsequent generation during the truncation process. This mechanism ensures that only the fittest individuals, determined by their performance in the optimization objectives, pass to the next generation, fostering a continuous progression of the population toward superior solutions.

Binary tournament selection

The optimization process uses a binary tournament method to select parents for the reproduction of offspring. This method randomly samples two individuals from the population and evaluates their dominance relationship, ultimately selecting the parent with a superior front ranking and CD. This strategic approach ensures that all individuals have an opportunity to participate in reproduction, thereby promoting overall diversity. However, fitter individuals are granted a higher probability of passing on their genomes to the subsequent generations, aligning with the principle of biological evolution and natural selection. Further information regarding this selection scheme can be found in the literature [56, 57].

Crossover

In the present study, a uniform crossover operator is utilized to generate new PNs by exchanging genetic information between pairs of parent networks. The selection of parent networks is performed through a binary tournament. The number of reproduced offspring from the crossover process is determined by a given crossover ratio (p_{c}) and is calculated by $2 \times \left\lceil \frac{p_{\mathrm{c}} \times n_{\mathrm{pop}}}{2} \right\rceil$. Each PN is represented by a vector of binary genome, and the uniform crossover operates independently on each genome (see Fig. 5.3). Notably, a pair of parents gives rise to two children, with the decision on the inheritance of genomes from each parent to each child being dictated by a uniform random distribution.

Mutation

The mutation operator introduces random changes into the genetic makeup of solutions, fostering diversity in the population and promoting exploration within the search space. First, a subset of $\lceil p_{\mathrm{m}} \times n_{\mathrm{pop}} \rceil$ individuals are randomly selected for

Table 5.1: Optimization algorithm parameters

Optimizer parameter	Value
Population size (n_{pop})	1200
Crossover ratio (p_{c})	0.85
Mutation ratio (p_{m})	0.05
Mutation rate (r_{m})	0.1

mutation from the parents' pool, where p_{m} is a specified mutation ratio. The severity of mutation is then dictated by the mutation rate (r_{m}), with $\lceil r_{\mathrm{m}} \times n_{\mathrm{g}} \rceil$ genomes being flipped at random positions (see Fig. 5.3) using a "bit mutation" operator. This targeted alteration in genetic information introduces variability among the individuals, contributing to the algorithm's capacity for effective exploration of the solution space. This inherent randomness is fundamental for avoiding premature convergence and promoting the continued exploration of the search space. The introduction of slight variations ensures that the optimization algorithm is not confined to a narrow region of the solution space and is better equipped to discover diverse and potentially optimal solutions. The values of algorithm parameters are given in Table 5.1. The number of generations (iterations) in optimization is specified based on the size of search space. It is also noteworthy that "crossover ratio" and "mutation ratio" indicate the proportion of the population that undergoes crossover and mutation operations, respectively. Once an individual is selected for mutation, only a portion of its genes undergoes mutation. "Mutation rate" defines the severity of the mutation by specifying this proportion.

5.2.5 System parameters

The proposed framework is employed to optimize the PN topology of an ADR porous reactor. This reactor facilitates the transport of a dilute solution through advection-diffusion mechanisms, extending from the inlet to outlet boundaries, while simultaneously an arbitrary solute species A is reacted in presence of active surface area. Depending on the configuration of parameters, the system may exhibit characteristics of either kinetic or hydraulic sluggishness. The optimization process is designed to yield a tailored PN topology that improves system performance by achieving a balanced compromise between transport and rate phenomena. This involves proper control of both surface area and permeability through alternation of PN morphology. The properties of the solution and solute are adopted from literature for vanadium ion redox reaction in a VRFB. The values of these properties as well as the operating

Table 5.2: System properties and operational conditions

Parameter	Unit	Value / range
Grid shape	-	$50 \times 50 \times 50$
Voxel size (d)	μm	40
Grid dimensions	mm^3	$2 \times 0.52 \times 0.52$
Number of candidate pores	-	8450
Solution density (ρ) [1]	$\mathrm{kg\,m^{-3}}$	1350
Solution viscosity (μ) [1]	Pa s	0.005
Solute diffusion coefficient (D_A) [1]	$\mathrm{m^2\,s^{-1}}$	3.9×10^{-10}
Kinetic constant per unit area (k_0) [1]	$\mathrm{m\,s^{-1}}$	5×10^{-7}
Solute concentration (C_{in}) [1]	$\mathrm{mol\,m^{-3}}$	600
Charge transfer coefficient (α) [1]	-	0.5
Temperature (T)	K	298
Pressure drop (Δp)	Pa	400
Overpotential (ηp)	V	0.3

conditions (boundary conditions) are presented in Table 5.2. Although the developed model does not involve all phenomena occurring in a VRFB, the reaction constant, k_r, is estimated according to the Butler-Volmer kinetics assuming a constant overpotential and a largely polarized condition (only forward reaction) as described below.

$$k_r = k_0 \exp\left(\frac{\alpha F}{RT}\eta\right) \tag{5.16}$$

In this equation, α, T, η, F, and R are charge transfer coefficient, temperature, overpotential, Faraday's constant, gas constant, respectively.

5.3 Results and discussion

A 3D background grid with shape $50 \times 50 \times 50$ and spacing of $40\,\mu\mathrm{m}$ is assumed as the PN design domain. The optimization process aimed to identify the optimal PN morphology within this $2 \times 0.52 \times 0.52\,\mathrm{mm}^3$ lattice, toggling candidate pores on and off under the assumption of flow occurring in the longitudinal direction ($2\,\mathrm{mm}$). Following the determination of the presence or absence of each potential pore in the configuration, the PN was constructed, and simulations were conducted using OpenPNM, as described in the preceding sections. This iterative procedure was repeated for 1000 generations, during which the optimizer generated an improved set

of Pareto optimal PN topologies in each iteration. The parent population pool initially consisted of 1200 solutions and 1080 new offspring were reproduced through crossover and mutation processes $n_{\mathrm{pop}} \times (p_{\mathrm{c}} + p_{\mathrm{m}}) = 1200 \times (0.85 + 0.05) = 1080$. Next, the objective function was evaluated, resulting in the model being solved over one million times in total during the optimization process. Such an ultra-large optimization with high resolution was only manageable through a cost-effective modeling method like PNM.

Fig. 5.4a illustrates the history of Pareto fronts of dual objectives over all generations, showing reaction rate and pumping cost of various non-dominated solutions. As optimization progressed, enhanced PN morphologies were generated, leading to higher conversion rates and lower pumping costs. It is noteworthy that all points on the Pareto graph of each generation can be considered as potential optimal points, depending on the trade-off between reaction rate and pumping power. If minimal pumping cost is crucial, the point on the bottom-left corner of the Pareto front can be chosen as the optimum design. Conversely, if maximal conversion rate is the goal, the point on the opposite extreme could be selected. The "ideal point" on this graph lies on the top-left corner, where a very high reaction rate could be achieved with minimal pumping requirements. The Pareto optimal solutions in this figure tend toward that ideal point. For instance, comparing points A_1 and B_1, the ending points of the Pareto fronts after and before optimization (generations 1000 and zero), reveals a 280% increase in reaction rate accompanied by a 6% reduction in pumping cost. Such a significant elevation in the conversion rate, along with an appreciable reduction in hydraulic requirements, was only achievable through a robust optimization process that led to proper configuration of the pores in the final PN. Furthermore, comparing points A_3 and B_3, situated at the other end of Pareto fronts of the optimal and initial generations (see Fig. 5.4a), shows a similar trend. The reaction rate increased by 15.2%, and pumping power decreased by 11.3%. Choosing any points between the two ends on the Pareto front depends on practical constraints and the trade-off between the two objectives. For instance, in a practical application such as VRFB, the net generated power (i.e. the difference between cell and pumping power) can determine a proper trade-off between the two objectives. In such cases, the framework presented in this study can be utilized with a single-objective optimization algorithm, such as GA, to produce innovative PN with improved performance. However, in the absence of any particular trade-off, points A_2 and B_2 are chosen for the sake of comparison in this study. These points have a median pumping power among all solutions in their corresponding Pareto front. A quantitative

Table 5.3: Optimization algorithm parameters

Parameters	**Cases**					
	A_1	A_2	A_3	B_1	B_2	B_3
Reaction rate ($\times 10^{-3}\,\mathrm{mol\,s^{-1}\,m^{-2}}$)	5.06	16.7	25.8	1.33	12.2	22.4
Pumping power ($\times 10^{-2}\,\mathrm{W\,m^{-2}}$)	2.01	2.74	3.89	2.15	2.6	4.39
Number of pores	7082	4540	3198	7847	5407	3084
Minimum pore diameter (μm)	23.5	23.3	23.3	26	21.8	23.6
Maximum pore diameter (μm)	53.9	67.7	88	46.4	60.5	116.7
Average pore diameter (μm)	30.3	31.7	32.6	30.6	31.4	32.8
Average throat diameter (μm)	16.7	17.1	17.7	16.6	16.9	17.7
Superficial velocity ($\mathrm{mm\,s^{-1}}$)	0.194	0.263	0.374	0.206	0.25	0.422
Porosity (-)	0.379	0.423	0.473	0.392	0.41	0.475
Permeability (D)	4.84	6.58	9.36	5.16	6.24	10.55
Specific surface area ($\mathrm{m^2\,m^{-3}}$)	8273	27086	36641	1827	19841	29882

comparison of these three representative points before and after optimization is reported in Table 5.3. A more detailed comparison of the PN of optimal solutions is provided later in this study.

Moreover, Figs. 5.4b and 5.4c show the convergence history of optimization process in terms of entire population and hypervolume, respectively. As shown in Fig. 5.4b, it is evident that the entire population, over generations, improved in both reaction rate and pumping cost, shifting toward the *ideal point*. This figure also confirms that while the randomly generated population at generation zero is spread on the plot surface, the solutions in subsequent generations become more converged. As a post-processing step, optimization convergence is tracked using a hypervolume indicator [58], shown in Fig. 5.4c. In this case, the hypervolume is the area under the Pareto plot in each generation with respect to a reference point. The reference point, assumed in this study as (pumping cost, reaction rate) = (0.0527 $\mathrm{W\,m^{-2}}$, 0), represents a relatively poor solution dominated by all Pareto solutions. The incremental trend of hypervolume plot in Fig. 5.4c indicates the improvement of Pareto front over generations. It is noticeable that the hypervolume indicator increased sharply in the first 200 generations, signifying rapid improvement at the beginning of the optimization process, followed by a gradual slowing down as the optimization reaches convergence.

While the optimization was conducted at a fixed pressure drop ($\Delta p = 400\,\mathrm{Pa}$), a more comprehensive understanding was sought by investigating the porous reactor's performance before and after optimization for a wide range of pressure drops.

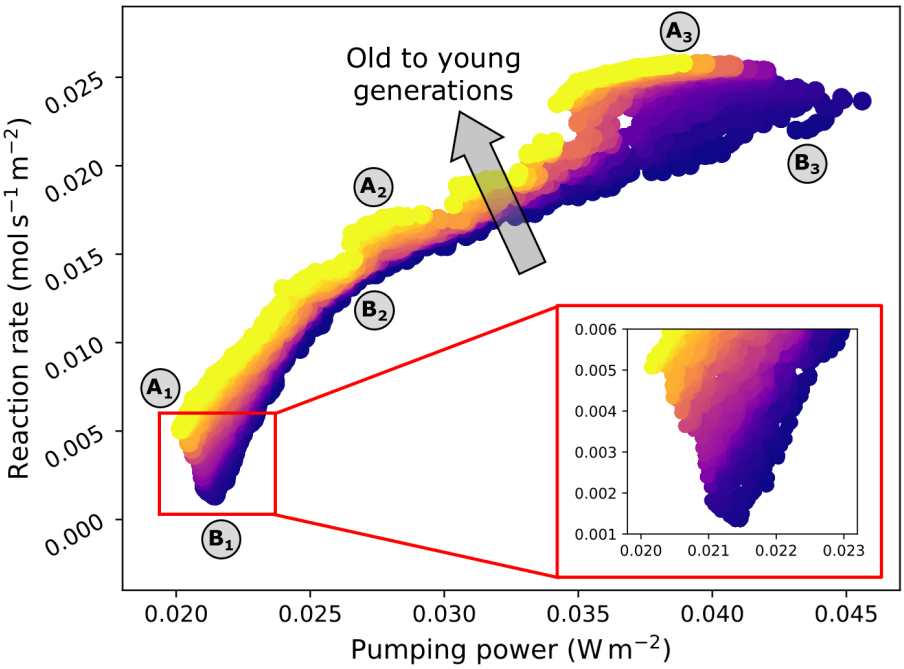
Old to young
generations
A1
A2
A3
B1
B2
B3
Reaction rate (mol s−1 m−2)
Pumping power (W m−2)
0.000
0.005
0.010
0.015
0.020
0.025
0.020
0.025
0.030
0.035
0.040
0.045
0.001
0.002
0.003
0.004
0.005
0.006
0.020
0.021
0.022
0.023

(a)

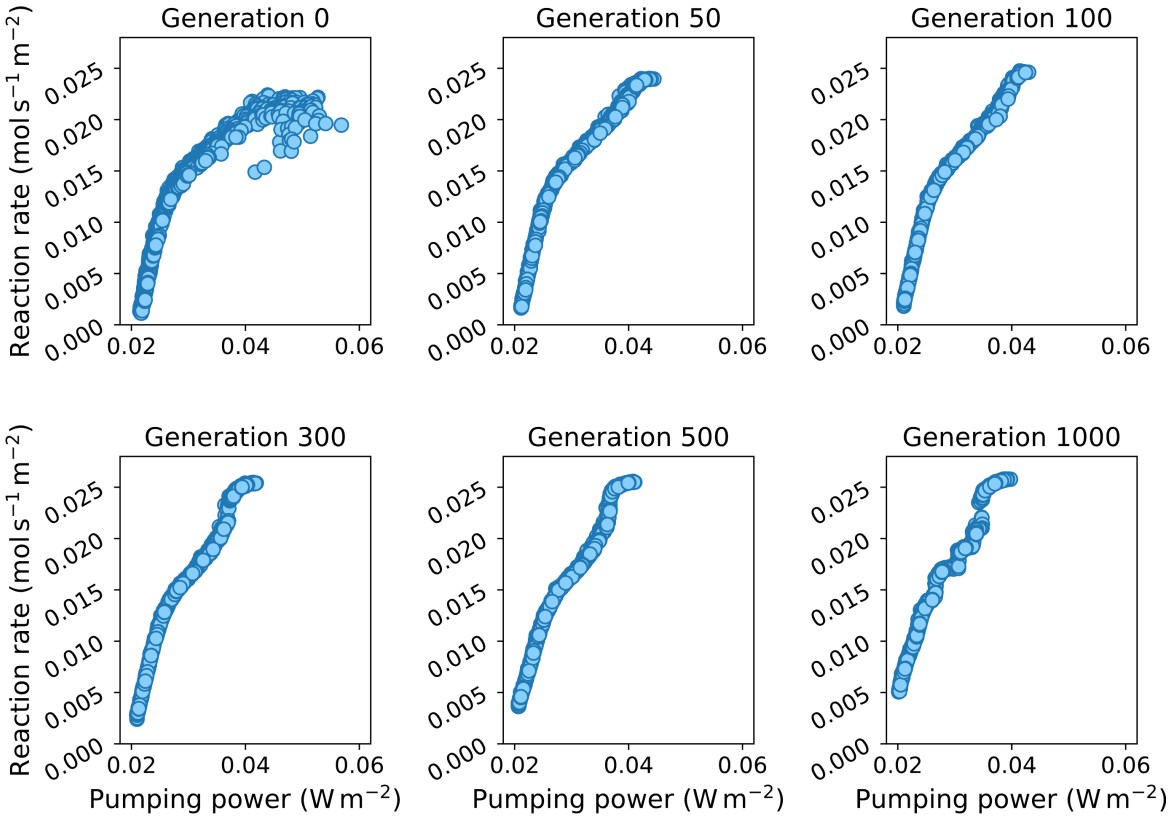
Generation 0
Generation 50
Generation 100
Generation 300
Generation 500
Generation 1000
Reaction rate (mol s−1 m−2)
Pumping power (W m−2)
0.000
0.005
0.010
0.015
0.020
0.025
0.02
0.04
0.06

(b)

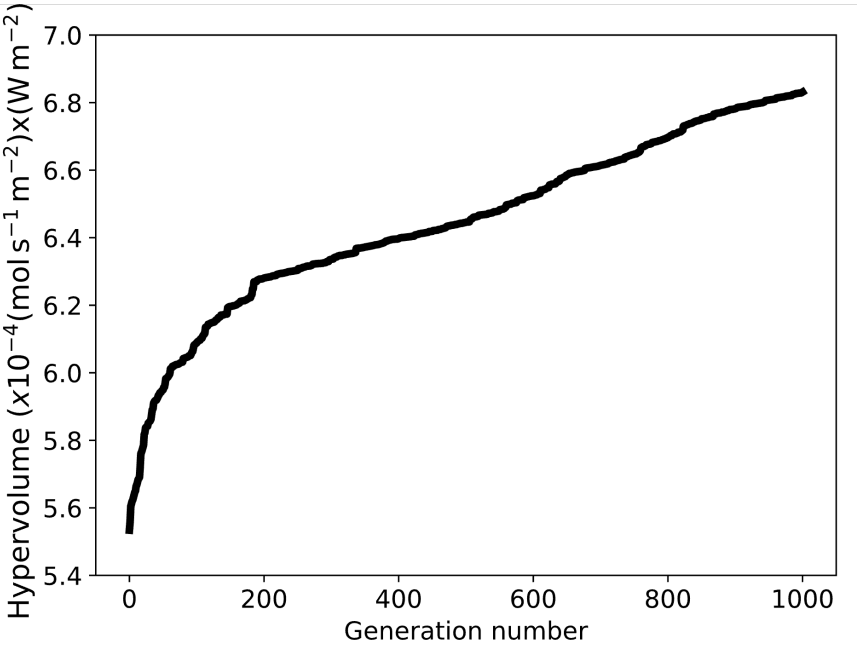

(c)

Figure 5.4: History of (a) Pareto fronts, (b) entire population, and (c) hypervolume over optimization process. In (a), each color spectrum represents Pareto optimal solutions of one generation, from dark purpule for generation zero and yellow for generation 1000.

Figs. 5.5a and 5.5b illustrate pressure drop and pumping power versus reaction rate, respectively, for six representative PNs. Comparing the conversion rate of PNs after optimization (points A) with their corresponding networks before optimization (points B), as depicted in Fig. 5.5a, clearly demonstrates the superior performance of optimal PNs across various pressure drops. Furthermore, it is observed that the pressure drop-reaction rate curve of A_3 shows the best performance among all other PNs in Fig. 5.5a, even when compared to PNs A_1 and A_2. However, it is important to note that while the reaction rate of A_3 is higher than other PNs at the same pressure drop, this higher conversion rate comes at the cost of a higher pumping cost, as confirmed by the pumping power-reaction rate curves shown in Fig. 5.5b. All curves in this figure are plotted for a pressure drop up to $1000\,\mathrm{Pa}$, similar to Fig. 5.5a. Clearly, A_3 demands a higher hydraulic power compared to A_1 and A_2. Moreover, A_3 has the capability to cover a wider range of pumping cost for a given pressure drop range, thanks to its higher permeability, which is not achievable by other PNs. Similarly, with a common pumping cost, A_3 exhibits a higher conversion rate (see Fig. 5.5b), but this is only possible with different pressure drops. Therefore, the choice of the

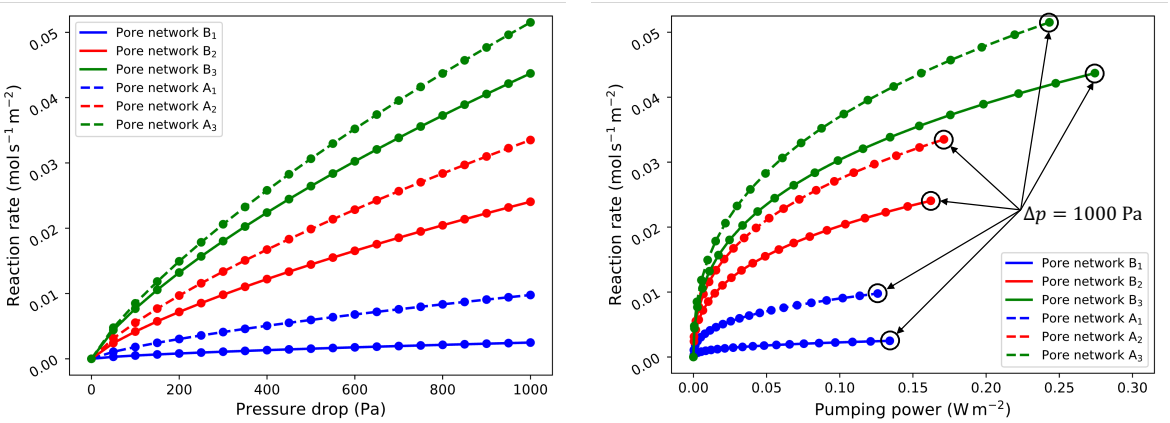

(a) **(b)**

Figure 5.5: (a) Pressure drop-reaction rate and (b) pumping power-reaction rate performance curves of representative PMs before and after optimization.

best PN depends on the application constraints and the trade-off between the reaction rate and pumping cost.

Fig. 5.6 demonstrates the morphology and simulation results of the initial and optimal representative PNs without throat nodes. A closer look at Fig. 5.6a reveals that PNs B_1 and A_1 contain a higher number of pores compared to B_3 and A_3, as quantitatively reported in Table 5.3. This condensed configuration leaves less space for the pores to grow in the given design domain, resulting in many relatively small pores. In contrast, by deleting some potential pores, the remaining pores in PNs B_3 and A_3 had the chance to become larger, with some pores exhibiting a diameter larger than $100\,\mu\mathrm{m}$ in B_3. Comparing the PNs before and after optimization illustrates how the network topologies evolved over the optimization process.

Additionally, in a PNM, throats serve as pathways for fluid transport. As explained earlier, the throat diameter is determined based on the minimum diameter of its neighboring pores. Therefore, a PN with larger pore diameters features larger throats on average, facilitating fluid flow. This is confirmed by Fig. 5.6b, which illustrates the velocity magnitude in the bundle of throats, and the superficial velocity stated in Table 5.3. According to Eq. (5.3), the hydraulic conductance of a cylindrical throat is proportional to the fourth power of its radius. Hence, enlarging a throat can greatly increase the flow rate passing through it with a fixed pressure difference. Since the reaction rate depends on the local concentration of active species, a fast delivery of reactant species may lead to a higher total conversion rate. However, it is noteworthy that an excess hydraulic conductance and flow rate may be obtained at the

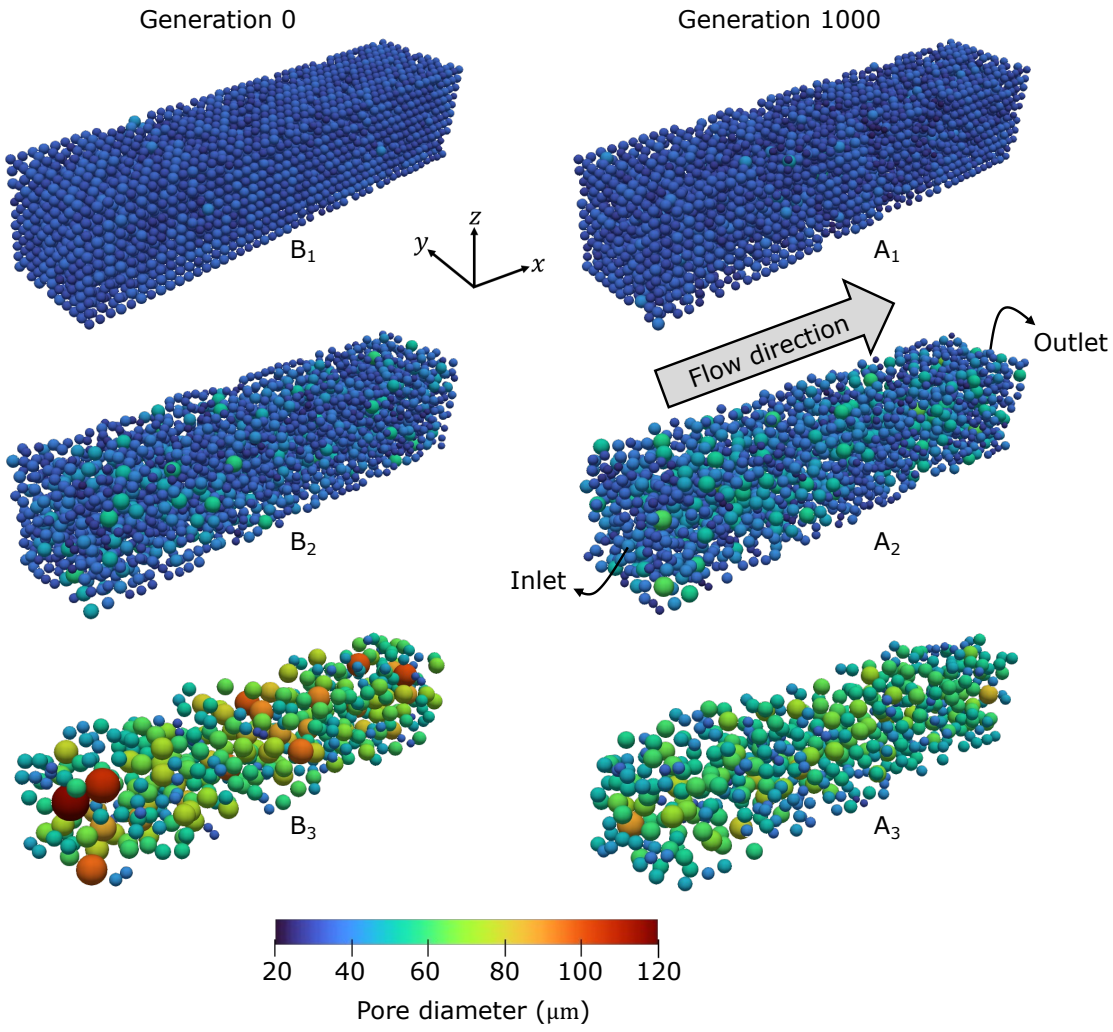
Generation 0
Generation 1000
B1
A1
z
y
x
Flow direction
Outlet
B2
A2
Inlet
B3
A3
20
40
60
80
100
120
Pore diameter (μm)

(a)

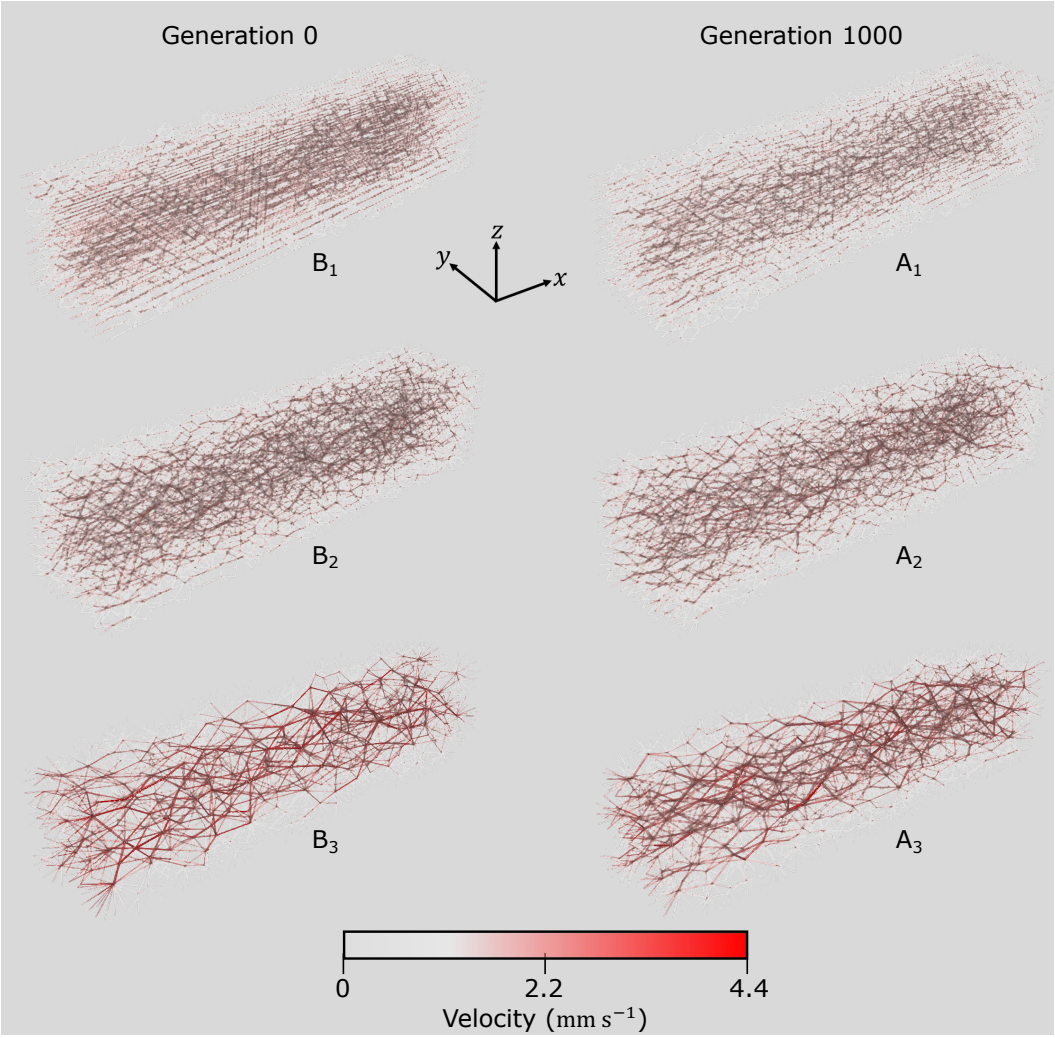
Generation 0
Generation 1000
B1
A1
B2
A2
B3
A3
z
y
x
0
2.2
4.4
Velocity (mm s−1)

(b)

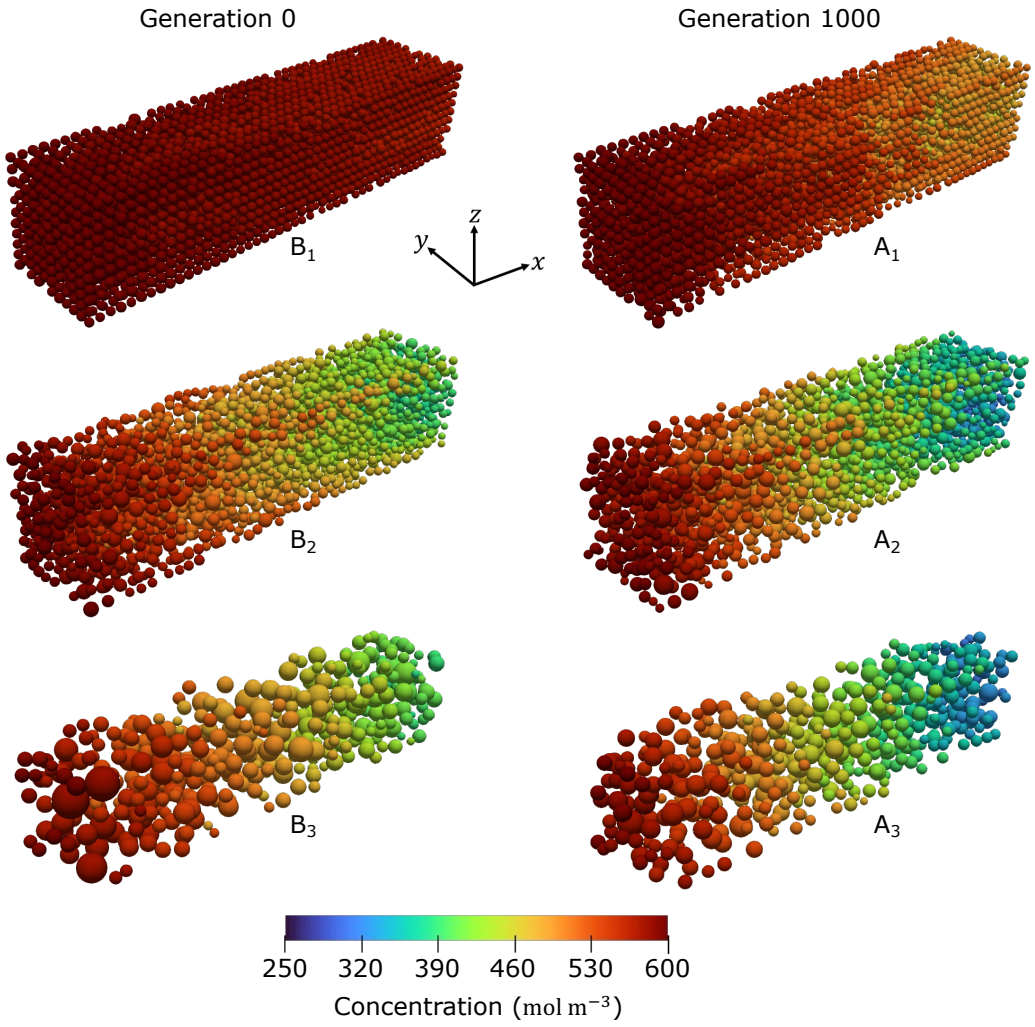

Figure 5.6: Comparison of representative PNs before and after optimization. (a) pore size, (b) solution velocity, and (c) bulk concentration distribution.

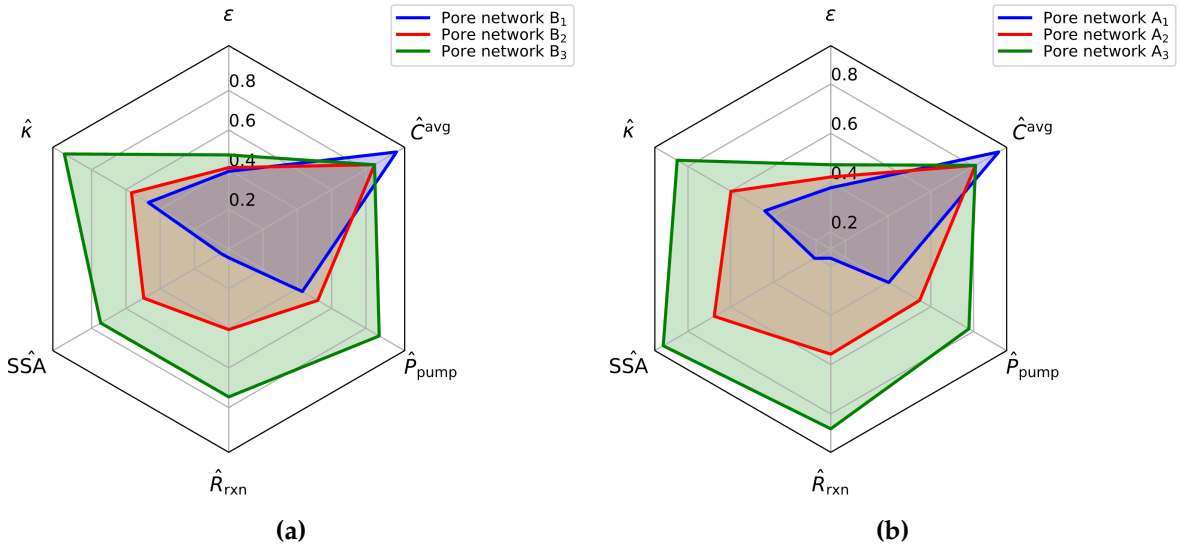

Figure 5.7: Macroscopic structural and performance properties of the representative PNs: (a) before optimization and (b) after optimization.

cost of higher pumping power and lower reactive surface area, without contributing to the total reaction rate. Therefore, during the evolution process from B_3 to A_3, for instance, the optimizer favored changing the topology so that very large pores were replaced with several smaller ones. In ADR systems, the mass transfer coefficient plays a key role in determining the rate of reactant consumption. According to Eq. (5.14), K_L is a function of Reynolds number, which itself depends on the fluid velocity. Therefore, even a concentrated solution with a high bulk concentration may not result in rapid chemical reaction if the convective fluid velocity is low. For example, the concentration distribution of PN A_1 in Fig. 5.6c indicates that the species concentration in the pores near outlet boundary is almost equal to those near inlet boundary. Due to the slow fluid flow in this network, the mass transfer coefficient is so low that a considerable portion of the active species exits the reactor without undergoing reaction. In contrast, the higher velocities observed in PNs A_2 and A_3 (refer to superficial velocity values in Table 5.3) and velocity magnitude in Fig. 5.6b) promote enhanced species transport from the bulk solution to the solid surface, resulting in a faster consumption of active species. The elevated reaction rate in A_3 corresponds to a lower bulk concentration in regions near the outlet, with the minimum concentration reaching approximately $284\,\mathrm{mol\,m^{-3}}$.

However, the fluid velocity, prescribed by the network hydraulic conductance, is not the sole determining factor in the overall performance of a PN. Another critical parameter in this multi-objective optimization problem is the active surface area. In a PNM, this value depends on the definition of the surface area and the geometrical

assumptions of the network. As discussed earlier, in this study, the reactive surface area of each "throat node," where the chemical reaction occurs, is assumed to be equal to the internal surface area of throat with which it is associated. The surface area of the pore bodies was excluded since the fraction of its area to associate with each throat is not easily determined. This assumption is justified on geometrical grounds because the internal surface area of a pore is reduced by the opening created by each intersecting throat, so the internal surface areas are quite low. In fact, the internal surface area of all pores in network A_3 was $1.81 \times 10^{-6}\,\mathrm{m}^2$, while the throat surface area was $1.05 \times 10^{-5}\,\mathrm{m}^2$, so on average we can expect ignoring this surface area only affects the active surface area by 17%. This assumption is also supported on physical grounds since the fluid velocity in pores is lower than throats so the reaction will be more mass transfer limited, thus would contribute relatively little reaction to each throat.

The radar charts in Fig. 5.7 display the topological characteristics and performance of the representative PNs before and after optimization. Here, ε, κ, SSA, R_{rxn}, P_{pump}, and C^{avg} denote porosity, permeability, specific surface area, reaction rate, pump power, and average bulk concentration, respectively. The values with a hat symbol ($\hat{}$) are normalized with respect to a common reference value, converting them all between 0 and 1. Porosity, permeability, and SSA values are calculated using OpenPNM for each network. In this context, SSA is defined as the ratio of the wetted surface area to the volume of the solid phase. Comparing the results before (B points) and after (A points) optimization reveals a considerable increase in SSA value for all three networks. The enhancement of SSA, resulting from an improved network topology, contributes to the increment of the reaction rate in all PNs. Additionally, permeability serves as an index of the overall network hydraulic conductance. Since the pressure drop was kept fixed during the optimization process, the pumping cost depends solely on permeability. For instance, the lower permeability ($9.36\,\mathrm{D}$ vs. $10.55\,\mathrm{D}$, 11.3% decrease) and higher SSA ($36641\,\mathrm{m}^2\,\mathrm{m}^{-3}$ vs. $29882\,\mathrm{m}^2\,\mathrm{m}^{-3}$, 22.6% increase) of A_3 compared to B_3 helped reduce the pumping requirement and increase the reaction rate after optimization.

The pore size distribution of the optimized networks (represented by points A) is illustrated Fig. 5.8. As depicted, the histogram of PN A_3 is right shifted compared to the other networks, indicating the presence of larger pores. PN A_3 comprises a number of pores exceeding a diameter size of $40\,\mu\mathrm{m}$, a characteristic not observed in PN A_1. Larger pores are associated with larger throats connected to them. As previously discussed, larger throats exhibit higher hydraulic conductivity, leading

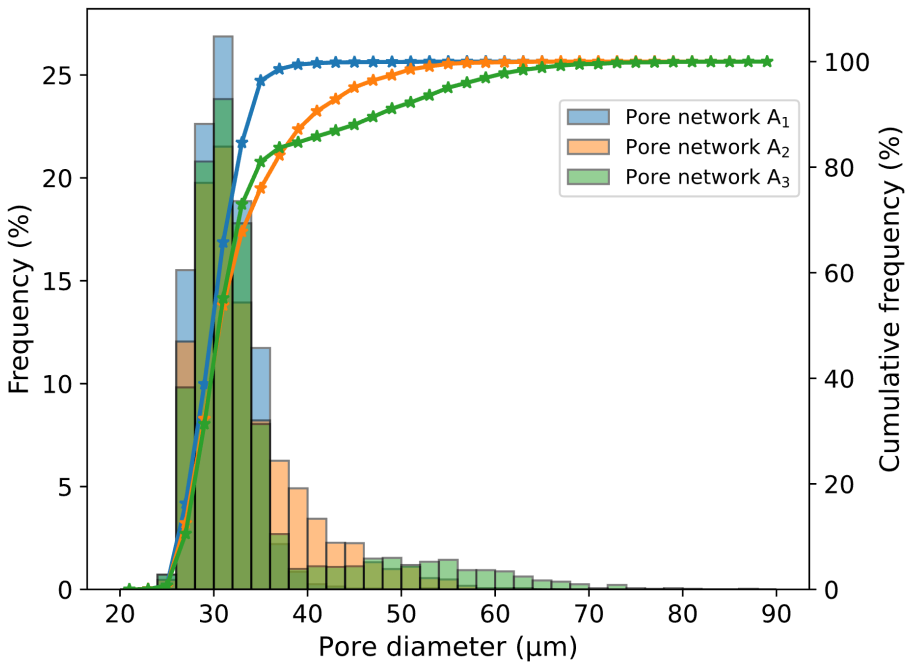

Figure 5.8: The pore size distribution of optimized PNs, displaying pore diameter frequency and the cumulative frequency in terms of percentange (%).

to an elevated Reynolds number. This, in turn, enhances mass transfer between the bulk fluid and the solid-liquid interface, increasing the likelihood of reactant species undergoing reaction before leaving the electrode. Moreover, the larger pores distributed in the longitudinal direction (see Fig. 5.6a) facilitate the rapid delivery of reactants to regions far from the inlet and therefore mitigate significant concentration depletion. In contrast, as demonstrated in Fig. 5.8, PN A_1 exhibits a more uniform pore size distribution within a condensed configuration.

Finally, the 3D rendered representations of the solid-phase porous reactor, derived from the dimensions of pores and throats across six representative PNs, are presented in Fig. 5.9. This figure showcase how the predicted networks can be turned into a solid object. While manufacturability of these tailored designs currently relies on the accuracy and resolution limitations of existing technologies, it is envisoned that the ongoing advancements in additive manufacturing methods, such as projection micro stereolithography [6], offer promising avenues for fabricating such intricate structures with greater precision and efficiency. The proposed PNM-NSGA optimization framework proves capable of tailoring innovative microstructures at a pore-scale with high resolution, encompassing multi-physics considerations without relying on a cubic lattice. Further studies are imperative to explore the impact of various operating and structural parameters, the trade-off between objectives, and

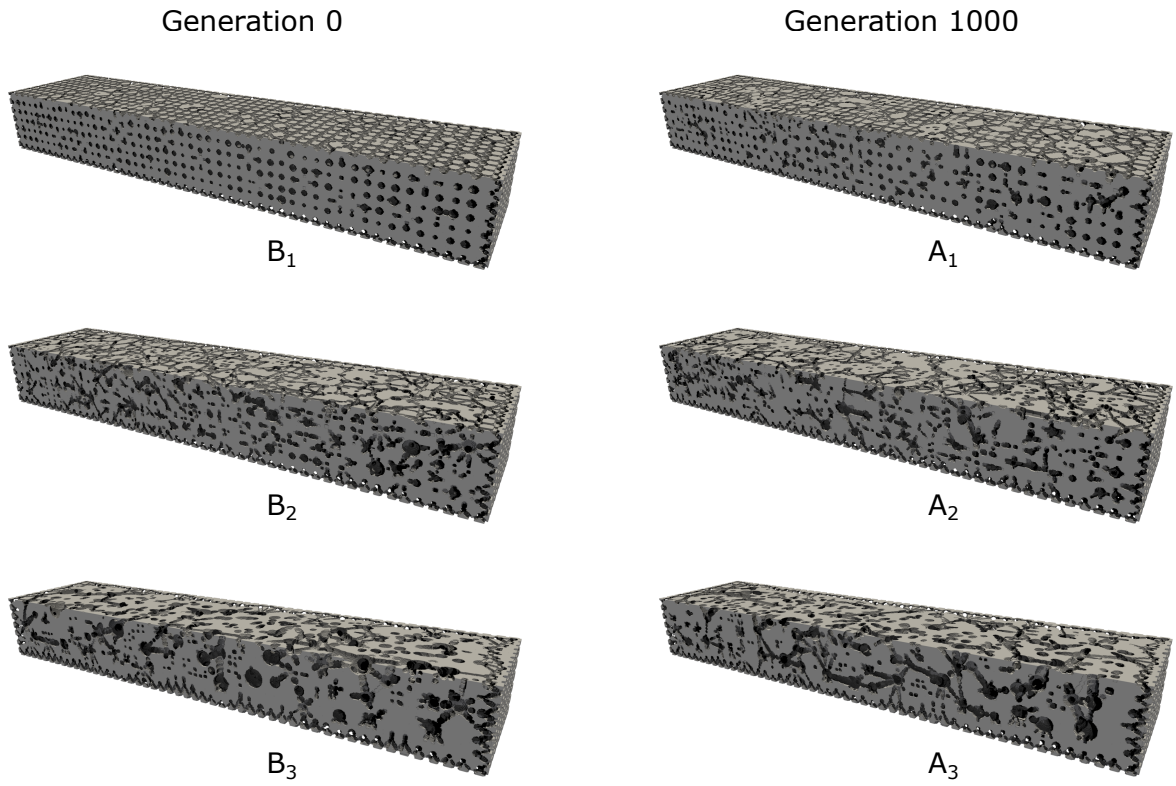

Figure 5.9: Solid-phase porous skeleton of networks generated by PNM-NSGA framework. The grey is solid phase.

the incorporation of additional physics and more complicated reaction kinetics.

5.4 Conclusions

This study presents a robust framework for the large-scale optimization of porous reactors by integrating PNM with the NSGA-II algorithm. The proposed approach capitalizes on the computationally efficient nature of PNM to model reactive transport in a porous reactor at the pore scale. It employs the NSGA-II multi-objective optimizer to enhance the porous network morphology, aiming to maximize conversion rates and minimize hydraulic requirements. Distinguished from previous studies, the proposed framework introduces the idea of background grid, and utilizes Delaunay tessellation as well a relaxation operation to provide greater freedom for the pore coordinates. Formulating the problem as a multi-objective optimization offers a versatile framework applicable to various applications with contradictory objectives, eliminating the need for a specific trade-off.

The proposed PNM-NSGA framework was applied to optimize the microstructure

of a $2 \times 0.52 \times 0.52\,\mathrm{mm}^3$ porous reactor, coupling advection-diffusion phenomena with a first-order chemical reaction. To account for the impact of convective flow on the mass transfer coefficient between bulk liquid and the solid-liquid interface, "throat nodes" were introduced to the developed PNM where a local mass transfer coefficient was incorporated into the reaction term. The algorithm generated a range of Pareto optimal solutions for various pumping costs. Comparison of the optimal solution with the lowest pumping cost on one end of the Pareto front with its corresponding PN in the initial generation revealed a significant 280% increase in reaction rate accompanied by a 6% decrease in pumping cost. This improvement is attributed to the precise placement and sizing of pores in the designated design domain. In the absence of a specific trade-off between objectives, three distinct optimal solutions were selected from different regions of the Pareto front and thoroughly compared. The presented methodology can be used for designing porous reactors with pore-scale resolution in various applications, such as electrodes for electrochemical energy devices (e.g., flow batteries, fuel cells, and electrolyzers) and catalytic reactors. With advancements in additive manufacturing techniques and manufacturability resolution, it is envisioned that these robust algorithmic methods will have broad application in generating high-performance porous reactors. Further exploration is necessary to extend this framework to accommodate additional physics, enhance its degree of freedom, and reduce computational costs. Additionally, more investigation is required concerning the manufacturability of the generated network topologies. Future research could compare the results obtained from the PNM-NSGA framework with those from the topology optimization of a macro-scale model. For example, the optimal pore network derived from the PNM-NSGA framework proposed in this study could be used to calculate volume-averaged structural properties, such as porosity distribution, and compare them with the optimal distribution obtained from the density-based topology optimization applied in the previous chapters. However, it is important to note that the compatibility of results from these two approaches heavily depends on the volume-averaging relationships fundamental to macro-scale modeling, which connect effective and intrinsic transport and reaction rate properties (e.g., diffusivity). As a result, directly translating findings between these approaches may involve complexities that warrant further, more comprehensive research.

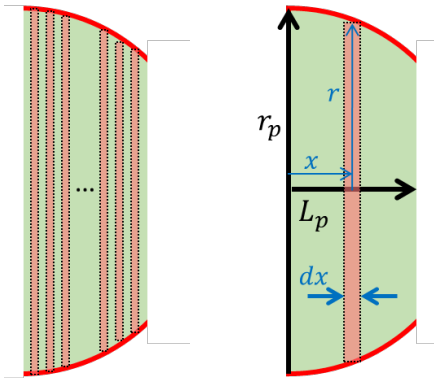

Figure 5.A.1: Representation of sphere segment in a pore-throat-pore conduit. (a) shows assumption of infinite number of differential rings in series, and (b) shows the geometric dimensions of an infinitesimal ring.

Appendix

5.A Derivation of hydraulic conductance for a sphere

The hydraulic conductance of pore segment, g_p^{h}, as expressed in Eq. (5.2) can be derived via two methods. First, the simpler approach is explained as follows. Since the cross section of a sphere is not constant when moving from a pole to the center, the Hagen-Poiseuille model cannot be used for evaluation of hydraulic conductance.

Assuming that the part of the sphere from center to L_p (see Fig. 5.A.1) consists of infinite number of infinitesimal cylinder-like rings in series, the Hagen-Poiseuille model can be used to calculate the overall hydraulic conductance by taking an integral of the hydraulic resistivity over this portion as follows:

$$\frac{1}{g_p^{\mathrm{h}}} = \int_0^{L_p} \frac{8\mu\, dx}{\pi r^4(x)} \tag{5.A.1}$$

where x denotes the distance from center of the sphere. The radius of an infinitesimal ring depends on x and is given by:

$$r(x) = \sqrt{r_p^2 - x^2} \tag{5.A.2}$$

By inserting Eq. (5.A.1) into Eq. (5.A.2) and calculating the integral, the overall hydraulic conductivity is expressed as:

$$\frac{1}{g_p^{\mathrm{h}}} = \int_0^{L_p} \frac{8\mu\, dx}{\pi(r_p^2 - x^2)^2} = \frac{4\mu}{\pi r_p^3}\left[\frac{r_p L_p}{r_p^2 - L_p^2} + \tanh^{-1}\left(\frac{L_p}{r_p}\right)\right] \tag{5.A.3}$$

A more comprehensive and robust derivation could be obtained based on the approximate analytical solution of laminar, single-phase flow in a gradually-varying channel of arbitrary cross-section that was previously studies by Bahrami and coworkers [43, 44]. They showed that the pressure drop in a conduit with slowly changing cross-section is expressed by:

$$-\frac{1}{Q}\left(\frac{dp}{dx}\right) = \mu\left[16\pi^2\left(\frac{I_p^*}{A^2(x)}\right) - \frac{2\rho Q}{\mu}\left(\frac{dA(x)/dx}{A^3(x)}\right)\right] \tag{5.A.4}$$

in which I_p^* is the specific polar moment of inertia and $A(x)$ is the cross-section area. For a circular cross-section, $A(x)$ is given by:

$$A(x) = \pi r^2(x) = \pi(r_p^2 - x^2) \tag{5.A.5}$$

The first and second terms on the right-hand-side of Eq. (5.A.4) correspond to frictional and inertial losses, respectively. Given the assumption that the cross-section area is changing gradually ($dA(x)/dx \to 0$), the frictional loss is typically substantially more than the inertial loss and therefore the second term could be neglected. The total pressure drop can be computed by integrating Eq. (5.A.4) over the length of L_p after ignoring the inertial term as follows:

$$\frac{\Delta p}{Q} = 16\pi^2\mu \int_0^{L_p} \frac{I_p^*}{A^2(x)}\, dx \tag{5.A.6}$$

Given the definition of hydraulic conductance as the ratio of the volumetric flow rate to the pressure drop ($g_p^{\mathrm{h}} = Q/\Delta p$) and knowing the specific polar moment of inertia of a circle is $\frac{1}{2\pi}$, the hydraulic conductance is derived as:

$$\frac{1}{g_p^{\mathrm{h}}} = 16\pi^2\mu \int_0^{L_p} \frac{\left(\frac{1}{2\pi}\right)}{[\pi(r_p^2 - x^2)]^2}\, dx = \frac{4\mu}{\pi r_p^3}\left[\frac{r_p L_p}{r_p^2 - L_p^2} + \tanh^{-1}\left(\frac{L_p}{r_p}\right)\right] \tag{5.A.7}$$

5.B Numerical analysis of rendered solid-phase images

To obtain further insight into the tailored designs generated by PNM-NSGA framework, the solid skeletons of representative pore networks (PNs) were analyzed using

Table 5.B.1: Porosity, permeability, and tortuosity of representative PNs obtained from numerical image analysis of the rendered solid-phase reactor microstructure.

PN	Porosity	Permeability – LBM (D)	Permeability – PNM (D)	Turosity – LBM (x / y / z)
A_1	0.4658	3.11	4.57	1.681 / 1.736 / 1.768
A_2	0.5247	4.89	6.17	1.673 / 1.750 / 1.719
A_3	0.5352	9.7	9.86	1.589 / 1.735 / 1.749
B_1	0.4667	3.26	4.92	1.634 / 1.718 / 1.728
B_2	0.5258	4.75	6.12	1.624 / 1.668 / 1.641
B_3	0.5507	12.9	12.8	1.548 / 1.662 / 1.637

direct numerical simulation. Permeability and tortuosity values obtained via the lattice Boltzmann method (LBM) are detailed in Table 5.B.1. It is important to note that, due to computational constraints, image analysis was limited to the central core region of the reactor, spanning $500\,\mu\mathrm{m}$ in size. Consequently, the values provided in this table may differ from those reported in the main manuscript, which were derived from pore network modeling (PNM) of the entire reactor. To facilitate comparison between the two methods, permeability for the core region was recalculated based on PNM, as indicated in Table 5.B.1. The permeability values obtained by LBM and PNM are fairly close, affirming the validity of the generated PNs through the proposed framework. Additionally, Fig. 5.B.1 illustrates the ratio of post-optimization to pre-optimization values for various pore radii and chord lengths.

Abbreviations

ADR	Advection-diffusion-reaction
BC	Boundary condition
CD	Crowding distance
DNS	Direct numerical simulation
FEM	Finite element method
FVM	Finite volume method
GA	Genetic algorithm
LBM	lattice Boltzmann method
MOICA	Multi-objective imperialist competitive algorithm
MOO	Multi-objective optimization
NSGA	Non-dominated sorting genetic algorithm

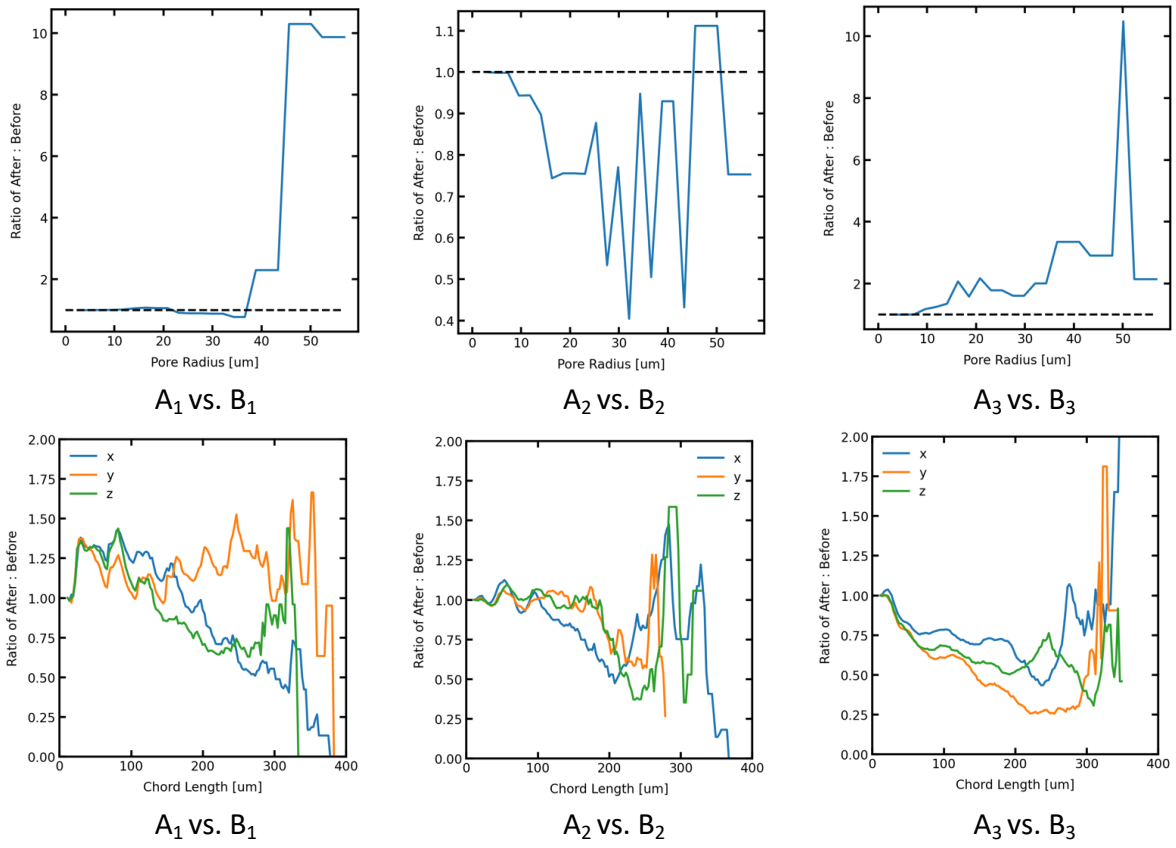

Figure 5.B.1: Ratio of after to before optimization for pore radius (top row) and chord length (bottom row) of various representative PNs.

PN	Pore network
PNM	Pore network modeling
PSO	Particle swarm optimization
REV	Representative elementary volume
SFO	Sailfish optimization
WOA	Whale optimization algorithm
XRT	X-ray tomography

Nomenclature

A_{s}	Wetted surface area	m^2
C	Concentration	$\mathrm{mol\,m^{-3}}$
d	Voxel (spacing) size	m
D_{A}	Solute diffusion coefficient	$\mathrm{m^2\,s^{-1}}$
D_{t}	Throat diameter	m
F_{obj}	Objective function	$\mathrm{mol\,s^{-1}}$
G	Total conductance	$\mathrm{m^3\,s^{-1}\,Pa^{-1}}$ or $\mathrm{m^2 s^{-1}}$
g	Conductance	$\mathrm{m^3\,s^{-1}\,Pa^{-1}}$ or $\mathrm{m^2 s^{-1}}$
k_{L}	Mass transfer coefficient	$\mathrm{m\,s^{-1}}$
k_{r}	Reaction constant	$\mathrm{m\,s^{-1}}$
L_{p}	Pore segment length	m
L_{t}	Throat length	m
n_{g}	Number of genomes (candidate pores)	$-$
n_{pop}	Population size	$-$
p	Pressure	Pa
p_{c}	Crossover ratio	$-$
p_{m}	Mutation ratio	$-$
Pe	Peclet number	$-$
Q	Volumetric flow rate	$\mathrm{m^3\,s^{-1}}$
r	Radius	m
r_{A}	Reaction rate	$\mathrm{mol\,s^{-1}}$
r_{m}	Mutation rate	$-$

Greek symbols

μ	Viscosity	$\mathrm{Pa\,s}$
ρ	Density	$\mathrm{kg\,m^{-3}}$

Subscripts/superscripts

d	Diffusive
h	Hydraulic
p	Pore
surf	Surface
t	Throat

Bibliography

[1] N. Misaghian, M. A. Sadeghi, K. M. Lee, E. P. L. Roberts, and J. T. Gostick, "Utilizing pore network modeling for performance analysis of multi-layer electrodes in vanadium redox flow batteries," *Journal of The Electrochemical Society*, vol. 170, p. 070520, July 2023.

[2] Y. Sun, S. Polani, F. Luo, S. Ott, P. Strasser, and F. Dionigi, "Advancements in cathode catalyst and cathode layer design for proton exchange membrane fuel cells," *Nature Communications*, vol. 12, Oct. 2021.

[3] P. Kočí, V. Novák, F. Štěpánek, M. Marek, and M. Kubíček, "Multi-scale modelling of reaction and transport in porous catalysts," *Chemical Engineering Science*, vol. 65, p. 412–419, Jan. 2010.

[4] J. Zhu, P. Wu, Y. Chao, J. Yu, W. Zhu, Z. Liu, and C. Xu, "Recent advances in 3d printing for catalytic applications," *Chemical Engineering Journal*, vol. 433, p. 134341, Apr. 2022.

[5] A. Ambrosi and M. Pumera, "3d-printing technologies for electrochemical applications," *Chemical Society Reviews*, vol. 45, no. 10, p. 2740–2755, 2016.

[6] M. D. Reale Batista, S. Chandrasekaran, B. D. Moran, M. Salazar de Troya, A. Pinongcos, Z. Wang, R. Hensleigh, A. Carleton, M. Zeng, T. Roy, D. Lin, X. Xue, V. A. Beck, D. A. Tortorelli, M. Stadermann, R. Zheng, Y. Li, and M. A. Worsley, "Design and additive manufacturing of optimized electrodes for energy storage applications," *Carbon*, vol. 205, p. 262–269, Mar. 2023.

[7] A. J. Capel, R. P. Rimington, M. P. Lewis, and S. D. R. Christie, "3d printing for chemical, pharmaceutical and biological applications," *Nature Reviews Chemistry*, vol. 2, p. 422–436, Nov. 2018.

[8] C. Xu, X. Li, T. Liu, and H. Zhang, "Design and synthesis of a free-standing carbon nano-fibrous web electrode with ultra large pores for high-performance vanadium flow batteries," *RSC Adv.*, vol. 7, no. 73, p. 45932–45937, 2017.

[9] Y. Liu, W. Zhou, Y. Lin, L. Chen, X. Chu, T. Zheng, S. Wan, and J. Lin, "Novel copper foam with ordered hole arrays as catalyst support for methanol steam reforming microreactor," *Applied Energy*, vol. 246, p. 24–37, July 2019.

[10] P. Trogadas, V. Ramani, P. Strasser, T. F. Fuller, and M. Coppens, "Hierarchically structured nanomaterials for electrochemical energy conversion," *Angewandte Chemie International Edition*, vol. 55, p. 122–148, Nov. 2015.

[11] P. Charoen-amornkitt, M. Alizadeh, T. Suzuki, and S. Tsushima, "Entropy generation analysis during adjoint variable-based topology optimization of porous reaction-diffusion systems under various design dimensionalities," *International Journal of Heat and Mass Transfer*, vol. 202, p. 123725, Mar. 2023.

[12] P. Charoen-amornkitt, M. Alizadeh, T. Suzuki, and S. Tsushima, "Topologically optimized anode catalyst layers of proton exchange membrane water electrolyzers," *ECS Transactions*, vol. 111, p. 87–95, May 2023.

[13] M. Alizadeh, P. Charoen-amornkitt, T. Suzuki, and S. Tsushima, "Mixed topology optimization: A self-guided boundary-independent approach for power sources," *Energy Conversion and Management*, vol. 294, p. 117567, Oct. 2023.

[14] S. Tsushima and T. Suzuki, "Modeling and simulation of vanadium redox flow battery with interdigitated flow field for optimizing electrode architecture," *Journal of The Electrochemical Society*, vol. 167, p. 020553, Jan. 2020.

[15] A. Donoso, E. Aranda, and D. Ruiz, "A new method for designing piezo transducers with connected two-phase electrode," *Computers & Structures*, vol. 275, p. 106936, Jan. 2023.

[16] S. Kambampati, J. S. Gray, and H. Alicia Kim, "Level set topology optimization of structures under stress and temperature constraints," *Computers & Structures*, vol. 235, p. 106265, July 2020.

[17] T. Roy, M. A. Salazar de Troya, M. A. Worsley, and V. A. Beck, "Topology optimization for the design of porous electrodes," *Structural and Multidisciplinary Optimization*, vol. 65, May 2022.

[18] S. L. Mitchell and M. Ortiz, "Computational multiobjective topology optimization of silicon anode structures for lithium-ion batteries," *Journal of Power Sources*, vol. 326, p. 242–251, Sept. 2016.

[19] X. Zheng, L. Chen, J.-W. Luo, Q. Yang, and W.-Q. Tao, "Topology optimization of diffusion–reaction processes in hierarchical porous structures," *Chemical Engineering Science*, vol. 287, p. 119806, Apr. 2024.

[20] M. Tomizawa, G. Inoue, K. Nagato, A. Tanaka, K. Park, and M. Nakao, "Heterogeneous pore-scale model analysis of micro-patterned pemfc cathodes," *Journal of Power Sources*, vol. 556, p. 232507, Feb. 2023.

[21] D. Zhang, A. Forner-Cuenca, O. O. Taiwo, V. Yufit, F. R. Brushett, N. P. Brandon, S. Gu, and Q. Cai, "Understanding the role of the porous electrode microstructure in redox flow battery performance using an experimentally validated 3d pore-scale lattice boltzmann model," *Journal of Power Sources*, vol. 447, p. 227249, Jan. 2020.

[22] P. Kočí, M. Isoz, M. Plachá, A. Arvajová, M. Václavík, M. Svoboda, E. Price, V. Novák, and D. Thompsett, "3d reconstruction and pore-scale modeling of coated catalytic filters for automotive exhaust gas aftertreatment," *Catalysis Today*, vol. 320, p. 165–174, Jan. 2019.

[23] L. Chen, R. Zhang, T. Min, Q. Kang, and W. Tao, "Pore-scale study of effects of macroscopic pores and their distributions on reactive transport in hierarchical porous media," *Chemical Engineering Journal*, vol. 349, p. 428–437, Oct. 2018.

[24] D. Zhang, Q. Cai, O. O. Taiwo, V. Yufit, N. P. Brandon, and S. Gu, "The effect of wetting area in carbon paper electrode on the performance of vanadium redox flow batteries: A three-dimensional lattice boltzmann study," *Electrochimica Acta*, vol. 283, p. 1806–1819, Sept. 2018.

[25] M. Liu, M. Shabaninejad, and P. Mostaghimi, "Impact of mineralogical heterogeneity on reactive transport modelling," *Computers & Geosciences*, vol. 104, p. 12–19, July 2017.

[26] X. Yang, Y. Mehmani, W. A. Perkins, A. Pasquali, M. Schönherr, K. Kim, M. Perego, M. L. Parks, N. Trask, M. T. Balhoff, M. C. Richmond, M. Geier, M. Krafczyk, L.-S. Luo, A. M. Tartakovsky, and T. D. Scheibe, "Intercomparison of 3d pore-scale flow and solute transport simulation methods," *Advances in Water Resources*, vol. 95, p. 176–189, Sept. 2016.

[27] X. Wei, W. Li, Q. Liu, W. Sun, S. Liu, S. Li, H. Wei, and L. Ma, "Pore-scale investigation on multiphase reactive transport for the conversion of levulinic acid to γ-valerolactone with ru/c catalyst," *Chemical Engineering Journal*, vol. 427, p. 130917, Jan. 2022.

[28] M. A. Sadeghi, M. Aghighi, J. Barralet, and J. T. Gostick, "Pore network modeling of reaction-diffusion in hierarchical porous particles: The effects of microstructure," *Chemical Engineering Journal*, vol. 330, p. 1002–1011, Dec. 2017.

[29] R. van Gorp, M. van der Heijden, M. Amin Sadeghi, J. Gostick, and A. Forner-Cuenca, "Bottom-up design of porous electrodes by combining a genetic algorithm and a pore network model," *Chemical Engineering Journal*, vol. 455, p. 139947, Jan. 2023.

[30] X. Huang, W. Zhou, B. Liu, and K. Jiang, "Pore network modeling of advection-diffusion-reaction in porous media: The effects of channels," *Chemical Engineering Science*, vol. 271, p. 118577, May 2023.

[31] M. Agnaou, M. A. Sadeghi, T. G. Tranter, and J. T. Gostick, "Modeling transport of charged species in pore networks: Solution of the nernst–planck equations coupled with fluid flow and charge conservation equations," *Computers & Geosciences*, vol. 140, p. 104505, July 2020.

[32] Z. Qie, A. Rabbani, Y. Liang, F. Sun, J. Behnsen, Y. Wang, S. Wang, Y. Zhang, H. Alhassawi, J. Gao, G. Zhao, M. Babaei, A. A. Garforth, Y. Jiao, and X. Fan, "Multiscale investigation of pore network heterogeneity and permeability of fluid catalytic cracking (fcc) particles," *Chemical Engineering Journal*, vol. 440, p. 135843, July 2022.

[33] J. T. Gostick, M. A. Ioannidis, M. W. Fowler, and M. D. Pritzker, "Pore network modeling of fibrous gas diffusion layers for polymer electrolyte membrane fuel cells," *Journal of Power Sources*, vol. 173, p. 277–290, Nov. 2007.

[34] M. A. Sadeghi, M. Agnaou, J. Barralet, and J. Gostick, "Dispersion modeling in pore networks: A comparison of common pore-scale models and alternative approaches," *Journal of Contaminant Hydrology*, vol. 228, p. 103578, Jan. 2020.

[35] R. Hannaoui, P. Horgue, F. Larachi, Y. Haroun, F. Augier, M. Quintard, and M. Prat, "Pore-network modeling of trickle bed reactors: Pressure drop analysis," *Chemical Engineering Journal*, vol. 262, p. 334–343, Feb. 2015.

[36] M. Moghaddam, A. Abbassi, J. Ghazanfarian, and S. Jalilian, "Investigation of microstructure effects on performance of hierarchically structured porous catalyst using a novel pore network model," *Chemical Engineering Journal*, vol. 388, p. 124261, May 2020.

[37] J. T. Gostick, "Random pore network modeling of fibrous pemfc gas diffusion media using voronoi and delaunay tessellations," *Journal of The Electrochemical Society*, vol. 160, no. 8, p. F731–F743, 2013.

[38] J. Gostick, M. Aghighi, J. Hinebaugh, T. Tranter, M. A. Hoeh, H. Day, B. Spellacy, M. H. Sharqawy, A. Bazylak, A. Burns, W. Lehnert, and A. Putz, "Openpnm: A pore network modeling package," *Computing in Science & Engineering*, vol. 18, p. 60–74, July 2016.

[39] M. Alizadeh, P. Charoen-amornkitt, T. Suzuki, and S. Tsushima, "A numerical simulation of evolution processes and entropy generation for optimal architecture of an electrochemical reaction-diffusion system: Comparison of two optimization strategies," *Journal of The Electrochemical Society*, vol. 170, p. 114520, Nov. 2023.

[40] M. Alizadeh, P. Charoen-amornkitt, T. Suzuki, and S. Tsushima, "Investigation of transport-reaction dynamics and local/global entropy production in topology optimization of two-species reaction-diffusion systems," *Chemical Engineering Science*, vol. 275, p. 118739, July 2023.

[41] M. Long, T. Suzuki, M. Alizadeh, S. Tsushima, and P. Charoen-amornkitt, "The influence of rib and porous reactor thickness on topologically optimized structure in reaction-diffusion systems," in *2023 IEEE Transportation Electrification Conference and Expo, Asia-Pacific (ITEC Asia-Pacific)*, IEEE, Nov. 2023.

[42] S. Lloyd, "Least squares quantization in pcm," *IEEE Transactions on Information Theory*, vol. 28, p. 129–137, Mar. 1982.

[43] M. Akbari, D. Sinton, and M. Bahrami, "Viscous flow in variable cross-section microchannels of arbitrary shapes," *International Journal of Heat and Mass Transfer*, vol. 54, p. 3970–3978, Aug. 2011.

[44] M. Bahrami, M. Michael Yovanovich, and J. Richard Culham, "A novel solution for pressure drop in singly connected microchannels of arbitrary cross-section," *International Journal of Heat and Mass Transfer*, vol. 50, p. 2492–2502, July 2007.

[45] S. Wan, X. Liang, H. Jiang, J. Sun, N. Djilali, and T. Zhao, "A coupled machine learning and genetic algorithm approach to the design of porous electrodes for redox flow batteries," *Applied Energy*, vol. 298, p. 117177, Sept. 2021.

[46] S. Papadopoulos and E. Azar, "Optimizing hvac operation in commercial buildings: A genetic algorithm multi-objective optimization framework," in *2016 Winter Simulation Conference (WSC)*, IEEE, Dec. 2016.

[47] M.-D. Yang, M.-D. Lin, Y.-H. Lin, and K.-T. Tsai, "Multiobjective optimization design of green building envelope material using a non-dominated sorting genetic algorithm," *Applied Thermal Engineering*, vol. 111, p. 1255–1264, Jan. 2017.

[48] L. Magnier and F. Haghighat, "Multiobjective optimization of building design using trnsys simulations, genetic algorithm, and artificial neural network," *Building and Environment*, vol. 45, p. 739–746, Mar. 2010.

[49] HuangMinshui, LingZhongzheng, SunChang, LeiYongzhi, XiangChunyan, WanZihao, and GuJianfeng, "Two-stage damage identification for bridge bearings based on sailfish optimization and element relative modal strain energy," *Structural Engineering and Mechanics*, vol. 86, pp. 715–730, 06 2023.

[50] M. Huang, X. Cheng, and Y. Lei, "Structural damage identification based on substructure method and improved whale optimization algorithm," *Journal of Civil Structural Health Monitoring*, vol. 11, p. 351–380, Jan. 2021.

[51] Z. Deng, M. Huang, N. Wan, and J. Zhang, "The current development of structural health monitoring for bridges: A review," *Buildings*, vol. 13, p. 1360, May 2023.

[52] S. A. Gohardani, M. Bagherian, and H. Vaziri, "A multi-objective imperialist competitive algorithm (moica) for finding motifs in dna sequences," *Mathematical Biosciences and Engineering*, vol. 16, no. 3, p. 1575–1596, 2019.

[53] X. Li, N. Xiao, C. Claramunt, and H. Lin, "Initialization strategies to enhancing the performance of genetic algorithms for the p-median problem," *Computers & Industrial Engineering*, vol. 61, p. 1024–1034, Nov. 2011.

[54] K. Deb, S. Agrawal, A. Pratap, and T. Meyarivan, *A Fast Elitist Non-dominated Sorting Genetic Algorithm for Multi-objective Optimization: NSGA-II*, p. 849–858. Springer Berlin Heidelberg, 2000.

[55] Z. He, M. Gao, Z. Li, Z. Guo, S. Ke, Z. Qi, X. Tu, B. Du, and X. Lai, "Parametrized multi-objective seismic optimization for precast concrete frame with a novel

post-tensioned energy dissipation beam-column joint," *Computers & Structures*, vol. 275, p. 106911, Jan. 2023.

[56] Y. Fang and J. Li, *A Review of Tournament Selection in Genetic Programming*, p. 181–192. Springer Berlin Heidelberg, 2010.

[57] T. Blickle and L. Thiele, "A comparison of selection schemes used in evolutionary algorithms," *Evolutionary Computation*, vol. 4, p. 361–394, Dec. 1996.

[58] C. Fonseca, L. Paquete, and M. Lopez-Ibanez, "An improved dimension-sweep algorithm for the hypervolume indicator," in *2006 IEEE International Conference on Evolutionary Computation*, IEEE, 2006.

Chapter 6

Conclusions and future work

Abstract

This final chapter provides a summary of the core conclusions and insights gained throughout the preceding chapters. The main findings as well as the critical learnings from each part of the research are revisited. Additionally, it outlines several promising avenues for future investigation, expanding on potential developments and areas that could benefit from further exploration.

This chapter is partially published as:

M. Alizadeh, P. Charoen-amornkitt, T. Suzuki, and S. Tsushima. "Recent advances in electrode optimization of electrochemical energy devices using topology optimization", *Progress in Energy*, **7** (2025): 118739.
https://doi.org/10.1088/2516-1083/ad8abd

6.1 Conclusions

This dissertation seeks to address the question of what constitutes a superior structural design for enhancing the performance of porous reactors in applications involving reactive transport phenomena. To tackle this question, a mathematical modeling and optimization approach was employed to systematically generate design solutions with improved performance. In terms of modeling, macro-homogeneous as well as pore-scale modeling were adopted to simulate systems performance. For optimization, density-based topology optimization (TO) and metaheuristic algorithms were applied to optimize the morphology of porous reactors in accordance to the utilized model. These methodologies were applied to various systems, ranging from a simple reaction-diffusion reactor—where only diffusion is coupled with chemical reactions—to a real-world application, the polymer electrolyte membrane fuel cell (PEMFC), in which multiple transport phenomena are integrated with complex electrochemical reactions. Furthermore, this work investigated the underlying physicochemical reasons behind improved designs, attempting to answer the question of what makes a better design truly better. To achieve this, entropy generation analysis was employed to track the optimization process from a physical standpoint. While conventional studies in mathematical optimization focus primarily on the conditions before and after optimization, often disregarding the evolution process unless it bears mathematical or algorithmic significance, this research delved into the intermediate stages of optimization. By doing so, it provided a physicochemical explanation for the characteristics of an optimal structural design in porous reactors. A brief summary and the key conclusions of each chapter are presented below.

In **Chapter 2**, a two-dimensional reaction-diffusion (RD) system was explored, focusing on two species involved in a first-order reversible chemical reaction. The primary goal was to optimize the porosity distribution within a porous reactor to improve the overall reaction rate. To achieve this, a TO method was applied to reshape the reactor's spatial structure, with the aim of forming effective diffusion pathways that facilitate delivery of reactant and discharge of product while keeping the net reaction rate as high as possible. Additionally, an entropy generation model was introduced to assess the system's irreversibilities, offering insights into the thermodynamic implications of the design modifications. The methodologies employed in this research included mathematical modeling of RD system, implemented using FreeFEM++, an open-source partial differential equation solver. The optimization process used the adjoint field method combined with a steepest descent algorithm to

refine the porosity distribution. The results demonstrated that the optimized porosity distribution enhanced system performance by 57% compared to a uniform layout with the same average porosity. The optimal design displayed a tree-root-like configuration, featuring higher porosity near the inlet and lower porosity near the outlet, thereby promoting more efficient diffusion and reaction dynamics. To gain further insights, both local and global rates of entropy production were evaluated to quantify the contributions from different mechanisms during the optimization. Entropy generation was categorized into "inevitable" and "controllable" components. The inevitable entropy refers to the entropy produced due to inherent limitations in the system, such as time and size constraints, which cannot be avoided. This contribution increases as the system's operational duty rises—meaning that as the system is pushed to perform more work or operate under more extreme conditions, inevitable entropy generation escalates accordingly. In contrast, the controllable component of entropy production can potentially be minimized by manipulating the driving forces or transport properties within the system. This component is influenced by design and operational parameters, such as flow rates, concentrations, and porosity distribution. While it is theoretically possible to reduce controllable entropy to zero by perfectly controlling the driving forces, practical limitations often hinder achieving these ideal conditions. Optimizing this controllable entropy is vital for enhancing overall system efficiency. Although the optimization in this chapter focused on maximizing the system's operational duty, scaled entropy was introduced as a normalized measure to account for inherent system limitations. The concept of scaled entropy helped to suppress the impact of inevitable entropy production and was computed based on the square of the reaction rate. While an approximation, it served as a useful index to assess how the optimization process contributed to the improved design.

In **Chapter 3**, building on the research from **Chapter 2**, the RD system was extended into an electrochemical reaction-diffusion (ERD) system. The chemical reaction was replaced by an electrochemical reaction involving electron movement throughout the electrode. Similar to the RD system, the objective was to enhance electrode performance by optimizing material spatial distribution. However, several aspects distinguish the work in this chapter from the RD system. First, the ERD system's physics involved both electron and ion transport resulting from the electrochemical reaction. Additionally, the well-known Butler-Volmer equation was employed to describe the nonlinear kinetics of the electrochemical reaction. Analogous to the catalyst layer (CL) of a PEMFC, the electrode was assumed to have a triple-phase

composition: void space for diffusion of reactant species, a solid phase for electron transport, and an electrolyte phase for ion transport. TO was used to find the optimal distribution of materials within the reactor to achieve the best performance. To thoroughly explore the concept of "best performance" in this context, two different optimization strategies, vertical and horizontal optimizations, were compared in detail. Vertical optimization involved minimizing overpotential at a fixed current density, while horizontal optimization focused on maximizing current density at a fixed overpotential. The former can be interpreted as finding the best material layout to minimize cost while maintaining a fixed doing of the system (current density). The latter, on the other hand, aimed to maximize system doing capacity at a fixed cost (overpotential). The findings revealed that introducing a heterogeneous material distribution within the electrode significantly enhances material utilization and overall performance. Moreover, the choice of the optimization point on the current density-voltage (I-V) curve is critical, as optimized designs may not perform well under varying operational conditions. The differences between vertical and horizontal optimization approaches were further analyzed from a physical perspective by comparing changes in entropy generation during optimization in both cases. The results showed that during optimization, the distribution of entropy production became more equipartitioned. This indicates that the contributions to entropy production from different processes (such as mass diffusion, electric charge transport, and electrochemical reactions) were more evenly balanced, a desirable outcome for improving system efficiency. This physicochemical insight could guide future electrochemical reactor designs and may help establish the upper performance limit for electrochemical systems under non-equilibrium conditions with a given material. A subsequent study [1], not included in this dissertation, demonstrated how employing a mixed TO approach can offer a self-guided method that is independent of the choice of the optimization point.

In **Chapter 4**, TO was employed for the real-world application of CL structural design in PEMFC. A two-phase flow model was developed to accurately simulate the electrochemical and transport phenomena within PEMFCs, especially at high current densities, and was validated against experimental data. The TO algorithm aimed to optimize the CL's material distribution, focusing on increasing output current density at constant voltage. Key findings suggest that an optimal CL design enhances performance by improving reactant delivery and reducing concentration overpotential through better material distribution, particularly under areas with high mass transport losses. This chapter established a robust optimization procedure for

CL design for PEMFC application, emphasizing the need for validated models and future explorations into 3D modeling to capture more complex behaviors and improve real-world applicability.

In **Chapter 5**, a pore-level optimization framework was developed for designing porous reactors involving advection, diffusion, and reaction. The proposed framework integrated pore network modeling (PNM) with metaheuristic optimization algorithms to systematically design porous reactors with high pore-scale resolution. Utilizing PNM enabled modeling reactive transport phenomena without relying on (semi-)empirical relations for describing macroscopic properties such as effective diffusivity and permeability. The investigated processes involved convective flow of an electrolyte solution and advection-diffusion transport of active species within the solution. In addition, the active species reacted in the presence of a solid porous skeleton. The modeling also introduced "throat nodes" to account for local velocity-dependent mass transfer coefficients, previously overlooked in the literature [2, 3]. All simulations were conducted using OpenPNM, an open-source Python-based package for PNM simulations. With the goal of going against the electrolyte flow while improving conversion performance, the optimization problem aimed to maximize the reaction rate while minimizing pumping requirements. By introducing a "background grid" of potential pore locations, this multi-objective optimization was formulated as a binary problem, where the existence of each pore in the final optimal network was algorithmically determined from the grid. A non-dominated sorting genetic algorithm II (NSGA-II) was employed to generate a range of Pareto optimal solutions. The optimization process led to a significant increase in reaction rates (up to 280%) while simultaneously reducing pumping costs by 6%. Furthermore, the study demonstrated that the pore configuration could be effectively tailored to meet desired performance metrics, establishing the proposed framework as a robust tool for high-resolution optimization of porous reactor morphologies.

6.2 Future outlook

Structural optimization and particularly TO hold the promise of crafting groundbreaking electrode structures capable of reducing material usage while enhancing the performance of electrochemical energy devices (EEDs). Nonetheless, several challenges loom on the horizon, including:

1. Given that topologically optimized electrode structures tend to be intricate, the fabrication process presents challenges, particularly due to the electrodes' thickness, often less than 1 mm (for PEFCs, it can be as thin as 10 microns). This issue caused many studies in this field to rely solely on mathematical computations to generate optimal designs but lack sufficient experimental validation to confirm these designs actually work well. Future research could explore innovative methods for fabricating the optimized design solutions generated through mathematical optimization. Additionally, future modeling and optimization studies might incorporate fabrication constraints to ensure the feasibility and practicality of the resulting designs.

2. The primary drawback of this approach lies in its high computational expense, stemming from the iterative assessment of the objective function. This cost can become unaffordable, especially for complex systems with a realistic size and 3D model. To mitigate this challenge, previous research endeavors have frequently resorted to simplifying phenomena into more manageable problems or reducing the design domain or dimensionality to curtail computational expenses. Hence, incorporating all the relevant physics into the TO posed a significant challenge. In addition to that, on the mathematics side, researchers are constantly refining the algorithms used in TO. Their goal is to speed up the optimization process using one or a combination of techniques, including but not limited to multi-grid solvers, model reduction, and machine learning [4].

3. The topologically optimized electrode structure represents a mathematical solution that depends on several parameters, including the objective function, algorithmic approach, tuning parameters, and so on. However, to eliminate dependence on these factors, a robust design theory is necessary. This theory would provide a solid framework for optimizing structures without relying on specific parameters, thus bypassing the optimization process.

4. In optimization techniques like TO, a mathematical model of the system is initially developed, which is solved for evaluation of objective function(s). To ensure reliable design solutions that translate to real-world performance improvements, validating these continuum models against experimental data is crucial. While existing studies using TO for electrode design have validated their models under various operating conditions (e.g. temperature, flow rate, and relative humidity), the applicability of these models to different structural designs remains unclear. To address this, future TO applications should incorporate validation with experimental data encompassing a broader range of

operational and structural variations. Specifically, the employed continuum models should accurately describe the correlation between local microstructure and overall performance [5].

5. Future research could explore the durability and degradation of tailored electrode structures, though this falls beyond the scope of the current thesis. The electrode structures presented here were optimized solely for performance. However, the durability and degradation of these designs occur on a different timescale from steady-state performance, requiring further investigation. To address this, potential approaches may include experimentally or numerically assessing the durability of these designs, or integrating durability models into the optimization process as an additional objective or constraint.

In terms of fabricating topologically optimized electrodes, there is a push to experimentally demonstrate the potency of topologically optimized porous electrodes in practical applications. Currently, the fabrication of these optimized designs proves challenging due to their geometrical complexity. However, with the ongoing progress in additive manufacturing and 3D printing technologies, it is envisioned that these advancements could be leveraged to create such complex structures [6–13]. In one notable study [14], conducted by Beck and Worsley's research team, projection micro-stereolithography was employed to fabricate electrodes for electric double-layer capacitors, as illustrated in Fig. 6.2.1 a and b , resulting in observed enhancements in capacitance. Specifically, a 77% and 99% increase in capacitance was achieved for the optimized electrode compared to the control lattice electrode in numerical simulations and experiments, respectively (see Fig. 6.2.1c). It is essential to note that this demonstration is currently limited to applications involving electrodes with a single material. There is substantial room for researchers to delve into the fabrication of complex structures incorporating multiple materials, such as electrodes for PEFCs containing electronically conductive materials, catalysts, and ionomers. Nevertheless, this type of structure holds promise as a potential avenue for advancing the performance of electrochemical energy storage systems.

In addressing computational costs, the field has long recognized the imperative need for efficient techniques to expedite the design process. To mitigate computational expenses, effective solution schemes and innovative methodologies have been developed. In recent years, machine learning technologies, particularly deep learning methods, have witnessed remarkable success across various applications. These methods have also been employed to alleviate the computational burden of TO by offering predictive solutions [4]. Many of these techniques are generative models,

trained on optimal solutions, which can forecast solutions for similar problems under diverse conditions. The generative models depend on existing optimal designs as training data, setting them apart from conventional TO algorithms. The predictive capabilities of these models are limited by the coverage of the training datasets, necessitating the consideration of new datasets and networks to accommodate diverse domain geometries or constraints. Motivated by these limitations, Deng et al. [15] recently proposed the Self-directed Online Learning Optimization (SOLO) algorithm to significantly expedite the TO process. This algorithm approximates the original costly-to-calculate function by replacing it with a Deep Neural Network (DNN), which learns and maps designs to objectives as a surrogate model. Based on the DNN's optimal predictions, a small amount of training data is dynamically generated. As the algorithm converges, the DNN adapts to the new training data, providing improved predictions in the area of interest. SOLO was tested on four types of simple problems—truss optimization, heat transfer enhancement, fluid-structure optimization, and compliance minimization—and outperformed state-of-the-art algorithms. It substantially reduced computational time by 2 to 5 orders of magnitude compared to directly applying gradient-free heuristic optimization. In the context of utilizing TO to discover groundbreaking electrode structures in EEDs, the integration of machine learning-assisted algorithms is particularly vital. Electrodes pose a complex 3D problem involving multiple non-linear coupled partial differential equations (mass, electronic charge, and ionic charge transports as well as electrochemical rate process). Therefore, employing machine learning techniques can significantly enhance the efficiency and effectiveness of TO processes in this domain. Various objective functions, algorithmic approaches, and tuning parameters yield diverse optimal solutions in TO. To ascertain whether a solution obtained is globally optimal, robust theoretical frameworks are essential. Recently, efforts have been made to link entropy generation to topologically optimized structures, proposing that the optimized structure should minimize entropy generation. Recent findings have indeed demonstrated a connection between entropy generation and optimized structures [16–19]. However, while entropy generation analysis offers valuable insights into electrode design, it falls short of becoming a comprehensive design theory capable of guiding the creation of optimal electrode structures. Research in establishing a theory to design electrodes for high-performance EEDs is pivotal for advancing energy storage and conversion technologies. While the ultimate goal is to develop a comprehensive design theory that obviates the need for TO, current TO outcomes

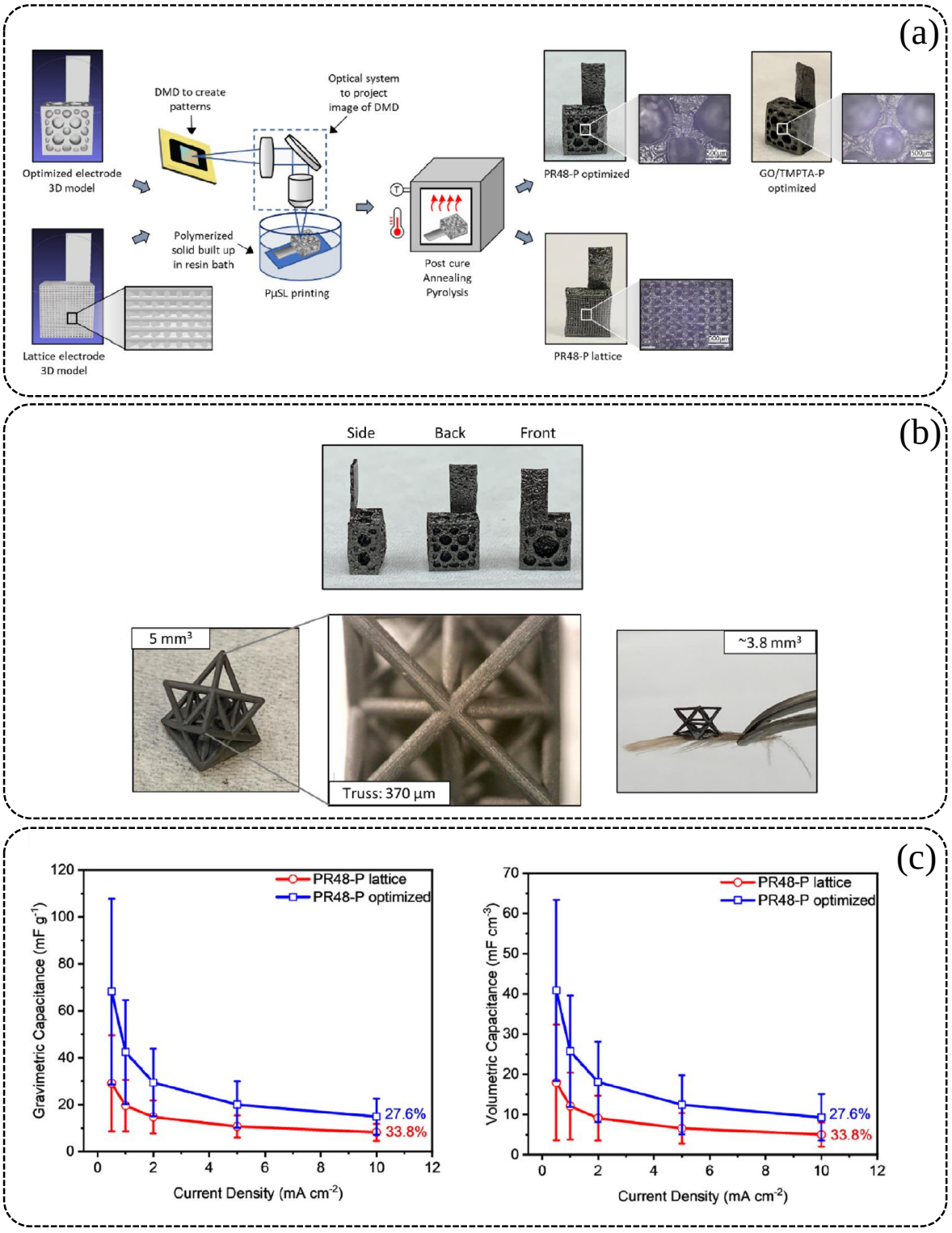

Figure 6.2.1: Examples of employing additive manufacturing to fabricate topologically optimized electrodes.

Figure 6.2.1 ***(continued from previous page)*****:** Schematics and images show (a) the experimental procedure of electrode fabrication employing 3D printing technology, (b) topologically optimized and lattice porous electrodes for supercapacitor application after printing, and (c) comparison between capacitances of topologically optimized and lattice porous electrodes showing the superiority of the topologically optimized electrode over the lattice electrode (Reprinted from Ref [14], Copyright (2023), with permission from Elsevier).

can serve as valuable benchmarks and represent the best available designs for specific applications. The key challenge now is to establish a robust theoretical framework capable of generating these optimal designs without relying on numerical techniques like TO. Such a theory would provide researchers with a systematic approach to electrode design, enhancing the efficiency and effectiveness of EEDs.

In summary, various structural optimization for the design of porous electrodes in electrochemical EEDs represents a new emerging research direction. Topologically optimized electrodes possess the potential to overcome longstanding barriers in efficiency, cost, and performance. The present thesis proposed some novel computer-aided design strategies for electrodes of EEDs. Furthermore, by exploring the intersection of natural design principles and engineering innovation, this thesis inspires future research directions that not only enhance technological capabilities but also deepen our understanding of complex systems in nature. The synthesis of cutting-edge research presented in this thesis is expected to stimulate fruitful discussions and inspire new avenues of inquiry, thereby contributing to the advancement of the global transition towards a sustainable energy future.

Abbreviations

CL	Catalyst layer
DNN	Deep Neural Network
EED	Electrochemical energy device
ERD	Electrochemical reaction-difussion
NSGA	Non-dominated sorting genetic algorithm
PEMFC	Polymer electrolyte membrane fuel cell
PNM	Pore network modeling
RD	Reaction-diffusion
SOLO	Self-directed Online Learning Optimization
TO	Topology optimization

Bibliography

[1] M. Alizadeh, P. Charoen-amornkitt, T. Suzuki, and S. Tsushima, "Mixed topology optimization: A self-guided boundary-independent approach for power sources," *Energy Conversion and Management*, vol. 294, p. 117567, Oct. 2023.

[2] R. van Gorp, M. van der Heijden, M. A. Sadeghi, J. Gostick, and A. Forner-Cuenca, "Bottom-up design of porous electrodes by combining a genetic algorithm and a pore network model," *Chemical Engineering Journal*, vol. 455, p. 139947, 2023.

[3] M. van der Heijden, G. Szendrei, V. de Haas, and A. Forner-Cuenca, "A versatile optimization framework for porous electrode design," *Digital Discovery*, 2024.

[4] S. Mukherjee, D. Lu, B. Raghavan, P. Breitkopf, S. Dutta, M. Xiao, and W. Zhang, "Accelerating large-scale topology optimization: State-of-the-art and challenges," *Archives of Computational Methods in Engineering*, vol. 28, p. 4549–4571, Jan. 2021.

[5] J. C. Bui, E. W. Lees, L. M. Pant, I. V. Zenyuk, A. T. Bell, and A. Z. Weber, "Continuum modeling of porous electrodes for electrochemical synthesis," *Chemical Reviews*, vol. 122, p. 11022–11084, May 2022.

[6] A. Ambrosi and M. Pumera, "3d-printing technologies for electrochemical applications," *Chemical Society Reviews*, vol. 45, no. 10, p. 2740–2755, 2016.

[7] C. Zhu, T. Liu, F. Qian, T. Y.-J. Han, E. B. Duoss, J. D. Kuntz, C. M. Spadaccini, M. A. Worsley, and Y. Li, "Supercapacitors based on three-dimensional hierarchical graphene aerogels with periodic macropores," *Nano Letters*, vol. 16, p. 3448–3456, Jan. 2016.

[8] L. Arenas, C. Ponce de León, and F. Walsh, "3d-printed porous electrodes for advanced electrochemical flow reactors: A ni/stainless steel electrode and its mass transport characteristics," *Electrochemistry Communications*, vol. 77, p. 133–137, Apr. 2017.

[9] J. Lölsberg, O. Starck, S. Stiefel, J. Hereijgers, T. Breugelmans, and M. Wessling, "3d-printed electrodes with improved mass transport properties," *ChemElectroChem*, vol. 4, p. 3309–3313, Oct. 2017.

[10] V. A. Beck, A. N. Ivanovskaya, S. Chandrasekaran, J.-B. Forien, S. E. Baker, E. B. Duoss, and M. A. Worsley, "Inertially enhanced mass transport using 3d-printed porous flow-through electrodes with periodic lattice structures," *Proceedings of the National Academy of Sciences*, vol. 118, Aug. 2021.

[11] E. Vaněčková, M. Bouša, V. Shestivska, J. Kubišta, P. Moreno-García, P. Broekmann, M. Rahaman, M. Zlámal, J. Heyda, M. Bernauer, T. Sebechlebská, and

V. Kolivoška, "Electrochemical reduction of carbon dioxide on 3d printed electrodes," *ChemElectroChem*, vol. 8, p. 2137–2149, June 2021.

[12] J. ZHU, H. ZHOU, C. WANG, L. ZHOU, S. YUAN, and W. ZHANG, "A review of topology optimization for additive manufacturing: Status and challenges," *Chinese Journal of Aeronautics*, vol. 34, p. 91–110, Jan. 2021.

[13] X. Xu, Y. H. Tan, J. Ding, and C. Guan, "3d printing of next-generation electrochemical energy storage devices: from multiscale to multimaterial," *ENERGY & ENVIRONMENTAL MATERIALS*, vol. 5, p. 427–438, June 2021.

[14] M. D. Reale Batista, S. Chandrasekaran, B. D. Moran, M. Salazar de Troya, A. Pinongcos, Z. Wang, R. Hensleigh, A. Carleton, M. Zeng, T. Roy, D. Lin, X. Xue, V. A. Beck, D. A. Tortorelli, M. Stadermann, R. Zheng, Y. Li, and M. A. Worsley, "Design and additive manufacturing of optimized electrodes for energy storage applications," *Carbon*, vol. 205, p. 262–269, Mar. 2023.

[15] C. Deng, Y. Wang, C. Qin, Y. Fu, and W. Lu, "Self-directed online machine learning for topology optimization," *Nature Communications*, vol. 13, Jan. 2022.

[16] P. Charoen-amornkitt, M. Alizadeh, T. Suzuki, and S. Tsushima, "Entropy generation analysis during adjoint variable-based topology optimization of porous reaction-diffusion systems under various design dimensionalities," *International Journal of Heat and Mass Transfer*, vol. 202, p. 123725, Mar. 2023.

[17] M. Alizadeh, P. Charoen-amornkitt, T. Suzuki, and S. Tsushima, "A numerical simulation of evolution processes and entropy generation for optimal architecture of an electrochemical reaction-diffusion system: Comparison of two optimization strategies," *Journal of The Electrochemical Society*, vol. 170, p. 114520, Nov. 2023.

[18] M. Alizadeh, P. Charoen-amornkitt, T. Suzuki, and S. Tsushima, "Investigation of transport-reaction dynamics and local/global entropy production in topology optimization of two-species reaction-diffusion systems," *Chemical Engineering Science*, vol. 275, p. 118739, July 2023.

[19] M. Alizadeh, P. Charoen-amornkitt, T. Suzuki, and S. Tsushima, "Analysis of local-global entropy generation in an electrochemical system," in *Proceeding of International Heat Transfer Conference 17*, Begellhouse, 2023.

Acknowledgements

First and foremost, I would like to express my deepest gratitude to my supervisor, Prof. Shohji Tsushima. His unwavering academic and non-academic support over the years has been invaluable. I am especially thankful for the opportunity he provided me to enter this PhD program and the flexibility he granted me to choose my own research path. Through his guidance, I have learned not only about science but also many important life lessons.

I am also deeply grateful to Assoc. Prof. Takahiro Suzuki for his continuous support throughout my PhD. His insights and encouragement have been instrumental in my academic and personal development.

My sincere thanks go to my dear friend, Asst. Prof. Patcharawat Charoen-amornkitt from King Mongkut's University of Technology Thonburi. As my collaborator and senior, he has provided immense support and mentorship throughout my research. I have learned a great deal from him, and his guidance has been a cornerstone of my work.

I would also like to extend my appreciation to all the members of Tsushima Lab over the past four years for their support and camaraderie. Special thanks to Ms. Chika Shimizu, our lab secretary, for her excellent administrative support, which has been crucial in ensuring the smooth progress of my research.

I am deeply thankful to Prof. Jeff Gostick from the University of Waterloo for the opportunity to collaborate with him during his sabbatical in our lab. The experience was incredibly enriching, and I gained valuable knowledge and skills under his mentorship.

My research and studies were made possible by the financial support from the Japan Society for the Promotion of Science (JSPS). The monthly stipend allowed me to focus on my research without financial concerns, and the research grant significantly enhanced the quality and outcomes of my work.

I am also grateful to the Marubun Research Promotion Foundation, TEPCO Memorial Foundation, and Yashima Environment Technology Foundation for providing travel grants that partially supported my attendance at various international conferences. These opportunities allowed me to disseminate my research on a global stage. Additionally, I thank the Kato Foundation for Promotion of Science for awarding me a Research Scholarship, which further supported my research endeavors.

On a personal note, I want to express my deepest and most heartfelt gratitude to my sister, Mehrasa. Her unwavering support and steadfast belief in me have been my anchor throughout this journey. More than just a source of strength, she has been my role model, embodying qualities of resilience, dedication, and compassion that I aspire to emulate. Her guidance and encouragement made it possible for me to pursue this PhD in Japan, and without her, this journey would have remained a distant dream.

I am forever grateful to my parents, Zoya and Ramezan, whose unconditional love and support have been the bedrock of my life. They have sacrificed so much to ensure that I had every opportunity to succeed. Their belief in my potential, even during times when I doubted myself, has been a constant source of motivation. They taught me the importance of education and the value of pursuing one's dreams, no matter how challenging the path may be. I am deeply grateful for the countless ways they have supported me—emotionally, financially, and spiritually—throughout this journey. This achievement is as much my family's as it is mine, and I dedicate this work to them with all my love and respect.

Finally, I would like to thank all my friends who have supported and encouraged me in various ways throughout this journey. Your kindness and friendship have meant a lot to me.

List of Publications

Journal papers (peer-reviewed) related to this thesis

1. **Mehrzad Alizadeh**, Patcharawat Charoen-amornkitt, Takahiro Suzuki, and Shohji Tsushima. "Recent advances in electrode optimization of electrochemical energy devices using topology optimization", *Progress in Energy* 7, no. 1 (2025): 012003. **[Review Paper]**

2. **Mehrzad Alizadeh**, Patcharawat Charoen-amornkitt, Takahiro Suzuki, and Shohji Tsushima. "A mathematically optimized design solution for structure of PEMFC catalyst layer based on a two-phase flow mode". *Journal of The Electrochemical Society* 171, no. 11 (2024): 114506. **[Original Paper]**

3. **Mehrzad Alizadeh**, Jeff Gostick, Takahiro Suzuki, and Shohji Tsushima. "Topological optimization for tailored designs of advection–diffusion-reaction porous reactors based on pore scale modeling and simulation: A PNM-NSGA framework". *Computers & Structures* 301 (2024): 107452. **[Original Paper]**

4. **Mehrzad Alizadeh**, Patcharawat Charoen-amornkitt, Takahiro Suzuki, and Shohji Tsushima. "A numerical simulation of evolution processes and entropy generation for optimal architecture of an electrochemical reaction-diffusion system: comparison of two optimization strategies". *Journal of The Electrochemical Society* 170, no. 11 (2023): 114520. **[Original Paper]**

5. **Mehrzad Alizadeh**, Patcharawat Charoen-amornkitt, Takahiro Suzuki, and Shohji Tsushima. "Investigation of transport-reaction dynamics and local/global entropy production in topology optimization of two-species reaction-diffusion systems". *Chemical Engineering Science* 275 (2023): 118739. **[Original Paper]**

Other journal papers (peer-reviewed)

1. **Mehrzad Alizadeh**, Patcharawat Charoen-amornkitt, Takahiro Suzuki, and Shohji Tsushima. "Mixed topology optimization: A self-guided boundary-independent approach for power sources". *Energy Conversion and Management* 294 (2023): 117567. **[Original Paper]**

2. Kyu-min Lee, **Mehrzad Alizadeh**, Takahiro Suzuki, Shohji Tsushima, Edward Roberts, and Jeff Gostick. "Multiphysics Simulation of Multi-layered Fibrous

Electrodes for the Vanadium Redox Flow Battery". *Journal of The Electrochemical Society*, 171 (2024): 090534. **[Original Paper]**

3. Mengly Long, **Mehrzad Alizadeh**, Patcharawat Charoen-amornkitt, Takahiro Suzuki, and Shohji Tsushima. "A method for estimating optimized porosity distribution in Reaction-Diffusion systems without reliance on topology optimization". *Chemical Engineering Science* 298 (2024): 120420. **[Original Paper]**

4. Phonlakrit Passakornjaras, Peerapat Orncompa, **Mehrzad Alizadeh**, Patcharawat Charoen-amornkitt, Takahiro Suzuki, and Shohji Tsushima. "Numerical Modeling and Topology Optimization for Designing the Anode Catalyst Layer in Proton Exchange Membrane Water Electrolyzers Considering Mass Transport Limitation". *Journal of The Electrochemical Society* 171 (2024): 074502. **[Original Paper]**

5. Patcharawat Charoen-amornkitt, **Mehrzad Alizadeh**, Takahiro Suzuki, and Shohji Tsushima. "Entropy generation analysis during adjoint variable-based topology optimization of porous reaction-diffusion systems under various design dimensionalities". *International Journal of Heat and Mass Transfer* 202 (2023): 123725. **[Original Paper]**

Conference papers (peer-reviewed) related to this thesis

1. **Mehrzad Alizadeh**, Patcharawat Charoen-Amornkitt, Takahiro Suzuki, and Shohji Tsushima. "Structural topology optimization and irreversibility analysis in an electrochemical reaction-diffusion system". In *AIP Conference Proceedings*, vol. 3086, no. 1. AIP Publishing, 2024.

2. **Mehrzad Alizadeh**, Patcharawat Charoen-amornkitt, Takahiro Suzuki, and Shohji Tsushima. "Analysis of local-global entropy generation in an electrochemical system". In *International Heat Transfer Conference Digital Library*. Begel House Inc., 2023.

Other conference papers (peer-reviewed)

1. Mengly Long, Patcharawat Charoen-Amornkitt, **Mehrzad Alizadeh**, Takahiro Suzuki, and Shohji Tsushima. "Effect of reaction and diffusion parameters on optimized porosity distribution in a reaction-diffusion system". In *AIP Conference Proceedings*, vol. 3086, no. 1. AIP Publishing, 2024.

2. Mengly Long, Takahiro Suzuki, **Mehrzad Alizadeh**, Shohji Tsushima, and Patcharawat Charoen-amornkitt. "The Influence of Rib and Porous Reactor Thickness on Topologically Optimized Structure in Reaction-Diffusion Systems". In *2023 IEEE Transportation Electrification Conference and Expo, Asia-Pacific (ITEC Asia-Pacific)*, pp. 1-7. IEEE, 2023.

3. Patcharawat Charoen-amornkitt, **Mehrzad Alizadeh**, Takahiro Suzuki, and Shohji Tsushima. "Topologically optimized anode catalyst layers of proton exchange membrane water electrolyzers". *ECS Transactions* 111, no. 4 (2023): 87.

4. Mengly Long, **Mehrzad Alizadeh**, Patcharawat Charoen-amornkitt, Takahiro Suzuki, and Shohji Tsushima. "Influence of reaction-diffusion parameters on topologically optimized porosity distribution in reaction-diffusion systems considering temperature dependence". 13th TSME-International Conference on Mechanical Engineering (TSME-ICoME 2023), Thai Society of Mechanical Engineers, December 12 - 15, 2023, Chiang Mai, Thailand, (in press).

5. Phonlakrit Passakornjaras, Peerapat Orncompa, **Mehrzad Alizadeh**, Takahiro Suzuki, Shohji Tsushima, and Patcharawat Charoen-amornkitt, "Topology optimization of anode catalyst layer for polymer electrolyte membrane water electrolyzers considering effect of gas coverage". 13th TSME-International Conference on Mechanical Engineering (TSME-ICoME 2023), Thai Society of Mechanical Engineers, December 12 - 15, 2023, Chiang Mai, Thailand, (in press).

List of Conference Abstracts

Conference oral presentations (first presenter)

1. **Mehrzad Alizadeh**, Jeff Gostick, Takahiro Suzuki, and Shohji Tsushima. "Optimizing porous electrode architecture: Leveraging pore network modeling to enhance flow battery performance". The 34th International Symposium on Transport Phenomena, Pacific Center of Thermal-Fluids Engineering, November 10 - 13, 2024, Taoyuan, Taiwan.

2. **Mehrzad Alizadeh**, Jeff Gostick, Takahiro Suzuki, and Shohji Tsushima. "Tailoring porous reactor topology: a pore-level multi-objective optimization approach". Third Asian Conference on Thermal Sciences (ACTS 2024), Asian Union of Thermal Science and Engineering (AUTSE), June 23 - 27, 2024, Shanghai, China.

3. **Mehrzad Alizadeh**, Jeff Gostick, Takahiro Suzuki, and Shohji Tsushima. "Engineered porous reactors with tailored microstructure for energy conversion applications: a pore network modeling and metaheuristic optimization approach". The International Workshop on Sustainable Energy Conversion Systems (IWSEC), Heat Transfer Society of Japan (HTSJ), May 29 - 30, 2024, Kobe, Japan.

4. **Mehrzad Alizadeh**, Jeff Gostick, Takahiro Suzuki, and Shohji Tsushima. "High-resolution topologically optimized design for porous reactors based on pore-scale modeling and simulation". 5th International Chemical Engineering Symposia, Society of Chemical Engineers Japan (SCEJ), March 18 - 20, 2024, Osaka, Japan.

5. **Mehrzad Alizadeh**, Jeff Gostick, Takahiro Suzuki, and Shohji Tsushima. "Optimizing pore network morphology for enhanced conversion rate in porous catalytic reactors". 64th Battery Symposium in Japan, The Committee of Battery Technology, The Electrochemical Society of Japan (ECSJ), November 28 - 30, 2023, Osaka, Japan.

6. **Mehrzad Alizadeh**, Mengly Long, Pengfei Sun, Patcharawat Charoen-Amornkitt, Takahiro Suzuki, and Shohji Tsushima. "Temperature effects on topologically-optimized structure of porous reaction-diffusion system". The 33rd International Symposium on Transport Phenomena, Pacific Center of Thermal-Fluids Engineering, September 24 - 27, 2023, Kumamoto, Japan.

7. **Mehrzad Alizadeh**, Patcharawat Charoen-Amornkitt, Takahiro Suzuki, and Shohji Tsushima. "Comparison of two optimization approaches in an electrochemical reaction-diffusion system from an entropy generation perspective". 15th Annual International Conference on Porous Media, The International Society for Porous Media (InterPore), May 22 - 25, 2023, Edinburgh, UK.

8. **Mehrzad Alizadeh**, Patcharawat Charoen-Amornkitt, Takahiro Suzuki, and Shohji Tsushima. "A numerical approach to optimize catalyst layer structure of polymer electrolyte fuel cells using non-isothermal three-dimensional simulation". 242nd ECS Meeting, The Electrochemical Society, October 9 - 13, 2022, Atlanta, USA.

9. **Mehrzad Alizadeh**, Patcharawat Charoen-Amornkitt, Takahiro Suzuki, and Shohji Tsushima. "Numerical modeling and simulation of polymer electrolyte fuel cells with different ionomer to carbon ratios in catalyst layers". 59th National Heat Transfer Symposium of Japan, Heat Transfer Society of Japan, May 18 - 20, 2022, Gifu, Japan.

Other conference oral presentations

1. Jeff Gostick, **Mehrzad Alizadeh**, Takahiro Suzuki, and Shohji Tsushima. "Going against the flow: Optimizing redox flow battery electrode structures for higher power at lower pumping cost". 75th Annual Meeting of the International Society of Electrochemistry, August 18 - 23, 2024, Montreal, Canada.

2. Pengfei Sun, **Mehrzad Alizadeh**, Patcharawat Charoen-Amornkitt, Takahiro Suzuki, and Shohji Tsushima. "Experimental analysis of the effect of pulsating flow on the overpotential of vanadium redox flow battery". Third Asian Conference on Thermal Sciences (ACTS 2024), Asian Union of Thermal Science and Engineering (AUTSE), June 23 - 27, 2024, Shanghai, China.

3. Poramet Aiemsathit, Pengfei Sun, **Mehrzad Alizadeh**, Yossapong Laoonual, Patcharawat Charoen-Amornkitt, Takahiro Suzuki, and Shohji Tsushima. "Improving all-vanadium redox flow batteries in flow-through cells through topology optimization of porous electrodes". Third Asian Conference on Thermal Sciences (ACTS 2024), Asian Union of Thermal Science and Engineering (AUTSE), June 23 - 27, 2024, Shanghai, China.

4. Peerapat Orncompa, Phonlakrit Passakornjaras, **Mehrzad Alizadeh**, Patcharawat Charoen-Amornkitt, Takahiro Suzuki, and Shohji Tsushima. "Optimization of anode catalyst layer in pemwe considering the presence of oxygen". Third

Asian Conference on Thermal Sciences (ACTS 2024), Asian Union of Thermal Science and Engineering (AUTSE), June 23 - 27, 2024, Shanghai, China.

5. Pengfei Sun, **Mehrzad Alizadeh**, Takahiro Suzuki, and Shohji Tsushima. "Experimental analysis of overpotential in vanadium redox flow batteries induced by pulsating flow". The International Workshop on Sustainable Energy Conversion Systems (IWSEC), Heat Transfer Society of Japan (HTSJ), May 29 - 30, 2024, Kobe, Japan.
6. Mengly Long, **Mehrzad Alizadeh**, Patcharawat Charoen-Amornkitt, Takahiro Suzuki, and Shohji Tsushima. "Effect of design dimensionality on topologically optimized porous structures of reaction-diffusion system". 64th Battery Symposium in Japan, The Committee of Battery Technology, The Electrochemical Society of Japan (ECSJ), November 28 - 30, 2023, Osaka, Japan.
7. Pengfei Sun, Kaito Matsuo, **Mehrzad Alizadeh**, Patcharawat Charoen-Amornkitt, Takahiro Suzuki, and Shohji Tsushima. "Investigation of polarization in vanadium redox flow batteries with a fluctuating supply of electrolyte solution". 244th ECS Meeting, The Electrochemical Society, October 8 - 12, 2023, Gothenburg, Sweden.
8. Patcharawat Charoen-Amornkitt, Mengly Long, **Mehrzad Alizadeh**, Takahiro Suzuki, and Shohji Tsushima. "Numerical analysis on optimization of porosity distribution in a reaction-diffusion system using an adjoint method". 59th National Heat Transfer Symposium of Japan, Heat Transfer Society of Japan, May 18 - 20, 2022, Gifu, Japan.

Conference poster presentations (first presenter)

1. **Mehrzad Alizadeh**, Jeff Gostick, Takahiro Suzuki, and Shohji Tsushima. "Optimization of porous reactors morphology based on pore network modeling and metaheuristic algorithms". 16th JHPCN Symposium, Joint Usage/Research Center for Interdisciplinary Large-scale Information Infrastructures (JHPCN), July 11 - 12, 2024, Toyko, Japan.
2. **Mehrzad Alizadeh**, Patcharawat Charoen-Amornkitt, Takahiro Suzuki, and Shohji Tsushima. "Optimization of material distribution in electrodes of power generating devices: a mixed approach". 244th ECS Meeting, The Electrochemical Society, October 8 - 12, 2023, Gothenburg, Sweden.

3. **Mehrzad Alizadeh**. "Toward next-generation electrochemical devices: A second law of thermodynamics approach". 14th HOPE Meeting, Japan Society for the Promotion of Science (JSPS), February 27 - March 3, 2023, Tsukuba, Japan.

4. **Mehrzad Alizadeh**, Patcharawat Charoen-Amornkitt, Takahiro Suzuki, and Shohji Tsushima. "Entropy generation analysis in a quasi-3D PEM fuel cell model with architectured electrocatalyst layer". 15th Annual International Conference on Porous Media, The International Society for Porous Media (InterPore), May 22 - 25, 2023, Edinburgh, UK.

5. **Mehrzad Alizadeh**, Patcharawat Charoen-Amornkitt, Takahiro Suzuki, and Shohji Tsushima. "Improvement of PEM fuel cell performance through a topologically optimized catalyst layer structure". 9th International Fuel Cell Workshop 2022 (IFCW2022), Yamanashi University, November 15 - 16, 2022, Kofu, Japan.

About the author

Mehrzad Alizadeh was born on April 15, 1994, in Babol, Iran. He received his BSc and MSc degrees in Mechanical Engineering from K. N. Toosi University of Technology, Iran, graduating in 2016 and 2019, respectively. In December 2020, he joined the "Reaction and Transport Dynamics in Energy Devices" lab at Osaka University, Japan, as a Research Student under the supervision of Prof. Shohji Tsushima. In April 2022, he began a PhD program in Mechanical Engineering at the same lab. He received a Young Scientists fellowship (DC1) from the Japan Society for the Promotion of Science (JSPS) to support his doctoral studies. During his PhD, he worked on modeling and optimizing the structure of electrodes for electrochemical energy devices with a focus on reactive transport phenomena within porous media.